INVESTIGATING THE FUNCTIONALISATION OF POLY-ETHER-ETHER-KETONE SURFACES THROUGH THE APPLICATION OF SURFACE TEXTURING FOR FRICTION AND WEAR CONTROL WITHIN ALL POLYMERIC JOINT PROSTHESIS

By

CHRISTOPHER WILLIAM HARRIS

A thesis submitted to
The University of Birmingham
for the degree of

DOCTOR OF PHILOSOPHY

School of Mechanical Engineering
The University of Birmingham
June 2018

Abstract

This thesis investigates the application of surface textures applied to an un-filled poly-ether-ether-ketone (PEEK) surface via laser ablation for the purpose of friction and wear control. Surface functionalisation was demonstrated by the manipulation of surface characteristics via texturing. Improving surface wettability characteristics showed that increasing surface hydrophilicity improved the surfaces' friction and wear performance.

Within durability tests a novel approach, in the form of acoustic emissions (AE), was employed to monitor tribological activity within an all PEEK sliding couple. AE output was correlated with individual strokes throughout the test and the magnitude and frequency of the captured AE signal was used to ascertain an understanding of tribological phenomena occurring within the tribo-system.

Texture parameters were investigated, showing a diameter/depth combination of 50μm and 20μm respectively were optimum for friction reduction when dispersed over the surface at a density of 20%. Friction reduction for textured surfaces was attributed, in part, to the generation of hydro-dynamic lift.

To verify hydrodynamic behaviour, the system was modelled using the Reynolds equation, and the viscous friction was computed and compared to empirical results. Good agreement across diameters and aspect ratio were captured however, the depth showed to vary considerably for shallower pores of smaller diameter.

Durability tests, showed that a textured surface outperformed an un-textured surface by 3 times. The primary mechanism contributing to the low friction and wear of textured surfaces was the retention of fluid within the contact zone and the reduction in abrasive wear particles through the wear trapping capabilities of the textured pores.

DEDICATIONS

For Lizzy

"Courage and grace are a true inspiration, you had them in abundance lil' sis, Love Forever"

And Kristie

"For all you do, for who you are, I will be forever grateful you are in my life.

Thank You"

Acknowledgments

I would like to express my deepest gratitude and thanks to supervisor, Dr. Karl Dearn for his full support, productive guidance and invaluable advice throughout this research, thank you.

And of course, I would like to thank my wife for her love, support and patience. And my parents for the encouragement and motivation to keep going throughout my study.

Contents

CHAPTER 1

Introduction and Literature Review

1.1 Introduction

The reduction of friction and wear within many applications represents a current and on-going challenge for tribologists across numerous industry sectors. In its simplest form, friction is the force that opposes the direction of motion. In the absence of adequate lubrication friction increases due to interactions between opposing surface asperities, encouraging deformation and adhesive forms of friction leading to the manifestation of various wear mechanisms culminating in surface degradation. While friction ultimately impacts the operational efficiency of components within a system through parasitic losses, the subsequent wear influences the longevity and reliability of frictional surfaces. In order to preserve the integrity of engineering surfaces various friction and wear reducing approaches have been employed, such as enhancing lubrication fluids, surface coatings/films and topological modifications.

Lubricant additives for base oils have confronted many of the problems associated with frictional losses of mechanical systems. Lubricant additives play an important role in enhancing an oils tribological performance. The formation of additive layers by either absorption via Van Der Waals forces, where polar ends of additive molecules attaches to the steel surface, or by a chemical reaction between active oil components and metallic surfaces at moderate to high temperatures to form low shear strength thin films (Bovington, 2010). Lubricant additives offer an array of performance improving properties in relation to their specific application including anti-wear, viscosity index

improvers and anti-oxidation. However, over time these additives become saturated and regular maintenance intervention is required to replenish the additives through re-lubricating components.

The application of hard surface coatings, within tribological systems enhances surface strength and reduces friction. Whereas soft coatings serve as a sacrificial layer whereby the surface wears to aid in the conformability between mating components such as journal bearings. The complexities associated with integrating the proper coating parameters in relation to its application is a major consideration; coating thickness, hardness, coating to substrate bonding and surface roughness influence tribological performance (Haque, et al., 2009). In addition, the application of a surface coating alters the properties such as surface energy, wettability and spreading characteristics of the original surface that could reduce the effectiveness of the lubricant in reducing friction and wear (Grischke, et al., 1998), (Ahmed & Bryne, 2012), (Kalin & Polajnar, 2014). This is due to commercial oils typically being optimized through lubricant additives, to be compatible with ferrous surfaces (Haque, et al., 2009). However, changes in properties such as surface tension, with the application of surface coatings, may affect the formation of a lubricant additive layer. Incorrectly applied surface coating parameters can result in catastrophic failures through de-bonding and delamination of the coating layer or the fracture of a hard coating bonded to a softer material. Both instances can lead to the generation of debris causing further damage to the surface layer.

Modifications of surface topology for friction control can be split into two broad sub-sets; the first is randomly generated surface roughness; a bi-product from conventional machining processes such as the honing of engine cylinders (Sabri & El Mansori, 2009). The second is the application of deterministic surface features designed to functionalise

a surface in the form of texturing (Etsion, 2005). Over the past three decades surface texturing has become widely considered as a viable technique for improving the tribological performance of mechanical components.

The concept of texture design for the functionalisation of a surface is inspired by elements of nature, mimicking the properties of bio-organisms to suit a required application. An example of which is the 'Lotus Effect' (Singh & Kahp-Yang Suh, 2013) where the micro-structure of a lotus leaf offers self-cleaning properties through super-hydrophobic wetting capabilities or the 'Sharks Skin Effect' that mimics the micro-structure of a sharks skin to reduce drag and friction force (Liu & Li, 2012).

It is the replication of articular surfaces for prosthetic applications that is a major challenge within the field of bio-tribology. Within biomedical applications synovia is the body's natural lubricating fluid. The exact lubricating mechanism of synovial fluid still remains a prominent area of study for researchers due to being a highly non-Newtonian fluid and with a complex nature. Moreover, the role of cartilage in its composition further complicates the problem of deriving the precise lubricating mechanisms within articular joints. Many theories on the subject of lubrication of natural joints have been put forward; early work, by Reynolds (Reynolds , 1886) postulated a fluid-film lubricating mechanism. The theory was supported by MacConaill (MacConaill, 1932) concluding that a Reynolds hydrodynamic wedge action contributes to the low friction within joints, suggesting that poorly fitting joints provided the geometry necessary to provide a fluid wedge effect. Charnley (Charnley, 1960) repeated McConial's (MacConaill, 1932) experiments with contradictory results indicating a boundary lubrication mechanism. The inconsistencies in experimental studies have led to further lubricating mechanisms being postulated over the last century. McCutchen alluded to the existence of fluid filled dimples on the

cartilage surface that would pressurize under compressive forces creating a hydrostatic effect increasing a surface's load bearing characteristics (McCutchen, 1959). McCutchen termed the findings as a 'weeping effect' in relation to a 'sponge' like action of the porous cartilage that weeps fluid, generating hydrostatic pressure between the surfaces (McCutchen, 1959). Alternative to McCutchen's proposed theorem Tanner related the contact conditions of synovial joints to mechanical components in gears and roller element bearings, both of which generate high contact pressures whilst still maintaining adequate friction and wear characteristics. Tanner suggested similarities in the mode of operation and the presence of an elasto-hydrodynamic lubrication (EHL) regime, however stipulated that the function of the porous cartilage is unknown. The model developed by Tanner calculated the friction coefficient to be lower than that of actual joints, attributing this to not accounting for surface roughness and asperity contact that would increase friction (Tanner, 1966). The concept of an EHL regime was also investigated by Dowson with good agreement with Tanner (Tanner, 1966). Dowson noted that human joints operate within the 'mixed' lubrication, EHL and boundary regime depending upon the action the joint is undergoing e.g., standing, walking etc. (Dowson, 1966).

The discussion above outlines the difficult task for tribologists to replicate the tribological performance of synovial joints for artificial prosthesis particularly in the absence of natural cartilage. Unlike mechanical applications the possibilities for improving tribological conditions are constrained, the examples of friction and wear reducing techniques; lubricant modifications and surface coatings, offer limited scope to improve lubrication within bio-medical applications.

The primary aim of this research is focussed on reducing the friction and wear rate in biomedical applications. Replicating the contact conditions that may be found in artificial joint devices, with the majority of works being concentrated upon material type and wear couple combinations.

1.2 Motivation for work

Friction control of articulating prosthetic surfaces is an essential feature within the mechanical design of medical devices. Imperative is the preservation of a components surface in order improve the longevity and efficiency over its service life.

Total prosthetic joint replacements tend to be constructed from the following material combinations metal-on-metal, polymer-on-metal or ceramic-on-ceramic. Such combinations perform well within their application however, such prosthesis still exhibit frailties with regard to their longevity. A common cause of failure within ultra-high-molecular-weight-polyethylene (UHMWPE) on metal combinations occurs through wear debris induced osteolysis that initiates prosthetic loosening (Ingham & Fisher, 2005). Friction and wear processes that occur within metal on metal wear couples contribute to the production of metal ion accumulations that present certain health risks (Zeh, et al., 2007) (Brown, 2006).Ceramic-on-ceramic frictional combinations have shown promise, recording low friction results within joint simulator studies. However, the reduced toughness and brittle nature of ceramic components could lead to component fracture (De Aza, et al., 2002) (Brown, 2006).

Although not as rigorously studied, the potential of polymer-on-polymer frictional couples remain an under explored combination, however they are of interest within the bio-medical field. The application of polymers could offer greater design flexibility in

relation to the conformability of mating surfaces. In addition, polymer composite design could provide the potential for application specific prosthesis. Furthermore, the prospect of all polymer implants can reduce stress shielding that induces bone resorption which occurs when harder materials are employed.

All PEEK couples have been studied in-vitro spine simulator tests for total disc replacement (TDR). Xin et *al.* showed that a PEEK-PEEK combination displayed a steady wear rate over the test duration, suggesting that the system operates within a mixed or boundary lubrication regime and that the primary wear mechanism was that of abrasion (Xin, et al., 2013). Studies conducted employing carbon-fibre-reinforced (CFR) PEEK have demonstrated lower wear rates compared to PEEK, and similar to that of UHMWPE when sliding against hard surfaces (Scholes & Unsworth, 2009). However, East et *al*. indicated that PEEK is more suitable than CFR PEEK for articulation within an all polymer sliding couple due to the carbon fibres acting as an abrasive, increasing wear (East, et al., 2015).

The friction and subsequent wear of soft articulating surfaces still remains a prominent issue within polymeric component design. Friction induced wear mechanisms of polymers represents a major obstacle in the operational longevity of polymeric based artificial joints. Kurtz et *al*. retrieved spinal disc replacements from 18 patients undergoing spinal TDR. Analysis of the implants showed evidence of surface morphology consistent with an abrasive and adhesive wear mechanism (Kurtz, et al., 2007). Eckold et *al*. investigated the nature of wear debris by conducting in-vitro wear studies using an UHMWPE TDR implant, concluding that abrasive and adhesive wear was the dominant wear mechanism in the early stages of testing (< 2million cycles). This

was followed by fatigue wear becoming more prevalent in the latter stages of testing (2-5 million cycles) (Eckold, et al., 2015).

One of the main problems with monitoring the frictional behaviour in polymers is that changes in load and speed have a limited effect on the friction recorded. Friction readings that are independent of speed have been observed between 1mm and 10mm/s, whilst loading in the range of 10N to 100N also offers little fluctuation in terms of the resultant friction (Myshkin, et al., 2005). Given this, the work in this thesis presents a novel approach to the in-test monitoring of polymers by the capture of acoustic emissions as a means of analysing frictional behaviour within an all polymer sliding contact.

Acoustic emissions (AE) are transient stress waves generated by an external stimulus. Within tribological applications these transient waves produced are generated by the interaction of two media in relative motion (Mba & Rao, 2006). AE signals would therefore be created in such instances as the initial interaction of surface asperities and become more pronounced with surface degradation through continual operation and the manifestation of wear mechanisms associated with a particular application. The incorporation of the acoustic emission technique for the monitoring of polymeric frictional contacts could provide a more holistic understanding of the differences in tribological performance between textured and non-textured polymers surfaces.

1.2.1 Aim

The specific aim of this research of the work presented was to explore functionalisation of a Poly-ether-ether-ketone surface via the application of surface textures for friction and wear control for application within an all PEEK prosthetic joint. The objectives to meet this aim were to:

i. Empirically assess the tribological properties of circular shaped dimple textures applied to a Poly-ether-ether-ketone (PEEK) surfaces, tested in relation to the experimental standards for the testing of polymeric surfaces for prosthetic joints.

ii. Experimentally derive optimum texture dimensions for improved frictional performance.

iii. Through theoretical modelling and experimental testing show evidence of the operational characteristics synonymous with the application of surface textures within tribological sliding systems.

iv. Verify the application of acoustic emissions for monitoring tribological phenomena within all polymer sliding systems.

v. Assess and explain the operational life cycle and durability of textured surfaces compared to un-textured surfaces using frictional data, acoustic emissions captured and wear morphology gathered from tests conducted under rigorous sliding conditions.

1.3 Literature Review

1.3.1 Tribology Background

Tribology is the science of friction, wear and lubrication, and covers the behaviour of interacting surfaces in relative motion. Leonardo Da Vinci is widely recognised with being one of the first of note to study the field of, what we now know as tribology, and is credited for defining the fundamental ‘laws’ of friction, which were later articulated by Guillaume Amontons in 1699 (Hutchings, 2016). Further developments in the findings of Da Vinci and Amontons was made by Charles-Augustin de Coulomb in 1785 who distinguished between static and kinetic friction, stating that each were independent of velocity (Khonsari & Booser, 2017). The findings of the aforementioned tribologists form the three laws of friction:

- Friction between two sliding surfaces is proportional to the load
- Friction is independent of the apparent area of contact between the two surfaces.
- Friction is independent of the sliding speed.

Friction

The primary components of friction within an un-lubricated sliding contact are adhesion and deformation (Bowden & Tabor, 1966) .The adhesion term relates to junction formation and growth between local asperities of two opposing surfaces. Under a tangential load the junctions are required to shear before gross sliding can commence. The deformation component arises through material yielding such as ploughing, grooving or crack initiation.

The type of friction a system experiences can broadly be separated in to two types; static and kinetic friction. Static friction occurs when there is no relative motion between two opposing surfaces. Relative motion occurs once the force resisting motion is overcome by the applied force. Kinetic friction can be described as the resistance force opposing the direct of motion. Both static and kinetic friction forces are described in Figure 1-1 where the transition between static and kinetic friction can be seen in Figure 1-2.

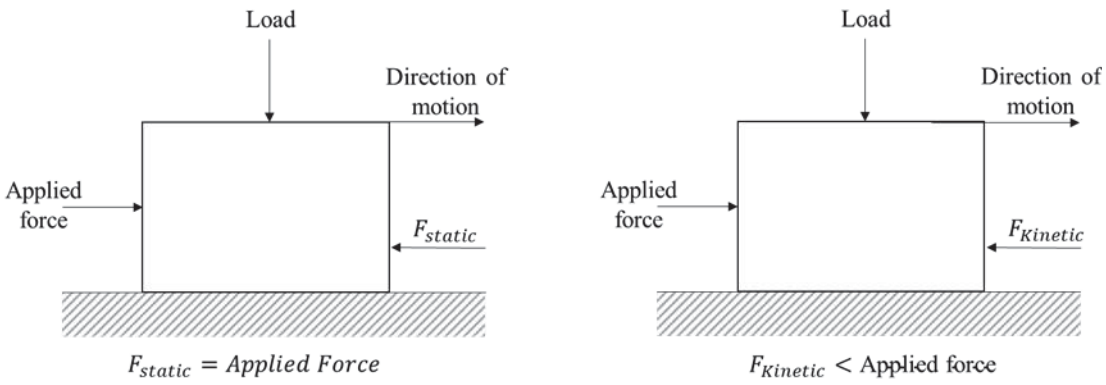

Figure 1-1: Diagram showing static and kinetic frictional forces acting on a body in the absence of lubrication.

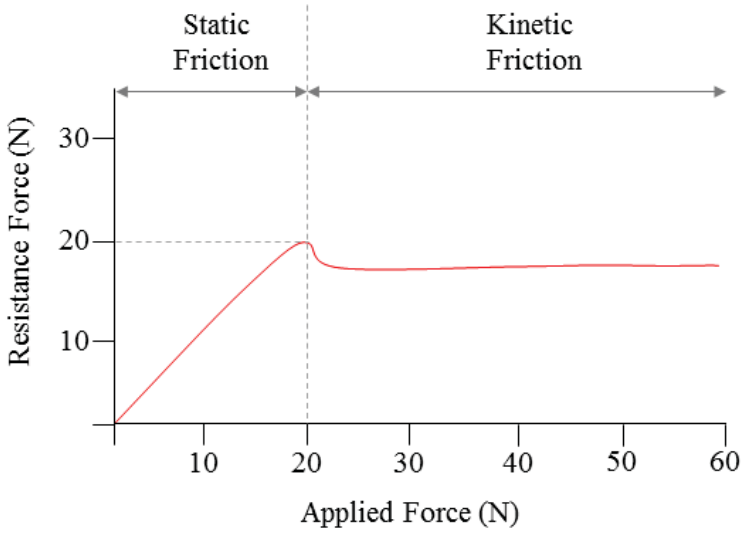

Figure 1-2: Transition from static to kinetic friction showing resistance force as a function of applied force

For friction within a lubricated contact an alternative form of friction arises; viscous friction. Viscous friction is where the force resisting an applied force is the viscous forces of the lubricant. This form of friction occurs within the hydrodynamic region of a lubricated systems operational envelope and can be adequately described by the Stribeck diagram, named after its author Richard Stribeck (1861-1950), (Hori, 2006).

Lubrication Regimes

The lubrication regimes that various engineering components operate within can be explained by use of the Stribeck curve shown in Figure 1-3. Where the y-axis denotes the friction coefficient and the x-axis is the Stribeck number given by:

$$\frac{U * \upsilon}{L}$$ **Equation 1-1**

Where U is sliding velocity, v is dynamic viscosity and L is the applied load.

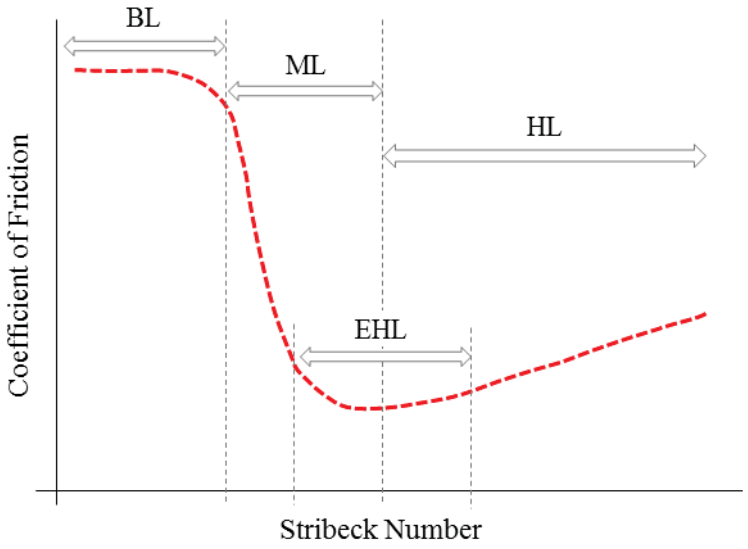

Figure 1-3: Stribeck diagram plotting coefficient of friction as a function of the Stribeck number. Annotated upon the diagram are the four lubrication regimes: BL – Boundary lubrication, ML – Mixed lubrication, EHL – Elasto-hydrodynamic lubrication, HL – Hydrodynamic lubrication

The primary lubrication regimes are illustrated in Figure 1-4a, b and c. The boundary regime exists where the local asperities are in contact and the load is entirely supported by the contact between the opposing surfaces. Within a mixed regime the load is partially supported by asperity contact in addition to a thin fluid film. Finally within the hydrodynamic region the load is entirely supported by the lubricating fluid.

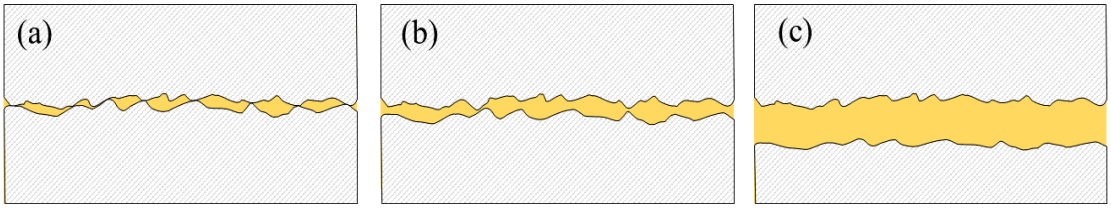

Figure 1-4: Illustration of lubrication regimes: (a) boundary (b) mixed (c) hydrodynamic

In many circumstances the mechanism for how a load is supported by a lubricating film is governed by its contact configuration which can be broadly set into two categories; conformal and non-conformal contact.

Elasto-Hydrodynamic Lubrication

Lubricated systems containing non-conforming solid bodies contact each other at a point or along a line. Mechanical components such as roller bearings and gear teeth experience such contact configurations and often operate within the elasto-hydrodynamic lubrication regime (EHL), which is shown within the on the Stribeck diagram (Figure 1-3). Within an EHL lubricated contact separation of opposing surfaces is of an equivalent order to that of the surface roughness and both asperity contact and lubricant support exist (Dwyer-Joyce, et al., 2011). Load support within a non-conforming contact relies upon the influence that the high pressure within the contact region has upon the visco-metrics

of the lubricating fluid. Moreover, the application of high loads leads to substantial local deformation of the opposing solid bodies (Dowson & Higginson, 1977).

Figure 1-5 shows the fluid pressure within an EHL contact whereby the inlet and outlet regions are partially flooded and the pressurised region is fully flooded (Ebner, et al., 2018). Fluid pressure gradually increases at the inlet to the contact zone. Within the pressurised region the high contact pressures cause the solid surfaces to deform. Under such high contact pressure the lubricating fluid's viscosity increases and the fluid becomes trapped within the contact separating the two surfaces. At outlet a constriction occurs caused by the deformation of the bodies and represents the region of minimum film thickness and highest fluid pressure.

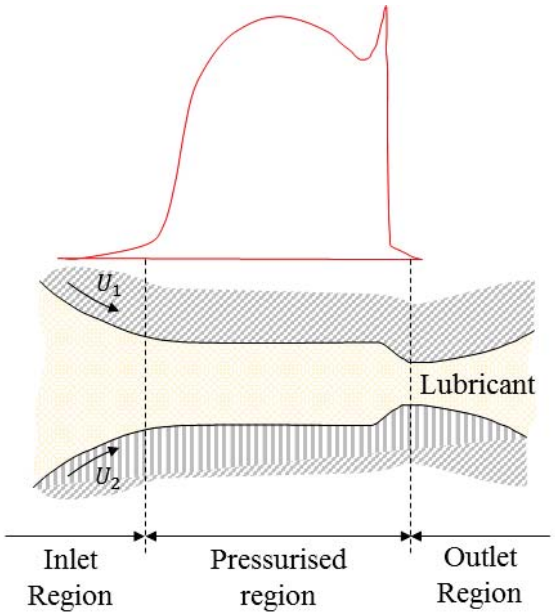

Figure 1-5: Illustration of deformation between two non-conformal bodies showing the resultant pressure profile of the lubricating fluid

Hydrodynamic Lubrication

Hydrodynamic lubrication is often found within many conformal contact configurations such as journal bearings and piston liner systems. In the case of a journal bearing shown in Figure 1-6, oil enters the top of the bearing. The rotational direction of the shaft forces the fluid to the right hand side of the bearing, where on the left hand side a low pressure cavitation region is present. The eccentricity of the journal and bearing creates a fluid film wedge. As fluid enters this region the converging gap between the two surfaces causes an increase in fluid pressure. The hydrodynamic pressure generated keeps the two surfaces from being in contact as the shaft rotates upon a film of oil (Hori, 2006). Owing to the separation of the two surfaces the friction generated within the hydrodynamic regime is caused by viscous forces acting against the direction of motion.

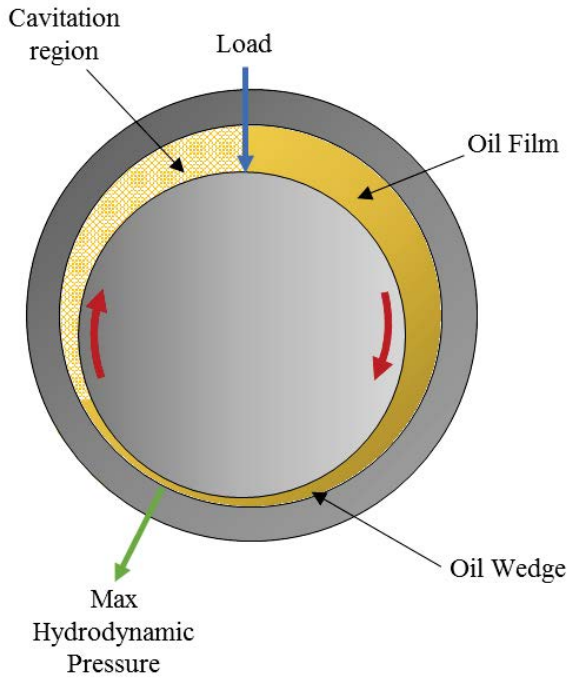

Figure 1-6: Hydrodynamic journal bearing showing oil wedge caused by the eccentricity of the shaft to bearing and the approximate location of maximum oil pressure.

Although during the early work within the field of tribology the notoriety and importance of the subject wasn't clearly understood until Osbourne Reynolds (Reynolds , 1886) released he's pioneering paper on hydrodynamic lubrication in 1886 (Stachowiak & Batchelor, 1993). The findings had huge practical implications where Reynolds showed that the hydrodynamic pressure developed by a fluid was sufficient enough to prevent contact between two opposing surfaces resulting in lower friction.

The equation of hydrodynamic pressure, more commonly known as the Reynolds equation, is given in Equation 1-2. The Reynolds equation is derived and an explanation provided in Chapter 5.

$$\frac{\partial}{\partial x}\left\{h^3\frac{\partial p}{\partial x}\right\}+\frac{\partial}{\partial z}\left\{h^3\frac{\partial p}{\partial z}\right\}=6\mu\frac{\partial h}{\partial x}U_2+12\mu(V_2-V_1) \qquad \textbf{Equation 1-2}$$

Wear

Wear can occur through mechanical or chemical means, however both include the removal of solid material. Six types of wear mechanisms are: (1) adhesive, (2) abrasive, (3) fatigue, (4) erosion, (5) corrosive and (6) electrical-arc induced wear (Bhushan, 2002). Of these six wear mechanisms the first three shall be explained in more detail owing to their relevance within the current research and their severity to mechanical components.

Adhesive Wear

Adhesive wear is the bonding of asperities at local contact spots and junction growth. The loss of material is caused by rupture of the junction through an applied force, such as sliding. Within such circumstances material is either transferred to the surface of the more dominant surface or is released as wear particles (Stachowiak & Batchelor, 1993).

Although the boundary regime is dominated by an adhesive wear mechanism the wear mode can also occur between lubricated contacts during periods of starvation or in instances where the functionality of the lubricant fluid is diminished.

Abrasive Wear

Abrasive wear is caused by hard asperities sliding over softer materials causing damage to the surface. In many cases the abrasive wear mechanism is caused by wear debris which is either attached to the opposing surface or are free. Particles that have adhered to the opposing surface is named second body abrasion and where free particles exist between the two surfaces the wear mechanism is expressed as third body abrasion. In both cases the resultant wear is that of plastic deformation of the surface through ploughing of the more ductile of the two surfaces. Terms associated with the severity of abrasive wear range from scratching up to more severe abrasive wear such as gouging (Bhushan, 2002).

Fatigue Wear

Fatigue wear is generated by repeated sliding or rolling cycles which cause high contact stresses. Wear particles are generated by the formation of surface or sub-surface cracks which propagate through the material. Once cracks adjoin fragments of the surface become free and are ejected from the surface. The result is the formation of pits on the surface, a mechanism known as pitting (Bhushan, 2002).

The objective of surface texturing as a tribological enhancing technology is to reduce the effects of friction between two opposing surfaces in relative motion. Within this, improving lubrication through hydrodynamic lift, providing a fluid film that reduces solid body contact. However improving lubrication in this sense cannot become detriment to the operational efficiency of the system, for instance increasing parasitic losses through

viscous friction. Therefore the ideal scenario is to operate within the hydrodynamic regime, illustrated in Figure 1-3, at a low Stribeck number.

In enhancing lubrication between the two opposing surfaces the adhesive wear mechanism can be minimised, improving the longevity of a components surface. Furthermore, abrasive wear particles can be removed from the contact zone by the flow of lubricant fluid, reducing second and third body abrasive wear.

The following section provides a literature survey of surface texturing within tribology, texture parameters and the potential benefits within the application of surface textures.

1.3.2 Surface Texturing in Tribology

Since the pioneering work at Technion, Israel, in the mid-1990's research conducted on surface texturing for improved tribological performance has been applied to various applications. The Technion group's first substantial contribution was through the texturing of mechanical seals (Etsion & Burstein, 1996). Etsion and Burstein (Etsion & Burstein, 1996) presented a model based upon the Reynolds equation to estimate seal performance with the introduction of surface micro-structures, finding increases in load capacity and enhanced seal performance. The authors also stated that seal performance fluctuated with varying texture parameters. Etsion and Halperin (Etsion & Halperin, 2002) empirically evaluated the application of surface textured mechanical seals validating the conceptual model of Etsion and Burstein (Etsion & Burstein, 1996) highlighting the hydrodynamic pressure generated by the micro-pores reduced frictional torque, seal face temperature and overall wear rate, moreover, optimum pore diameter was shown to be influenced by fluid viscosity. Further contributions by the Technion group have included the modelling and experimental validation of micro structures

imparted on the surface of parallel thrust bearings (Brizmer, et al., 2003) and the surface texturing of reciprocating automotive components (Ronen, et al., 2001) (Ryk, et al., 2002) (Etsion, 2004). Ronen et *al.* (Ronen, et al., 2001) theoretically evaluated the concept of surface texturing within a reciprocating system based upon a piston-cylinder arrangement. The parametric study evaluated the effect of texture parameters on pressure generation and the average viscous friction force during reciprocating sliding, finding that an optimum dimensionless parameter of texture depth/diameter termed aspect ratio exists. The ratio has since been adopted in many experimental studies as a means of deriving optimum texture parameters. However, it should be noted that Ronen et *al*., eluded to texture parameters being application-specific based upon a system's characteristics (Ronen, et al., 2001).

1.3.3 Surface Texture Parameters

The geometric parameters of surface textures are governed by the shape of the texture. Circular pores (Kovalchenko, et al., 2005), (Borghi, et al., 2008), triangles (Chen , et al., 2016), (Wang, et al., 2013), squares (Pettersson & Jacobson, 2003), (Rahmani, et al., 2007), grooves (Pettersson & Jacobson, 2003), (Yuan, et al., 2011) and ellipses (Yu, et al., 2010), (Hsu, et al., 2014) possessing varying dimensions and orientations have all been studied both theoretically and experimentally. Figure 1-7 depicts the variations in texture geometry studied for enhancing tribological performance where *w*, *d* and *l* describe the width, diameter and length of the texture. The texture parameter p, describes the pitch between the textures which relates to the density at which the textures are dispersed over the surface.

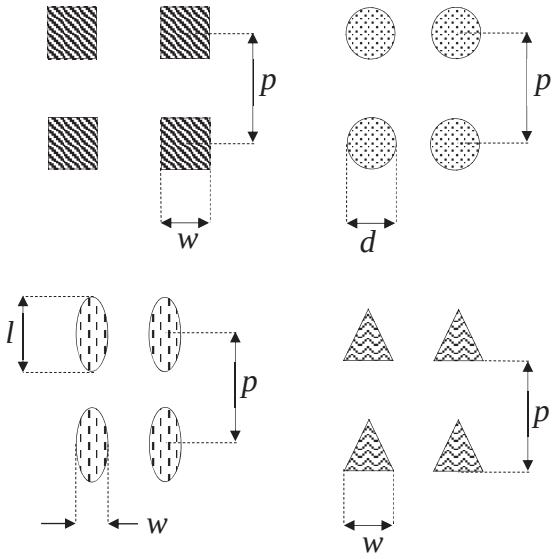

Figure 1-7: Variation in texture shapes. Where w (width), d (diameter), l (length) and p (pitch) describe the geometric parameters of each texture.

1.3.4 Benefits of Surface Texturing

One of the primary characteristics of surface textures for improving the tribological performance of a surface is driven by hydrodynamic theory. Figure 1-8a shows a singular textured pore on the lower surface and a plain upper surface moving relative to one another at velocity *(U)* with the opposing surfaces being separated by a lubricating fluid film. As the fluid travels in the direction of motion the pore creates an artificial diverging/ converging wedge. Figure 1-8b shows the pressure distribution across the pore owing to this effect. Aided by the relative motion of the upper and lower surfaces the fluid permeates to the surface. The convergence of the textured profile, tending towards the surface creates a pressure gradient which increases near the outlet of the pore. The hydrodynamic pressure generated creates hydrodynamic lift that separates the opposing bodies, reducing friction and wear of the surfaces.

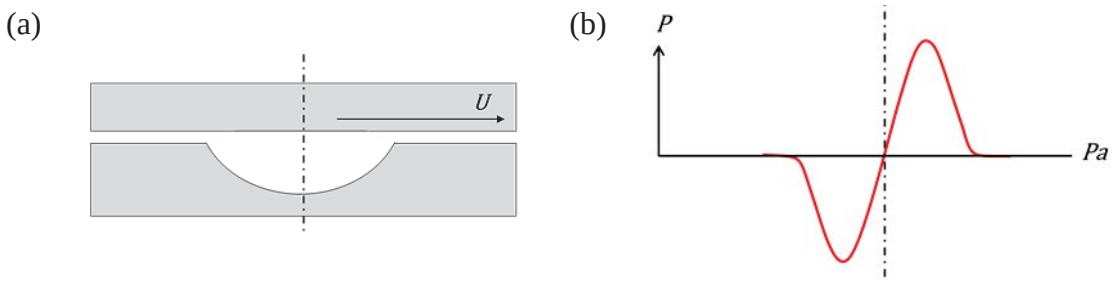

Figure 1-8: (a) Textured pore cross section profile (b) Pressure distribution across the textured pore (without cavitation)

In addition to encouraging hydrodynamic effects textured pores have been found to invite beneficial tribological effects such as a secondary supply of lubrication (Etsion, 2005) from fluid retained within the texture cavity permeating to the surface in times of lubricant starvation. An additional benefit of the application of surface textures is the wear debris trapping capabilities of the surface (Pettersson & Jacobson, 2003). The presence of wear particles within the contact zone can cause abrasive wear. Wear debris entrapped within the textured pores has been shown to reduce the abrasive component of surface wear. Under continuous motion the fluid establishes a steady state film and the possibility of abrasive wear naturally reduces by the increasing distance between the surfaces. However, under reciprocating motion, where the film thickness fluctuates across a stroke, wear debris trapped between the surfaces at the stroke extremities encourages 2nd and 3rd body abrasion. Therefore, the wear trapping capabilities are more relevant to contacts undergoing reciprocating motion than those of continual motion.

1.3.5 Optimization of Surface Texture Parameters

The optimisation of texture parameters for improved tribological performance has become a devoted area of study. The majority of investigations are experimental, employing a trial and error methodology. To a lesser extent theoretical studies have been undertaken, developing analytical models in order to predict such characteristics as

hydrodynamic pressure, friction force and load carrying capacity. In the following sections both experimental and analytical investigations are reviewed.

Kovalchenko et *al*. assessed the effect of laser surface texturing (LST) on transitions in lubrication regimes. Six specimens were tested in a pin-on-disc experiment. Discs 1 and 2 were ground and polished respectively; discs 3 – 6 having varying texture diameters, depths and densities. Identical tests were carried out employing two types of lubricant; a high and low viscosity PAO based lubricant oil. The coefficient of friction (COF) was found to drastically reduce for both lubricant types for two of the four textured specimens. The resultant Stribeck Curve for the ground, polished and best performing textured surface demonstrated the impact of micro-dimples. Shifts in the transition of lubrication regimes to higher loads and lower speeds for the low viscosity lubricant were noted. The high viscosity test observed no transition between regimes where Kovalchenko et *al*, presumed the specimen to be operating in the hydro-dynamic regime (Kovalchenko, et al., 2005).

This phenomenon was agreed upon by Borghi et *al.* in a pin-on-disc experiment of nitride steel replicating a starved lubrication system and observed the impact of wear with the presence of a dimpled texture. Substantial reductions in COF were recorded, in addition to changes in transitions of lubrication regimes within the Stribeck curve. The wear of each textured and non-textured specimen was analysed by scanning electron microscopy (SEM). The non-textured specimen was found to have oil and wear particles in the groove track, an occurrence of such would increase wear, promoting third body abrasion. Paradoxically to this no wear debris was found in the pin/disc interface of the textured specimen. Both lubricant and debris filled the micro-cavities, thus adding proof to the

hypothesis that dimples act as micro-reservoirs for lubricant and a mechanism for catching wear debris (Borghi, et al., 2008).

The effect of micro-dimples under boundary conditions was investigated by Hu and Hu. The experimental investigation assessed the effect of dimple density on tribological performance whereby a high and low viscosity lubricant was employed in identical experiments. They found that the dimple density had a profound effect with operational parameters such as load and lubricant type. At low loads applying low viscosity lubricant it was found that all textured samples out-performed the un-textured surface, within this the optimum dimple density was found to be the lowest tested of 8.5% density (Hu & Hu, 2012). The authors cite the earlier work of Yan et *al*. as a means of explaining this occurrence. Yan et *al.* stated that the large distance between the dimples is beneficial in enhancing load capacity, in addition to a reduced and providing uniform contact pressure. They also hypothesise that low viscosity fluids reduced resistance to flow compared with high viscosity fluid generating hydro-dynamic pressure (Yan, et al., 2010).

In higher load tests the highest dimple density of 35% out performed all other dimple arrays with low viscosity lubricant. They determined that under high load there may not have been enough oil flow to maintain a constant fluid film, increasing friction; not by the flow of lubricant over the surface but the supply provided by the higher density of dimples present on the surface. Under high load with high viscosity lubricant the lower dimple density array out performed all others (Hu & Hu, 2012). Anderson et *al*. attribute this to the higher viscosity oil attaining higher load carrying capabilities due to the high viscosity and spreading characteristics of the lubricant (Anderson, et al., 2007).

The effect of micro-cavities operating under mixed lubrication conditions was studied by Dumitru et *al.* Textures were applied to the surface at diameters ranging between 50 to 100μm and the depths of between 5 to 8μm. Comparing the textured to an un-textured surface the textured surfaces showed that the introduction of micro-cavities can drastically improve the lifetime of the sample (Dumitru, et al., 2000).

Tang *et al.* conducted reciprocating tribology tests employing a steel on steel conformal configuration. Three different diameters were examined, 300μm, 500μm and 700μm that produced three varying densities of 2%, 5% and 10%; all textures had a fixed depth of 50μm. They found that 5% density produced both the lowest friction and drastically reduced the wear compared to non-textured samples (Tang, et al., 2013).

1.3.6 Surface Texturing within Bio-Medical Applications

Investigations into the application of surface textures within bio-medical applications have had varying degrees of success. Sagbas and Durakbasa investigated the effect of surface textures had on the friction between articulating surfaces causing temperature rises between the acetabular cup and femoral head. A textured vitamin E blend UHWPE acetabular was paired with a cobalt chromium femoral component. It was shown that textured surfaces registered lower temperature rise compared to an un-textured surface. This was attributed to the textures contributing to the reduction of frictional heating of the surfaces (Sagbas & Durakbasa, 2013). Ito et *al.* studied the effect of surface textured patterns upon cobalt-chrome femoral head sliding against a UHMWPE socket. The textured surface was compared to a non-textured surface within a hip joint simulator. Reductions in wear of 68% for the textured compared to the non-textured surface was reported. They attributed the substantial reduction in wear to two factors, firstly the reduction in abrasive wear owing to the capturing of wear debris within the textured

cavities and secondly the improved lubrication of the surface through a secondary supply of lubricant stored within the texture (Ito, et al., 2000).

The positive results in terms of surface texturing within hip simulators reported by Ito et *al.* was inconsistent with studies conducted with the texturing within a metal on metal implants. Gao *et al*. found within a theoretical study of hip joint lubrication that the dimpled surface textures had a detrimental effect on the fluid film lubrication within the EHL regime (Gao, et al., 2010).

The contrasting reports on the application of surface textures may be due to the difference in the material employed. The majority of work has been conducted with stiffer material such as metals and ceramics; however, limited publications of the same magnitude have employed lower moduli materials.

1.3.7 Surface Texturing of Low Moduli Materials

Huang *et al.* assessed the frictional performance of surface textures within a steel-Polydimethylsiloxane (PDMS) conformal sliding couple, lubricated with a glycol/water fluid mix. They found that hydrophilic surfaces outperformed hydrophobic surfaces obtaining a lower friction coefficient where the optimum texture parameters for reduced friction was a diameter of 50μm and a density of 22.9% (Huang, et al., 2012). Varying the diameter and the number of pores within the contact zone resulted in an overall increase in sliding friction with an increase in texture diameter. Moreover, it was shown that changes in the number of pores within the contact zone served only to shift the magnitude of friction obtained.

Zhang et *al.* investigated the role of surface textures applied to UHWPE sliding against steel, finding that the optimum texture parameters for frictional performance were a

diameter and depth combination of 50μm and 10μm respectively and a density of 22.9%. Across the varying experimental conditions, the friction reduced between 66.7 and 85.7%. However, the optimum parameters derived for improved wear resistance were shown to be a diameter of 50μm, depth of 15μm and a density of 29.9% where the average wear depth was 35.5% of that measured of the non-textured surface (Zhang, et al., 2012). Zhang et *al.* also simulated the stress distribution surrounding a single texture by FEM analysis and compared UHMWPE with SiC models. The results highlighted differences in the way the textured and counter surface interacted. SiC registered a higher stress distribution around the texture compared to the less stiff UHMWPE (Zhang, et al., 2013).

Yuan et *al.* studied the orientation effects of textured grooves and suggested that rises in friction were due to an 'edge effect' of the texture. FEM analysis indicated high contact stresses were induced at the edge of the texture that opposed the direction of sliding (Yuan, et al., 2011).

Cho and Choi studied the effect of surface textures applied to UHMWPE and sliding against steel under boundary lubricated conditions. Dimpled textures were dispersed at densities of between 5-25% at depths of 20-75μm with a fixed diameter of 50μm. The authors reported that all textured samples reduced the friction coefficient compared to non-textured surfaces, where the optimum area density and texture depth were found to be 25% and 25μm respectively (Cho & Choi, 2014).

Kustandi et *al.* investigated surface textures applied to UHMWPE. Within reciprocating sliding experiments, a silicon nitride ball was employed as the counter surface sliding under dry conditions. It was shown that under loads ranging from 60 to 200mN that the friction reduced between 8-35% compared with the un-textured sample. Furthermore, the

presence of textures contributed to a reduction in material transfer and wear scar geometry (Kustandi, et al., 2009).

1.3.8 Summary of Surface Texturing within Tribology

Table 1-1 provides the texture parameters, textured material type, test type, conclusion and, where given, lubricant data from the sourced literature applying dimple shaped textures to a surface for friction and wear control.

Improved lubrication, reduced friction and low wear rates have all been stated across various studies within the reviewed literature of surface texturing tribological investigations. The coefficient of friction and wear are the primary metrics for which the performance of textured surfaces are assessed. However, the variability in friction within polymeric surfaces is relatively low, therefore interpreting such a parameter to assess a polymer surfaces longevity can be difficult. For this reason an additional real-time measurement parameter was employed in the form of acoustic emissions to monitor the tribological system. The following section explains the source of acoustic emissions (AE), the testing employing AE and acoustic emissions within tribology.

Table 1-1: Summary of experimental surface texture studies for friction and wear control presented with the review of literature

Author	Texture Parameter Combinations Diameter (μm) / Depth (μm) / Density (%)				Textured Material	Lubricant Type and Viscosity	Test Type/ Contact Geometry	Conclusions
Kovalchenko, 2005	78/5.5/12	58/5/15	80/6.5/12		Hardened H-13 Steel	PAO-based lubricant (Mobil 1) 124.7cSt @ 40°C / 17.7cSt @ 100°C PAO-based lubricant (Mobil 1) 54.8cSt @ 40°C / 10.1cSt @ 100°C	Pin-on-disk Conformal Contact	Laser textures reduced friction and expanded the range of hydrodynamic regime. The removal of bulges on the edge of the textures was imperative to optimize the effect of surface textures for which a lower area dimple density was most beneficial for lubrication regime transitions.
Borghi, 2008	100/50/40				30NiCrMo12 Nitriding Steel	Shell Helix Ultra 5W-40 79.1 cSt @ 40°C / 13.1 cSt @ 100°C	Pin-on-disk Conformal Contact	Under staved lubrication conditions (single drop of lubricant) the coefficient of friction reduced by 75% from un-textured to textured surface. Under dry sliding conditions under a load of 1N friction coefficient reduced by 10% from un-textured to textured surface. Wear debris was shown to fill the pores and improve the tribological performance.
Hu & Hu, 2012	100/30/8.5	100/30/17	100/30/35		2024 Aluminium Alloy	Commercially available PAO-based lubricant 395cSt @ 40°C / 16.8cSt @ 100°C Commercially available PAO-based lubricant 40cSt @ 40°C / 3.9cSt @ 100°C	Pin-on-disk Conformal Contact	Textured surfaces led to a reduction in friction coefficient contributing to an extended wear life under boundary lubrication. Testing with low and high viscosity oil showed a density of 8.5% to be optimum expanding the range of mixed lubrication regime.
Yan, 2010	50/5/5-20	100/10/5-20	200/10/5-20	300/10/5-20	Cr Plated Cast Iron	CD15W-40 Engine Oil	Ring-on-Disk Conformal Contact	Textured surfaces with a dimple pattern of 100-200μm diameter, 5-10μm depth and 5% density were found to be optimum under the load/speed ranges employed within the study. Analysis of variance concluded that the aspect ratio was the most important parameter with a depth-over-diameter ratio in the range of 0.025-0.1 being optimal.
Anderson, 2007	35/25/8	50/12/30	50/12/31		M2 High Speed Steel	Stamping/drawing process oil <1cSt viscosity @ 40°C Stamping/drawing process oil 1.3cSt viscosity @ 40°C Extrusion/drawing process oil 109cSt viscosity @ 40°C	Oscillating friction test Conformal Contact	Textured surfaces reduced friction across the texture parameters assessed. High viscosity lubricant combined with low density textures and large depth compared to diameter improved tribological performance significantly. Low viscous oils benefitted tribologically when tested with surfaces of higher texture density and smaller aspect ratio.
Dumitru, 2000	10/8/60				AISI 440C Steel	Commercially available Mineral Oil	Ball-on-disc	Tribology tests showed that textures significantly increased the lifetime of the laser processed samples compared to the un-textured surface.
Ito, 2000	approx. 250/260				Cobalt Chrome (Co-Cr)	Distilled Water	Hip-Joint Simulator	The introduction of concave patterns on the surface of Co-Cr reduced polyethylene wear. Non-patterned wear was 23.1mg compared to 7.2mg for the patterned surface. The reduction in wear was attributed to trapping of wear particles and an improvement in lubricity by the supply of lubricant from the textures.
Huang, 2012	50/5/(2.6-40.1)		200/5/(2.6-40.1)		PDMS	Deionised Water 0.9 mPa.s 90% Glycol 84.4 mPa.s	Pin-on-disk Non-conformal Contact	For a hydrophobic surface textures were found to be critical in reducing friction with the optimum diameter and density parameters being 50μm and 40.1 % respectively. Through observations of the wetting behaviour I was suggested that textures could prevent lubricant exclusion from the contact zone and act as a lubricant reservoir.
Zhang, 2013	50/15/5-40				UHMWPE	Distilled Water	Ring-on-Disk Conformal Contact	At high loads textures applied to a UHMWPE surface can effectively reduce friction. Furthermore, Wear resistance of a UHMWPE surface was improved by textures reducing the average wear scar depth by 36% with a texture density of 30% compared to an un-textured surface.

1.4 Acoustic Emissions

When a material undergoes elastic deformation produced by the application of an external stimulus a localised stress field is generated storing mechanical strain energy. The dissipation of this energy occurs through material failure such as crack initiation/growth or yielding. The acoustic emission (AE) signal is defined as the transient elastic waves that propagate through the material by the rapid release of energy stored within the stress field (Mba, 2003). The redistribution of stress causes miniscule movements of molecules through the material emanating as high frequency stress waves. A primitive example of AE is that of 'tin cry'; audible sounds in the form of 'creaking' occur during the heat treatment of tin. These 'acoustic emissions' are related to martensitic deformations produced by the twinning of tin crystals. An AE sensor detects these molecular movements caused within or on the surface of a material and converts them to an electrical signal. Figure 1-9 depicts the source and wave propagation within a signal. The signal acquired is either of a burst or continuous type also seen in the figure below.

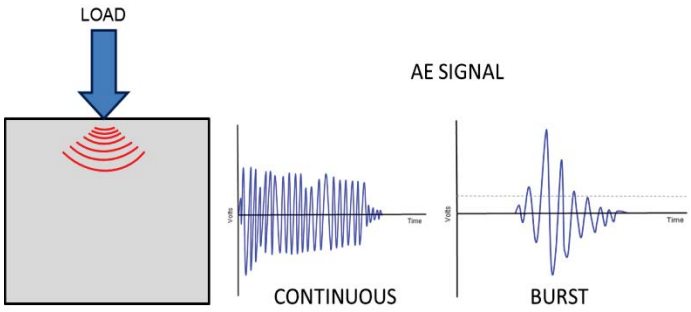

Figure 1-9: Wave propagation emanating from an area of stimulus (load) and captured signal types, continuous and burst.

The magnitude of energy released differs with the type and extent of deformation experienced at the origin of an AE source. For instance, plastic deformation will be more detectable than elastic deformation or phase transformations due to the molecular activity

being more severe. Most detected AE signals originate through the permanent deformation of a material and can be employed to identify the presence of material defects.

1.4.1 Acoustic Emission Signal

Frequency Response

The selection of an appropriate frequency range for the detection and processing of acoustic emission signals is a critical component in the application of AE monitoring. The primary purpose of defining this optimum frequency band is the detection of insipient material faults that can manifest themselves as more prominent tribological phenomena later in a components operational life. Attenuation of background noise is a critical factor of frequency selection, however, too high detection frequencies could discriminate discrete AE signals that maybe indicative of certain tribological phenomena. Paradoxically, the application of low detection frequencies could permit the inclusion of non-AE related signals. It is important to note that both background noise and AE signal reduce with an increasing frequency range; however, the rate at which attenuation of background noise occurs is faster than that of AE signals.

The high frequency regions that AE sensors are capable of operating in provides intrinsic benefits in comparison to traditional vibration monitoring. Low frequency signatures have a high background noise level that can mask the manifestation of developing material faults. As a consequence, fault detection within low frequency monitoring only occurs once the fault frequency signature rises above that of the background noise. Moreover, research has shown that the capturing of insipient faults and material

disturbances are more detectable at higher frequencies and that as material degradation increases the detection frequency range drops (Hase, 2015).

Acoustic emission activity emanating from bearing defects was investigated by Catlin. The author reported that AE signals detected within the high frequency range of AE represented bearing defects as oppose to mechanical origins such as imbalance, misalignment, looseness and shaft bending. Moreover, capturing high frequency content relating to bearing faults was made possible by having the AE sensor close to the bearing (Catlin, 1983).

Frequency spectra analyses of acoustic emission signals have shown that AE waves carry energies across a wide frequency range. Furthermore, research has shown that the most prominent AE frequency bandwidth used in practise for fault detection is between 100 kHz – 300 kHz, where high-pass filtering above 100 kHz is employed to remove unwanted low frequency vibrations originating from mechanical equipment (Swindlehurst, 1973).

Amplitude Response

An acoustic emission pulse consists of different frequencies and amplitudes. The amplitude response of an AE signal is related to the release of energy contained within the AE pulse.

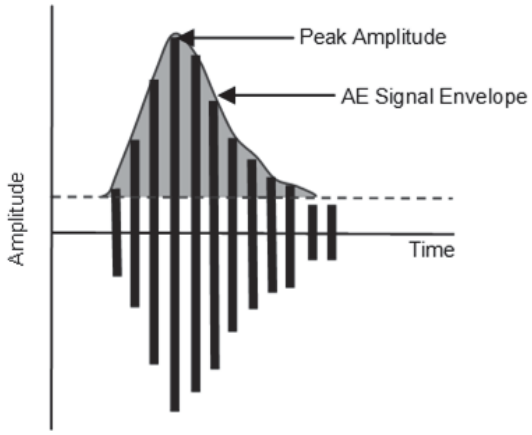

Figure 1-10: AE burst Signal, the area beneath the signal envelope and above the pre-determined threshold level (red dashed-line) is proportional to the strain energy released.

As already discussed the energy is drawn from the elastic energy stored within the stress field. The magnitude of which is proportional to the amplitude of the signal acquired. As seen in Figure 1-10 the area encompassed by the signal is related to the energy of the signal burst. Furthermore, the magnitude of energy and signal amplitude increases with the severity of the source event (Pollock, 1973). However, the detected energy and amplitude is not identical to that emitted directly from the source; this is due to signal attenuation.

Attenuation

As the AE pulse travels through a material the amplitude of the signal reduces; this is known as attenuation. Attenuation is attributed to various factors including geometric spreading, scattering at structural boundaries and absorption (Grosse, 2008). Although

attenuation affects all signals within the frequency spectra it is more prominent at higher frequencies.

Geometric spreading is the ‘spreading’ of a wave through a structure, if the structure in question had infinite dimensions the wave would spread and continue to attenuate. The second form of attenuation is scattering. This is attributed to the deflection of AE signals through discontinuities such as material defects or the physical boundaries of the structure. The final source of attenuation is due to absorption. Acoustic emission wave energy is partially absorbed and converted to heat and is a factor that in general affects non-metallic materials.

1.4.2 Acoustic Emission Parameters

Once an AE signal exceeds a pre-defined voltage threshold it is recorded and relevant information relating to the conventional characteristics of an AE waveform can be extracted and studied. Figure 1-11 depicts an AE signal with common AE parameters super-imposed on the signal.

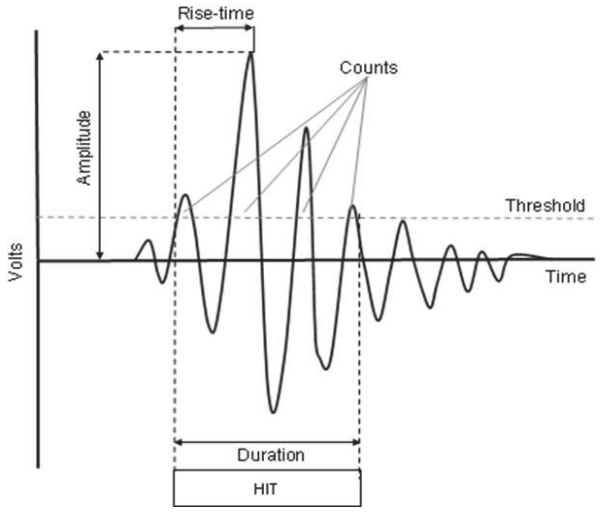

Figure 1-11: AE signal response annotated with the different features and parameters

The following descriptions are definitions for each AE parameter.

HIT: A signal that exceeds the threshold and triggers the acquisition system to accumulate data.

COUNT: The number of times within the duration of the signal, where one signal waveform exceeds a present threshold.

COUNT RATE: Acoustic emission, emission rate or count rate of the time rate at which the emission counts occurs

AMPLITUDE: A peak voltage of the signal waveform, expressed in decibels.

DURATION: Expressed in micro-seconds it is the time interval between the trigger time and the time of dissipation of the signal below the pre-defined threshold.

RISE TIME: The time interval between the triggered time of AE signal and the time of the peak amplitude.

1.4.3 Application of Acoustic Emissions Testing

The acoustic emissions technique is an established form of non-destructive testing with AE signals capable of indicating variations within the microstructure of materials generated by deformation or fracture. The technique has been employed within multiple studies evaluating material defects and failure mechanisms.

Berkovits and Fang employed various AE parameters to investigate the initiation, closure and growth of fatigue cracks and expressed the capabilities of AE monitoring for determining the time and source of micro crack initiation (Berkovits & Fang, 1995).

Roberts and Talebzadeh monitored crack propagation employing narrow band filtering that enabled the encapsulation of AE activity from the vicinity of the fatigue crack. The author stipulated three regions of crack growth culminating in eventual failure, throughout which AE events increased with the number of cycles and postulates their relation to fatigue crack growth (Roberts & Talebzadeh, 2003).

Further applications within materials science include AE monitoring of phase changes; martensitic transformations that take place under the heating or cooling of a material. Spiech and Schwoeble found AE to be sensitive to transformation in the atomic structure of a material (Speich & Schwoeble, 1975).

1.4.4 Acoustic Emissions in Tribology

Sun et *al.* investigated the application of acoustic emission and electrostatic (ES) wear monitoring of bearing steel within a ball on disc configuration. Long distance wear tests identified three distinct regions of AE activity prior to the system attaining steady state conditions. These regions were studied during specific time terminal tests in addition to SEM analysis. The authors characterised these regions as running in, delamination and

oxidation. Throughout these phases severe plastic deformation along with the onset of delamination, in addition, the formation of pits and the entrapment of debris were identified. AE root-mean-square (RMS) and ES signals were found to be sensitive and identified features relating to each wear mode. Good correlation was also found between AE RMS and friction signals. Furthermore, a promising correlation existed between the integrated AE RMS signal and the volume loss of the ball specimen (Sun, et al., 2005).

The application of AE signal analysis of the friction and wear behaviour within sliding contacts was investigated by Jiaa and Dornfield. The authors demonstrated the potential of AE RMS signal in addition to SEM analysis for detection and diagnosis of wear mechanisms. Three regions were characterised from the study; running in, steady state and self-acceleration. Based upon AE activity and micrographs from each region the authors postulated a varying dominant wear mechanism throughout these regions. Running-in showed a lower wear rate with the authors suggesting that AE activity derived from asperity deformation through ploughing by wear particles or hard asperities. Region 2 was characterised by a higher wear rate than region 1, attaining higher AE RMS signals. The formation of shallow pits and cracks were observed indicating the process of delamination was the prominent wear mechanism. Region 3 showed the evolution of wear mechanisms from that of delamination to that of tribo-chemical wear. This was indicated by the formation of an oxide layer on the wear track (Jiaa & Dornfeld, 1990).

Boness et *al.* investigated dry and lubricated sliding contact within a ball on cylinder configuration. Distinct similarities were found between dry and lubricated tests when RMS signals were examined using log-log plots. The authors suggested that important wear phenomena between lubricated surfaces may be a time-expanded version of the wear behaviour obtained for dry sliding conditions. Furthermore, the application of AE

monitoring could not only indicate occurrences of wear mechanisms at any given time, but in addition employed a means to provide a qualitative measure of wear rate when the integrated RMS signal against wear scar volume (Boness, et al., 1990).

Lingard et *al*. (Lingard, et al., 1993) measured acoustic emissions within dry sliding conditions to determine relationships between AE and wear-friction parameters. No discernible relationship was found between wear and AE output, however, after an initial running-in period an almost linear relationship was identified between wear scar length and AE count rate. Moreover, a further linear relationship was acknowledged between the work of friction and cumulative AE output when analysed in the form of log-log plots.

Hisakado et *al.* employed the AE count rate parameter to investigate its relationship of friction and wear within a pin on disc tribometer under various lubricating conditions. AE count rate increased with a decline in lubrication, and a limited correlation was ascertained when comparing AE count rate and the friction coefficient for each individual lubricant condition. However, increases in the mean friction coefficient were found to increase with increasing average AE count rate. Furthermore, good agreement was established between the average AE count rate and the sum of specific wear rate across the pin and disk specimens (Hisakado & Warashina, 1998).

Hase et *al.* (Hase , et al., 2012) examined the AE signals generated during adhesive wear and abrasive mechanical wear tests. A micro-sliding friction machine was employed within adhesive wear tests. The generated AE signal and frequency spectra showed that high AE frequency detected was related to the generation of wear elements and transfer particles with the magnitude of wear affecting the detected AE signal.

Abrasive wear test were performed using a steel pin against emery paper. Burst type AE signals were generated which originated from cutting and ploughing mechanisms. Testing emery paper with varying grain sizes the results indicate that the amplitude of the frequency spectrum is dependent upon the grain size and the removal capability of the grains. Hase et *al.* summarised by stating that the wear mechanism can be recognised from the features of the AE spectrum.

Hase et *al.* (Hase, et al., 2016) conducted acoustic emission studies for the early detection of seizure within journal bearings. Tests were performed upon a journal bearing-type friction-and-wear tester to investigate the relationship between the changes in wear and AE signals. Micrographs of the worn surfaces show that wear progressed over time and the primary wear mechanism was adhesion. Variations in AE RMS were categorised in into four regions; region 1 categorised as a run-in region, region 2 a steady state region with wear progressed steadily. Region 3 showed an increase in AE content and region 4 showed even further increases leading to failure. The frequency spectra captured at pre and post seizure showed distinct similarities between 0 – 1.5 MHz, however the frequency rises and peaks at approximately 1.9 MHz before falling. Hase et *al.* concluded that the early fault detection of seizure through acoustic emission technique was possible stating that the adhesion mechanism was a prelude to seizure and generates AE content above 1 MHz.

The sources of AE discussed above describe some of the friction and wear process generally encountered within tribological contacts, along with adhesion, abrasion and chemical reactions. These irreversible changes of a materials structure are governed by the material properties and operational conditions. Variations of loading conditions, speed and temperature can all effect AE signal characteristics; frequency, amplitude, signal type

(continuous or burst), rise and decay time along with pulse duration. To systematically evaluate these characteristics, in relation to surface/material phenomena, AE parameters are extracted to interpret raw AE signal data.

1.5 Summary

The review of literature undertaken throughout Chapter 1 describes the advantages that surface textures have to offer in terms of reducing friction and enhancing the longevity of a components surface during operation. Enhancing the interaction between the lubricating fluid and surface whilst maintaining operating temperatures; which can be responsible for weakening the material, can provide improvements in surface durability.

In relation to polymers, the constitutive failure mode of a polymer surface within prosthetic implants is through the accumulative wear of the surface which is predominantly caused by abrasive mechanisms. For a component that predominantly operates within the mixed/boundary lubrication regime, improving the lubrication of the surfaces can reduce the adhesion mode of wear that is often the dominant preceding wear mechanism that produces abrasive wear particles.

The monitoring of parameters such as friction within a polymeric systems can be ambiguous and conventional lubricant film monitoring to indicate material contact whilst in operation presents difficulties. In order to counter this the acoustic emission (AE) technique offers a means of monitoring material contact and tribological activity during operation. Abrasive wear, for instance, is likely to generate higher AE content, given the wear morphology can produce surface deformation such as scratching and gouging. Conversely, improved lubrication of the surfaces should manifest as lower AE content given the reduction in contact between the two surfaces and any interaction with, or in

the generation of, wear particles. Hence, AE is a novel technique that can enable a direct comparison between textured and non-textured surfaces during operation. Furthermore, within a polymeric sliding couple AE could provide pertinent information relating to surface interactions that would be difficult to interpret from frictional readings.

Research conducted in the area of surface texturing has been dominated by the application of surface textures via laser ablation applied to typically harder materials such as steel and the employment of oil based lubricants, as highlighted in Table 1-1. Summarised within which are the texture parameters, textured material type, test type, conclusion and, where given, lubricant data from the sourced literature applying dimple shaped textures to a surface for friction and wear control.

Improved lubrication, reduced friction and low wear rates have all been stated across various studies within the reviewed literature of surface texturing tribological investigations. The coefficient of friction and wear are the primary metrics for which the performance of textured surfaces are assessed. However, the variability in friction within polymeric surfaces is relatively low, therefore interpreting such a parameter to assess a polymer surfaces longevity can be difficult. For this reason an additional real-time measurement parameter was employed in the form of acoustic emissions to monitor the tribological system. The following section explains the source of acoustic emissions (AE), the testing employing AE and acoustic emissions within tribology.

Studies conducted on the texturing of low moduli materials has a primary focus upon the technique employed to generate textures and the optimum texture parameter combinations. The majority of these studies have also employed a steel counter-part within tribological testing.

To date no work has been conducted on the texturing of PEEK and assessing the effects within a PEEK-on-PEEK sliding system. Furthermore, no work has been attempted to monitor the performance via acoustic emissions in order to evaluate tribological phenomena within an all PEEK sliding couple.

In order to assess the tribological effects of the surface texturing of PEEK the primary research questions to be satisfied within this thesis are as follows:

1. Will surface textures, applied by laser ablation, provide friction and wear reducing effects when applied upon a PEEK substrate?
2. Would the application of surface textures improve lubrication, from a typical boundary/mixed lubrication regime to a mixed/hydrodynamic regime?
3. What are the friction and wear reducing mechanisms occurring that would improve or diminish the durability of a PEEK textured surface compared to an un-textured surface?

CHAPTER 2

Experimental Details

2.1 Equipment

2.1.1 TE-77

The TE-77 is a reciprocating tribometer manufactured by Phoenix Tribology Ltd, a schematic of the machine layout is provided in Figure 2-1. Rotary motion from the motor is transferred to linear motion via a scotch yoke mechanism that can provide reciprocating frequencies from 1-50Hz. The scotch yoke mechanism houses a splined eccentric cam that enables a variable stroke length (2-25mm) and can be adjusted manually on an eccentric splined shaft from the motor. The shaft from the scotch yoke is attached to the upper specimen holder. The moving upper specimen is loaded by a lever mechanism against the stationary lower sample via a running plate located on a loading stirrup. A needle roller cam follower located within the upper specimen holder allows for a reduced frictional response as the moving upper specimen holder reciprocates under the applied load that can be varied from 1-1000N. The normal force is measured by a strain gauge transducer mounted on the lever and operated by a servo hydraulic motor. The lower specimen fixed via two M4 counter sunk screw to the base of the lubricant bath and clamped to a block. The block is heated via four electrical resistance elements. A thermo-couple inserted through the side of the lubricant bath monitors the temperature.

The experimental parameters are controlled through inputting a sequential programme within Compend2000 software running on the host PC. Parameters such as load, temperature, sliding time and reciprocating frequency are all defined within the test sequence.

The Friction force is measured by a piezo-electric force transducer that is mounted on the same sub-base as the heater block. The voltage developed is passed through a DC converter that produces a time smoothed value of friction force. The resultant friction signal takes the form of a square wave with the value being considered as an average friction force over a specified time interval. The friction measurements are collected by data acquisition software Compend 2000 at a rate of 1Hz and the coefficient of friction is calculated within the software using Amonton's first law of friction where the friction force is directly proportional to the applied load. The system also allows for the acquisition of high speed frictional data. The data acquisition rate can be pre-set to capture the frictional response in relation to stroke length within individual stroke lengths.

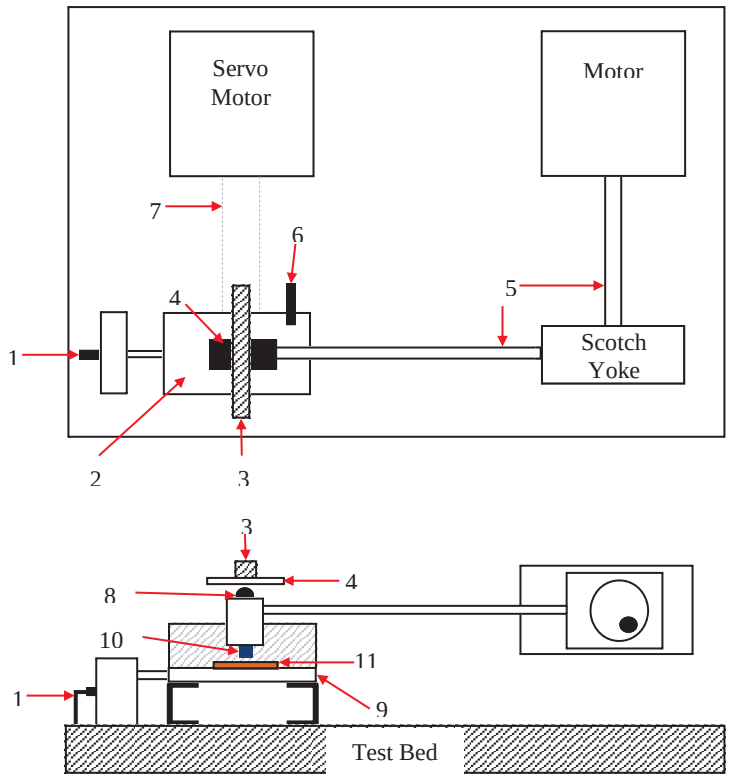

Figure 2-1: Layout schematic of TE77 identifying key mechansims and instrumentation. (1) Piezo-electric tranducer, (2) lubricant bath, (3) load stirup, (4) running plate, (5) connector shafts, (6) thermocouple, (7) lever (situated beneath test bed), (8) needle roller, (9) heater block, (10) upper specimen, (11) lower specimen.

2.1.2 HFRR

The high frequency reciprocating rig (HFRR – PCS Instruments, London, UK) is an oscillatory friction and wear machine, where the oscillatory motion is provided by an electro-magnetic vibrator. The upper sample is held within the moving part of the system and the lower sample is positioned within a lubricant bath that is located upon a heater block, heated by two 24VAC, 15W cartridge heaters. Lubricant temperature was monitored by a thermocouple inserted through the side wall of the bath, a schematic of the HFRR and layout is shown in Figure 2-2. The friction force is measured via a force transducer located at the rear of the heater block. The applied load is inputted into the HFRR system and the coefficient of friction is calculated by capturing the friction force over each stroke and averaging over a 1 second time interval. The COF is then provided in real-time and for post-test analysis.

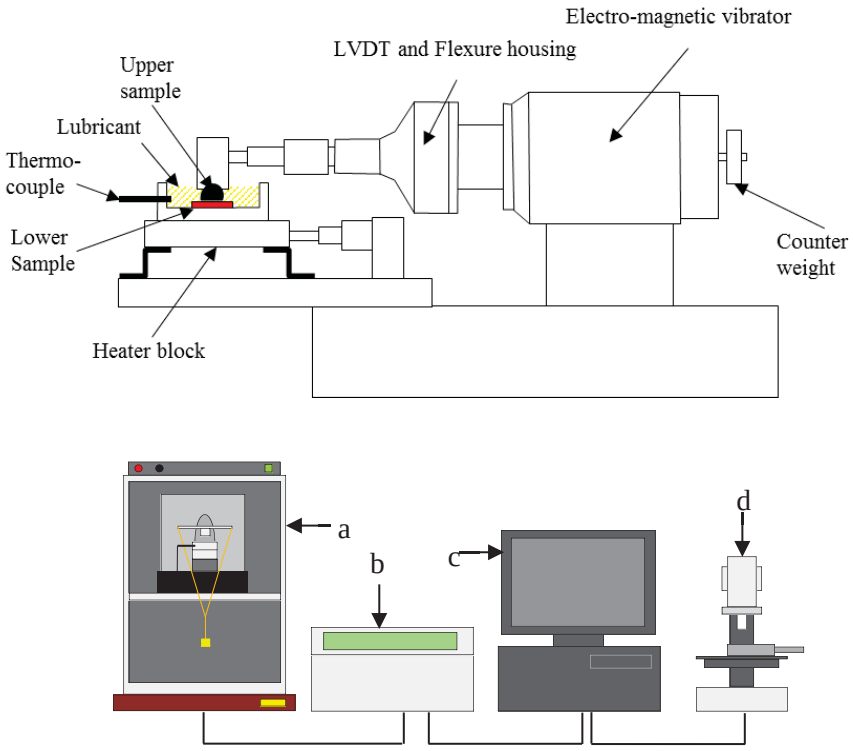

Figure 2-2: HFRR schematic and layout: (a) HFRR, (b) control unit, (c) PC, (d) microscope powered by AutoHFRR Software.Acoustic Emission System Architecture

The block diagram in Figure 2-3 provides the system layout from the capturing of an AE signal, pre-amplification and signal conditioning.

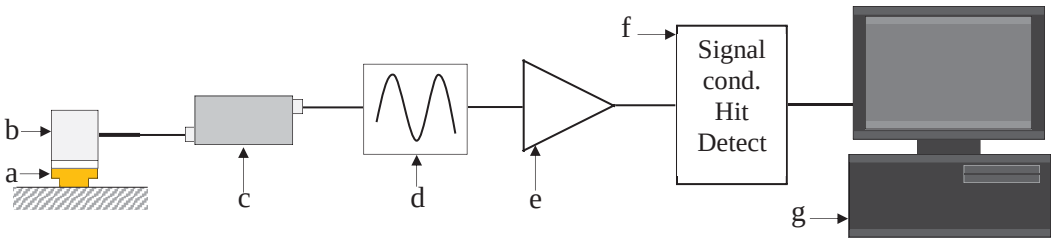

Figure 2-3: AE system architecture. (a) Specimen, (b) AE sensor acoustically coupled to specimen via general purpose silicon grease, (c) Pre-amplifier amplifies raw signal by 60dB, (d) signal filtering corresponding to pre-determined parameters, (e) amplifier, (f) signal conditioning and hit detection, (g) results displayed on PC.

Acoustic Emission Sensor

An Acoustic emission sensor, Figure 2-4, converts inter material motions into electrical signals. The sensor employs piezoelectric crystals that vibrate at their resonant frequency when excited by an external stimulus, such as the propagation of an acoustic emission waveform. The elastic response of the piezoelectric element generates an electrical discharge in the form of voltage. The AE sensor employed within the tests is a Nano30 medium frequency resonant miniature type.

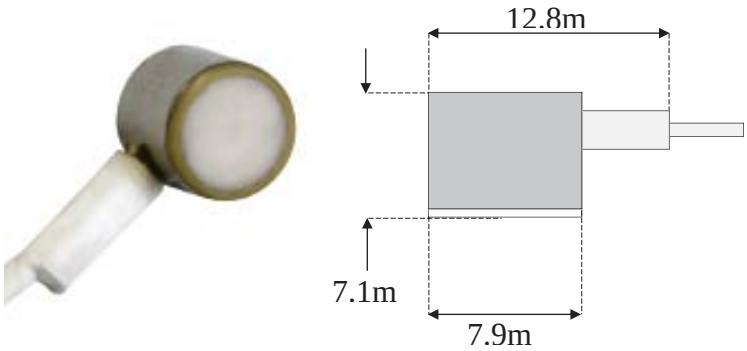

Figure 2-4: Nano30 medium frequency resonant miniature acoustic emission sensor

The characteristic response of the piezoelectric element is linear; for example an increase of input motion results in an increase in output voltage of the same rate. It is the ratio of output voltage amplitude/input motion amplitude that is the measure of the sensors sensitivity. The sensitivity of a sensor varies with the frequency of the waveform that strikes the piezoelectric element. The graph in Figure 2-5 shows the calibration curve for the Nano30 sensor. The curve provides details of frequency response from 0 –1.6MHz.

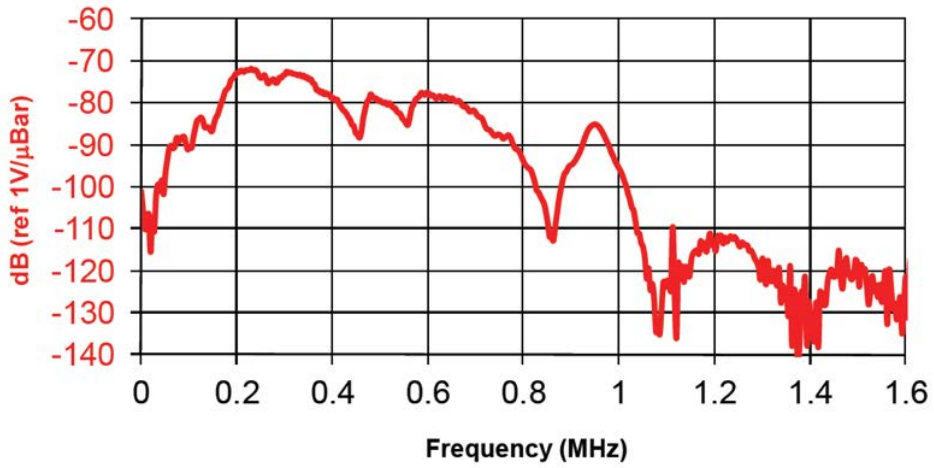

Figure 2-5: Nano30 acoustic emission sensor calibration curve

Pre-Amplification

Due to the minute voltage output of an AE signal the detected response is passed through a pre-amplifier located in close proximity to the AE sensor. Typically the amplification gain is in the range 40dB to 60dB. Where the expression for gain in decibels (dB) is given in equation 1, the unit is described as the logarithmic ratio of voltage output/input.

$$Gain\ (dB) = 20\ log_{10}\ \frac{V_o}{V_i}$$ **Equation 2-1**

Where V_o and V_i are the voltage output and input respectively. The aforementioned typical gain of 40dB and 60dB will provide an increase in voltage amplitude by a factor of 100 and 1000 respectively.

Data Acquisition

The captured AE signal is processed through a Mistras data acquisition 8-channel AE system connected to a motherboard and housed within a PC chassis. The system has a built in data acquisition software, AEwin^{TM} that enables the signal to be processed both in real time and through post-test analysis. The AE signal detection and storage is a hit-based system that allows only the collection of data within the pre-determined amplitude and frequency bands stipulated within the programme layout. The captured signal data was then manipulated to provide intrinsic details relating to the characteristics of the signal through common AE parameters such as counts, energy, hits and RMS.

2.2 Materials

Upper samples were produced from 8mm extruded Victrex PEEK 450g round bar. Lower test pieces were manufactured from an extruded block of Victrex PEEK 450g 150mm x 150mm 50mm. The block was cut using water jetting into 80 samples approximately 20mm x 65mm x 6mm. When under taken this machining process care was taken to cut parallel to the direction of the polymer fibres.

The individual samples were then machined using a vertical milling machine, this was to ensure that the surfaces of each sample were parallel, where the sample is located within a vice upon a set of parallel fixtures and each side was the machined with a 25mm slot cutter to a thickness of 4.5mm.

2.2.1 Lower Sample Preparation

The surfaces were finished by polishing with silicon carbide polishing paper. The operation was performed by hand employing purpose made jigs and fixtures. The process is depicted in Figure 2-6; polishing paper was fixed to a ground plate via double sided adhesive tape. The sample was secured to a ground square block of mild steel, 100mm x 50mm x 50mm by M5 counter sunk screws. The polishing was then performed by sliding the block over the polishing against a guide rail in order to maintain the direction of the surface roughness in the same direction across all samples. A schematic depicts the process layout in Figure 2-6, where the silicon carbide (SiC) polishing paper employed was initially 400 grit; upon visually inspection of the surface the grit of the polishing paper was incrementally increased to 600, 800, 1000, 1200, 1500 and finally 2000. The grit particle size ranges from course (400) to fine (2000). The resultant surface finish is related to the grit of the paper employed during polishing. Low grit polishing paper will generate a rougher surface than the smooth surface produced by a 2000 grit paper. The method of incrementally increasing the polishing paper enables asperities to be gradually reduced to form a flat surface to a fine surface finish.

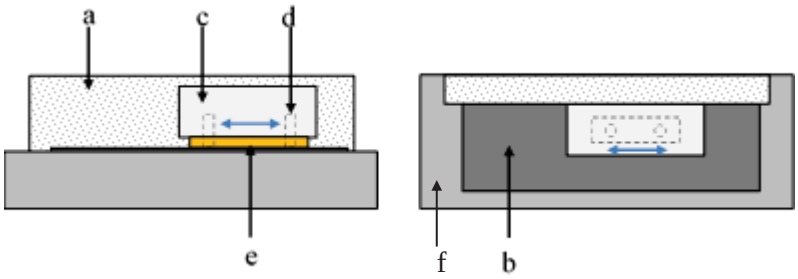

Figure 2-6: Surface polishing arrangement. (a) Guide rail, (b) abrasive paper, (c) square ground block, (d) M4 counter sink bolts, (e) specimen, (f) flat surface. Arrows highlight the direction of motion of the block in order to polish the specimen surface

The samples were brought to a final finished thickness of 4mm by undertaking the same procedure with 2000 grit polishing paper. The thickness was inspected using digital vernier calipers until the target thickness was reached.

2.2.2 Upper Sample Preparation

The geometry of the upper sample varies across each chapter, however the surface finish for upper samples in Chapters 4 and 7 underwent identical processes and were produced to the same surface finish criteria.

The surfaces were polished using a milling machine. A purpose made jig was designed to accommodate 6 samples, a schematic diagram of which is shown in Figure 2-7. The jig was located within the chuck of the miller's spindle. A ground plate was held perpendicular to the spindle and was located upon a pair of ground square steel plates within the vice. A dial test indicator (DTI) was positioned on the head of the milling machine. The DTI stylus was ran across the ground plate to ensure the spindle and plate were perpendicular. Once the setup was complete polishing paper was attached to the plate via double sided adhesive tape; 600, 800, 1000, 1200, 1500 and finally 2000 grit paper was used to attain an average surface roughness of 0.12µm+/-0.02µm.

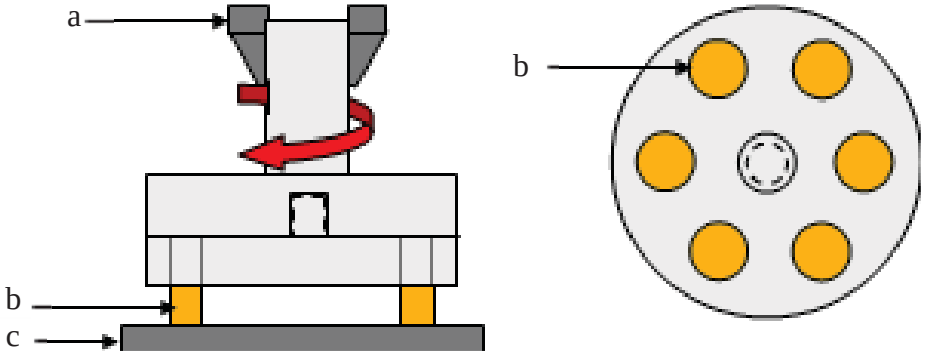

Figure 2-7: Polishing set-up for upper samples. (a) Specimen holder located in milling chuck, (b) lower sample, (c) ground block.

A curved surface was used as the upper surface within Chapter 6 in order to provide a non-conformal contact geometry with a flat lower surface. The surface was manufactured by firstly applying a domed shaped profile using a radius tool. The surface was then finished using a purpose made polishing block. Polishing paper was attached to the surface using double sided adhesive tape and the polishing procedure was performed upon a lathe rotating at 500RPM, the procedure is depicted in Figure 2-8. The sample was finished to a radius of 9.3mm+/-0.05 and the resultant surface roughness attained was 0.8 μm+/-0.3μm.

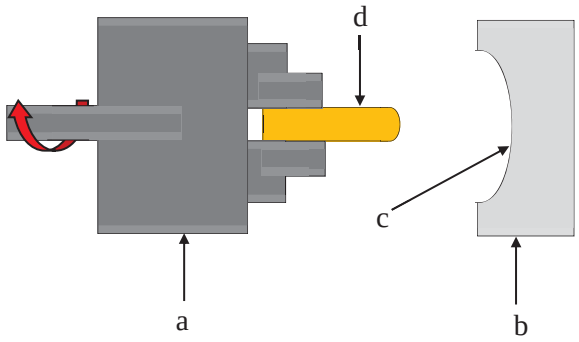

Figure 2-8: Machine process for polishing curved surfaces. (a) Lathe chuck rotating at 500RPM, (b) steel polishing block with 9.5mm internal radius machined, polishing paper is located on radius via double-sided adhesive tape, (d) upper sample

The highly polished surface of each sample, upper and lower, were assessed in terms of their average surface roughness (Ra) and profile using a G4 Alicona infinite focus surface measuring device.

2.2.3 Surface Preparation

Once the samples were machined all surfaces were thoroughly cleaned prior to testing in order to reduce contamination. Firstly, the samples were washed using tap water to remove any debris from the machining process and wiped dry using a lint free cloth. The samples were then submerged in distilled water heated to 40°C and held within a

reciprocating bath for 15 minutes; the samples were then dried using a lint-free cloth. Finally, the samples were submerged in acetone for 3 minutes and then dried in air.

2.3 Laser Surface Texturing

Surface textures were applied to the surface by laser ablation and was undertaken by the laser research group at the University of Birmingham using a multi-axis laser micro machining platform with an Yb-doped laser source (Amplitude Systems). The texturing process employs femtosecond laser pulses that are focused via a lens onto a substrate that is mounted upon a computer-controlled XY-AC linear and rotary stage, focussing the laser on the surface results in material ejection. During this process of irradiation of the PEEK surface the material is ejected in the form of species such as atoms, ions and clusters (Hammouti, et al., 2015) The depth of ablation by this process is dependent on the following parameters; beam energy density, laser pulse duration and laser wavelength in addition to the heat of vaporisation of the material.

The resultant geometry of the textures approximates that of a spherical segment shaped dimple defined by three parameters; diameter, depth and density. Figure 2-9 shows three texture diameters at various densities.

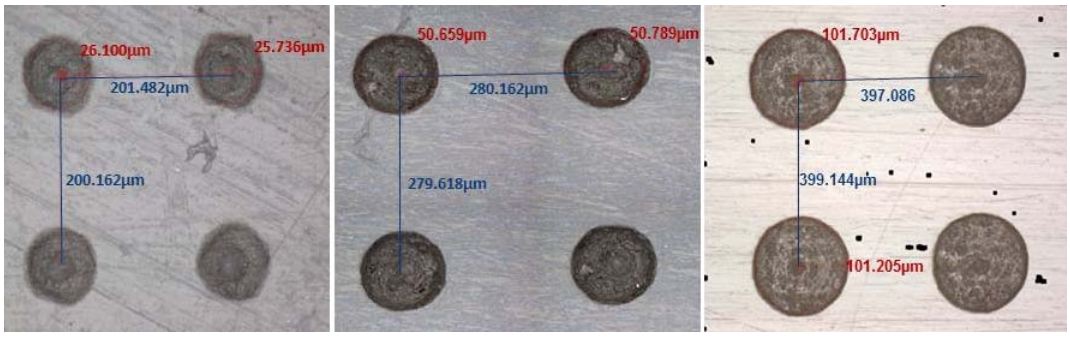

Figure 2-9: Three differing textures diameters at three differing densities. The figure illustrates the circular shape of the cavities providing the pore radii and distance between the textures (defined as density). (a) 25µm radius (50µm diameter), 5% density, (b) 50µm radius (100µm diameter), 10% density, (c) 100µm radius (200µm diameter), 20% density.

Figure 2-10a, b and c illustrates the depth parameter of the circular pores, where 5µm, 10µm and 20µm texture depths are shown. The diameter and density of the textures shown are 200µm and 5% respectively.

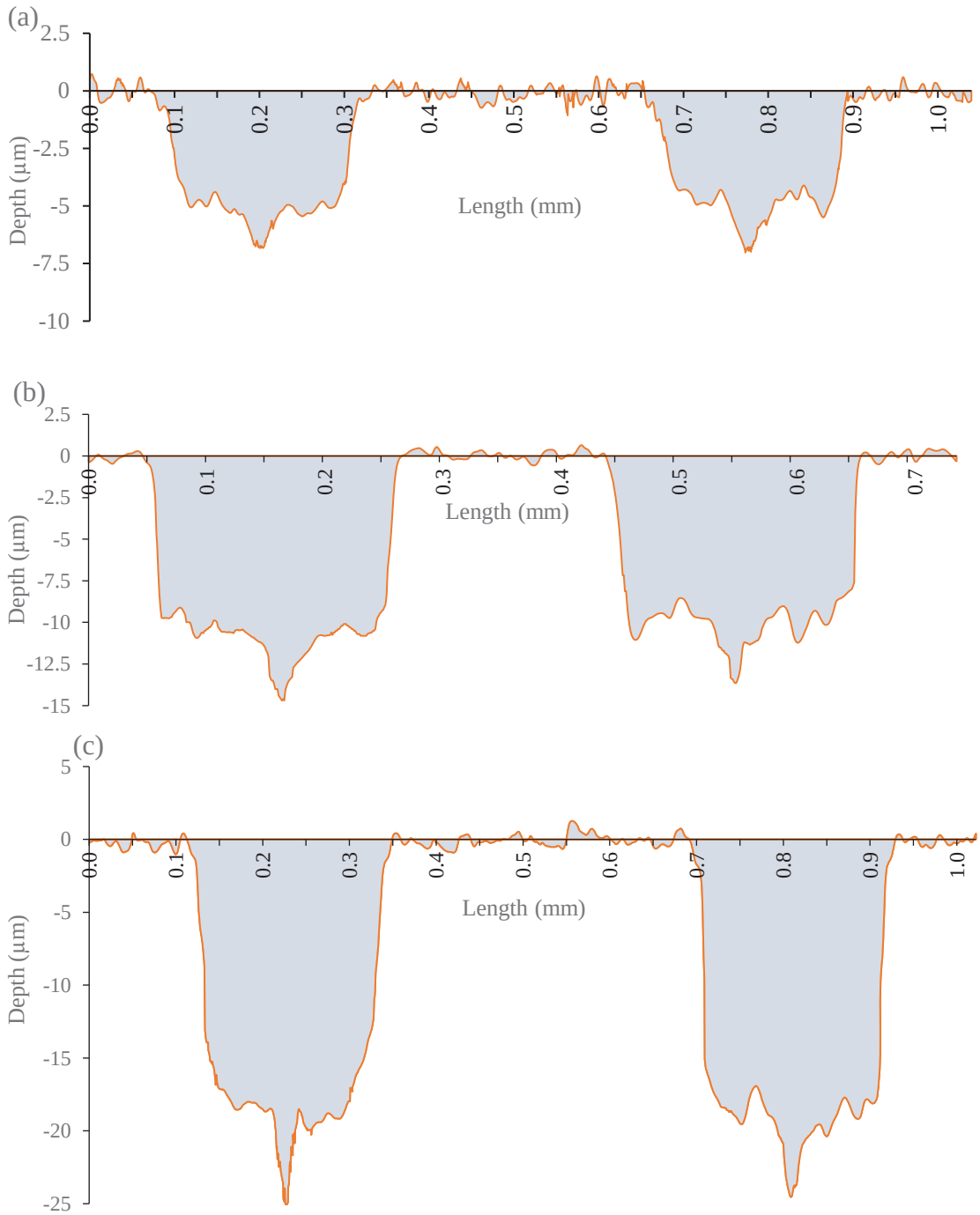

Figure 2-10: Surface texture profiles (a) 5µm depth of a 200µm diameter texture applied at a density of 5%, (b) 10µm depth of a 200µm diameter texture applied at a density of 5%, (c) 20µm depth of a 200µm diameter texture applied at a density of 5%.

2.4 Summary of Experimental Methods

The shape of the cross-section given within Figure 2-10 is not a true representation of the actual textures. This is due to the aspect ratio of the diagram where the x-axis is given in mm and the y-axis in µm. Given this the true shape of the pores would be approximately that of a spherical segment as shown in Figure 2-11.

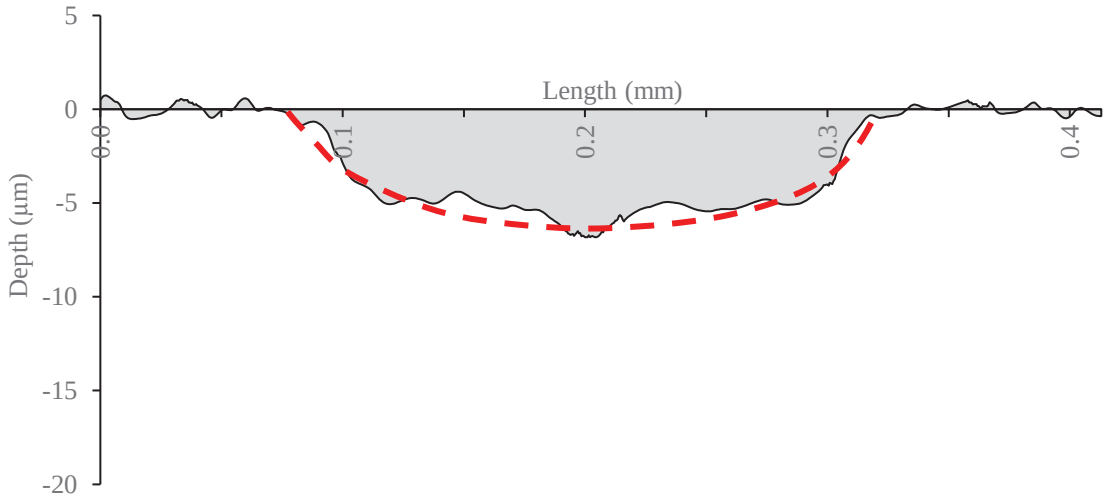

Figure 2-11: Shape approximation of surface textures

The cross-sectional diagram of the textures presented in Figure 2-10 and Figure 2-11 shows that the edges are free form bulges that occur upon the outer rim of the pores during laser surface texturing of metallic surfaces.

The experimental study undertaken in Chapter 3 was performed upon the HFRR test rig prior to the acquisition of the TE-77. The TE-77 was then employed for all other experimental studies throughout this thesis owing to the greater flexibility in experimental parameters and data acquisition capabilities that the TE-77 offers, as described in Chapter 2.11.

The acoustic emission technique was not employed within the experimental investigations presented in Chapters 3 and 4 due to the system having not been acquired by that point in time.

The location and fixing of the sensors to the TE-77 and upper samples was achieved through manufacturing a sensor/sample holder that was clamped within the TE-77. Full details of the arrangement is provided within Chapter 6.2.

CHAPTER 3

Improving the Surface Wettability of PEEK by Surface Texturing to Enhance Lubrication for Reduced Friction and Wear

3.1 Introduction

The following study is conducted to investigate the feasibility of applying surface textures to Poly-ether-ether-ketone (PEEK) to improve the wetting capabilities of the surface for the purpose of friction and wear reduction within thin-film mixed/boundary lubricated conditions. Polymers typically have low surface energies owing to the weak molecular forces bonding atoms together, which result in hydrophobic wetting conditions. Wettability is a crucial property to improve the lubricating characteristics of a surface within frictional contacts and in facilitating friction and wear reducing mechanisms. In order to evaluate the role of surface textures relating to surface wettability and friction and wear phenomena, the objective of the study was to assess the lubricating characteristics of the PEEK surface relating to the modification of surface topography.

3.2 Experimental Methods

Experimental Details

The tests were conducted upon a HFRR (detailed description provided in section 2.12) and ran at a reciprocating frequency of 2Hz for 15 minutes under a 10N load and a stroke length of 2mm. The lubricant employed was Castrol 80W-90 lubricant oil maintained at a temperature of 80°C. The viscosity values are provided below in Table 3-1 .

Table 3-1: Lubricant properties Castrol 80W-90 (Castrol, 2014)

Parameter	Unit	Measurement
Viscosity, kinematic 40°C	mm^2/s	109
Viscosity, kinematic 100°C	mm^2/s	15.1

Materials

The upper sample was a 6mm ANSII 52100 steel ball; truncated to allow a conformal contact configuration. The lower sample was a PEEK disc 10mm in diameter and 4mm thick. Four surface conditions were examined within the study; a plane surface (denoted as the control specimen), and three different textured surfaces. Figure 3-1a and Figure 3-1b shows the upper and lower specimens and Figure 3-2 illustrates the contact configuration in relation the samples geometry.

(a) (b)

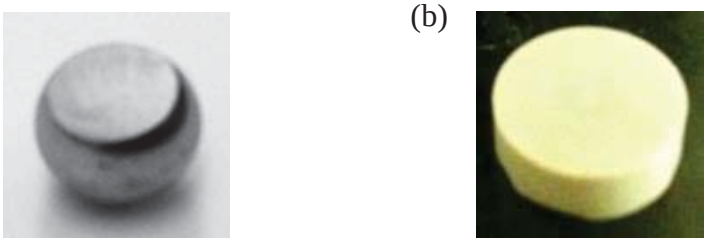

Figure 3-1:(a) Upper specimen - ANSI 52100 6mm Steel ball to provide a flat surface with a diameter of 2mm and a surface roughness (Ra) of 0.1µm (+/-0.02µm). (b) Lower specimen - PEEK disc of 8mm diameter, 4mm thick with a surface roughness (Ra) of 0.1µm(+/-0.02µm)

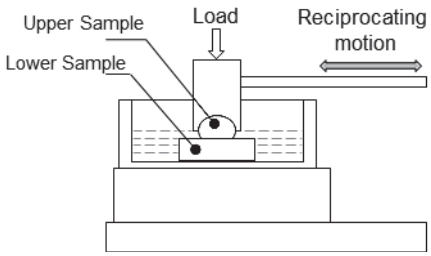

Figure 3-2: Contact configuration in relation to the sample geometry and experimental layout. Illustrating loading direction and direction of motion.

Both upper and lower surfaces employed throughout the tests were polished to a surface roughness (Ra) of 0.12μm (+/-0.02μm) prior to any treatment being applied; the surface roughness was measured by means of an Alicona G4 system. The PEEK samples were cut by a parting-off tool in a lathe at a length of 4.1mm from an 8mm extruded rod. The surfaces were then polished using 400, 600, 800, 1000, and 1200 grit Silicone Carbide (SiC) polishing paper. The polishing procedure was undertaken such that the final thickness was 4mm +/- 0.01 and was measured using digital callipers.

To ensure a conformal contact and parallelism between the opposing surfaces the ANSII 52100 Steel samples were polished using a milling machine, where the samples were held within a purpose made fixture. The apparatus is illustrated in Figure 3-3, where the polishing block was setup perpendicular to the miller's spindle using a dial test indicator. The ball carrier is shown in Figure 3-4 with a diameter of 8mm and a length of 25mm (inclusive of the ball). The carrier was located into slots of 8.1mm diameter to ensure a clearance/transition fit.

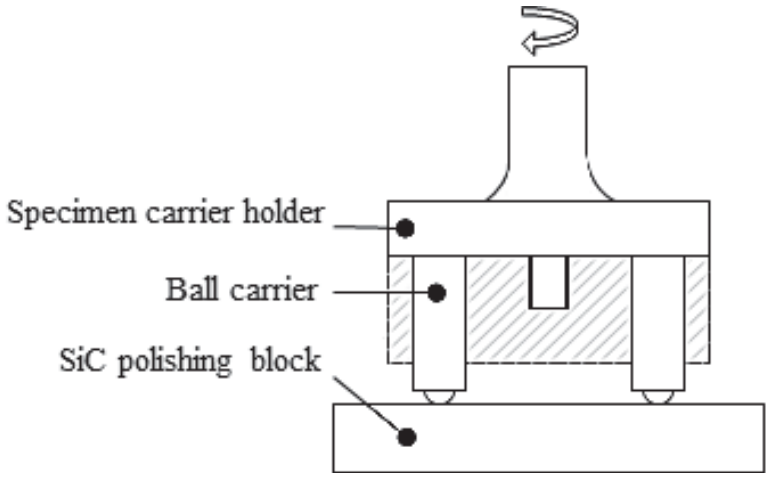

Figure 3-3: Purpose made specimen holder for the polishing of a flat surface on the ANSII 52100 Steel ball. The ball is held in the carrier which is inserted into the slots of the holder.

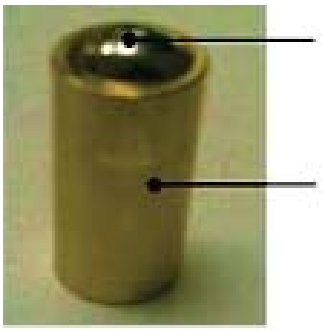

Figure 3-4: Ball carrier: 6mm ANSI Steel ball secured into ball carrier by means of an interference fit.

Surface Texturing

Arrays of textured pores were created by laser ablation using the method described in Chapter 2.3, at a depth of 10µm with a diameter of 100µm. The texture parameter varied during the study was the texture density.

The texture density was chosen as the variant owing to the review of literature (Bogdan , 2012) (Huang, et al., 2012) (Kovalchenko, et al., 2005). Authors investigating the effect of texture density have shown that variations in the texture density have a profound effect on the wetting capabilities and frictional behaviour of a surface. Moreover, these studies elucidated a dis-association in the relationship between density and other texture parameters.

Bogdan, studied the contact angle and surface energy of textured surfaces using a pendant drop wettability test, finding that variations are more profound by changes in the surface texture density compared to variations in texture diameter (Bogdan , 2012). Huang et *al*. showed that hydrophilic surfaces substantially out-perform hydrophobic surfaces in terms of friction reduction. Furthermore, Huang et *al*. assessed the frictional performance of surface textures within a steel-PDMS conformal sliding couple, lubricated with a glycol/water fluid mix. Varying the diameter and the number of pores within the contact

zone resulted in an overall increase in sliding friction with an increase in texture diameter. Moreover it was shown that changes in the number of pores within the contact zone served only to approximately shift the magnitude of friction obtained (Huang, et al., 2012). Kolvachanko et *al*. conducted uni-directional sliding tests with textures of similar texture diameter and depth and variable density. The results showed that by increasing the texture density the coefficient of friction increased across the Stribeck curve (Kovalchenko, et al., 2005).

Textures were dispersed over the surfaces at 10%, 20% and 30% densities depicted in Figure 3-5a, b and c respectively and Figure 3-6 shows a cross-sectional image taken through the centre of one textured pore.

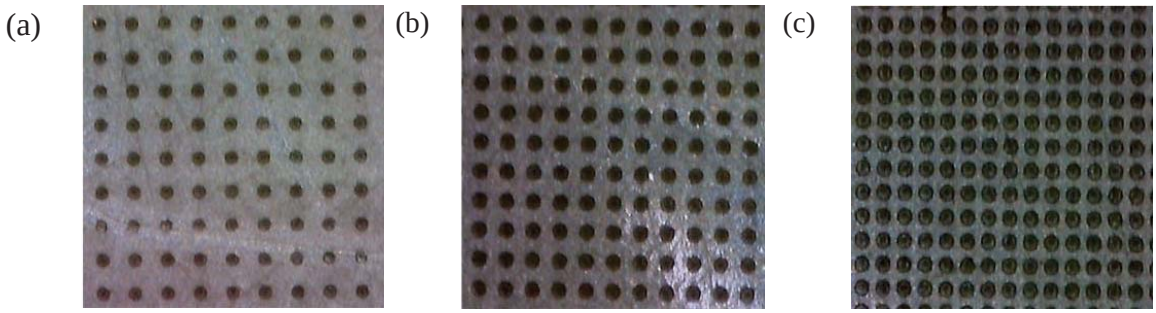

Figure 3-5: Surface textures produced by laser ablation using a Yb-doped femtosecond laser. Circular pore textures of 100µm diameter and 10µm depth dispersed over a PEEK surface at (a) 10%, (b) 20% and (c) 30%.

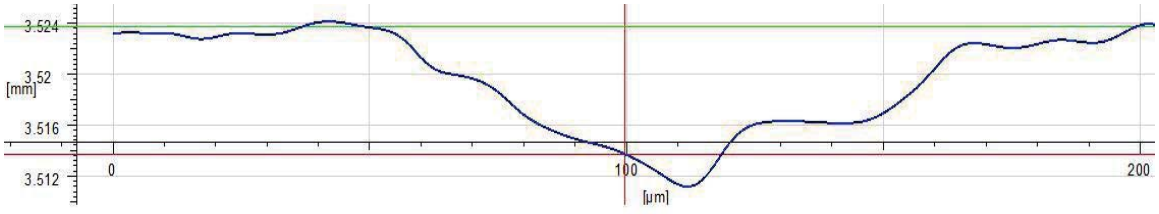

Figure 3-6: Cross-section of a singular textured pore of 100µm diameter and 10µm depth produced by laser ablation using a Yb-doped femtosecond laser

3.3 Results

3.3.1 Coefficient of Friction

Figure 3-7 shows the average coefficient of friction (COF) obtained from each test conducted where the error bars represent the maximum and minimum coefficient of friction. The average COF is taken as the average across the full 15minute test for each specimen and is presented in Table 3-2.

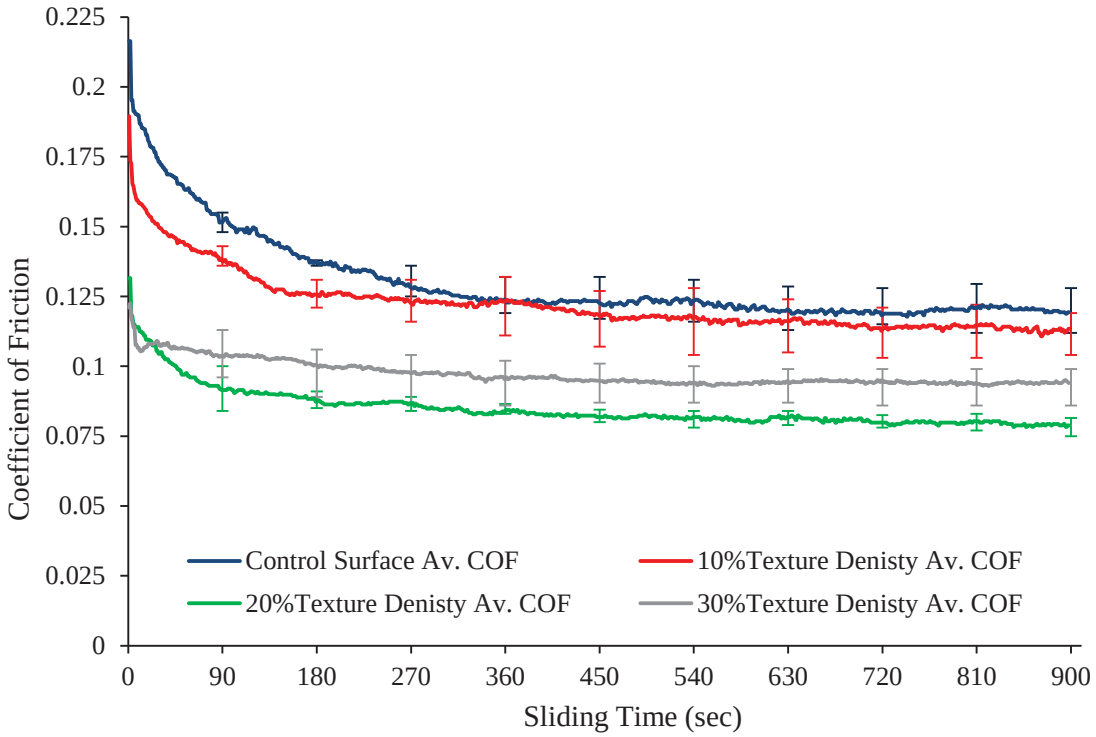

Figure 3-7: COF vs. Sliding time for a lubricated contact under the following conditions; Load 10N, frequency 2Hz, stroke length 2mm. Tests were performed with un-textured and textured surfaces of 100µm diameter and 10µm depth at densities of 10%, 20% and 30%. Tests were carried out three times for each surface type where error bars provide the upper and lower COF for each test at specific time intervals and the trace-line depicts the AV COF taken across the three test repetitions per surface type.

Table 3-2: Average coefficient of friction for different surface textures

	Plain	10%	20%	30%
Av. COF (µ)	0.13	0.12	0.08	0.10
Standard Deviation	0.0056	0.0077	0.0028	0.0079

The effects of the surface textures on the friction trace, and the resultant average COF for PEEK show that for specimens with 20% and 30% texture densities the average coefficient of friction is 0.08 and 0.1 respectively. The 10% texture densities and the controlled surface had average coefficient of friction values of 0.13 and 0.12 respectively. This suggests that at higher texture densities a mechanism is established that enhances the lubrication between the surfaces, and that such a mechanism responsible for friction reduction cannot be achieved at low texture densities or in the case of an un-textured surface. The average COF of the specimen with the 30% texture density was higher than that achieved at the 20% density, implying that this mechanism may become saturated when the texture density exceeds a certain percentage.

Further observations are seen pertaining to the initial friction peak of each surface treatment. Figure 3-8 depicts the average friction trace for each sample over the initial 30 seconds. It can be seen that the control surface and 10% density surface obtain high initial peaks. Conversely, the higher density textures (20% and 30%) show a substantially reduced initial friction peak. Moreover the introduction of surface textures also effects the time it takes for the friction coefficient to reach steady state. Table 3-3 provides the peak coefficient of friction and the approximate time required to attain steady state conditions. The time is taken from the point where the variation in the coefficient of friction falls between +/- 0.0025.

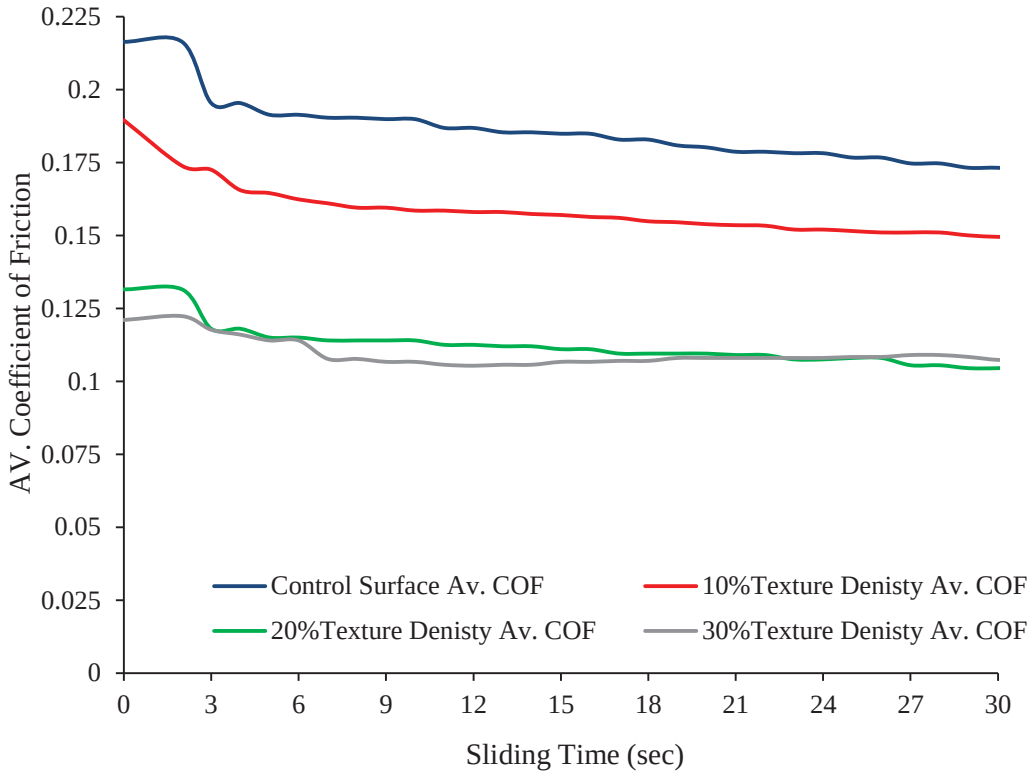

Figure 3-8: Average COF vs Sliding time for 0 - 30seconds of test under a load of 10N, sliding frequency of 2Hz and stroke length of 2mm. Surface textures were 100µm and 10µm covering the surface at densities of 10%, 20% and 30%. The average is taken across the 3 test repetitions for each surface treatment. The plot highlights the difference in the force required to provide dynamic motion of the surfaces corresponding to surface type.

Table 3-3: Time to steady state and initial peak friction results

	Plain	10%	20%	30%
Time (s) to Steady state	575	550	320	220
Steady state COF	0.116	0.113	0.08	0.094
Peak COF	0.22	0.19	0.13	0.12
Standard Deviation	0.0183	0.0195	0.0105	0.012503

3.3.2 Wear Assessment

The wear scar images in Figure 3-9 a-d provide further evidence of the enhanced lubricating mechanisms the surface textures offer. Dotted lines highlight the wear track width encompassing the wear scar. Numerical annotations appoint to the damage

sustained upon the surface; (1) groove like ridges, (2) dis-colouration of the surface due to polishing, (3) minor dis-colouration in the region of wear scar, (4) dis-colouration of the surface due to polishing.

Observed is the increase in surface damage for the control, 10% and 30% density textured surfaces. Clear wear scar morphology of the surfaces show that, in the first instance, mild scarring of the surface for the control specimen and then heavy polishing for the 10% and 30% density surface. The 20% density image indicates light contact between the upper and lower specimen. A diminutive wear scar compared to the other tests specimens is observed where light polishing of the surface is observed by the slight dis-colouration in the vicinity of the contact region.

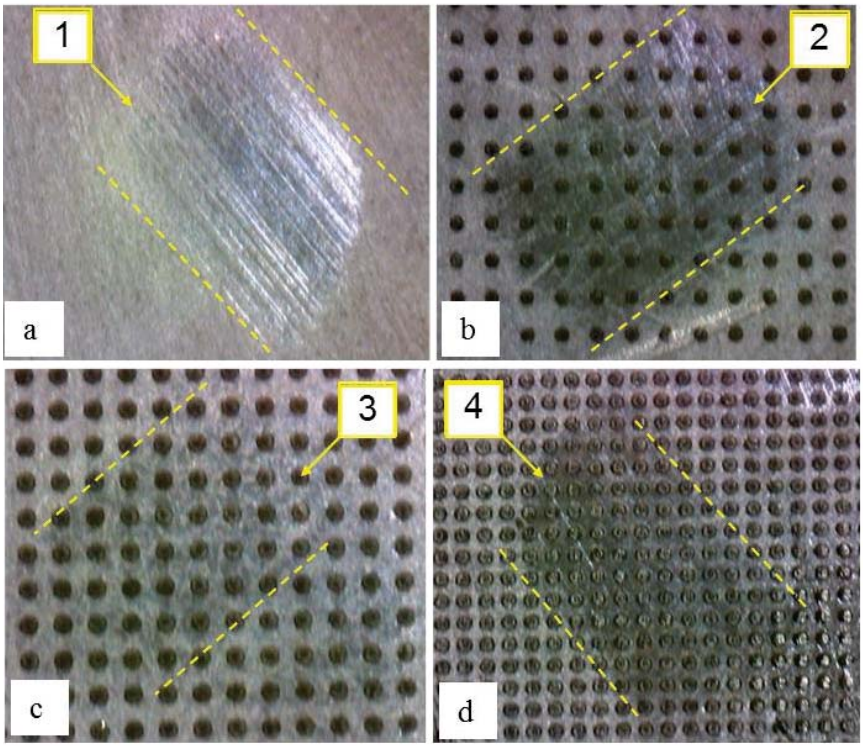

Figure 3-9: Wear Scar Images: (a) Control (unprocessed surface) (b) 10% Density (c) 20% Density (d) 30% Density Dotted lines encompass the wear track width, annotations highlight wear damage (1) groove like ridges in the direction of sliding, (2) dis-coloration of surface due to scuffing damage, (3) minor dis-colouration, (4) discoloration of surface due to scuffing damage.

3.3.3 Surface Wettability

The wettability of PEEK using both water and a synthetic poly-alpha-olefin (PAO, Chevron Philips, Texas, USA) oil in two different viscosity grades was studied by Kalin and Polajnar (Kalin & Polajnar, 2014). The investigation showed that water had a contact angle of 68.6°, whilst the PAO oil had contact angles of 12.5° for the high viscosity oil and 9.9° for the lower viscosity oil. Furthermore, the spreading characteristics were also studied by (Kalin & Polajnar, 2014) showing that the PAO oil (high and low viscosity) had superior spreading effects compared to water. Therefore to elucidate the effect of surface textures on the wetting properties of PEEK distilled water was used as the test fluid during the pendent drop wettability study.

Figure 3-10 presents the images of the pendent drop wettability tests and Table 3-4 provides the average contact angle over three repeated tests for each surface treatment. The wetting capabilities of a surface are assessed by its ability to allow a drop of fluid to spread on the surface. The wetting criteria is that for surfaces with a contact angle of >90° the surface is hydrophobic, <90° hydrophilic (Qin, et al., 2013). The control and 10% density samples produced a larger contact angle, showing a reduction in hydrophilicity compared to the 20% and 30% densities that showed superior hydrophilicity as indicated in the results from Figure 3-10 and Table 3-4. The results also indicates that the surface demonstrates enhanced fluid retention and improved spreading capabilities on the surfaces with higher texture densities.

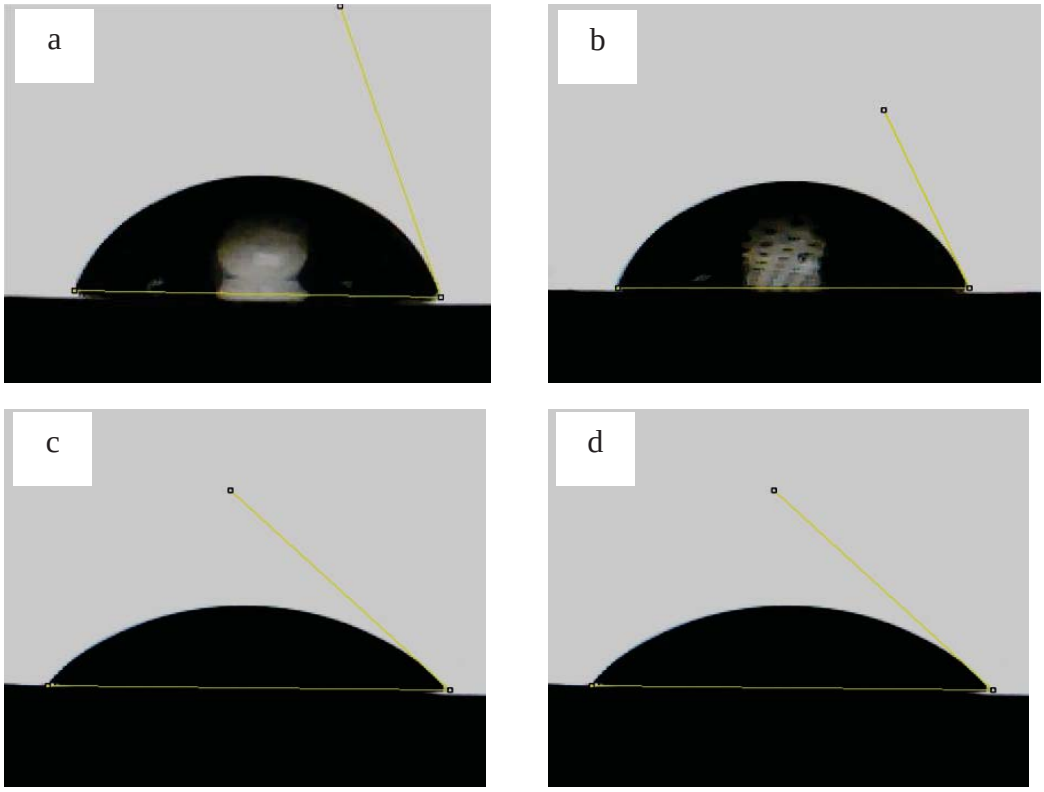

Figure 3-10: Water droplet showing contact angle: (a) Control (unprocessed surface), (b) 10% Density, (c) 20% Density, (d) 30% Density

Table 3-4: Wetting results showing contact angle for each surface treatment.

	TEST 1	TEST 2	TEST 3	AV. Contact Angle (°)
CONTROL	70.23	76.8	73.5	73.51
10%	65	63	60	62.66667
20%	41	42	40	41
30%	42	45	43	43.33333

3.4 Discussion

The coefficient of friction traces show that surface textures with a density coverage of more than 10% enhances the tribological performance. The reduction of friction and wear observed is attributed to the variation in the interaction between the lubricating fluid and the PEEK surface across all surface treatments. This is further substantiated in Figure 3-11 that shows the average coefficient of friction and contact angle as a function of surface treatment. There is a strong correlation between the resultant average friction coefficient and the wetting capabilities of the surface.

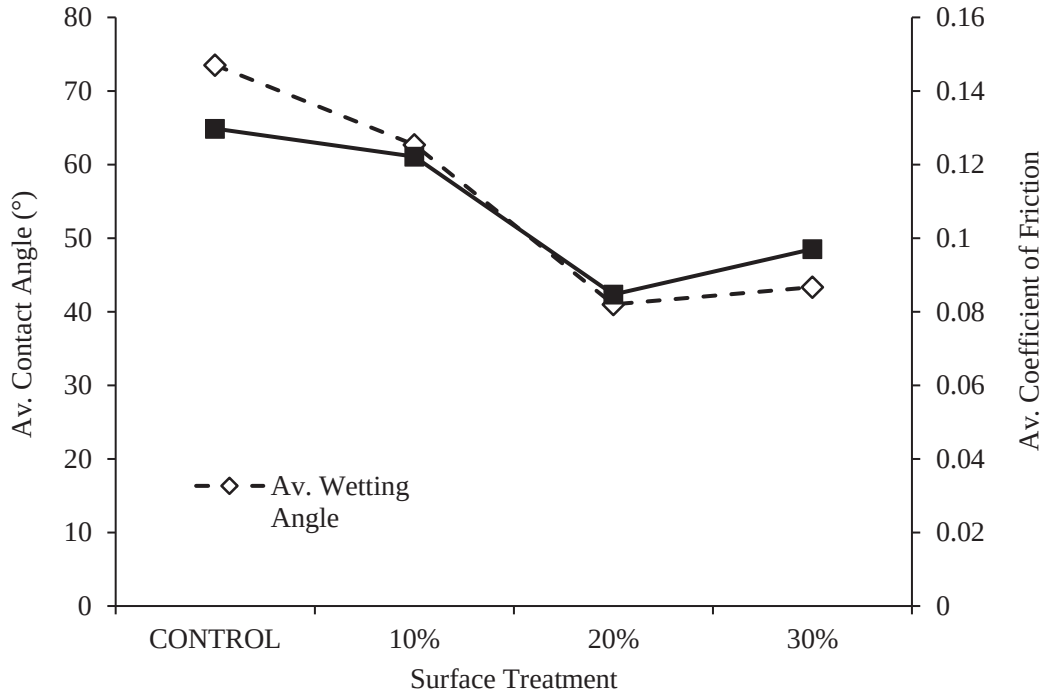

Figure 3-11: Correlation graph plotting average contact angle and Av. COF vs. Surface treatment

The low surface energy typical of polymers has detrimental effects relating to the wetting and lubricating capabilities of the surface. An increase in hydrophobic behaviour serves as a mechanism to repel fluid from its surface. The effects of which are demonstrated in

the friction analysis. Initially, once a load is applied the fluid is more readily expelled from the contact region, due to the low surface energy of the surfaces verging on hydrophobic. In this instance it is hypothesised that an adhesive mechanism transpires owing to the lack of lubricating media separating the opposing bodies. According to Myshkin *et al*. adhesive bonds are formed when the surfaces were in solid contact causing a proliferation in asperity contact and adhesive bonds are formed owing to the hydrogen bonds and Van Der Waals forces. On the application of a tangential force these junctions between the two surfaces are sheared (Myshkin, et al., 2005). To overcome this, the force required for the transition from static to kinetic friction resulting in relative motion increases, consequentially causing an increase in the initial friction peak observed in Figure 3-8. Increased friction throughout the test is attributed to the lack of lubricant on the surface owing to the reduced wetting capabilities of the control and 10% density surfaces. As illustrated within Figure 3-12 as the upper sample comes into contact with the lower surface under an applied load lubricant is ‘squeezed’ out of the sides. Once the upper surface is in motion sliding across the lower surface the lubricating fluid is expelled from the contact zone creating a boundary lubricated contact, with asperities in contact. Conversely, the enhanced wetting capabilities of the 20% and 30% textured surfaces enhances lubrication of the surface. However at 30% density the friction and contact angle increases compared to 20% density. This suggests that a saturation limit may exists that limits how much the density can be increased before the textures become detrimental to frictional performance.

An increase in hydrophilicity contributes to the preservation of a thin film of lubricant on the surface, partially separating the two opposing bodies whilst also filling the textured pores as shown in Figure 3-12.

(a)

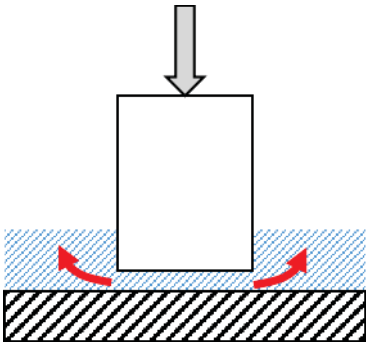

Upper surface being brought into contact with lower surface with lubricant fluid being ‘squeezed’ out from sides.

(b)

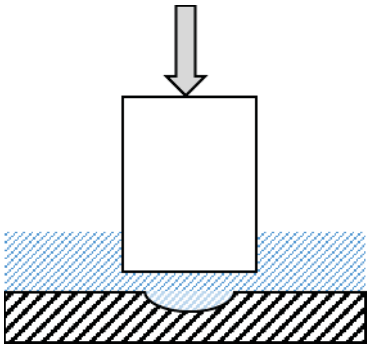

Upper sample being brought into contact with textured lower surface where lubricant fluid fills the pores.

(c)

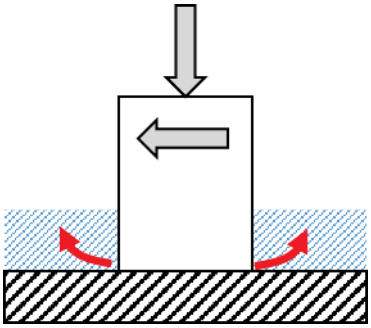

Once sliding commences lubricant if fully expelled from contact zone resulting in boundary lubrication regime.

(d)

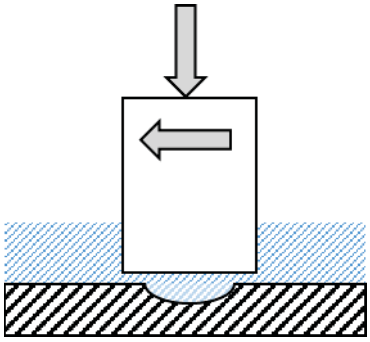

As sliding commences a thin fluid film of lubricant is maintained with fluid filling textured pores.

Figure 3-12: (a) Fluid being squeezed out of contact zone as vertical load is applied. (b) Fluid filling the texture cavity as vertical load is applied. (c) Fluid expelled from contact zone once sliding commences. (d) Fluid filling texture, maintaining thin fluid film.

The significance of lubricant retention aiding wear debris expulsion is that the wear scar for a control specimen exhibits scarring of the surface created by an abrasive wear mechanism. Operating within the boundary regime asperities are removed during sliding, resulting in the production of wear debris. The lack of fluid to aid expulsion of wear particles from the contact zone results in the abrasive wear of the control surface. Conversely the textured surfaces exhibit polishing of the surface, attributed to a boost in lubrication. Enhancing fluid retention on the surface enables the generated wear particles

to be expelled, either from the contact zone or into the textured cavities, removing the possibility of abrasive wear. Polishing of the textured surfaces occurs owing to the asperity contact at discrete points suggesting that the textured surfaces were operating within the mixed/hydrodynamic lubrication regime. Moreover, the lack of wear on the surface with a 20% texture density indicates that a hydrodynamic mechanism was present

It has been shown that the presence of a lubricating media eases the transition from static to kinetic friction when a tangential force is applied, preventing the formation of adhesive junctions and thus reducing the force required to generate relative motion. Once sliding commences the preservation of a lubricant film via fluid retention facilitates the generation of hydrodynamic pressure lifting the surface apart, providing enhanced frictional performance.

The effects of the surface/liquid interaction can also be observed by the length of time taken for the friction to attain steady state. It has been shown that the 20% and 30% densities take a substantially shorter time to reach steady state friction. The fluid retention and preservation on the surfaces described above provides more stable sliding conditions. This is not the case for the control and 10% density specimens where the lubricant is continually expelled from the contact zone. The resultant boundary condition encourages asperity contact between the surfaces. Once this occurs a running-in period ensues whereby adhesive junctions are sheared and asperities flattened until the system attains a steady state.

3.5 Conclusions

The aim of this chapter was to investigate the influence of surface textures in relation to the surface wettability and friction and wear behaviour.

It was found that varying the density coverage of textures over a surface had a substantial effect on the resultant friction, wear and wetting capabilities of the surface. A strong correlation was found to exist between the resultant friction and the surface wetting, where friction reduction coincided with decreases in wetting angle. This suggests that a primary mechanism for reducing the friction and wear within an all PEEK sliding couple is improving the wetting capabilities. This enabled the preservation of a lubricant film and fluid retention acting as a secondary supply of lubrication. Furthermore, fluid retained within the dimpled pores can encourage additional friction and wear reducing mechanisms.

The un-textured and 10% density surfaces were shown to exhibit low hydrophilic properties, where increasing the texture density increased the hydrophilicity of the surface. However, at 30% texture density friction increases along with the wetting contact angle signifying a reduction in hydrophilic properties. This suggests that there is a saturation limit whereby friction can be improved so far by increasing the texture density until textures become detrimental to friction and wear. From the surfaces tested it was found that a texture density coverage of 20% was the optimum value.

CHAPTER 4

Investigation of Depth and Diameter Parameters for Optimal Performance

4.1 Introduction

The review of literature presented in Chapter 1.3 showed a relationship between texture diameter and depth, where an aspect ratio (diameter/depth) is often defined as being optimum in relation to frictional performance. However, a number of problems arise when applying such parameters to new studies. Firstly, such an aspect ratio can be created by an array of numerical combinations. The production and testing of such a wide range of texture parameters questions the feasibility of experimentally evaluating surface textures on such a scale. Secondly, textures interpreted as an aspect ratio negates the suitable assessment regarding the influence of the independent effects that the diameter and depth parameters produce.

To surmount these problems a statistical approach is adopted in the treatment of results for the purpose of firstly; predicting the coefficient of friction (COF) for surface textures not empirically evaluated, allowing a holistic understanding of the frictional performance across a broad range of texture parameters. Secondly, isolate the independent effects of texture diameter and depth in order to ascertain an appreciation of the influence of each parameter relating to the resultant coefficient of friction.

4.2 Experimental Methods

Short duration reciprocating sliding tests were undertaken on a Phoenix Plint TE77 high frequency reciprocating test rig, a full description of which is given in Chapter 2.1.1. The

advantages of using the TE-77 over the HFRR is that it enables a greater flexibility in experimental parameters also described in Chapter 2.1.1. The COF is used to gauge performance and compare across different surface structures. Nine texture combinations were empirically evaluated by varying the diameter and depths between 50, 100, 200μm and 5, 10, 20μm respectively. A density coverage of 20% was chosen in relation to the results obtained in Chapter 3 which were in reasonable agreement with the findings of Zhang et al. indicating an optimum density of 19.9-29.9% (Zhang, et al., 2013). Whilst Huang et al. when undertaking a Stribeck study between hydrophobic and textured hydrophilic surfaces prescribed an optimum density of 22.9% (Huang, et al., 2012). Moreover, a review of the literature, also presented in Chapter 3 reveals the dis-association in the relationship between density and other texture parameters in relation to friction. The control surface (plain, un-textured surface) represents the criterion for the frictional performance of surface textures to be compared against. The coefficient of friction (COF) is calculated from a tangential force measurement, captured at a rate of 1 per second over the test duration of 1800 seconds. The upper sample was a flat ended 5mm diameter pin sliding at 1Hz in a conformal contact configuration across a flat plate under a load of 70N. The corresponding contact pressure was 3.56MPa and calculated according to Equation 4 1.

$$Contact\ pressure = \frac{Applied\ Force}{Area\ of\ pin\ face} \qquad \textbf{Equation 4.1}$$

The contact zone was fully immersed in a lubricating fluid of Reagent grade distilled water maintained at a temperature of 37°C. Tests were conducted for each of the nine texture diameter depth combinations and repeated three times culminating in a total of 27 tests. Test conditions were adapted from ASTM F732 ‘Standard Test Method for Wear

Testing of Polymeric Materials Used in Total Joint Prostheses' (ASTM F732-00, 2011). A full account of experimental and surface texture parameters are provided in Table 4.1 and Table 4.2 respectively.

Table 4-1: Experimental Parameters

Load	70N
Contact area	19.6mm^2
Contact Pressure	3.56MPa
Reciprocating Frequency	1 cycle/second
Stroke length	7.5mm
Mean sliding speed	15mm/sec
Lubricant	Distilled Water
Lubricant temp.	37°C

Table 4-2: Surface Texture Parameters – Density set at 20%

Diameter	50 μm	100 μm	200 μm
Depth	5 μm	5 μm	5 μm
	10 μm	10 μm	10 μm
	20 μm	20 μm	20 μm

4.3 Results and Discussion

4.3.1 Coefficient of Friction

Figure 4-1 to Figure 4-4 shows the coefficient of friction as a function of sliding time for each diameter at the specified depths. The error bars denote the maximum and minimum COF at specified intervals with the trace line representing the mean of the three test repetitions. It can be observed that the textures attain a lower coefficient of friction across all diameter and depth combinations compared to that of the control specimen.

Furthermore, the effect of cavity depth can be seen to vary in relation to each texture diameter.

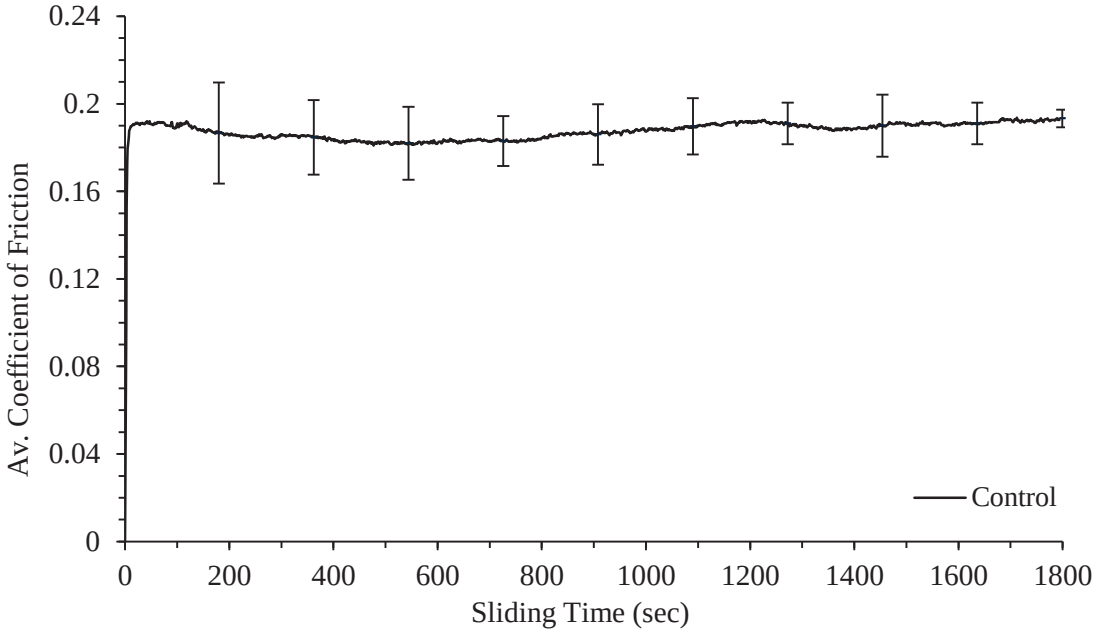

Figure 4-1: COF vs Sliding time for control surface (trace line is the average COF across 3 test repetitions relative to sliding time and the error bars denote the maximum and minimum COF across the 3 test repetitions)

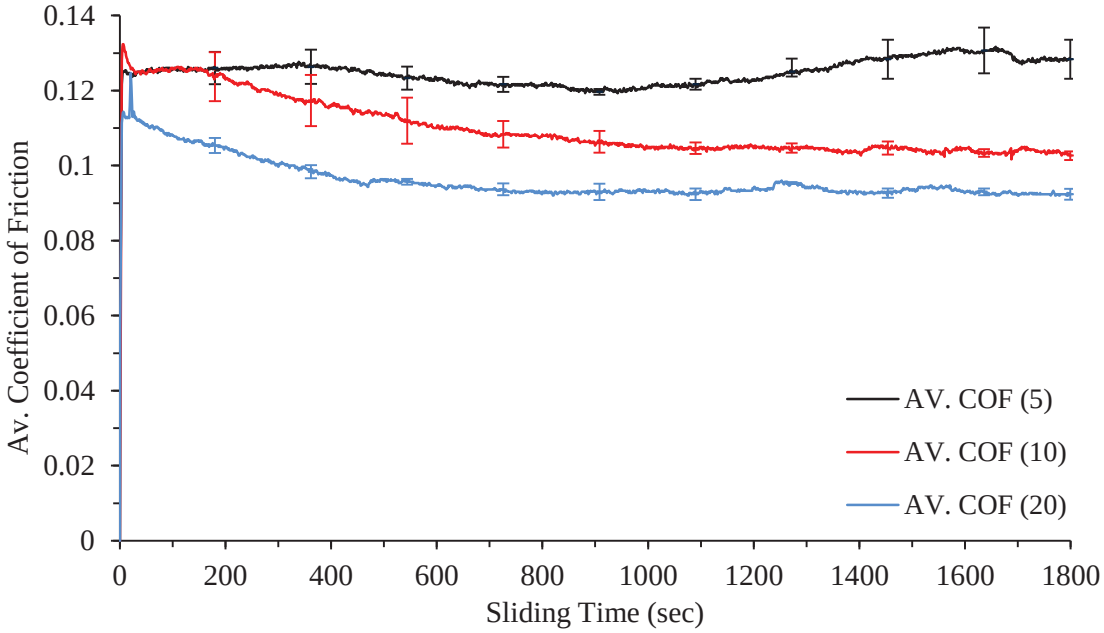

Figure 4-2: COF vs Sliding time for textured surface; 50um diameter, various depths (trace lines are the average COF across 3 test repetitions for each depth relative to sliding time and the error bars denote the maximum and minimum COF across the 3 test repetitions performed for each depth)

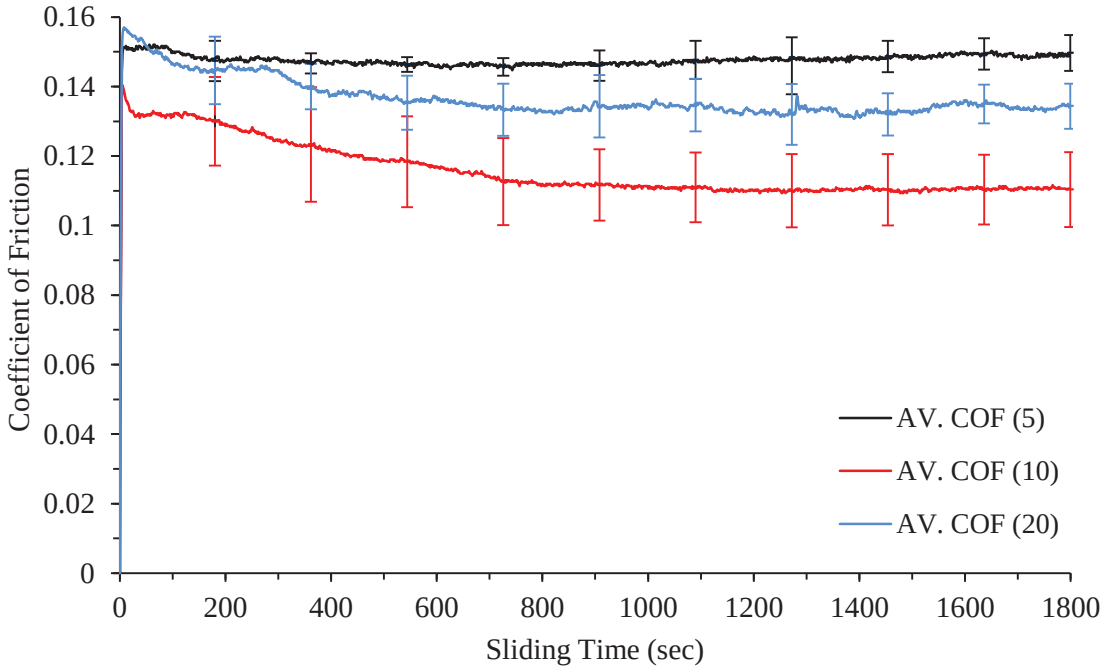

Figure 4-3: COF vs Sliding time for textured surface; 100um diameter, various depths (trace lines are the average COF across 3 test repetitions for each depth relative to sliding time and the error bars denote the maximum and minimum COF across the 3 test repetitions performed for each depth)

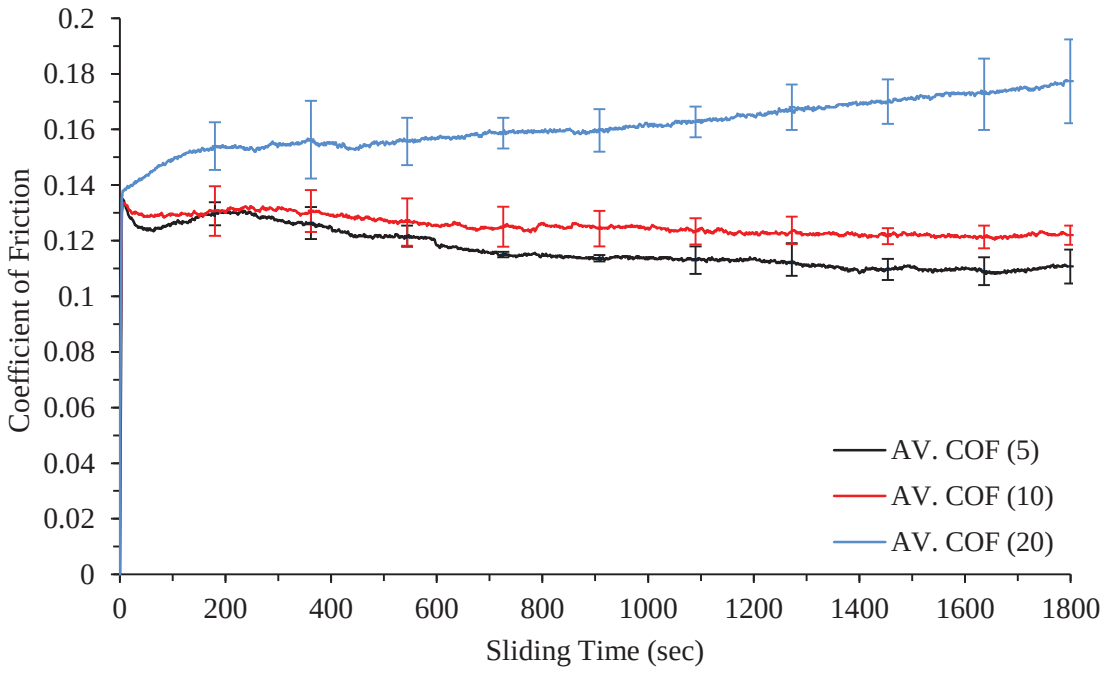

Figure 4-4: COF vs Sliding time for textured surface; 200um diameter, various depths (trace lines are the average COF across 3 test repetitions for each depth relative to sliding time and the error bars denote the maximum and minimum COF across the 3 test repetitions performed for each depth)

Figure 4-5 provides a holistic view of the variation in average COF corresponding to surface structure. The upper and lower error bars represent the maximum and minimum average coefficient recorded and the mid-point marker denotes the average COF over the three test repetitions. The average coefficient of friction is taken as the mean value across the full 1800 seconds sliding time for each individual test. The initial peaks in friction prior to the system attaining steady-state was included in the average coefficient of friction results owing to the significant effect that the surface textures have been shown (Chapter 3) to have in firstly, the initial friction peak and the time taken to attain a steady state frictional output.

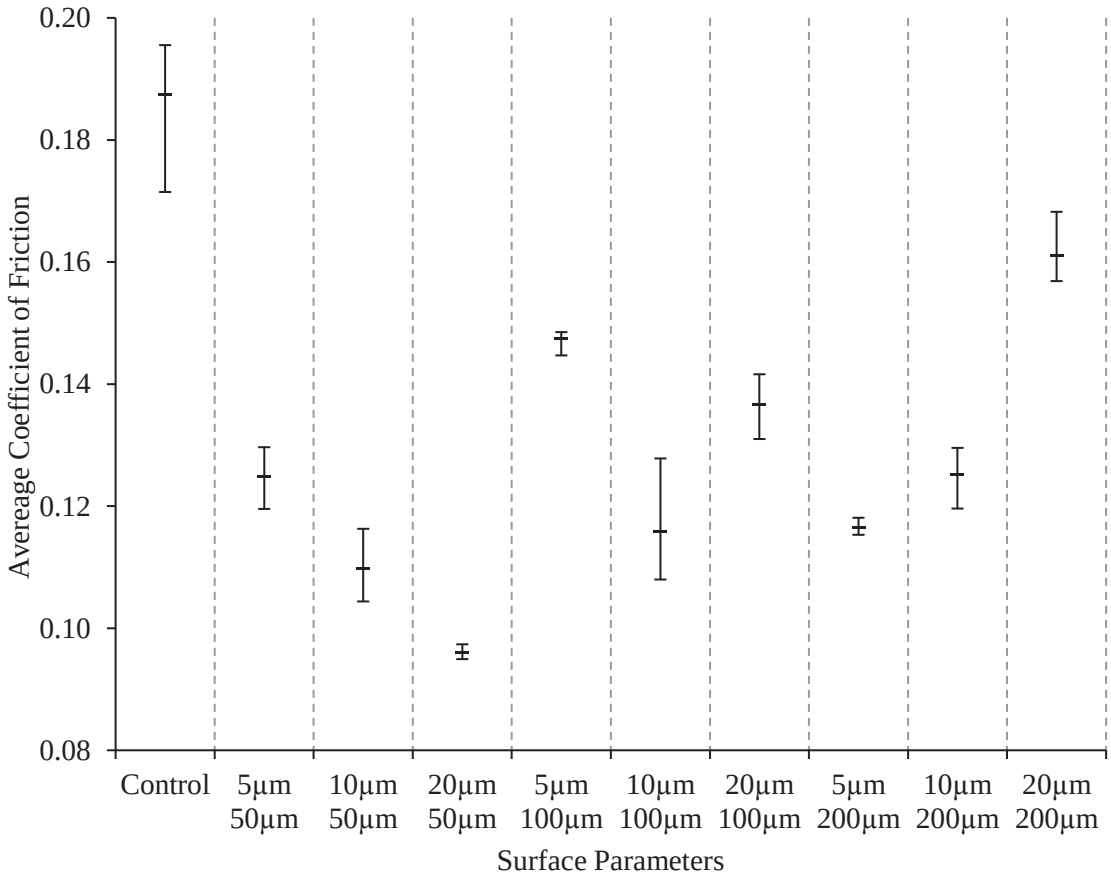

Figure 4-5: Average COF vs. Surface Parameters (error bars represent the maximum and minimum AV. COF of the 3 test repetitions per surface texture combination)

The lowest average coefficient of friction observed in Figure 4-5 derived from a texture diameter of 50µm at a depth of 20µm, recording an average across the three tests repetitions of 0.096. The highest average COF from the textured surfaces was produced from a texture diameter and depth combination of 200µm and 20µm respectively. Furthermore it can be seen that a general increase in the average coefficient of friction occurs with an increase in texture diameter. Such trends cannot be observed in relation to texture depth, as the response in the depth parameter fluctuated with variations in texture diameter.

4.3.2 Factor Effect

In order to quantify the effect of texture diameter and depth in reducing friction relative to the un-textured surface factor effect analysis was undertaken. The two parameters, diameter and depth were denoted as factor A and B respectively. Table 4-3 depicts how the analysis was constructed, where diameters are grouped column wise and depths are grouped row wise and the factor effect is calculated by;

$$Factor\ Effect = \frac{Av.COF\ (Control) - AV.Factor\ (A,B)}{\sigma\ (Factor\ A,B)} \qquad \textbf{Equation 4-2}$$

Table 4-3: Effect analysis construction table

		Factor A (Diameter, µm)											
		50			100			200			Av.	σ	Eff.
Factor B (Depth, µm)	5	0.124	0.120	0.130	0.145	0.149	0.149	0.115	0.118	0.116	0.130	0.014	4.066
	10	0.109	0.116	0.104	0.108	0.128	0.112	0.130	0.126	0.120	0.117	0.009	7.494
	20	0.096	0.095	0.097	0.142	0.131	0.137	0.157	0.158	0.168	0.131	0.029	1.950
	Av		0.110			0.133			0.134				
	σ		0.013			0.015			0.021				
	Eff		5.896			3.551			2.543				

Figure 4-6 shows a graphical interpretation of the factor effect analysis. As suggested in the output from Figure 4-5 the effect of friction reduction decreases as texture diameter increases, with 50µm diameter textures obtaining the highest positive effect on friction reduction and 200µm diameter pores shown to be the least effective.

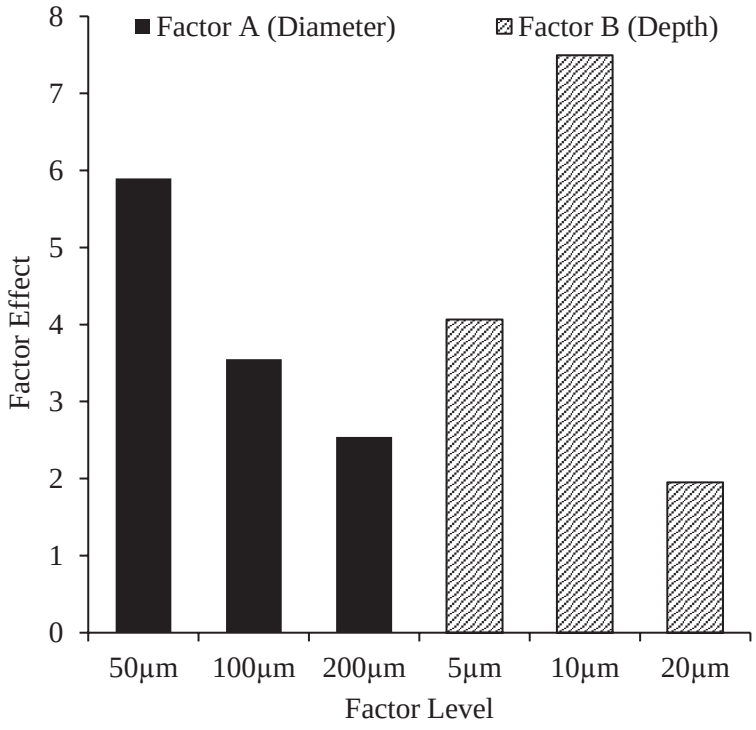

Figure 4-6: Factor Effect: Identifying texture parameters that have the most effect in reducing friction.

However, the effect of pore depth contrasts from what is perceived to be optimum from Figure 4-5 with 10µm depths having the overall highest positive effect in terms of friction reduction followed by 5µm and finally 20µm. It is clear therefore that there is no defined overall optimum depth and that the parameter optimum varies corresponding to a change in diameter.

4.3.3 Regression Model

In order to evaluate the frictional performance of surface textures over a wider range of diameter and depth parameters, a regression model is constructed based upon the experimental values obtained for the average coefficient of friction results. The purpose of the model is to predict the COF for various texture parameter combinations outside of that empirically evaluated. Figure 4-7 shows the coefficient of friction plotted across the diameters for various depths and Figure 4-8 shows the COF plotted across the depths at different diameters. It can be seen in both Figure 4-7and Figure 4-8, that a 2nd order polynomial trend-line adequately describes the relationship between the experimental values of COF and textures with various diameter and depth combinations. The strength of the relationship is indicated by the coefficient of determination, namely the R-squared value, being 1.

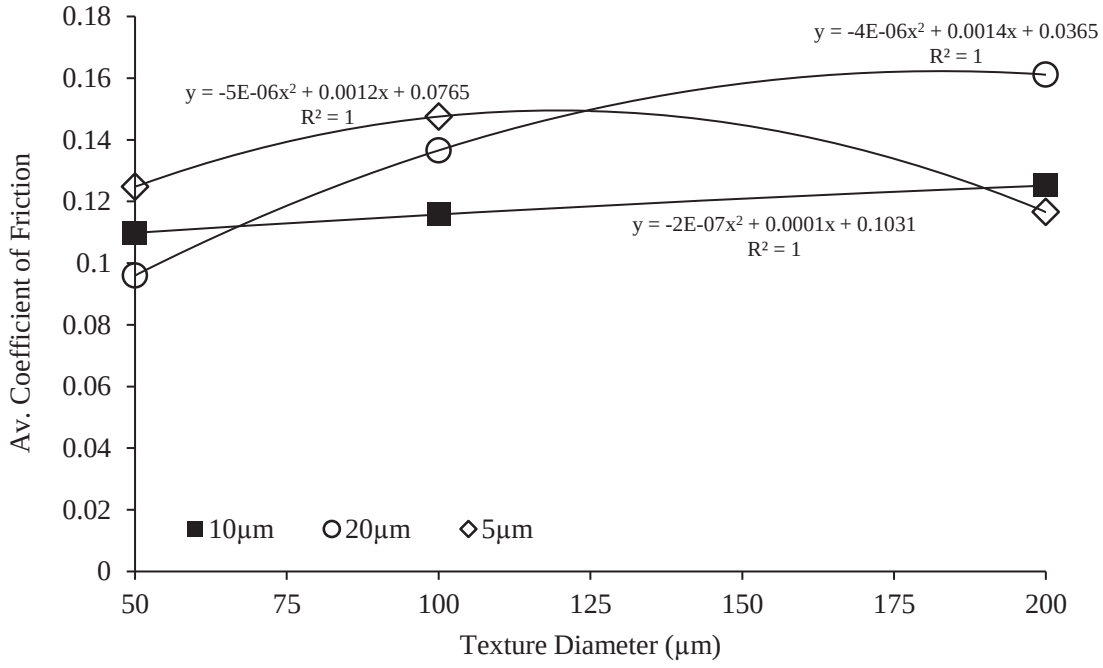

Figure 4-7: Polynomial curve fit of experimental data for texture depths over various diameters, with curve fit equations and R-squared value.

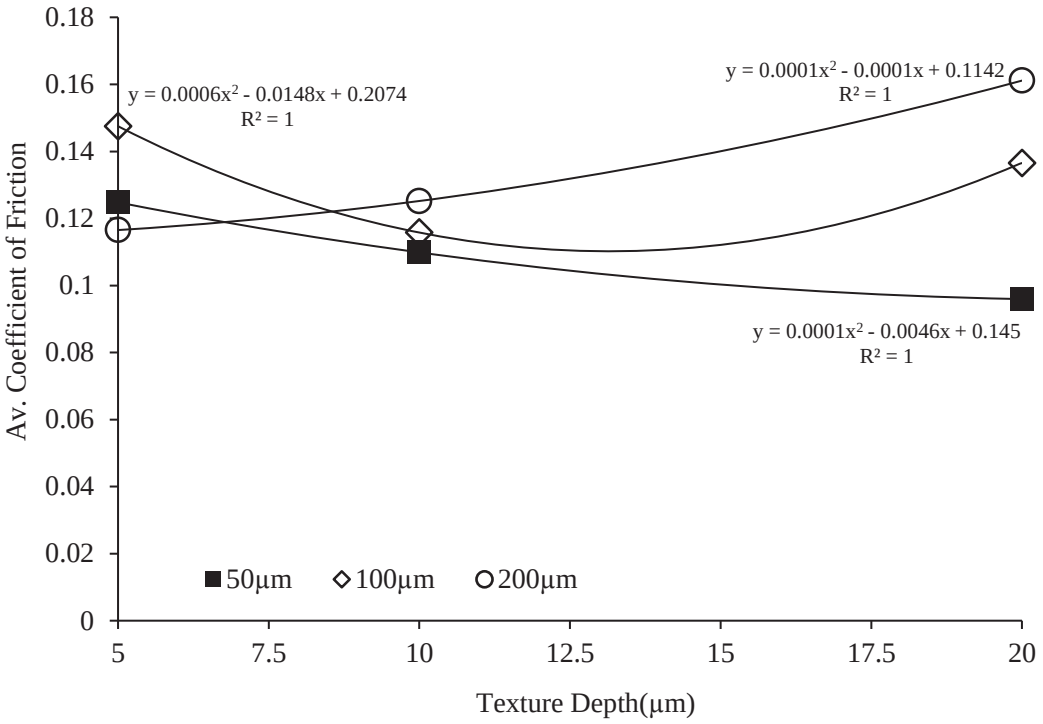

Figure 4-8: Polynomial curve fit of experimental data for texture diameters over various depths, with curve fit equations and R-squared value.

On finding the polynomial coefficients the values for the average coefficient of friction outside that experimentally acquired are predicted. Figure 4-9 and Figure 4-10 shows the overall effect that the diameter and depth has on the resultant average coefficient of friction.

Increasing the diameter increases the friction coefficient, however, attenuation in the average friction coefficient reduces past pore diameters above 120µm, after which the effect upon the COF tends to begin to level, as shown in Figure 4-9. Figure 4-10 shows the effect that the depth parameter has upon the resultant coefficient of friction. Initially the average COF shows a steady decline as the depth increases from 5µm to 10µm. In the depth range of between 10µm and 15µm the reduction in the coefficient of friction tends to be less substantial, exhibiting a variation of $7.59 \bullet 10^{-6}$, where the average COF reaches

a minimum at a depth of 12.5µm before rising. As the depth increases from 15µm to 20µm an increase in the average friction coefficient is observed.

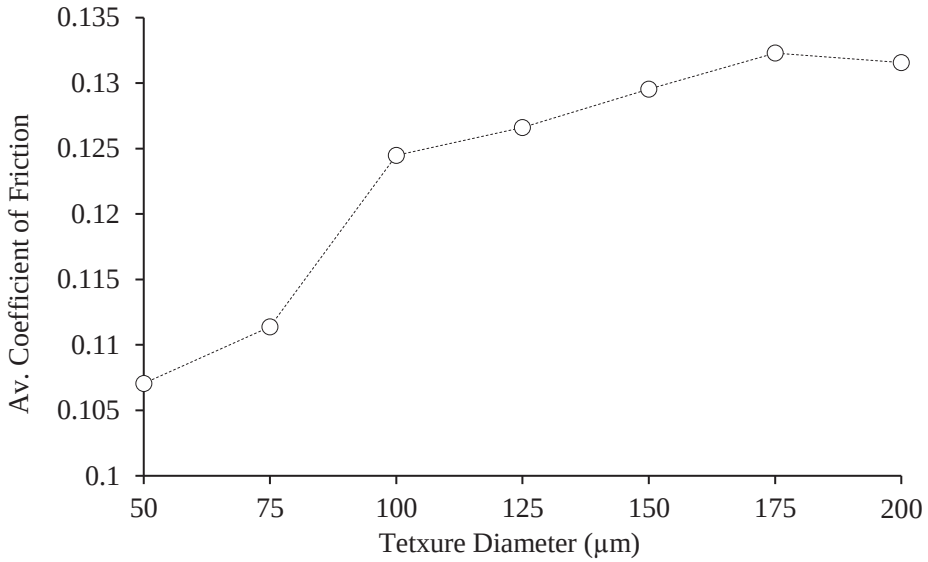

Figure 4-9: Overall effect of texture diameter on the average COF.

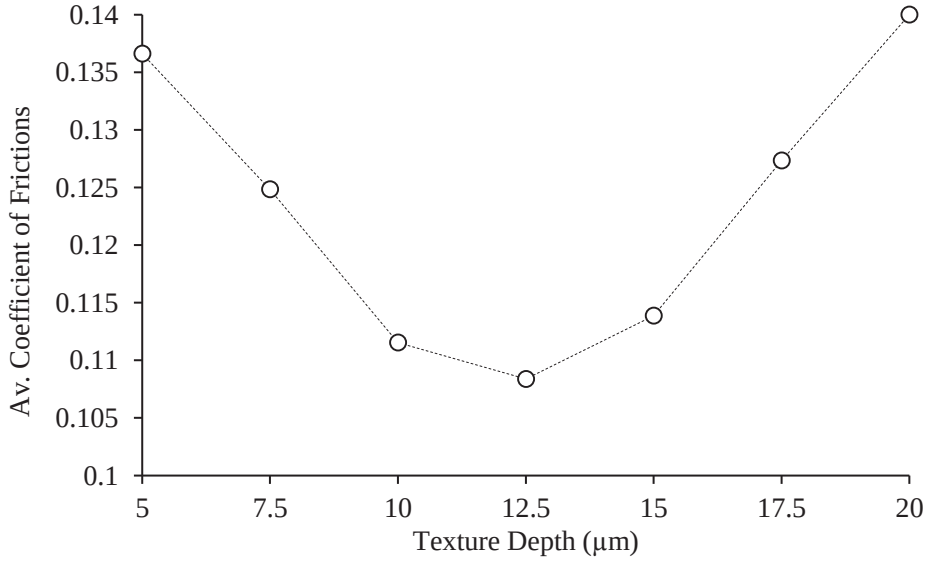

Figure 4-10: Overall effect of texture depth on the average COF.

Figure 4-11 shows the average coefficient of friction as a function of the aspect ratio (depth/diameter), observed is the higher the aspect ratio the greater the COF. As the aspect ratio reduces similar reductions occur in the coefficient of friction.

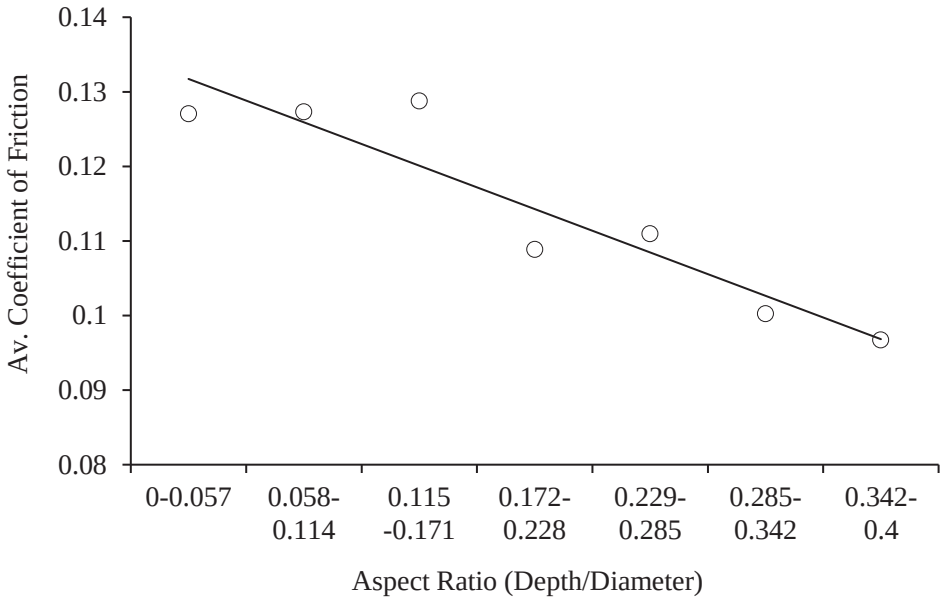

Figure 4-11: Overall effect of texture aspect ratio (depth/diameter) on the average COF. The trend line indicates an negative trend whereby the COF reduces with an increase in aspect ratio

Figure 4-12 is a 3-dimensional representation of the regression model with a contour plot directly beneath the surface. The plot identifies regions where the coefficient of friction is estimated to be at a minimum and how the COF varies corresponding to changes in texture depth and diameter. At smaller diameters up to 75μm the depth has negligible influence on the average coefficient of friction. However, as the diameter increases the depth parameter becomes more influential.

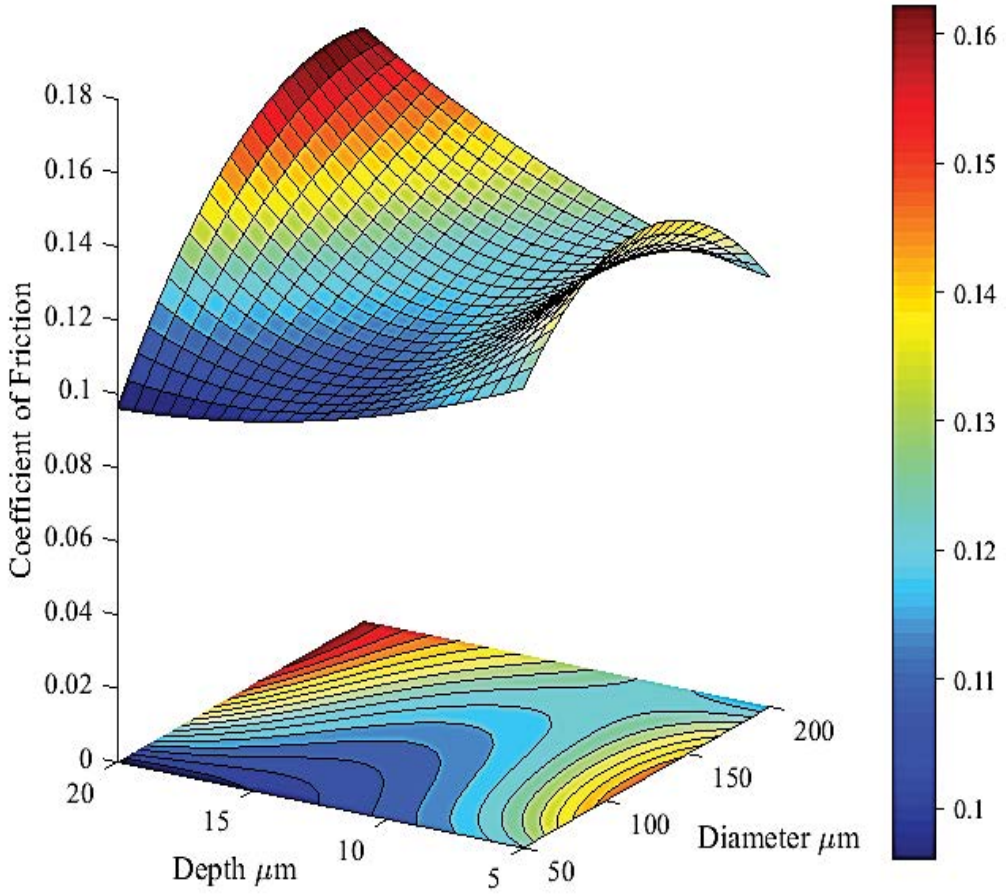

Figure 4-12: 3-Dimensional representation of the regression model, showing the effect of diameter and depth combinations has upon the average coefficient of friction.

4.3.4 Analysis of Variance

Analysis of the factor effects and regression model suggest that both the diameter and depth have a significant effect upon the resultant friction. Furthermore the analysis indicates a dependence upon a specific diameter and depth combination in order to achieve optimum friction reduction. In order to determine whether, firstly, the texture diameter and depth are both statistically significant parameters and secondly, an interaction exists between the two texture parameters, and within which, the influence they have upon the resultant coefficient of friction a two-way analysis of variance (ANOVA) with repetition test was undertaken.

The statistical technique assesses the difference in the means of a dependent variable across two independent variables. The two independent variables are diameter (Factor A) and depth (Factor B) and the dependent variable is the average coefficient of friction. For the analysis of variance to be implemented the following conditions are to be met:

1. The residual effects are normally distributed
2. Equal variance between different groups
3. The samples are independent

Table 4-4 shows the data sets used in the construction of the analysis. The analysis was used to determine the statistical significance of each independent variable; furthermore the interaction between texture diameter and depth is employed as a means of elucidating the dependence of COF output on specific texture combinations.

Table 4-4: Two-way ANOVA data set showing Factor notation

		Factor A (Diameter)		
		50µm	**100µm**	**200µm**
Factor B (Depth)	**5µm**	0.124 0.120 0.130	0.145 0.149 0.149	0.115 0.118 0.116
	10µm	0.109 0.116 0.104	0.108 0.128 0.112	0.130 0.126 0.120
	20µm	0.096 0.095 0.097	0.142 0.131 0.137	0.157 0.158 0.168

Prior to executing an analysis of variance the data was examined to ensure that the criterion for performing ANOVA is satisfied. The data used is the average coefficient of friction that is computed over the full test duration (1800 seconds) from all 27

independent runs and the results are organised into experimental run order. To examine the distribution of the empirical data, Figure 4-13 shows the frequency histogram. The number of bins is decided through applying Sturge's formula (Venables & Ripley, 1999) shown in Equation 4-3.

$$k = Log_2 n + 1 \qquad \textbf{Equation 4-3}$$

A Total of fifteen bins are prescribed between the maximum and minimum average coefficient of friction of 0.095 and 0.168 respectively. The frequency histogram in Figure 4-13 shows the distribution to be fairly symmetrical and produces an approximately bell-shaped normal distribution. Further analysis of the distribution; is shown in the normal probability plot, Figure 4-14. The coefficient of friction is plotted against the predicted values; z-scores which are given by the excel function NORM.INV that calculates the z-scores from the population mean, standard deviation and the cumulative probability (pi) that is based upon the average coefficient of friction data.

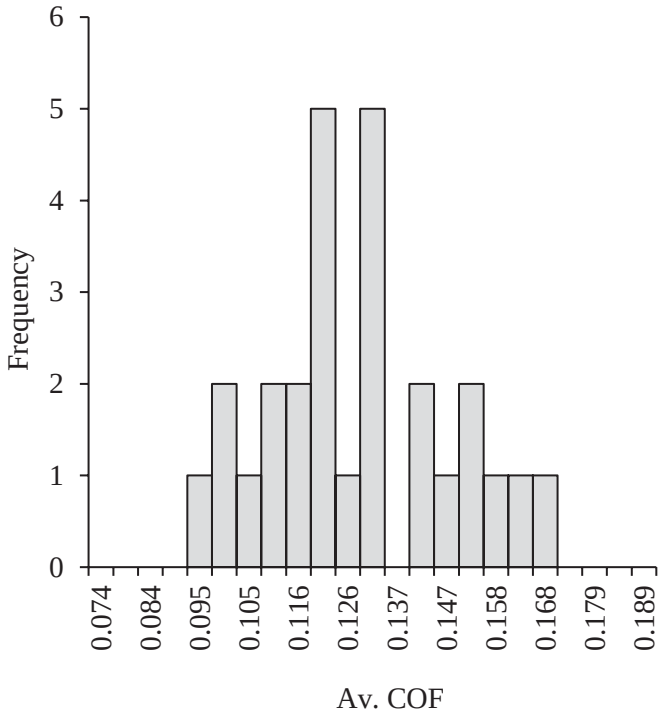

Figure 4-13: Frequency histogram of Av. COF showing an approximate bell-shaped curve

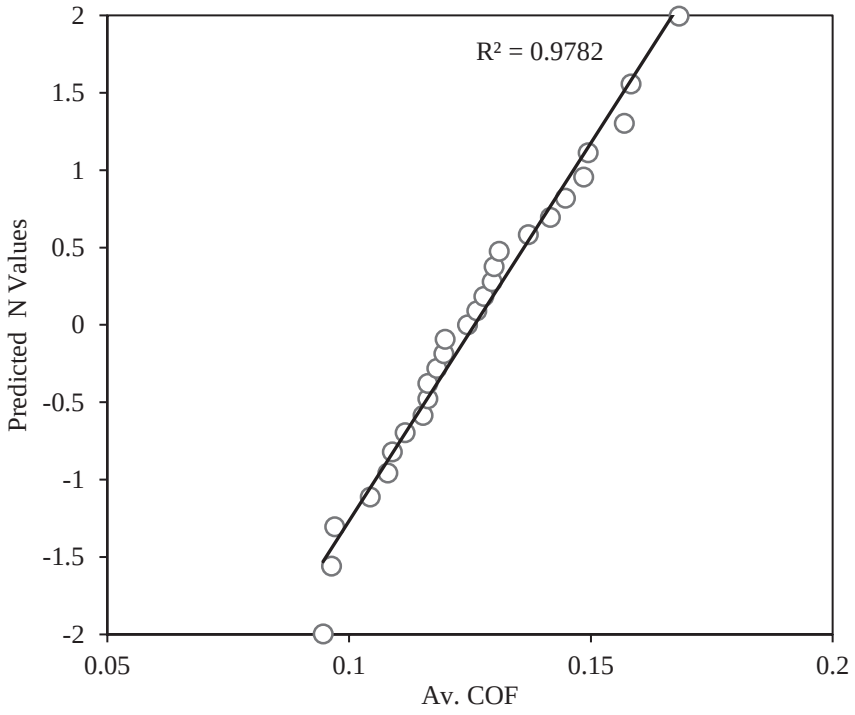

Figure 4-14: Normal probability plot of predicted values vs. Av. COF

The linearity of the fit when the predicted values are plotted against the average coefficient of friction provides further indication that the data presented is normally

distributed, hence adhering to condition one of the criteria for an analysis of variance test to be undertaken.

Assumption two states the requirement for the variance of the residuals to be equal. Figure 4-15 shows the residuals plotted against the experimental run order with the distribution curve plotted alongside.

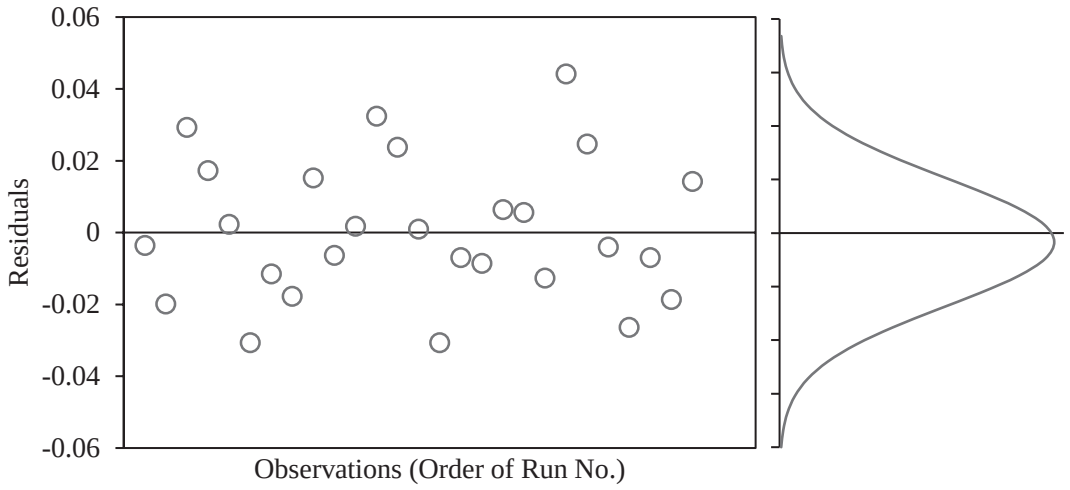

Figure 4-15: Residual vs. Run order plot and normal distribution curve

The residual plot (Figure 4-15) shows no apparent trend and the variance on either side of the mean is approximately constant, furthermore the data points lie on or are in close proximity to the mean line with no evident outliers. The residual variance is therefore judged to be equal, complying with assumption two of the ANOVA criterion. The distribution curve on the right hand side of the residual plot shows a minor skewness tending towards the negative half, however, the robustness of the ANOVA test allows for small deviations from the normal. The criteria for satisfying assumption three are settled through experimental design, where all average coefficient of friction samples are taken from independent tests.

The two-way analysis of variance test is performed using Microsoft Excel's data analysis add-on toolbox. The data input is as presented in Table 4-4, where a significance alpha (α) level 0.05 is employed as a criterion for accepting or rejecting the null hypothesis (Table 4-5) based on the resultant p-value. The ANOVA output is provided in Table 4-6 where SS is the sum-of-squares for between-group variability, df is the degrees of freedom and MS is the mean square. The F-value is a measure of if the means of differing samples are statistically different. The P-value is calculated from the F-value, the magnitude of the P-value indicates whether the null hypothesis is accepted or rejected based upon the chosen significance level, which in the case of the current experiment is $\alpha = 0.05$.

Table 4-5: Null hypothesis for Factor A (diameter) Factor B (depth) and Factor A,B interaction

The texture diameter has no significant effect on the COF	$H_O = \mu_A = \mu_B$
The texture depth has no significant effect on the COF	$H_O = \mu_A = \mu_B$
There is no interaction between diameter and depth and the COF is independent of texture parameter combination	

Table 4-6: ANOVA Results

Source of Variation	SS	df	MS	F	P-value	F crit
Depth	0.001101	2	0.00055	17.95805	5.15213E-05	3.554557
Diameter	0.003343	2	0.001672	54.52978	2.29819E-08	3.554557
Interaction	0.005054	4	0.001263	41.2161	7.90685E-09	2.927744
Within	0.000552	18	3.07E-05			
Total	0.010049	26				

Due to the p-values being less than the alpha significance criterion of 0.05 the null hypotheses are rejected and it is concluded that both texture diameter and depth are

statistically significant and that both factors affect the resultant coefficient of friction. Moreover, the analysis also highlights the indelible relationship between the two parameters where the magnitude in the effect of one factor is dependent upon the level of the other factor. This is portrayed in the interaction p-value that also falls significantly below the alpha value.

4.3.5 Tukey's Mean Separation

The analysis of variance test indicated a difference in the means for at least one of the test combinations. In order to validate that the mean values were all independent, and more pertinently that the coefficient of friction is dependent upon the diameter/depth combination, a mean value separation procedure in the form of a Tukey test was performed.

The procedure works by comparing the means empirically gathered to the computed critical mean difference (CMD). If the value falls above the CMD then there is a statistically significant difference. Tukey's critical mean difference is calculated according to Equation 4-4, where q is the studentized range statistic taken from the T-Table.

$$CMD = q\frac{MS_{error}}{\eta}$$ **Equation 4-4**

Where q is the studentized range statistic, MSerror is the mean sum of squares and η the number of test repetitions. Calculation of Equation 4-4, the CMD is computed to be 0.00915. Construction of the Tukey table is provided in Table 4-7 where the headers outline the means for each factor level in ascending order (column) and descending (row) order. The cell values are the differences in the means related to the corresponding depth and diameter.

Table 4-7:Tukey Test Table

Diameter	50µm	50µm	100µm	200µm	50µm	200µm	100µm	100µm	200µm
Depth	20µm	10µm	10µm	5µm	5µm	10µm	20µm	5µm	20µm
Av.COF	0.09598	0.10986	0.11578	0.11656	0.12476	0.12519	0.13655	0.14753	0.1611
0.161122	0.06514	0.05125	0.0453	0.04455	0.03635	0.03593	0.02456	0.01358	
0.147537	0.05155	0.03767	0.03175	0.03097	0.02277	0.02234	0.01098		
0.136556	0.04057	0.02669	0.02077	0.01999	0.01179	0.01136			
0.125193	0.02921	0.01532	0.00941	0.00862	0.00043				
0.124763	0.02878	0.01489	0.00898	0.0082					
0.116563	0.02058	0.00669	0.00078						
0.11578	0.01979	0.00591							
0.109864	0.01388								
0.095982									

Statistically significant differences in Average Coefficient of Friction

No statistically significant differences in Average Coefficient of Friction

Table 4-7 shows that 29 of the 36 texture combinations show a statistically significant difference in the average coefficient of friction, whereas the differences between the remaining 7 texture combinations are not significant. This is attributed to the difference in form of the effects. For instance, the average coefficient of friction for a 50µm diameter reduced when the depth was increased; however, the average coefficient of friction for textures with a 200µm diameter tended to rise when the depth was increased. The intermediate value of 100µm diameter identified a pivot point at 10µm depth; increasing or decreasing the depth from this point only served to cause an increase in the coefficient of friction.

The effect of depth across each of the tested diameters fluctuated. This is noted more pertinently in Figure 4-16a and Figure 4-16b. The plots depict a graphical interpretation of the ANOVA results. Observed is the cross over regions where the difference in the average coefficient of friction becomes statistically insignificant, at which point no texture combination offers a distinct advantage and that statistically all texture combinations will generate statistically similar results in terms of the coefficient of

friction. Moreover, the interaction between the two texture parameters is evidently seen as neither of the lines tends to lie parallel with one another.

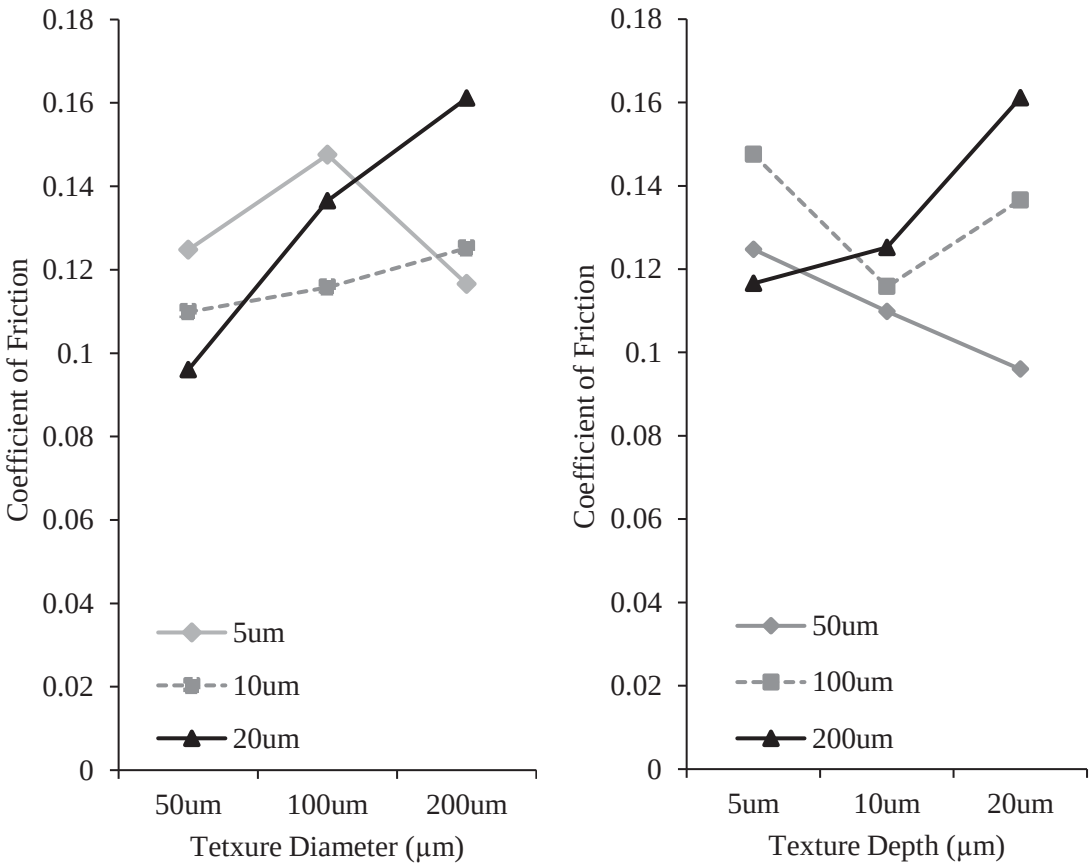

Figure 4-16: Graphical interpretation of ANOVA (a) COF vs. texture diameter, (b) COF vs. texture depth

The analysis of means demonstrates the relationship between the texture parameters, diameter and depth. It is shown that the average coefficient of friction is dependent upon the texture parameters employed and that each texture combination will provide its own unique output in terms of the average coefficient of friction. However, the independence of the output in relation to the texture parameters employed becomes obscured owing to the diverse effects of texture depth across various diameters.

4.4 Conclusion

The aim of the chapter was to analyse the frictional behaviour of various texture depth and diameter combinations and model the effects of each parameter to produce a holistic understanding of the influence of both texture parameters over a wider range. The individual effect of each parameter was isolated and statistically treated in order to define which, if either parameter was more influential than the other on the resultant coefficient of friction.

The optimum texture parameters to provide maximum friction reduction were found to be a diameter of 50μm and a depth of 20μm. The regression model constructed from the empirically derived average coefficient of friction values provided a holistic insight into the parameter effects. The effect of texture diameter increased the average coefficient of friction whereas the depth was found to have differing effects that was dependent upon the diameter employed. An analysis of variance highlights the statistical significance of both diameter and depth parameters whilst also demonstrating the dependence of the frictional output on the parameters combination employed. A Tukey test concluded that all but seven of the average coefficient of friction results were independent and unique. However the seven that failed were attributed to the diverse effect of texture depth for different diameters creating a cross-over region whereby a statistically similar coefficient of friction was obtained.

CHAPTER 5

Numerical Modelling of Hydrodynamic Pressure and Friction Force in Force in Relation to Texture Parameters

5.1 Introduction

One of the primary sources of friction reduction concerning the application of surface textures is that the cavities can serve as a micro hydrodynamic bearing in mixed and hydrodynamic regimes (Etsion, 2005). This is attributed to the converging surfaces as the fluid flows from the bottom of the texture to the surface. In order to substantiate the presence of hydrodynamic phenomena, in relation to the texture parameters experimental conditions of the work conducted in Chapter 4, the following chapter derives a theoretical model describing the hydrodynamic pressure within the fluid film developed under the experimental conditions.

The two-dimensional Reynolds equation was employed to model the hydrodynamic pressure in relation to the physical parameters outlined in Chapter 4. The model was non-dimensionalised and solved using a finite element method (FEM) and the friction force owing to fluid shear was then calculated. Statistical treatment of the results was under taken and compared to the findings from Chapter 4.

5.2 Texture Geometry

The geometric model of the surface textures are presented in Figure 5-1. The textures are represented as a spherical segment with a base radius *rp* and depth *hp* located within an imaginary small cell (Etsion, 2013). The area of the cell (*2rl)* is a function of the texture

density (*sp*) and diameter (*2rp*) according to Equation 5-1. It is assumed that the nominal surfaces are parallel and separated by a thin fluid film of thickness *c*.

$$r_l = \frac{r_p}{2}\left(\frac{\pi}{s_p}\right) \qquad \textbf{Equation 5-1}$$

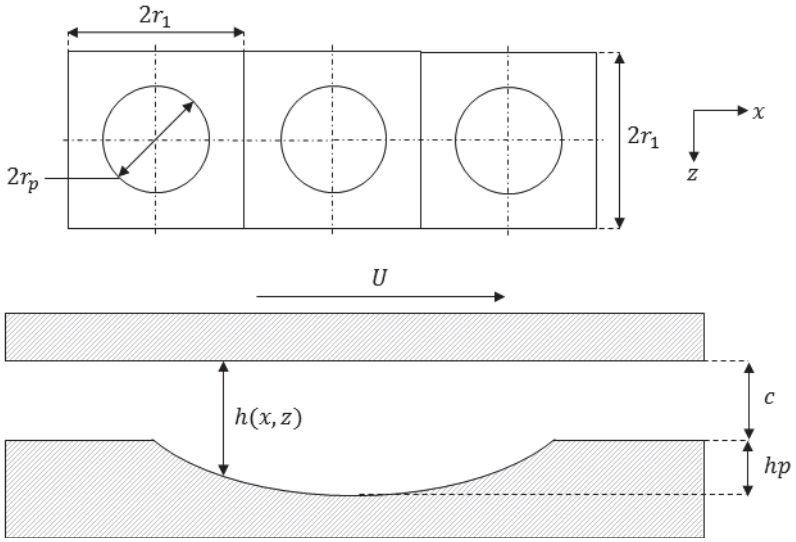

Figure 5-1: Surface geometry and notation. Plan view of 3 consecutive textures indicating texture cell length ($2r_1$), texture diameter ($2r_p$) and coordinate scheme. Bottom figure shows cross section across one textured cell separated by an initial gap, c. Where h(x,z) is the instantaneous film thickness and hp is the depth of the textured pore.

For the purpose of simplifying the analytical model further assumptions were made pertaining to the pressure distribution between the opposing surfaces. Firstly the pressure distribution in the longitudinal (x) direction was considered to be periodic in relation to consecutive strokes, therefore only one stroke across the three pores shown in Figure 5-1 was analysed. Secondly owing to the direction of motion only occurring along the x axis the lateral (z-direction) pressure distribution was assumed to repeat itself across adjacent textures. Therefore, as can be seen in Figure 5-1 only a single texture pore width was employed within the model.

5.3 Governing Equation

The Reynolds equation provided the governing equation that describes the pressure field generated within a thin film of lubricant separating two surfaces. The equation is derived by coupling the equation of momentum and the continuity equation under the following assumptions:

a) The fluid is Newtonian and incompressible.
b) The fluid viscosity is constant.
c) Inertia and body forces are negligible.
d) The pressure gradient across the film thickness is negligible.
e) The effect of surface curvature is neglected.
f) Fluid flow is assumed to be laminar.
g) No slip between fluid and surface boundary.

5.3.1 Force Balance

Figure 5-2 shows the development of flow velocity within a converging gap. The flow profiles are constructed of two components; pressure induced (Poiseuille) and shear (Couette) flow conditions. The outward profile of Poiseuille flow dictates the distortion of the velocity distribution at the trailing and leading edges. At inlet the distribution becomes retarded, curving inwards, however, at outlet pressure induced flow travels in the direction of motion providing a boost in the velocity. At maximum pressure the gradient is zero, at which point the flow condition consists of Couette shear flow only.

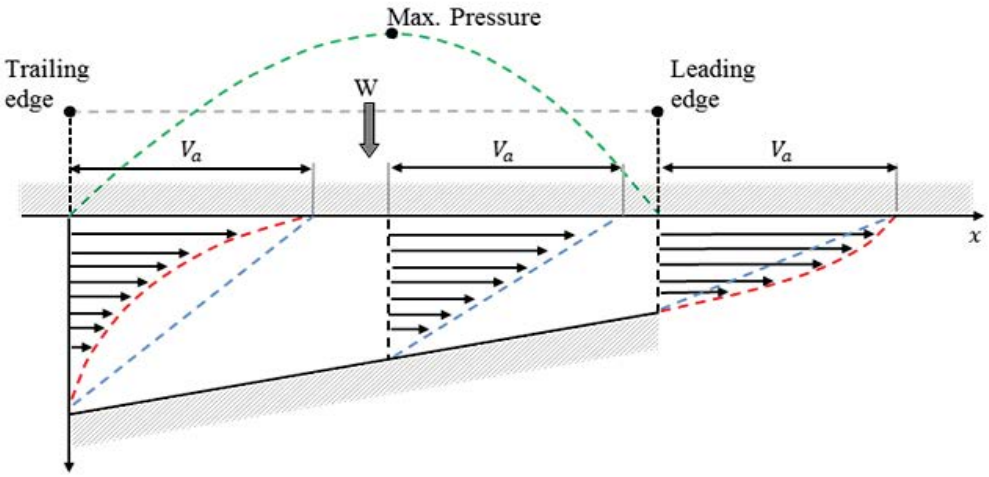

Figure 5-2: Velocity distribution curves of fluid flow between a plane surface moving at a velocity (v_a) relative and an inclined plate. Blue dash highlights Couette flow and Red dash provides the resultant velocity profile of Couette and Poiseuille flow. Green dash provides the fluid pressure profile between the surfaces (Schmid, et al., 2014)**.**

Figure 5-3 describes the shear forces acting on the fluid layers between a moving plate travelling at a velocity (v), and a fixed bottom plate. As the top plate translates the top layer of fluid moves with it, each fluid layer exerts a force on the layer beneath, thus creating a shearing force which reduces with the distance away from the moving plate. Figure 5-4 exhibits the shear and pressure forces acting on a fluid element. The pressure that drives the direction of flow is opposed by the pressure gradient created by the converging surfaces. The pressure gradient counterbalances the larger shear force acting on the left side of the fluid element in Figure 5-4.

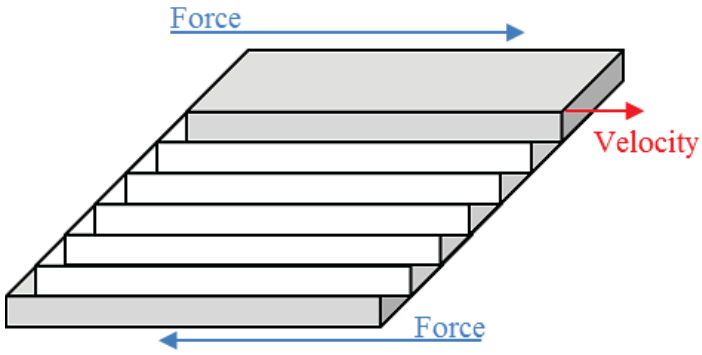

Figure 5-3: The direction shearing forces across a fluid film between a fixed lower surface and an upper plate moving at a velocity.

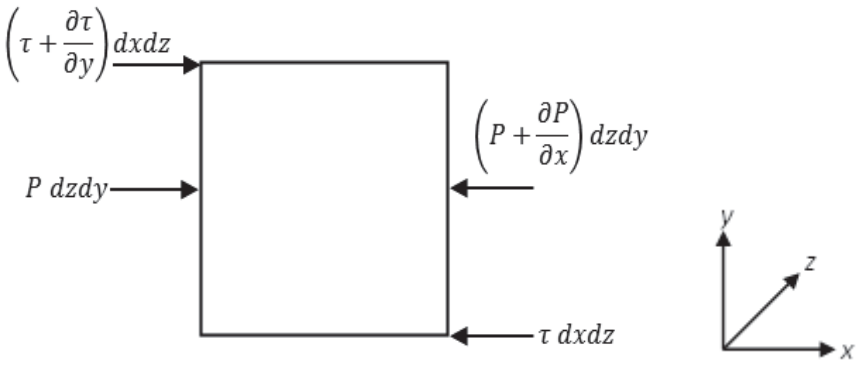

Figure 5-4: The Shearing and pressure forces acting upon a fluid element between two inclined surfaces. Where the left hand side (inlet) is the summation of shearing force and pressure owing to flow and the right hand side is the shearing force plus the pressure gradient owing to surface convergence.

The force balance taken from the fluid element notation in Figure 5-4 is represented by Equation 5-2.

$$pdy\ dz + \left(\tau + \frac{\partial \tau}{\partial x} dy\right) dx\ dz = \left(p + \frac{\partial p}{\partial x} dx\right) dy\ dz + \tau dx\ dz \qquad \textbf{Equation 5-2}$$

On cancelling out each side Equation 5-2 reduces to;

$$\left(\frac{\partial \tau}{\partial x} = \frac{\partial p}{\partial x}\right) \qquad \textbf{Equation 5-3}$$

The lubricant in this case is purified water (detailed in Chapter 4) which is both a Newtonian and incompressible fluid. This validates assumption (a) from section 5.3.

Furthermore, the low sliding velocity and diminutive cross sectional area to be analysed, owing to the thin fluid film, a low Reynolds number is assumed resulting in laminar flow between the surfaces, assumption (f)). In this case the shear stress for a Newtonian fluid in laminar flow is:

$$\tau = \mu \frac{\partial u}{\partial y}$$ **Equation 5-4**

Assumption (b) prescribes a constant temperature throughout the fluid film. The primary source of temperature increase for the given system derives from frictional heating, generated by contact between the opposing surfaces on some level. However, given that the surfaces are assumed to be separated by a thin fluid film any heat increases due to friction are negligible and a constant temperature can be assumed. The viscosity of water, like other fluids are effected by variations in pressure. Increases in pressure in the range of 0 – 30MPa operating at a temperature of above 55°C exhibits a proliferation in the relative viscosity of water (Wonham, 1967). The system to be modelled exhibits relatively low contact pressures, based upon the experimental study in Chapter 4 (3.54MPa), relative to the range provided. Furthermore the viscosity-pressure relationship presented by Wonham for temperatures between 20°C and 50°C show that negligible changes in viscosity occur at pressures below that of 10MPa. Given the constant temperature and negligible effect of pressure the viscosity is assumed to be constant. Assuming a constant viscosity (assumption b) and negligible pressure variation across the film thickness (assumption d) the expressions for pressure in the x and z directions described in Figure

5-4 are represented as a function of fluid viscosity and velocity by Equation 5-5 and Equation 5-6 respectively.

$$\frac{\partial}{\partial y}\left(\mu\frac{\partial^2 u}{\partial y^2}\right)=\frac{\partial p}{\partial x}$$ **Equation 5-5**

$$\frac{\partial}{\partial y}\left(\mu\frac{\partial^2 w}{\partial y^2}\right)=\frac{\partial p}{\partial z}$$ **Equation 5-6**

5.3.2 Flow Velocity

Figure 5-5 provides the velocity notation and coordinates relating to the upper surface and a singular textured pore separated by a fluid with a film thickness, $h_{x,z}$.

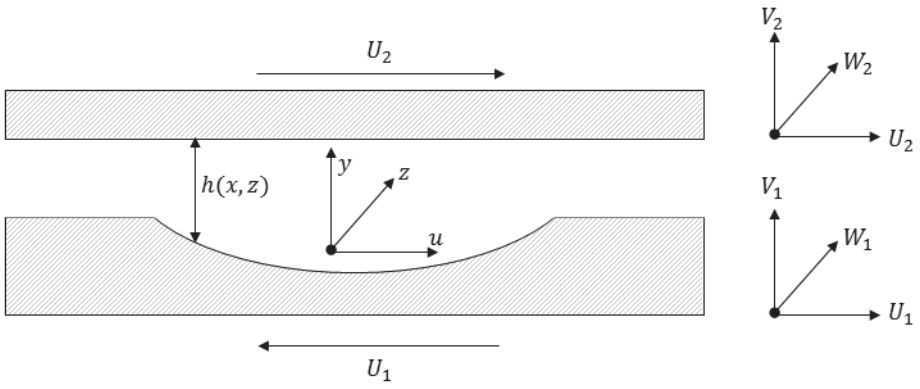

Figure 5-5: The instantaneous film thickness (*h x,z*) and velocity notation corresponding to coordinate scheme for an upper surface and textured a textured singular pore on the lower surface travelling in relative motion.

Integrating Equation 5-5 and Equation 56 twice provides the flow velocity in the *x* and *z* directions, given in Equation 5-7 and Equation 5-8 respectively.

$$\mu u=\frac{\partial p}{\partial x}\frac{y^2}{2}+C_1 y+C_2$$ **Equation 5-7**

$$\mu w = \frac{\partial p}{\partial z}\frac{y^2}{2} + C_1 y + C_2$$ **Equation 5-8**

Assuming no slip at the boundaries (assumption g) provides the following boundary conditions**:**

$$u = U_1, at\ y = 0$$ **Equation 5-9**

$$u = U_2, at\ y = h$$

Relating to the experimental layout in Chapter 4 the lower surface was fixed to the base of the lubricant bath hence, from the notation in Figure 5-5 $U_1 = W_1 = 0$. Applying the boundary conditions the flow velocity in the x and z directions respectively are:

$$u = \left(\frac{y^2 - yh}{2\mu}\right)\frac{\partial p}{\partial x} + (U_2)\frac{y}{h}$$ **Equation 5-10**

$$w = \left(\frac{y^2 - yh}{2\mu}\right)\frac{\partial p}{\partial z} + (W_2)\frac{y}{h}$$ **Equation 5-11**

Equation 5-10 and Equation 5-11 describe the flow velocity as a summation of the Couette and Poiseuille flow. The former is the flow velocity attributed to the movement of the surfaces, represented by the left hand side of Equation 5-10 and Equation 5-11. The latter flow condition is the pressure induced flow velocity. The combination of both flows is visualised by the velocity distribution curves (Figure 5-2).

5.3.3 Continuity Equation

The principle concept that the continuity equation acknowledges is that of mass conservation, where the net flow at outlet must be equal to the reduction in mass within a volume of fluid. The continuity equation is as follows;

$$\frac{\partial \rho}{\partial t} + \frac{\partial}{\partial x}(\rho u) + \frac{\partial}{\partial y}(\rho v) + \frac{\partial}{\partial z}(\rho w) = 0$$ **Equation 5-12**

Where density is assumed to be constant, the continuity equation reduces to;

$$\frac{\partial u}{\partial x} + \frac{\partial v}{\partial y} + \frac{\partial w}{\partial z} = 0$$ **Equation 5-13**

Expressing the continuity equation in integrated form between the limits of *y = 0, to y = h* gives;

$$\int_0^h \frac{\partial u}{\partial x} dy + |v|_0^h + \int_0^h \frac{\partial w}{\partial z} dy = 0$$ **Equation 5-14**

Applying Equation 5-10 and Equation 5-11 to the first and third terms in Equation 5-14 and integrating yields;

$$\int_0^h \frac{\partial}{\partial x} u dy = -\frac{\partial p}{\partial x}\frac{h^3}{12\mu} + \frac{1}{2}U_2 h$$ **Equation 5-15**

$$\int_0^h \frac{\partial}{\partial z} w dy = -\frac{\partial p}{\partial z}\frac{h^3}{12\mu} + \frac{1}{2}W_2 h$$ **Equation 5-16**

5.4 The Reynolds Equation

The Reynolds equation is obtained by substituting Equation 5-15 and Equation 5-16 into the continuity equation. The direction of relative motion was along the x axis, hence $W_2 = 0$, yields;

$$\frac{\partial}{\partial x}\left\{h^3\frac{\partial p}{\partial x}\right\}+\frac{\partial}{\partial z}\left\{h^3\frac{\partial p}{\partial z}\right\}=6\mu\frac{\partial h}{\partial x}U_2+12\mu(V_2-V_1) \qquad \textbf{Equation 5-17}$$

Equation 5-17 is the general form of the Reynolds equation for hydrodynamic pressure between converging surfaces for an incompressible thin film fluid undergoing squeeze film action. The terms on the LHS of Equation 5-17 are the pressure terms and on the RHS are the source terms. The first expression on the RHS is referred to as the wedge action caused by the convergence of two opposing surfaces. The second expression on the RHS is the squeeze film term. Where the bottom surface was fixed, hence, $V_1 = 0$, it was assumed that during a reciprocating stroke the upper surface undergoes a sinusoidal motion. The velocity increases through the stroke, where the film thickness ($h_{x,z}$) increases until a maximum velocity is obtained, $h_{x,z}$ then reduces to a minimum, at which point a squeezing action of the fluid from the contact zone occurs at the extremities of the stroke length. Therefore the squeeze motion changes by h with respect to t, time; Equation 5-17 is presented as:

$$\left\{h^3\frac{\partial^2 p}{\partial x^2}\right\}+\left\{h^3\frac{\partial^2 p}{\partial z^2}\right\}=6\mu U\frac{\partial h}{\partial x}+12\mu\frac{\partial h}{\partial t} \qquad \textbf{Equation 5-18}$$

5.5 System Parameters

5.5.1 Sliding Velocity

The motion of the upper surface was driven by a scotch yoke mechanism that provided simple harmonic motion. The mechanism is schematically depicted in Figure 5-6 and shows the conversion of constant rotation to reciprocating motion.

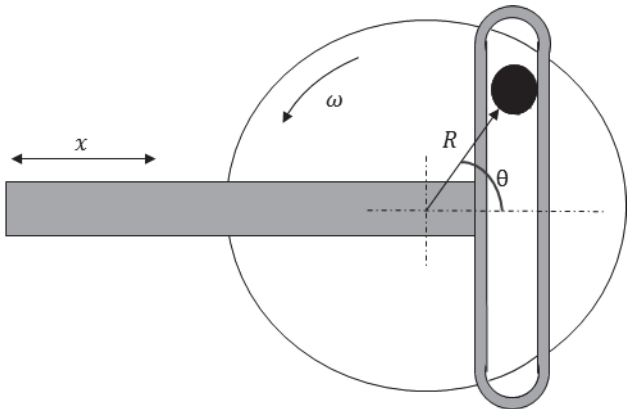

Figure 5-6: Scotch yoke mechanism schematic illustrating the conversion of rotational motion to linear reciprocating movement at a length of displacement *x* in relation to the angle *θ* and radius *R*.

The velocity, U, is the rate of change in the displacement with respect to time as expressed by Equation 5-19.

$$U = \frac{dx}{dt} = \omega R cos(\omega t) \qquad \text{Equation 5-19}$$

Applying the experimental parameters from Chapter 4; *R* was taken as half the stroke length, *ω (rad/s)* was calculated from 60 RPM in order to provide a 1Hz reciprocating frequency and *t* is the length of time to be analysed. Figure 5-7 plots the resultant velocity as a function of θ.

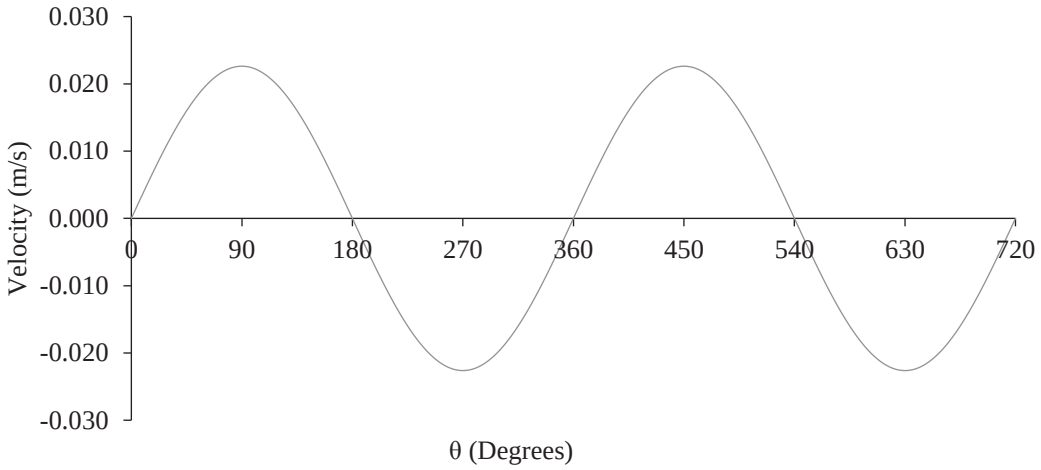

Figure 5-7: Velocity profile produced by a scotch yoke mechanism with a radius R equivalent to the experimental stroke length, rotating at 60RPM over a time scale of 2 seconds. The example illustrates 2 complete rotations (720°) corresponding to 4 strokes contained within 2 reciprocating cycles.

5.5.2 Squeeze Film

As previously described, the sinusoidal motion of the upper surface increases the fluid film thickness as the velocity increases to a point at mid stroke providing maximum film thickness. The film thickness reduces with a decrease in velocity corresponding to the velocity profile in Figure 5-7. As the moving surface reduces to zero velocity the gap separating the surfaces reduces, causing a squeeze action of the lubricating fluid. The film thickness *(ct)* owing to a sinusoidal squeeze is given in Equation 5-20, where h_o is the minimum film thickness, c is the amplitude of the sinusoidal change of the film thickness and f is the frequency (Hori, 2006).

$$ct = h_0 + c(cos2\pi ft - 1) \qquad \textbf{Equation 5-20}$$

It was assumed that the initial film thickness (h_o) at either end of the stroke length is zero owing to the velocity also being zero. The amplitude of film thickness *(c)* was taken as the height of the gap between the two plane surfaces as identified in Figure 5-1. The

frequency *(f)* was the reciprocating frequency from the empirical study in Chapter 4, 1Hz, and *t* is the time relating to *1/f*.

5.5.3 Cavitation

The phenomenon of cavitation is the formation of air pockets within a flowing liquid owing to a reduction in pressure. The reduction in pressure in the context of the present study occurs where the fluid enters the textured pore, at which point the surfaces diverge from one another, increasing the surface area. In order to account for cavitation at the entry point of textures within the model sufficient boundary conditions were applied in the form of the Reynolds boundary condition (also known as the Swift-Steiber condition) which infers that the pressure reduces to zero at the boundary of the cavitation zone (Ronen, et al., 2001) (Tomanik, 2013). Figure 5-8 identifies the position of the cavitation boundary with respect to the direction normal to the velocity.

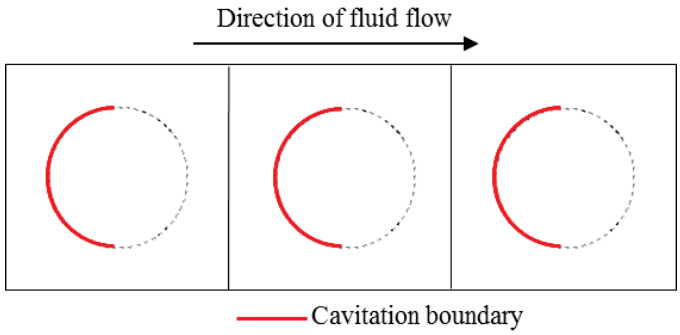

Figure 5-8: The Cavitation boundary of 50% of textured pore circumference for 3 consecutive textures. The cavitation boundary is positioned in relation to the direction of fluid flow along the x-axis.

5.5.4 Non-Dimensional Reynolds Equation

In order to solve the Reynolds equation analytically Equation 5-18 was reduced to a dimensionless form; where Cartesian coordinates (X,Z), the local film thickness (H), pressure (P), time (T) and velocity (U) are defined as;

$$X = \frac{x}{r_p}; Z = \frac{z}{r_p};\ H = \frac{h}{hp};\ P = \frac{p}{P_a}; T = \frac{t}{T_o}; U = \frac{u}{r_c \omega};$$ **Equation 5-21**

Substituting the dimensionless parameters into Equation 5-18 and rearranging provides the Reynolds equation in non-dimensional form.

$$\left(H^3 \frac{\partial^2 P}{\partial X^2}\right) + \left(H^3 \frac{\partial^2 P}{\partial Z^2}\right) = \psi U \frac{\partial H}{\partial X} + \xi \frac{\partial H}{\partial T}$$ **Equation 5-22**

Where,

$$\psi = \frac{6\mu r_c \omega {r_p}^3}{h_p P_a};\ \xi = \frac{12\mu}{T_o P_a}$$ **Equation 5-23**

5.5.5 Local film thickness

The local film thickness of the parallel surfaces is expressed as;

$$h = \begin{cases} ct + h_{px}\,(x,z) & when\ X^2 + Z^2 < r_P \\ ct & X^2 + Z^2 \geq r_P \end{cases}$$ **Equation 5-24**

A singular textured pore was modelled as a spherical cap as suggested by Ronen and Etsion (Ronen, et al., 2001) (Figure 5-9) with a depth, h_p, and diameter $2r_p$ and is expressed in Equation 5-25 where $h_{p(x,z)}$ is the texture depth relative to *x*.

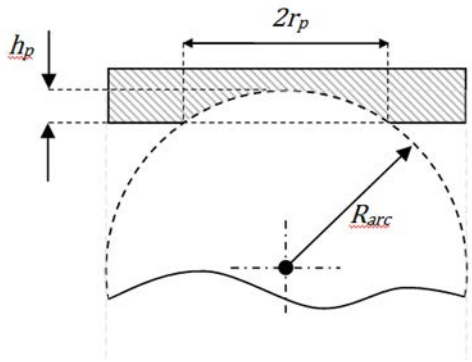

Figure 5-9: Textured pore modelled as a spherical cap with a length equivalent to the texture diameter $2r_p$, and sagitta represented by the depth h_p

$$h_{px}(x,z) = ct + \sqrt{\left(\frac{h_p^2 + r_p^2}{2h_p}\right)^2 - (x^2 + z^2)} - \frac{r_p^2 - h_p^2}{2h_p} \qquad \textbf{Equation 5-25}$$

On substituting non-dimensional parameters the dimensionless film thickness (H) is;

$$H(X,Z) = \begin{cases} \dfrac{ct + \sqrt{\left(\frac{h_p^2 + r_p^2}{2h_p}\right)^2 - (x^2 + z^2)} - \frac{r_p^2 - h_p^2}{2h_p}}{hp} & X^2 + Z^2 < 1 \\ ct & X^2 + Z^2 \geq 1 \end{cases}$$

Equation 5-26

5.6 Finite Difference Method

The Reynolds equation is a partial differential equation and in order to solve it numerically a finite difference approach was utilised, where, the derivatives were replaced by a combination of approximated linear algebraic equations and solved sequentially. The technique; finite difference, refers to the approximated value of a function between some given value of x_0 and increment $(x_0 + \Delta x)$ in a discretized domain, as diagrammatised in Figure 5-10.

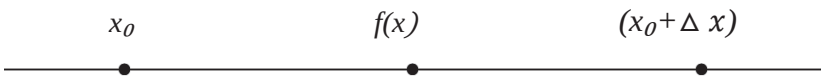

Figure 5-10: Finite difference method, approximating the value of f(x) in relation to a given value x_0.

This can be expressed by the definition of a derivative given in Equation 5-27.

$$\frac{\partial f}{\partial x} = \lim_{h \to 0} \left(\frac{(f(x_o + \Delta x) - f(x_o))}{\Delta x} \right) \qquad \textbf{Equation 5-27}$$

The derivative $\partial f/dx$ is a particular point in space or time within the partitioned domain. Such approximations carry a certain element of error between the exact solution and that derived numerically. The 'truncation error' is attributed to replacing the differential operator to a difference one.

The approximation of partial derivatives was undertaken by using the Taylor Series given in Equation 5-28 and Equation 5-29.

$$f(x + \Delta x) = f(x) + \Delta x \frac{\partial f}{\partial x} + \frac{1}{2}(\Delta x)^2 \frac{\partial f^2}{\partial x^2} + \ldots\ldots \qquad \textbf{Equation 5-28}$$

$$f(x - \Delta x) = f(x) - \Delta x \frac{\partial f}{\partial x} + \frac{1}{2}(\Delta x)^2 \frac{\partial f^2}{\partial x^2} + \ldots\ldots \qquad \textbf{Equation 5-29}$$

From Equation 5-28 and Equation 5-29 the forward and backward approximations are defined and subtracted from one another. The result is a first order central difference approximation in the form of;

$$\frac{\partial f}{\partial x} = \frac{f(x + \Delta x) - f(x - \Delta x)}{2 \Delta x} \qquad \textbf{Equation 5-30}$$

The second order central difference approximation is defined by adding the forward and backward Taylor expressions, yielding;

$$\frac{\partial^2 f}{\partial x^2} = \frac{f(x - \Delta x) - 2f(x) + f(x + \Delta x)}{x^2}$$ **Equation 5-31**

The Taylor Series was applied to the Reynolds equation by discretizing the surface into a series of nodes with the following notation as seen in Figure 5-11. Where *P* is the pressure and *i,j* is the coordinate notation relating to x and z respectively. As the pressure is a function of the film thickness, the value of *h* was expressed at every half node to predict the pressure generated at $P_{i,j.}$

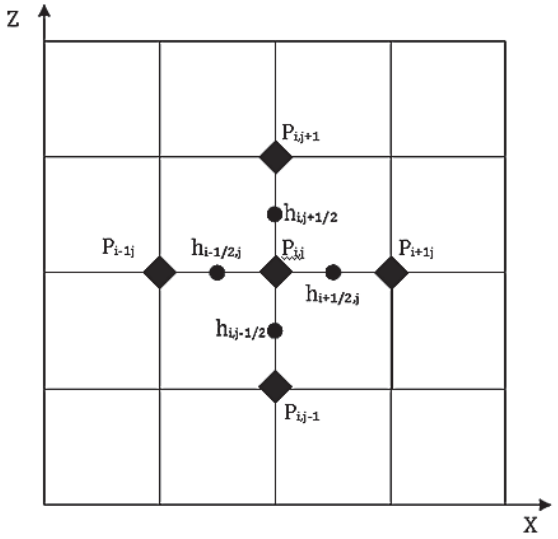

Figure 5-11: Discretization of the surface into a uniform arrangement of pressure nodes. Where *i,j* subscripts denote the *x* and *z* coordinates and *h* is the film thickness at a half step between pressure nodes.

Using the notation within Figure 5-11 and substituting into Equation 5-30 and Equation 5-31 provides an approximation for the first and second order derivatives, respectively.

$$\frac{\partial P_{i,j}}{\partial x} = \frac{P_{i+1,j} - P_{i-,j}}{2 \Delta X}$$ **Equation 5-32**

$$\frac{\partial}{\partial X}\left(\frac{\partial P_{i,j}}{\partial X}\right) = \frac{P_{i+1,j} - 2P_{i,j} + P_{i-1,j}}{\Delta X^2}$$ **Equation 5-33**

Applying the three derivatives of the Reynolds equation to the discretized domain shown in Figure 5-11; expressing these terms as applied to the Taylor series gives;

$$\left(H^3 \frac{\partial^2 P}{\partial X^2}\right) = \frac{H^3_{i+0.5,j} \cdot P_{i+1,j} - H^3_{i+0.5,j} \cdot P_{i,j} + H^3_{i-0.5,j} \cdot P_{i,j} + H^3_{i-0.5,j} \cdot P_{i-1,j}}{(X)^2}$$ **Equation 5-34**

$$\left(H^3 \frac{\partial^2 P}{\partial Z^2}\right) = \frac{H^3_{i+0.5,j} \cdot P_{i+1,j} - H^3_{i+0.5,j} \cdot P_{i,j} + H^3_{i-0.5,j} \cdot P_{i,j} + H^3_{i-0.5,j} \cdot P_{i-1,j}}{(Z)^2}$$ **Equation 5-35**

$$\left(\frac{\partial H}{\partial X}\right) = \frac{H_{i+1,j} - H_{i-1,j}}{2 \Delta X}$$ **Equation 5-36**

$$\left(\frac{\partial H}{\partial T}\right) = \frac{H_{i+1,j} - H_{i-1,j}}{2 \Delta T}$$ **Equation 5-37**

Substituting Taylor series into the Reynolds equation and rearranging for $P_{i,j}$ yields;

$$P_{i,j} = \frac{H^3_{i+0.5}}{H^3_{i+0.5} + H^3_{i-0.5} + 2H^3} \cdot P_{i+1,j} + \frac{H^3_{i-0.5}}{H^3_{i+0.5} + H^3_{i-0.5} + 2H^3} \cdot P_{i-1,j} + \frac{H^3}{H^3_{i+0.5} + H^3_{i-0.5} + 2H^3} \cdot P_{i+1,j} + \frac{H^3}{H^3_{i+0.5} + H^3_{i-0.5} + 2H^3} \cdot P_{i-1,j} - \frac{\psi U \Delta X \Delta Z^2}{2} + \frac{2 \Delta T}{\xi} \cdot \frac{(-H_{i-1} + H_{i+1})}{H^3_{i+0.5} + H^3_{i-0.5} + 2H^3}$$ **Equation 5-38**

The procedure for evaluating the pressure at each node is an iterative process, whereby the results of each iteration converge to a solution. In order to achieve this, Jacobi's iterative procedure is employed. The strategy of the Jacobi method is to find a new value

of $P_{i,j}$ based upon the previously iterated value of pressure. The iterative process is repeated until the convergence criteria is met, represented as;

$$Convergence\ Criteria = \frac{P(k) - P(k-1)}{P(k-1)} =< 0.0001 \qquad \textbf{Equation 5-39}$$

5.7 Force Balance

Figure 5-12 shows the forces acting upon the system, identified are the applied load opposed by the generated hydrodynamic pressure. For the system to be in equilibrium the normal load applied (F_L) must be equivalent to the force produced from hydrodynamic pressure (F_P).

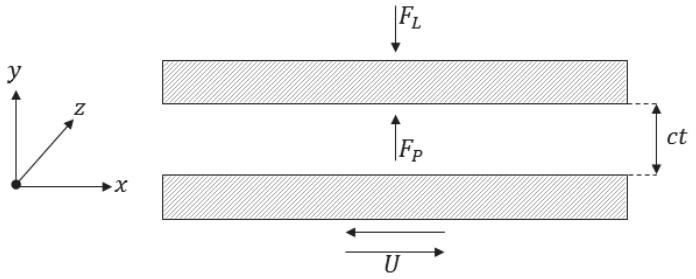

Figure 5-1: Force balance diagram between two opposing surfaces separated by a film of fluid. The diagram identifies an arbitrary applied load (F_L) balanced in equilibrium by an opposing force from the generation of hydrodynamic pressure (F_P).

The magnitude of pressure produced is a function of the initial film thickness (*ct*), where, as the gap between the two surfaces reduces the pressure increases. Therefore, the force balance is carried out by varying *ct* until the hydrodynamic pressure generated is equal to the applied load. The non-dimensional force F_p is calculated by integrating the resultant hydrodynamic pressure over the area and dividing by the atmospheric pressure, and is expressed by;

$$\overline{F_p} = \iint pdxdz\,/p_a$$ **Equation 5-40**

5.7.1 Load Scaling

The surface area of a textured cell is a function of the diameter and density of the pore. The purpose of the theoretical study was to compare the resultant friction force to that observed within the empirical tests in Chapter 4, for this reason the texture density is held constant at 20%. The diameter however was varied between 50µm and 200µm, and the depth between 5µm and 20µm. The variation in diameter subsequently produced textured cells of differing surface areas, where under a constant applied load across all texture diameters would produce a disparity in the resultant contact pressure. In order to maintain a constant contact pressure across all texture parameters employed within the theoretical study an arbitrary load was scaled relative to the area of the three textured cells as follows.

The surface area of all textures are scaled relative to the surface area of the upper sample employed in Chapter 4, this provides a constant independent value for all textured areas within the theoretical study to be scaled against. The percentage of theoretical area relative to experimental area acts as a scaling factor.

$$Scale\ Factor = \left(\frac{Theoretical\ Area}{Experimental\ Area}\right) \cdot 100$$ **Equation 5-41**

The next step was to calculate the applied load (F_L) in relation the scaling factor

$$Applied\ Load = \left(\frac{Scale\ Factor}{100}\right) \cdot Constant\ Arbitrary\ Load$$ **Equation 5-42**

The non-dimensional force (F_L) was calculated by;

$$F_L = Applied\ Load/p_a$$ **Equation 5-43**

5.8 Friction Force

The friction force owing to the shearing of fluid between the opposing surfaces was obtained by integrating the shear stress (τ) over the area of the three consecutive textured cells;

$$F = \int_0^L \int_0^B \tau dx dz$$ **Equation 5-44**

The shear stress in relation to viscosity and shear rate is defined in Equation 5-4. Applying this relationship and combining with the expression derived for the velocity, *u*, by differentiating Equation 5-10 with respect to *y* provides the shear stress (τ).

$$\tau = \left(\frac{\mu U}{h}\right) + \frac{\partial p}{\partial x}\frac{h}{2}$$ **Equation 5-45**

Substituting the expression for shear stress into Equation 5-45 yields;

$$Ff = \int_0^L \int_0^B \left(\frac{\mu U}{h}\right) + \frac{\partial p}{\partial x}\frac{h}{2}$$ **Equation 5-46**

The friction force expressed in non-dimensional form is;

$$\overline{Ff} = \int_0^L \int_0^B \left(\frac{\mu U}{h}\right) + \frac{\partial p}{\partial x}\frac{h}{2} \Big/ p_a$$ **Equation 5-47**

5.9 Computational Procedure

The numerical procedures described in the preceding sections are demonstrated schematically within Figure 5-13.

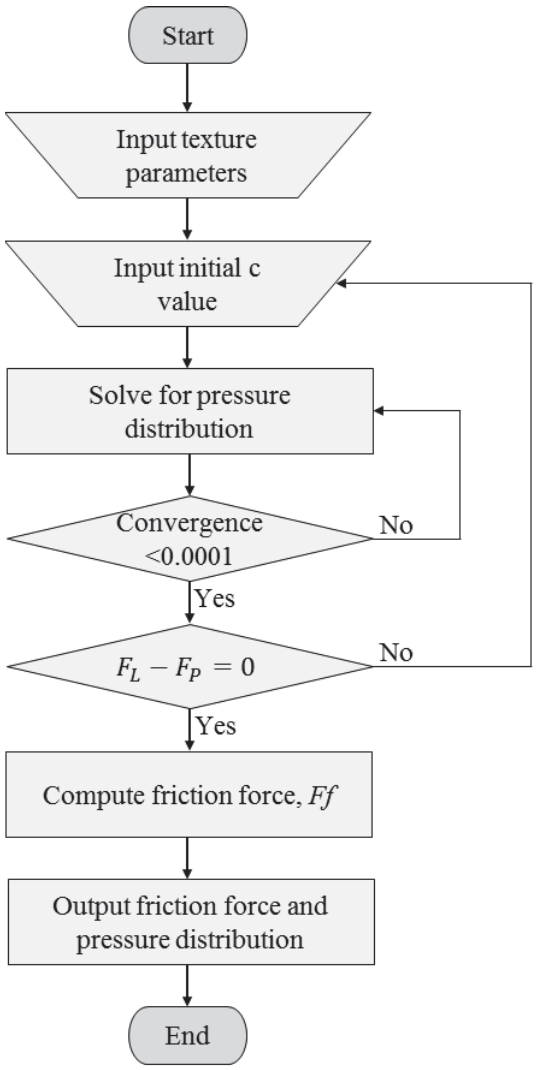

Figure 5-13: Flowchart identifying the computation procedure to determine the force between applied load and hydrodynamic pressure through to the calculation of friction in relation to the specified surface texture parameters.

5.10 Results

5.10.1 Non-Dimensional Pressure Distribution

The pressure distribution developed within the lubricant during one reciprocating stroke across three consecutive textures with dimensions of 50µm diameter and 10µm depth is displayed in Figure 5-14. The pressure variation across the stroke corresponded with the variation in velocity, which in turn affected the initial gap between the two surfaces. As the velocity increased near centre of the stroke the pressure generated reduced owing to the increase in the film thickness between the parallel surfaces.

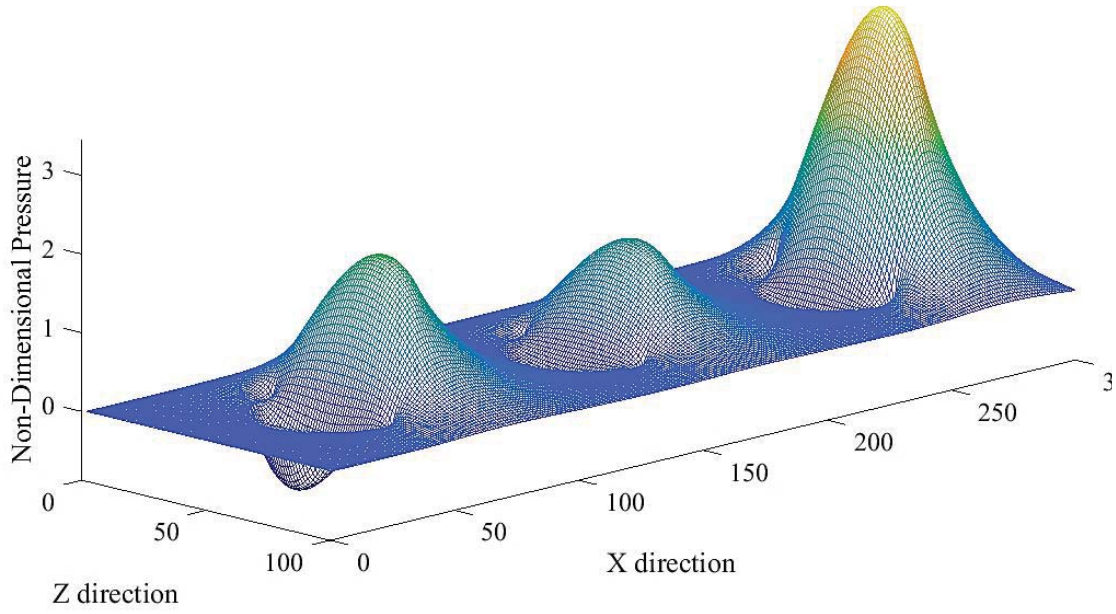

Figure 5-14:Non-dimensional pressure distribution within one reciprocating stroke across three consecutive textures with a diameter of 50µm and depth 10µm.

The influence of velocity is observed in Figure 5-15 showing the pressure profile along the x-axis plotted alongside the velocity relative to the textured pores. The pressure increases to a maximum towards the exit of each textured pore owing to the convergence of the opposing surfaces. As the velocity reduces after the centre of the stroke the pressure

produced by traversing and then exiting the third pore generates a pressure spike. This is attributed to the squeeze film action where fluid is entrapped and becomes pressurised by the convergence of the surfaces.

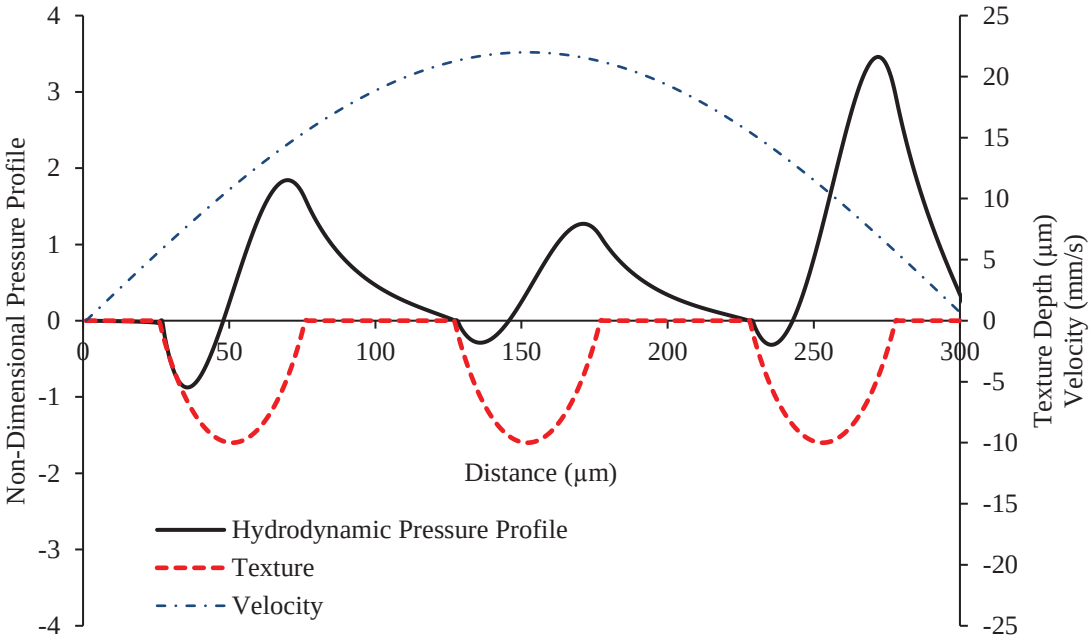

Figure 5-15: Hydrodynamic pressure distribution plotted with respect x axis over 1 reciprocating stroke moving at velocity (v) across 3 consecutive textured pores with dimensions of 50µm diameter and a of depth 10µm.

Both Figure 5-14 and Figure 5-15 show that the pressure produced is not confined to the vicinity of the textured pore, but, is observed to encapsulate much of the textured cell.

5.10.2 Factor Effect and Normalised Friction Force

To validate the theoretical model, the friction force taken from the experimental study in Chapter 4 was compared to the modelled friction force. The comparison of the two sets of data was undertaken by means of evaluating the parameter effects in the same manner as reported in the previous chapter. For convenience the expression for computing the factor effect is provided in Equation 5-48. Where Ff is the friction force, A and B

notations describe the factor investigated; A being the diameter and B the depth and the average of the control was the friction force measured from the unprocessed surface.

$$Factor\ Effect = \frac{Av.Ff\ (Control) - AV.Ff\ (A,B)}{\sigma\ (Factor\ A,B)} \qquad \textbf{Equation 5-48}$$

In adopting this method, a value for the control of the theoretical results to be compared to was required. To do so, two assumptions were made; firstly it was assumed that the theoretical friction force was higher than that of the textured surfaces, as observed by the empirical results. Secondly, the increase in friction force from the maximum recorded for a textured surface to the control surface (unprocessed surface) occurred at the same rate. Given these assumptions the percentage increase was employed as a means to predict the friction force for an unprocessed surface corresponding to the theoretical values derived in the analytical study.

In both experimental and theoretical cases the highest friction force obtained was for a diameter of 200μm and a depth of 20μm. The percentage difference between the friction force of the experimental control specimen (14.05N) and the highest textured specimen (11.28N) was 22%. Applying the percentage difference to the analytical study, where the maximum friction force attained was 1.72, the approximated value for an unprocessed surface (control), in the context of the analytical model, was 2.14.

Figure 5-16 shows the factor effects in terms of diameter and Figure 5-17 for the depth parameter. In both cases the effect is measured by its influence on reducing the friction force, hence, larger values describe a larger effect in friction reduction.

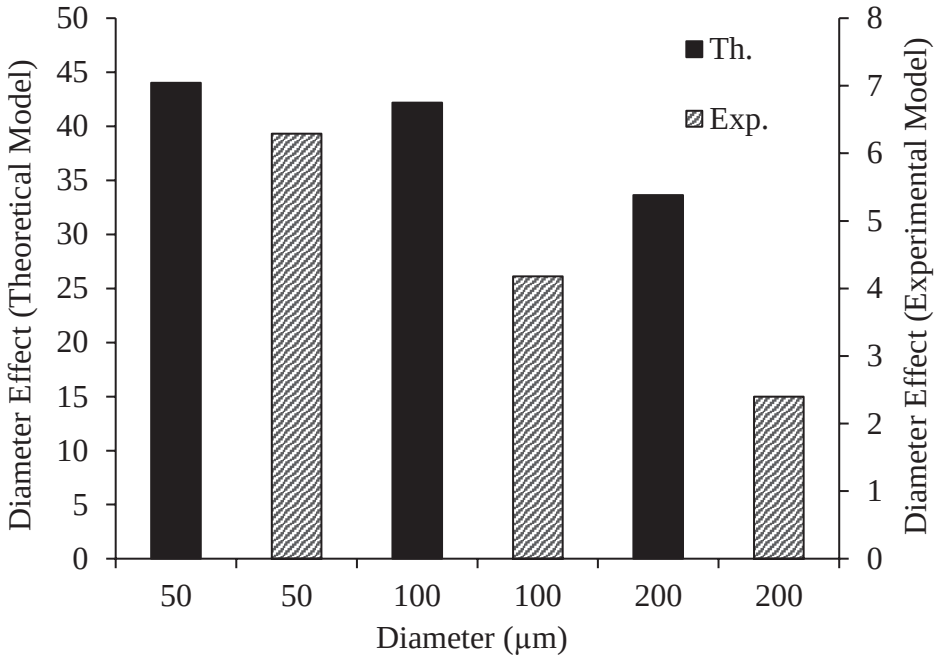

Figure 5-16: Comparing the effect of texture diameter in reducing friction between experimental and theoretical model. Diameter parameters employed 50,100 and 200µm and compared to the experimental test results obtained in Chapter 4.

The effect analysis from Figure 5-16 shows a similar trend in the effect of the diameter factor between theoretical and experimental values. Both sets of data show that the diameter of 50µm is most effective in reducing friction. As the diameter increases both theoretical and experimental effects prescribe a decreasing effect in reducing friction, where 200µm is shown as the least effective.

The comparison in the effect of depth between the modelled and experimental values shown in Figure 5-17 identifies large disparities between the two data sets. The modelled parameter effect reduces as the texture depth increases. This is seen to contrast when compared to the experimental results whereby the effect in reducing friction initially increases, obtaining maximum friction reducing capabilities at 10µm before the effect of depth in reducing friction decreases to a minimum at 20µm.

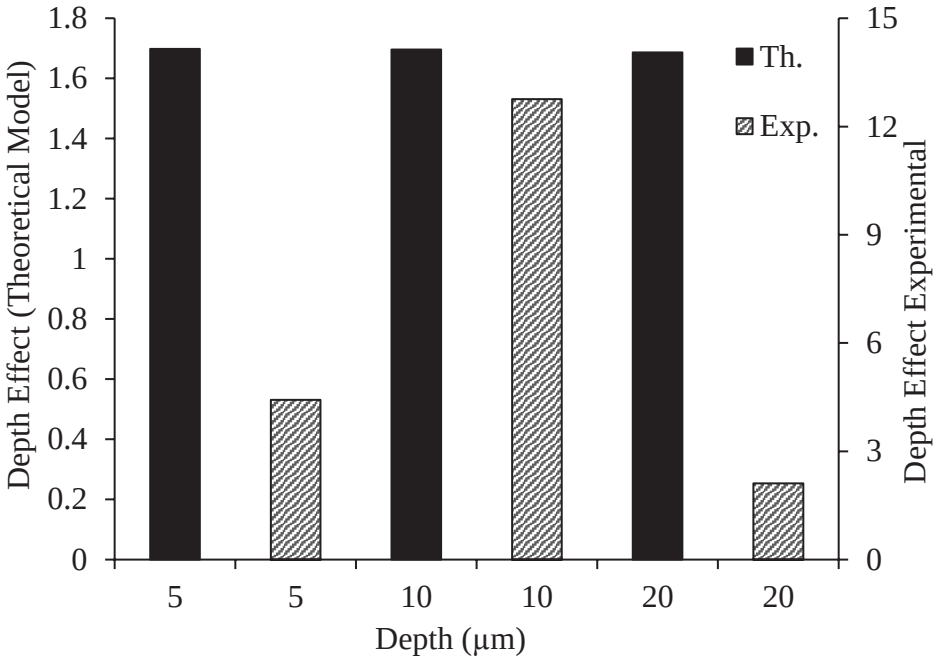

Figure 5-17: Comparing the effect of texture depth in reducing friction between experimental and theoretical model. Depth parameters employed 5, 10 and 20µm and compared to the experimental test results obtained in Chapter 4.

In order to attain a holistic understanding of the factor effects over a wider range of texture parameters the following analysis includes the statistically modelled values of coefficient of friction acquired from the regression model in Chapter 4. In this instance the friction force is obtained by multiplying the coefficient of friction by the experimental load of 75N. On computing the friction force the average is taken across each diameter over the various depths. The same method was employed to compute the depth effect, whereby the average is taken across each depth over the various diameters.

To adequately compare the modelled non-dimensional and experimentally derived friction force the results are normalised according to Equation 5-49.

$$\beta = \frac{Variable - \bar{x}}{\sigma} \qquad \textbf{Equation 5-49}$$

Where the variable is the friction force to be standardized, $\bar{x}$ and σ are the population mean and standard deviation of each data set and β is the friction force in standardized form. Table 5-1 and Table 5-2 provides the non-dimensional and experimental friction force together with the normalised friction force for factors diameter and depth respectively.

Table 5-1: Normalised friction force (Diameter Effect)

	Experimental		**Theoretical**	
Diameter (μm)	Friction Force (N)	Normalised Friction Force	ND Friction Force	Normalised ND Friction Force
50	0.405	-1.599	7.494	-1.613
75	0.735	-0.913	7.797	-1.183
100	1.012	-0.336	8.714	0.120
125	1.267	0.196	8.863	0.332
150	1.476	0.629	9.067	0.623
175	1.612	0.913	9.260	0.897
200	1.706	1.109	9.210	0.825

ND=Non Dimensional

Table 5-2: Normalised friction force (Depth Effect)

	Experimental		**Theoretical**	
Depth (μm)	Friction Force (N)	Normalised Friction Force	ND Friction Force	Normalised ND Friction Force
5	9.562	1.068	1.154	-1.157
7.5	8.739	0.125	1.158	-0.914
10	7.809	-0.939	1.164	-0.585
12.5	7.587	-1.193	1.170	-0.171
15	7.971	-0.753	1.179	0.329
17.5	8.913	0.325	1.188	0.914
20	9.824	1.367	1.200	1.584

ND=Non Dimensional

The effect of diameter is presented in Figure 5-18. Good agreement is observed between the theoretical model and experimental model where increasing the diameter results in an increase of friction force.

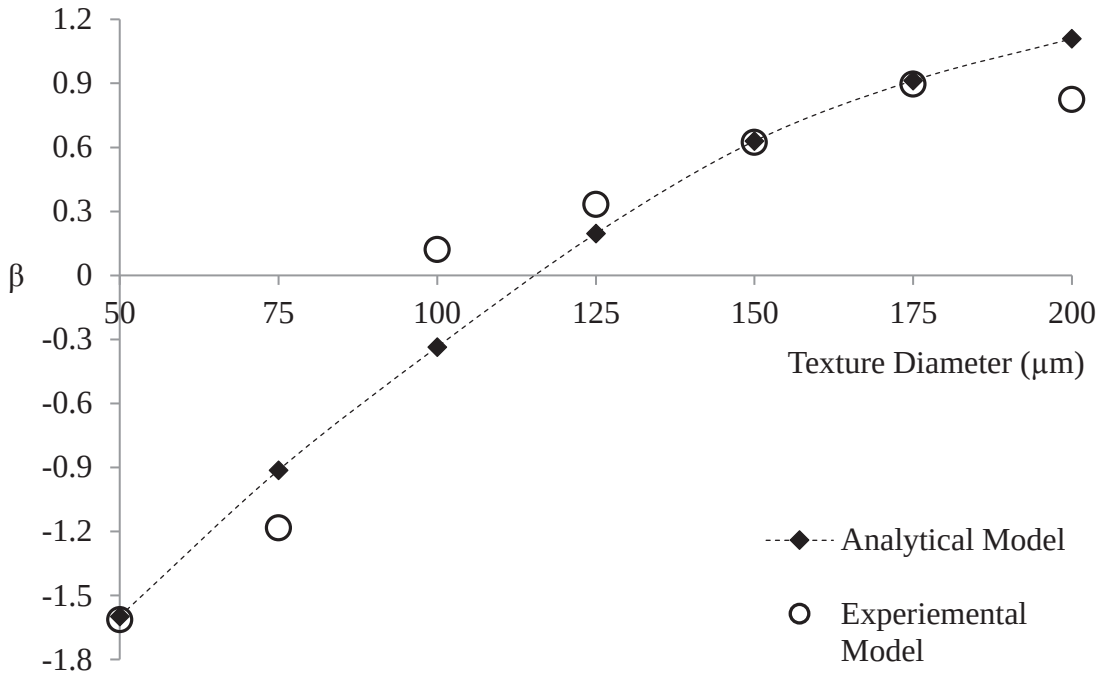

Figure 5-18: Comparing the normalised friction force for theoretical and experimental model at various diameters in the range from 50μm to 200μm at 25μm intervals.

The effect of texture depth is depicted in Figure 5-19. The model developed based upon the experimental results mimics a shoe horn effect whereby the optimum depth is in the region between 10μm and 15μm. This differs from the theoretical model that predicts an increase in friction force as the textures become deeper. Reasonable agreement is attained between the depths of 12.5μm and 20μm however, suggesting that the model struggles to encapsulate the practical conditions for textures with depths lower than 12.5μm. This is attributed to the assumptions made pertaining to the notion of the textures being fully flooded.

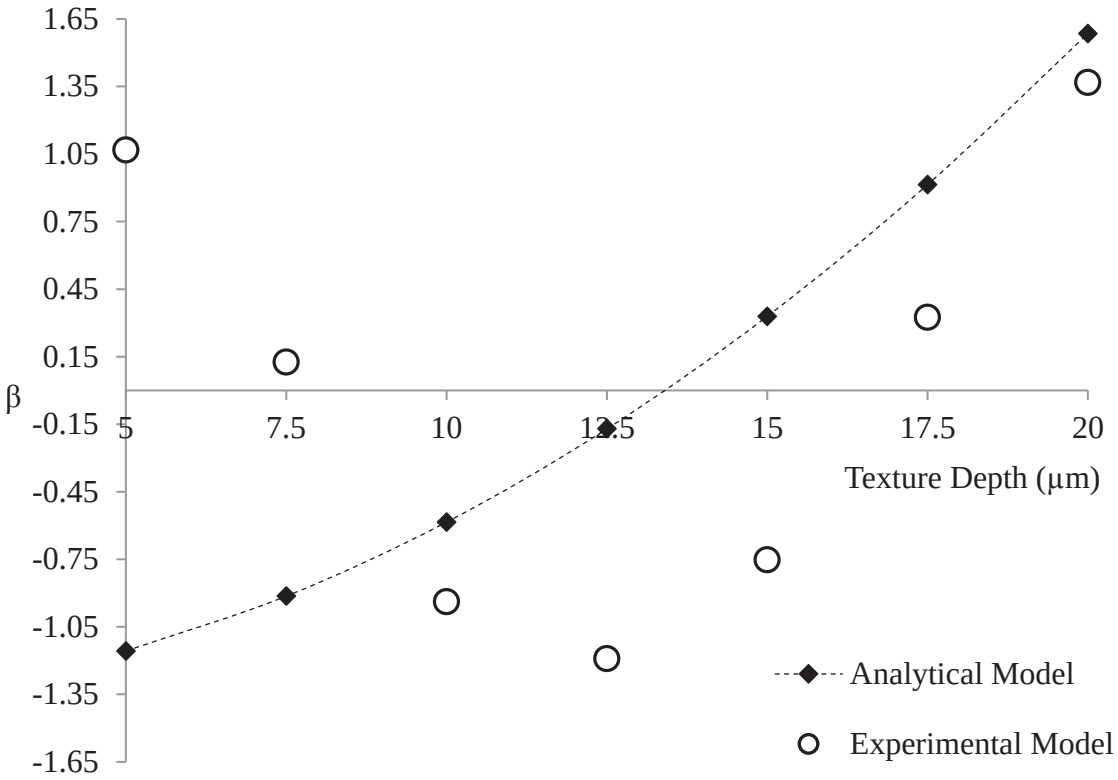

Figure 5-19: Comparing the normalised friction force for theoretical and experimental models at various depths in the range from 5μm to 20μm at 2.5μm intervals.

Figure 5-20 assesses the correlation between the experimental model and theoretical model when the results are expressed in terms of an aspect ratio. The aspect ratio is calculated as depth/diameter with the minimum and maximum aspect ratio being 0.025 and 0.4 respectively. The aspect ratio range is partitioned into seven separate bins and the values assigned to each bin range is the average of the friction force that falls within those limits, the friction force is then standardized using Equation 5-49. Table 5-3 provides the aspect ratio ranges, normal and non-dimensional friction force in addition to the normalised friction force.

Table 5-3: Normalised friction force (Aspect Ratio Effect)

		Experimental		Theoretical	
Aspect Ratio	Bin No.	Friction Force	Normalised Friction Force	ND Friction Force	Normalised ND Friction Force
0-0.057	1	8.893	0.949	1.508	1.417
0.058- 0.114	2	8.912	0.968	1.330	1.008
0.115-0.171	3	9.013	1.076	1.120	0.522
0.172-0.228	4	7.620	-0.403	0.801	-0.214
0.229-0.285	5	7.768	-0.246	0.643	-0.577
0.285-0.342	6	7.019	-1.040	0.414	-1.107
0.342-0.4	7	6.771	-1.304	0.439	-1.048

ND=Non Dimensional

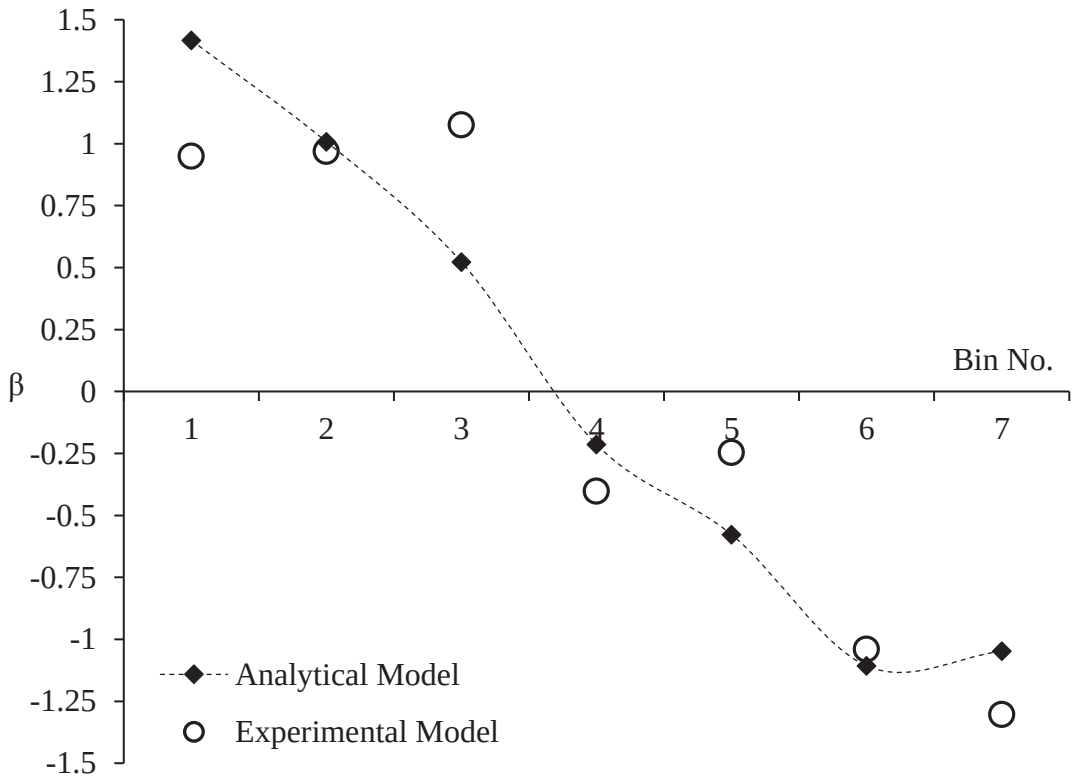

Figure 5-20: Comparing the normalised friction force for theoretical and experimental models against assigned bin number. The bin number correlates to the aspect ratios provided in Table 3-3. The aspect ratio is partitioned into 7 equally divided sections providing an averaged value for each bin.

Combining the diameter and depth in terms of the aspect ratio provides a reasonable agreement between the two data sets, identifying an overall reduction in friction force as the aspect ratio increases.

From the analysis conducted it is shown that the model fails to predict the friction force at depths below 12.5μm. In order to evaluate where these discrepancies between the experimental and theoretical model lie, Figure 5-21 provides a contour graph describing the level of variation in the friction between the normalised (β) experimental and normalised (β) theoretical models. The difference between the two β values was calculated according to Equation 5-50. In instances where the variance produced a negative output the result is made positive by multiplying by -1 to give the difference in positive form.

$$Level\ of\ Variance = \beta_{theoretical} - \beta_{experiemntal} \quad \textbf{Equation 5-50}$$

At wider diameters across all depths the level of variation is negligible indicating that the model produces a good correlation in the magnitude of friction at diameters from 175μm across all depth. Moreover, reasonable correlation was attained as the depth reduces at diameters from 75μm to 175μm. The level of variation, however, increases as the depth reduces to below 7.5μm and diameter reduces below 150μm where the variation between theoretical and experimental β values are at the highest levels. In the case of deeper textures, the variation increases as the depth increases above 17.5μm at diameters below 75μm.

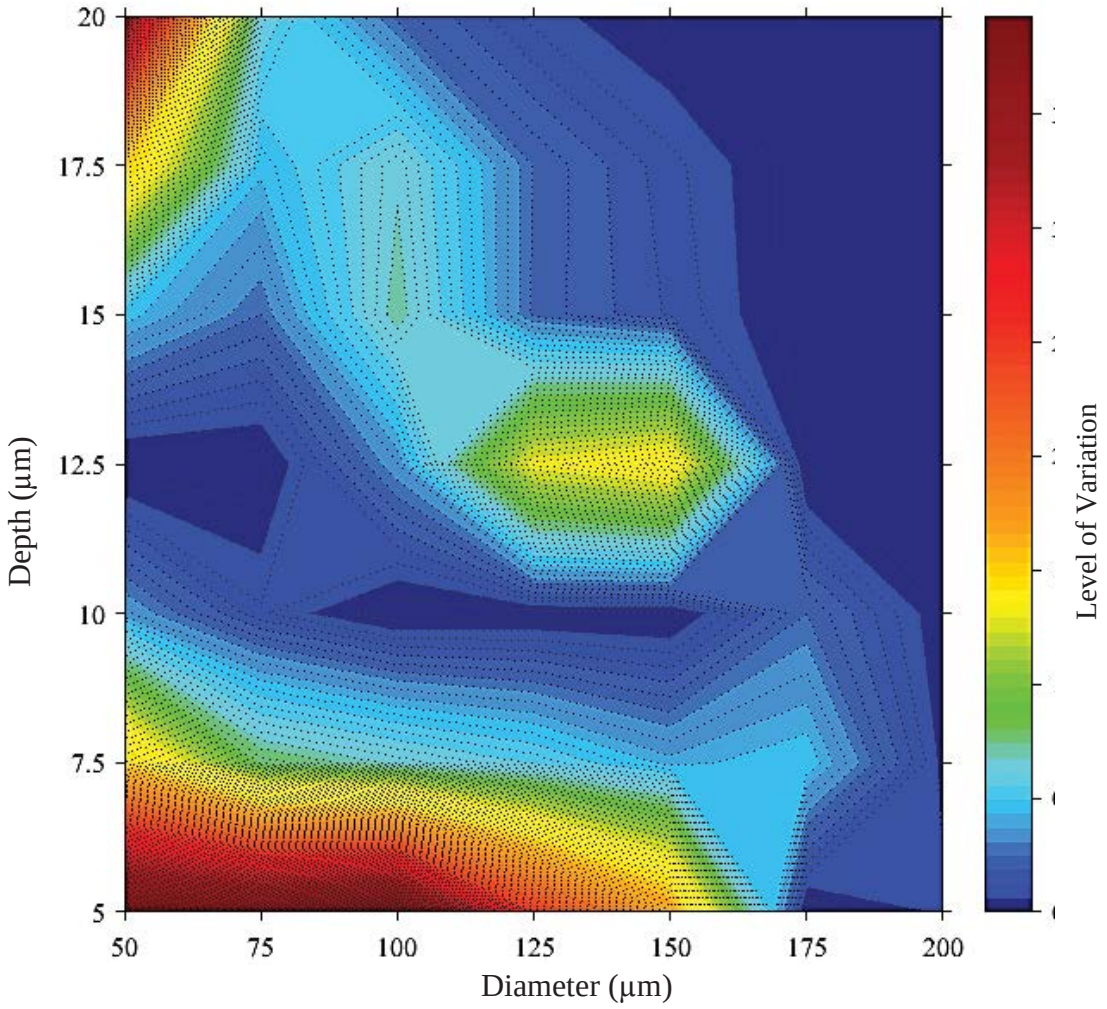

Figure 5-21: Contour plot and corresponding colour bar expressing the level of variation in β between experimental and theoretical models. The variation is measured by comparing all texture parameter combinations indicated on the depth and diameter axis.

5.11 Discussion

The numerical model developed predicts the hydro-dynamic pressure and friction force produced in relation to the parameters set. It is shown that that hydro-dynamic pressure produced differs throughout the stroke owing to the variation in velocity and the subsequent changes in film thickness. It can be seen that as the velocity increases the pressure produced reduces, this is attributed to an increase in the distance between the surfaces. The pressure developed towards the end of the stroke increases. Two factors

influence this phenomena, firstly the decrease in velocity at the extremity of the stroke causes the gap between the two surfaces to reduce. Subsequently the bulk fluid at this point becomes pressurised owing to a squeeze effect. To exemplify the described phenomena Figure 5-22 shows the friction force as a function of time for 4 reciprocating strokes for a control (un-textured) and textured surface of 100µm diameter and 10µm depth. The high speed data was captured at a frequency of 100Hz over 4 seconds.

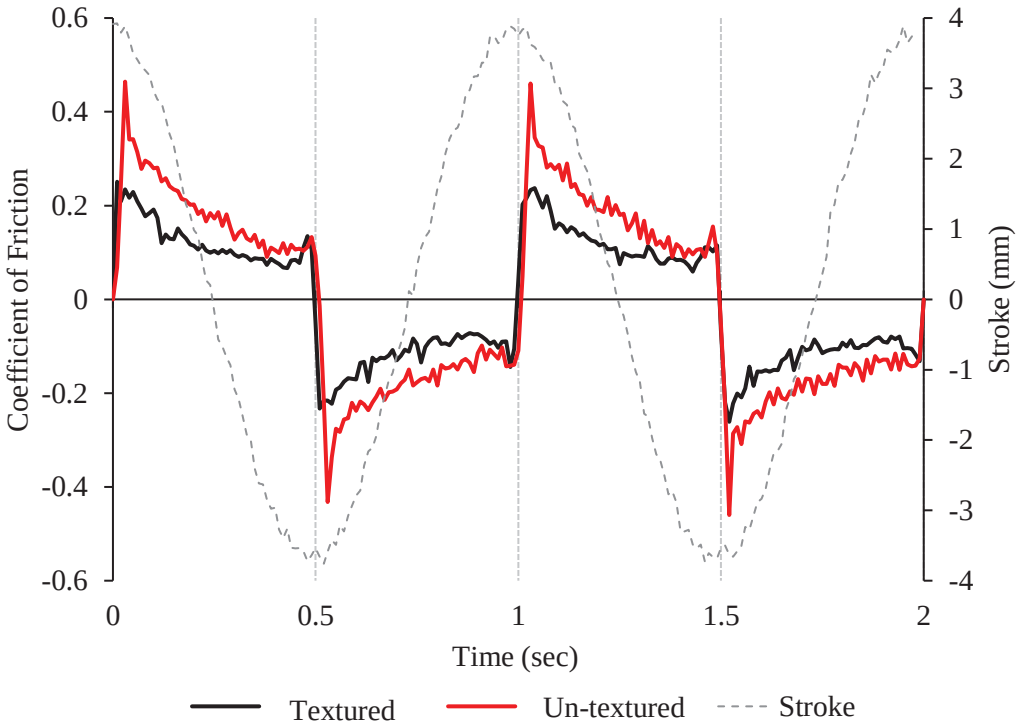

Figure 5-22: Friction force and Stroke length vs. Sliding time for a control (un-textured) and a textured surface. Friction data captured at 100Hz over 2 seconds. Tests conducted at 1Hz reciprocating frequency, load of 50N with water lubrication maintained at 37°C.

Figure 5-23 demonstrates the notion of a friction reducing mechanism in the form of a squeeze effect by the general form of the friction trace. If no squeeze effect were present the friction trace would be approximately symmetrical around the centre stroke, however, both control and textured surface exhibit a distinct drop in friction near the end of the

stroke. Each individual reciprocating stroke can be sectioned into three regions of tribological activity, as shown in Figure 5-23.

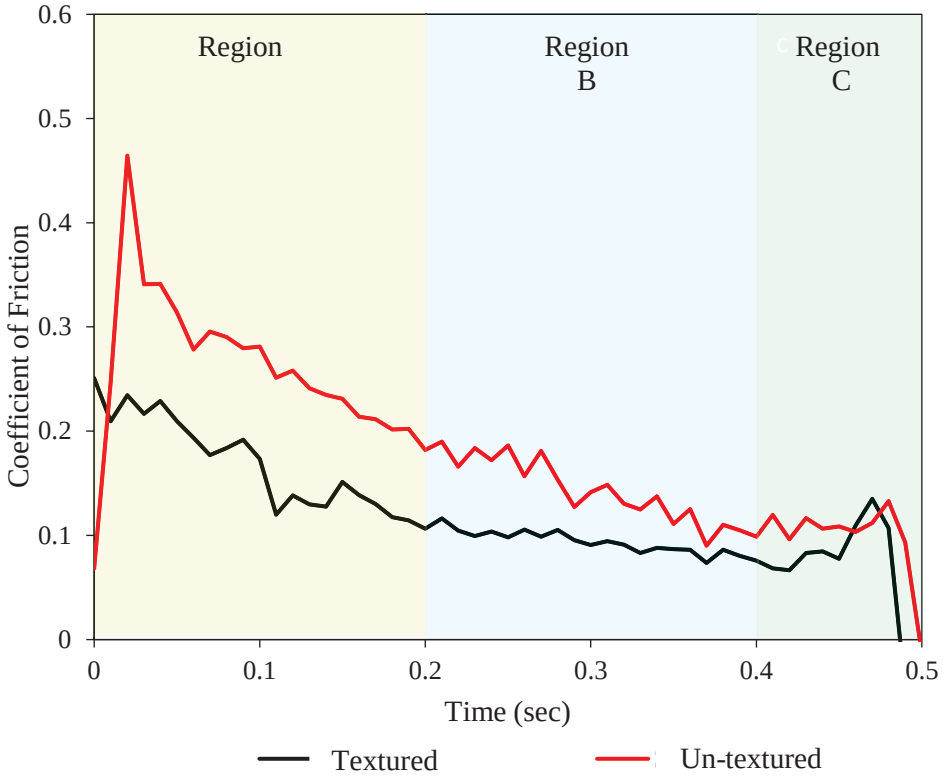

Figure 5-23: Friction force vs Sliding time for a control (un-textured) and textured surface exemplifying three lubrication regions of tribological phenomena relating to the regime. Region A: Boundary/mixed lubrication, Region B: Hydrodynamic and squeeze film lubrication, Region C: Mixed/boundary lubrication

Throughout region A the friction initially increases; as the applied tangential force is required to surpass the limiting friction force to transition from static to kinetic motion. Once sliding commences the velocity at this point is insufficient to generate a fluid film between the surfaces, hence surface asperities are in contact providing a boundary/mixed lubrication regime. Within region B the hydrodynamic and squeeze effect is dominant as the friction force falls owing to the formation of a fluid film, which is a product of the velocity increasing within the stroke. Region C befalls as the film thickness reduces, corresponding with a reduction in velocity resulting in asperity contact between the

opposing surfaces and entrapment of wear particles. At which point the lubrication regime reverts to a mixed/boundary state.

Figure 5-24 shows a comparison of the instantaneous friction force across one stroke for the numerical model and the captured high speed friction force data for the first and third stroke shown in Figure 5-23. The data for hydrodynamic pressure and film thickness are each contained within a set of 2-dimensional matrices of dimensions *n* x *m* where *n* is the *x* direction and m is the *z* direction. In order to calculate the instantaneous friction force the 2-dimesional nodal values for film thickness and pressure were partitioned along the *x*-axis creating a series of 1 x *m* matrices. Using Equation 5-47 the instantaneous friction force was calculated across the stroke length corresponding to the velocity profile. Comparing theoretical and analytical data it can be seen that within region A and B the two diverge, attributed to the tribological activity described, and which is not accounted for within the model. However, region B shows a good fit in terms of their respective form illustrating the notion of hydrodynamic pressure and squeeze film action is present within the system.

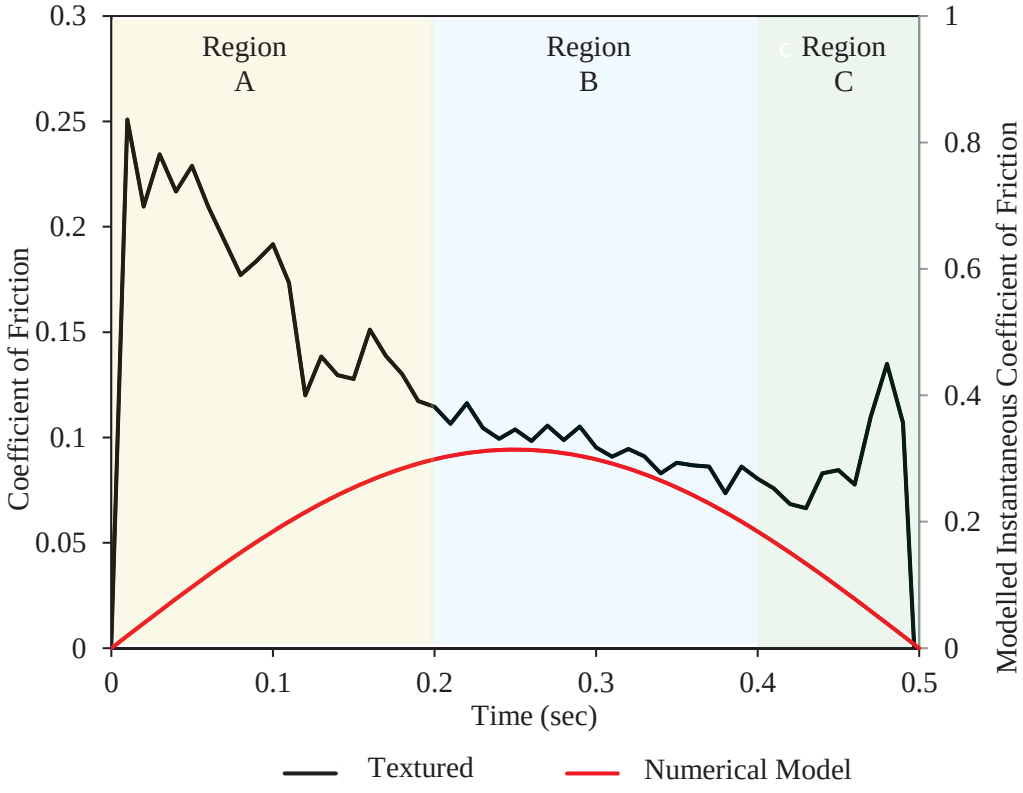

Figure 5-24: Experimental friction force for a textured surface vs the Numerical modelled instantaneous friction force for a textured surface of 100µm diameter and 10µm depth. The plot highlights the three regions of tribological activity expected within a reciprocating contact where Region A: Boundary/mixed lubrication, Region B: Hydrodynamic and squeeze film lubrication, Region C: Mixed/boundary lubrication.

The comparison of the friction force between the experimental and numerical model illustrates the fact that the model does not account for the tribological activity that occurs throughout the complete reciprocating stroke. It has been shown within the friction analysis of Chapter 3 and Chapter 4 that the limiting friction force, as the system transitions from static to kinetic friction, differs when varying the texture geometry and surface coverage. Given this, one credible source of variation between the analytical model and experimental results could be the different effect that textures have on the limiting friction force that occurs as the stroke reverses direction.

The effect of diameter shows good agreement between experimental and theoretical models, by increasing the diameter results in an overall increase in friction force. The strong correlation between the two suggests the theoretical model can adequately predict the friction force based upon the texture diameter.

However, assessing the effect of depth and comparing between experimental and theoretical models provides differences in the form each model perceives the effect. From Figure 5-17 the experimental results indicate that an optimum texture depth lies in the region between 10μm and 15μm, as also expressed in Chapter 4, Figure 4-10. However, conversely the model indicates no definitive optimum value for the depth parameter, with the model predicting that the friction force rises as the texture deepens. The model suggests a more linear output whereby the friction force increases as the texture depth increases. Reasonable agreement is found however, between the depths of 12.5μm and 20μm, at which point both models provide an increase in friction force with an increasing depth.

Comparing the effect of aspect ratio from Figure 5-20 also provides a reasonable agreement between experimental and theoretical model. However, the agreement could be interpreted to derive from the strength of correlation found between the two models in relation to the effect in diameter.

Directly comparing the standardized friction force between both models presented, the level of variance between the two sets of data, illustrated in Figure 5-21 shows that the validity of the theoretical model tends to drop when required to predict the friction force at diameters below 150μm and depths below 7.5μm. As the texture cavity deepens the model shows discrepancies in predicting the friction force at diameters less than 75μm

and at depths of more than 17.5μm. As described above it can be seen in Figure 5-21 that the variation between experimental and theoretical modelled friction force is at a maximum at deepest and shallowest depth analysed. Between the depths of 10μm and 15μm, across all the diameters employed within the study, shows that the level of variation is small, however rises slightly in the region between 125μm and 150μm. The highest correlation across the depths is between 175μm and 200μm, where the level of variance reduces to a minimum between approximately 10μm and 20μm depths.

The variation in friction force between the experimental and theoretical models presented provides an indication of under which parameters the theoretical model fails to adequately predict the experimental friction force. The level of variance experienced in these instances is attributed to changes in flow parameters, and that the model does not encapsulate the operating conditions of the system with textures of a smaller diameter and at the extremes of shallow and deepest depths. In order to explain this, the main assumptions pertaining to the fluid flow involving the diameter and depth texture parameters are scrutinized.

The textured cavities are assumed to be fully flooded; however, the fully flooding of smaller diameter textures may be impeded by the physical size of the textured pore. A mixture of fluid and air may exist within the dimpled pore in the form of a cavitation region at the bottom of the texture, thus reducing the depth that the fluid operates over. The possibility of this phenomena increases when lower diameters are compared to larger diameters. Across all the depths employed within the study, Figure 5-21 shows that the level of variation in friction force between experimental and theoretical models is lower for textures of a wider diameter compared to narrower textures. It is conceivable therefore

that the physical size of the textured pores affects the fluids ability to fill the entire volume of the cavities in order to adhere to the fully flooded assumption.

The existence of a cavitation region at the bottom of the texture cavity is assumed to cause discrepancies in the theoretical model when predicting friction force for smaller diameter textures at the extremities of texture depth. The cavitation phenomenon is also relevant in explaining the variation in friction force seen across the texture diameters. Figure 5-8 describes the imposed cavitation region on the surface for each textured pore, where the cavitation region begins at the outer edge of the cavity and covers 50% of the texture circumference. However, it is possible that the cavitation region varies with a change in diameter. Varying the cavitation percentage in corresponding to a change in the texture diameter would in turn increase or decrease the hydro-dynamic pressure generated, subsequently causing variations in the friction force.

5.12 Conclusion

The two-dimensional Reynolds equation was solved in order to quantify and illustrate the effect of surface textures through one reciprocating stroke. The theoretical model employed the conditions relating to the experimental study performed in Chapter 4. Friction force was then computed as a function of the pressure and film thickness and the results were compared to the experimental model derived in Chapter 4. The key findings from the study are:

- In assessing the effects of texture diameter in reducing friction, good agreement between experimental and theoretical models was shown

- In contrast, however, a poor fit was established in monitoring the effect of depth. As the depth increased beyond 12.5μm the two models displayed a better correlation.
- The variance between the standardized friction force between experimental and theoretical models identified large disparities. Firstly, when predicting the friction force for shallow depths of 5μm to 7.5μm at texture diameters of between 125μm and 50μm. Secondly, at deeper texture depths of 17.5μm and 20μm at diameters of between 50μm to 75μm.
- Three distinct regions of tribological phenomena were identified within a reciprocating stroke with the modelled instantaneous friction force exhibiting a good fit for the hydrodynamic squeeze film region of the stroke.
- The variation of friction force within region A and C are attributed to the level of contact exhibited, not accounted for within the model and represents a source of variation when comparing the effect of diameter and depth.
- The lack of fit between the models at the fringes of the depths explored for lower texture diameters is attributed to a hypothesised cavitation region at the bottom of the texture affecting the fully flooded assumptions of the model.
- In addition, it was proposed that the cavitation region highlighted around the circumference of the texture diameter vary according to the texture diameter.
- The models showed good agreement for texture combinations outside of those stipulated, particular at increasing diameters across all depths, therefore illustrating the primary source of friction reduction in relation to the experimental conditions is through the presence of hydrodynamic phenomena.

CHAPTER 6

The Application of Acoustic Emission Monitoring For Tribological Phenomena within Polymeric Sliding Couples

6.1 Introduction

Tribological testing and monitoring of polymeric surfaces is often confined to observing the friction coefficient. However, conclusions based solely on the real-time monitoring of the coefficient of friction can be ambiguous as changes in load and speed have a limited effect on the resultant friction. For instance speed independent friction is observed between 1mm and 10mm/s, whilst loading in the range of 10N to 100N also offers little fluctuation in terms of the friction produced (Myshkin, et al., 2005). In light of this, acoustic emission (AE) monitoring offers a novel approach for evaluating the contact between two sliding polymer surfaces.

Acoustic emissions are strain waves that emanate from a point of stimulus as a result of the material yielding on some scale. From tribological perspective the magnitude of contact, sliding force and sliding time would all generate a variation in surface interaction characteristics. Hence increasingly more sever sliding would give rise to a proliferation in AE activity.

Therefore, the purpose of the following chapter is to investigate the correlation between acoustic emissions and the magnitude of sliding wear, thus allowing a real time assessment of surface interaction.

6.2 Experimental Method

Empirical tests were conducted with two experimental variables; speed and load within a non-conformal ball-plane contact configuration. Tests were undertaken on a Phoenix Plint TE-77 test rig as described in Chapter 2.1.1, with a stroke length of 9.2mm under loads of 10N and 30N, reciprocating at a frequency of 1 and 2Hz. All independent studies were conducted three times equating to a total of 12 experimental runs.

The load was varied to assess the AE response corresponding to surface wear under different loading conditions. The motivation for varying the speed was to firstly, increase the sliding distance and secondly increase the sliding force. This served as a means of expediting the wear processes when comparing surfaces that have undergone identical loading. Furthermore, elongating the sliding duration and increasing the sliding force would diversify the levels of wear.

6.2.1 Acoustic Emission Architecture

The acoustic emission sensor (Mistras) was mounted in direct contact with the upper specimen 4mm above the contact region; Figure 6-1 shows a schematic of the AE sensor and upper specimen layout. The sensor was acoustically coupled to the upper specimen by multi-purpose silicone grease. The signal captured by the AE sensor was passed through a pre-amplifier set at 60dB gain where it was then passed to a computer for processing. A cut-off frequency and amplitude threshold of 100Hz and 10dB was set to discriminate noise produced by the TE-77, isolating the AE emissions originating from the contact within the frictional couple.

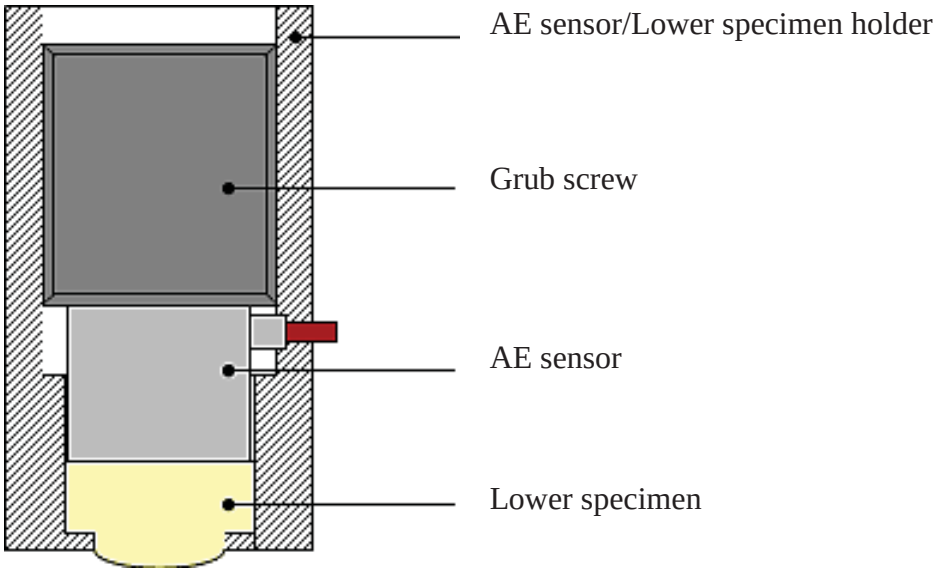

Figure 6-1: AE sensor/Upper specimen holder. Lower sample is inserted into the holder from the top, acoustic coupling (multi-purpose silicone grease is applied to the sensor and located within the holder. The grub screw holder maintains the positioning of the sensor

The AE response was firstly compared to the coefficient of friction for the purpose of highlighting the limited difference in response that the friction measurement offers under different sliding conditions. The acoustic emission parameter for which the coefficient of friction was compared to is the cumulative root mean square (RMS) voltage of the captured raw signal. Acoustic emission signals were captured over an interval of 90 seconds, the cumulative RMS voltage was therefore the sum of the all the root-mean square voltages captured within the specific time frame.

6.3 Results

6.3.1 Coefficient of Friction

Figure 6-2 shows the coefficient of friction vs. sliding distance for low and high-speed test under a load of 10N. It can be observed that the initial peak; the transition from static to kinetic friction, is higher for the low speed test. The difference in the peak value is attributed to the sliding force. In both circumstances the sliding force had to overcome the viscous forces of the surfaces, hence for high speed which generates a higher sliding force, these are overcome more easily than that of the low speed test that generates lesser sliding force. Once steady state conditions commenced the friction coefficient levelled out and remain approximately constant throughout the duration of the test regardless of sliding distance.

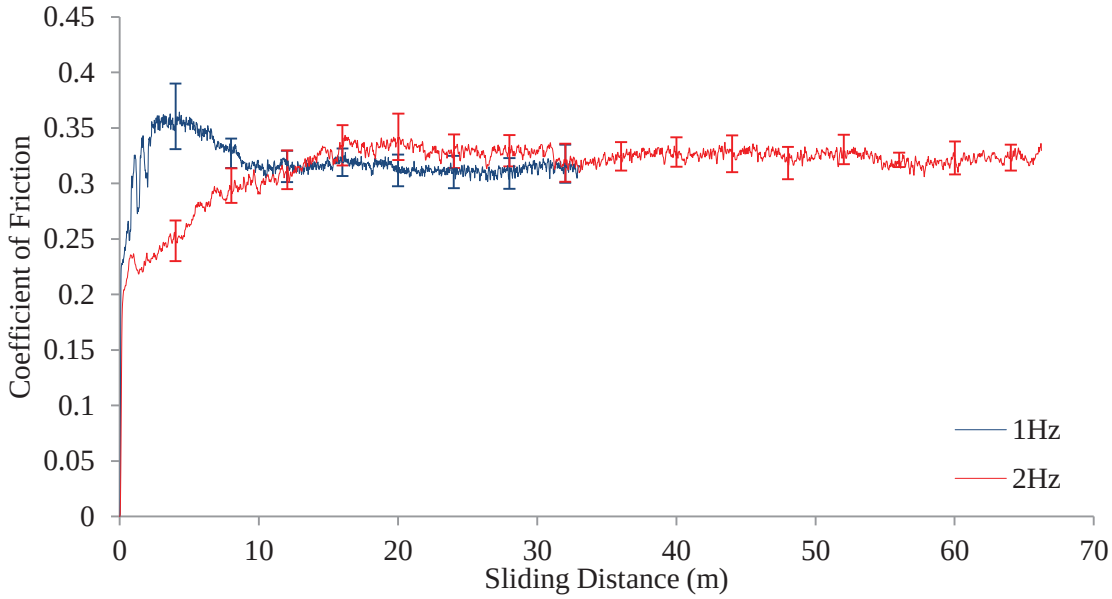

Figure 6-2: COF vs. Sliding distance for a non-conformal ball (9.2mm radius) and plane contact configuration, reciprocating at frequencies of 1Hz and 2Hz under an applied load of 10N. Error bars represent 1 standard deviation across the three replicated test. Trace line identifies the mean of the three tests.

Figure 6-3 shows the same test as Figure 6-2 in terms of sliding time, where it can be seen that no appreciable difference can be ascertained between the two sliding conditions.

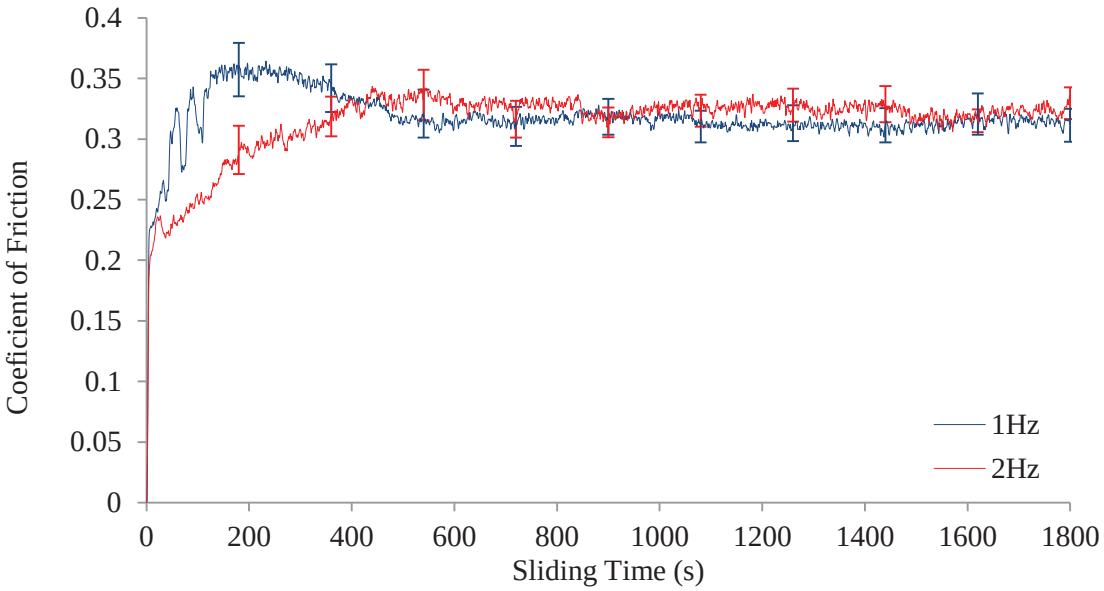

Figure 6-3: COF vs. Sliding time for a non-conformal ball (9.2mm radius) and plane contact configuration, reciprocating at frequencies of 1Hz and 2Hz under an applied load of 10N. Error bars represent 1 standard deviation across the three replicated test. Trace line identifies the mean of the three tests.

Figure 6-4 shows the coefficient of friction vs. sliding distance under a 30N loading. Similar to the 10N friction trace in Figure 6-2 the initial friction peak for 1Hz reciprocating frequency exceeds that of tests conducted at 2Hz. The low speed test exhibited no steady state with the coefficient of friction continuing to rise. Conversely the high speed examination was shown to reach a steady state friction output at around 30 meters.

Figure 6-5 shows the two sliding conditions for a 30N load plotted as a function of sliding time. Observed is a clear distinction between the two sliding speeds where the high-speed registered a slightly higher coefficient of friction reading.

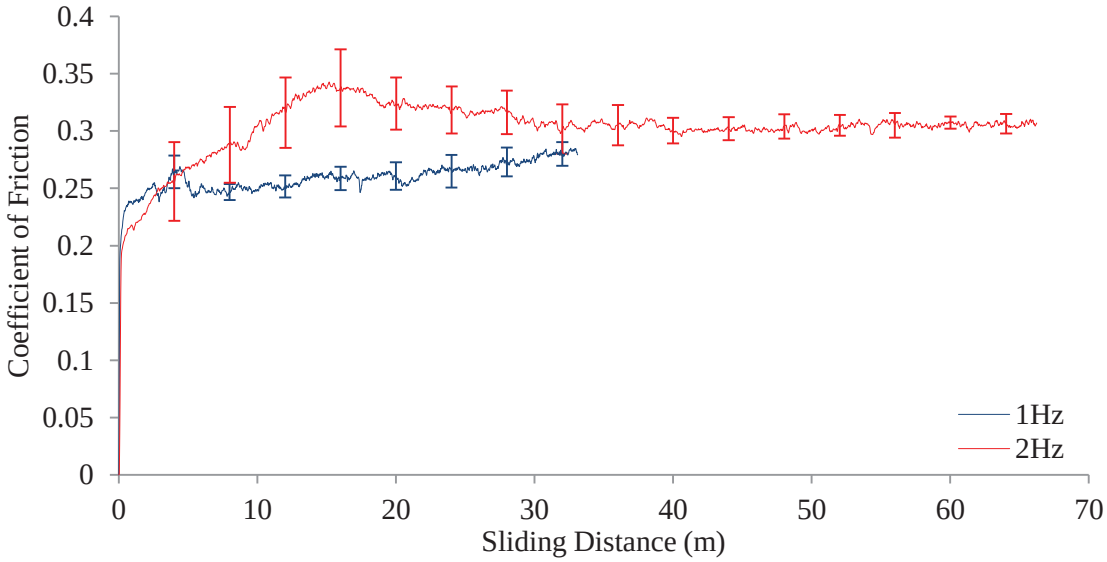

Figure 6-4: COF vs. Sliding distance for a non-conformal ball (9.2mm radius) and plane contact configuration, reciprocating at frequencies of 1Hz and 2Hz under an applied load of 30N. Error bars represent 1 standard deviation across the three replicated test. Trace line identifies the mean of the three tests.

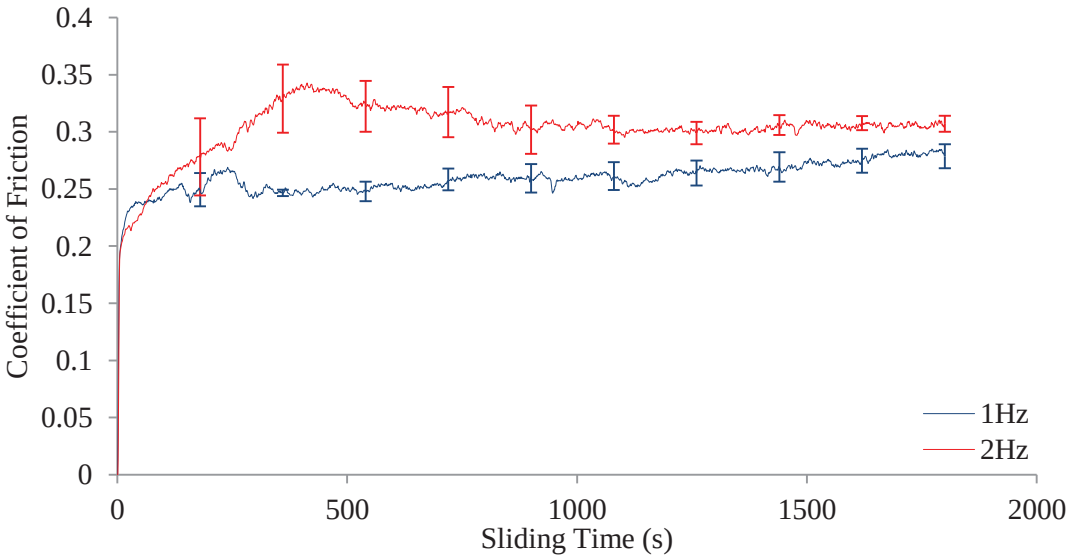

Figure 6-5: COF vs. Sliding time for a non-conformal ball (9.2mm radius) and plane contact configuration, reciprocating at frequencies of 1Hz and 2Hz under an applied load of 30N. Error bars represent 1 standard deviation across the three replicated test. Trace line identifies the mean of the three tests.

It can be seen by the friction results across all sliding conditions the surfaces exhibit higher friction than that of the lubricated tests undertaken within Chapters 3 and 4. The increase in friction is attributed to, firstly the removal of a lubricating fluid no film can

be established a thin film too fully or partially separate the surfaces resulting in solid body contact between the opposing surfaces. Another reason is that with the exclusion of a lubricating fluid the surface temperature increases through frictional heating which alters the material properties weakening the surface. In both circumstances adhesive and abrasive wear modes are allowed to manifest resulting in deformation of the surface and increased friction.

Figure 6-6 shows the symptomatic effects of the frictional assessment of polymers. The plot denotes the average friction coefficient for each test condition; the error bars represent the upper and lower values of a 95% confidence interval. Hence, there is a 95% chance the population mean resides within the confidence region. As can be seen the error bars all coincide with one another at some point, thus corroborating the notion that load and speed have a limited effect on the resultant friction.

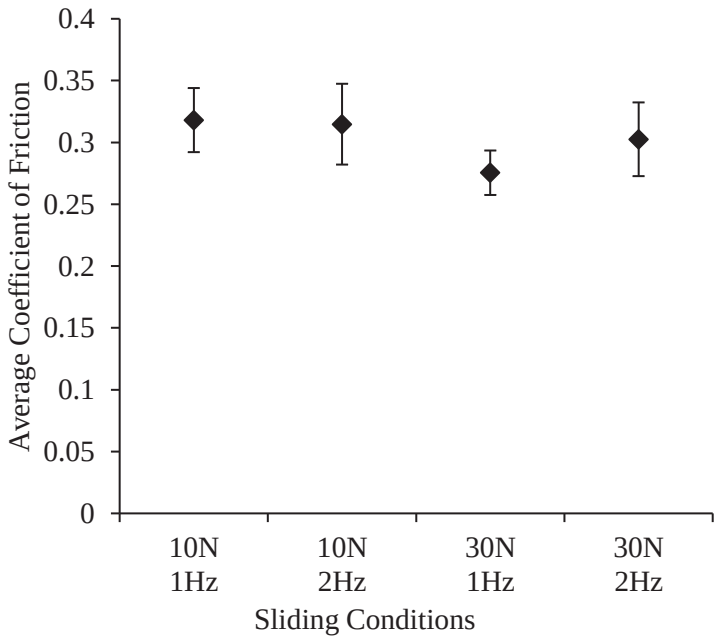

Figure 6-6: Av. COF vs. Sliding conditions for a non-conformal ball (9.2mm radius) and plane contact configuration, reciprocating at frequencies of 1Hz and 2Hz under an applied load of 10N and 30N with water as a lubricant at 25°C. Error bars represent upper and lower limits of a 95% confidence interval across the Av. COF for each independent test repetition.

6.3.2 Wear Assessment

Figure 6-7 through to Figure 6-10 depict the wear scar images for each test conducted arranged in run order corresponding to sliding condition. The wear scar diameter (WSD) is taken as the region that encapsulates all visual surface degradation. As can be seen the magnitude of visual wear varies in relation to sliding conditions. Furthermore, varying levels of material transfer are also observed. This is attributed to the boundary lubrication condition that culminates in substantial contact between the opposing surfaces. The absence of a lubricating media gives rise to frictional heating where the polymer at the contact interface becomes highly elastic and encourages the transfer of material. The adhesive mechanism of friction in this instance is accompanied by the deformation mode of friction. The wear of all ball surfaces show signs of surface fatigue in the form of crack or scratches of some degree, caused by the cyclic loading of the reciprocating stroke.

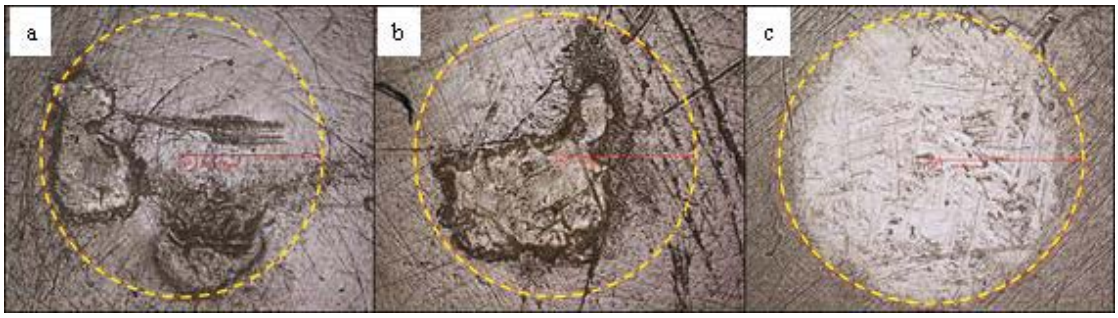

Figure 6-7: WSD on the face of the ball (upper specimen) for three identical tests conducted under the test conditions of 1Hz reciprocating frequency subjected to a 10N load with water as the lubricating fluid at room temperature (25°C). (a) Run 1: WSD 358µm, (b) Run 2: WSD 476µm and (c) Run 3: WSD 503µm.

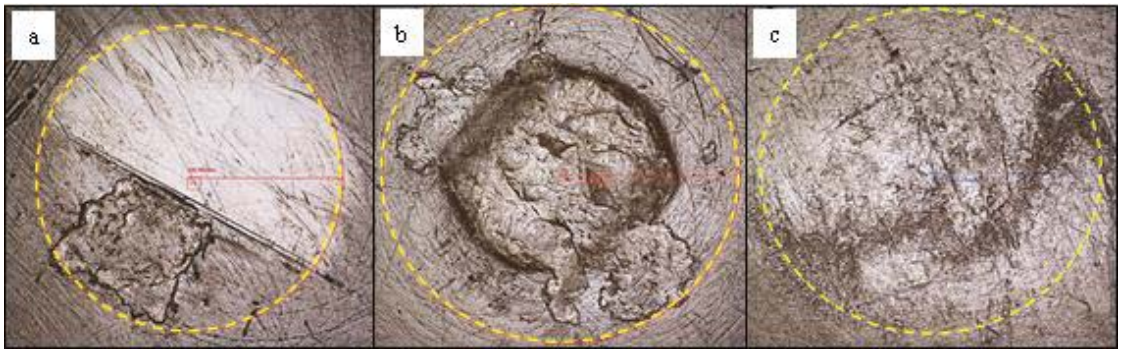

Figure 6-8: WSD on the face of the ball (upper specimen) for three identical tests conducted under the test conditions of 2Hz reciprocating frequency subjected to a 10N load with water as the lubricating fluid at room temperature (25°C). (a) Run 1: WSD 507µm, (b) Run 2: WSD 622µm and (c) Run 3: WSD 594µm.

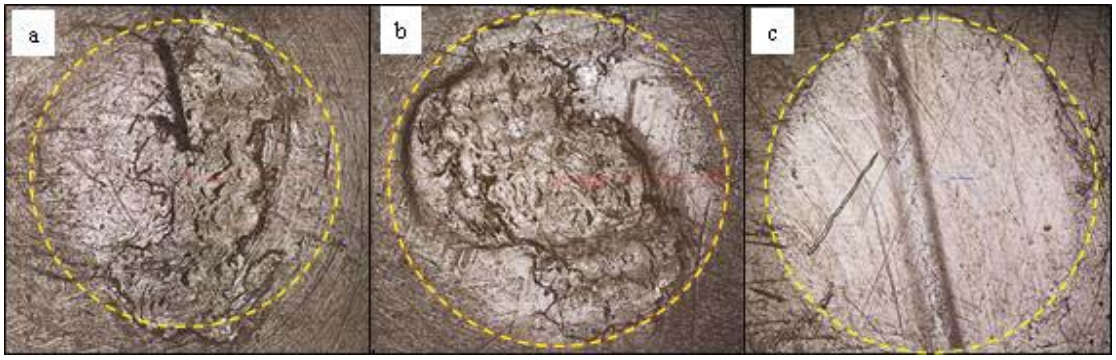

Figure 6-9: WSD on the face of the ball (upper specimen) for three identical tests conducted under the test conditions of 1Hz reciprocating frequency subjected to a 30N load with water as the lubricating fluid at room temperature (25°C). (a) Run 1: WSD 665µm, (b) Run 2: WSD 623µm and (c) Run 3: WSD 626 µm.

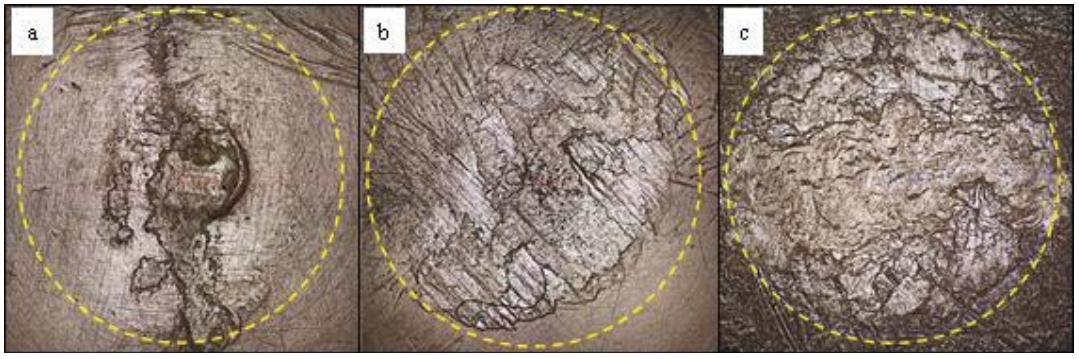

Figure 6-10: WSD on the face of the ball (upper specimen) for three identical tests conducted under the test conditions of 2Hz reciprocating frequency subjected to a 10N load with water as the lubricating fluid at room temperature (25°C). (a) Run 1: WSD 930µm, (b) Run 2: WSD 1101µm and (c) Run 3: WSD 705µm.

The wear scar diameters across all tests conducted are shown in Figure 6-11. The trend-line indicates a linear relationship between the sliding condition and wear scar diameter illustrating that increases in both speed and load results in a proliferation of the wear scar diameter.

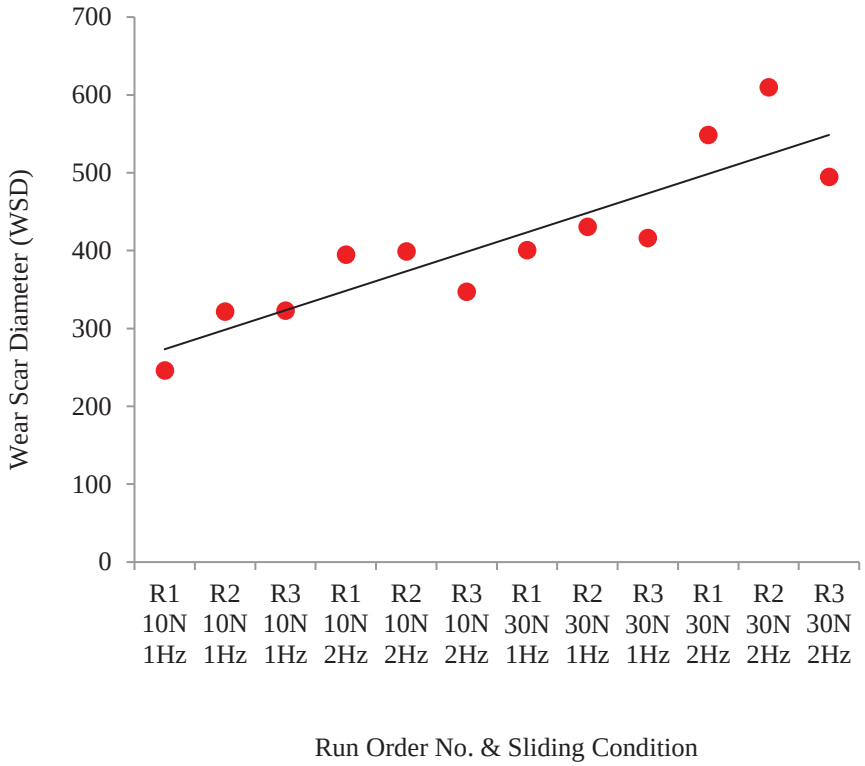

Figure 6-11: WSD vs. Run order and Sliding Conditions under water lubricated conditions. R1, R2, and R3 are the Run numbers corresponding to the wear scar diameters in Figure 6-7 to Figure 6-10. Sliding Conditions denote the load and reciprocating sliding frequency.

The wear of the lower samples was evaluated using the volumetric difference of the lower specimen from before and after the test. Volume (V) of each sample was calculated according to Equation 6-1, where m is the mass, which was measured using an analytical balance with a resolution of 0.00001g and ρ is the density of the Victrex PEEK 450g polymer and was 1300 kg/m^3 taken from Victrex PEEK 450g data sheet .

$$V = \frac{m}{\rho}$$ **Equation 6-1**

The plot displayed in Figure 6-12 shows the volumetric wear experienced under each sliding condition corresponding to the test run number. Similar to the WSD's provided in Figure 6-11 the volumetric wear of the lower specimen increases with both the normal load and reciprocating sliding frequency.

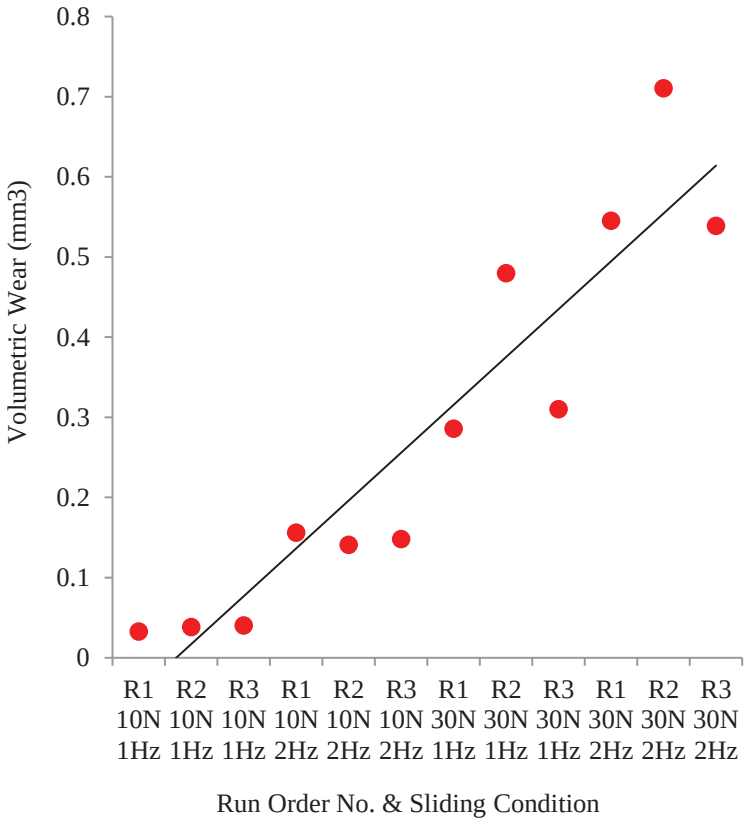

Figure 6-12: Volumetric wear vs. Run order and Sliding Conditions under water lubricated conditions. R1, R2, and R3 are the Run numbers corresponding to the wear scar diameters in Figure 6-7 to Figure 6-10. Sliding Conditions denote the load and reciprocating sliding frequency.

6.3.3 Acoustic Emission Response

Figure 6-13 and Figure 6-14 shows the cumulative root mean square voltage as a function of sliding distance and sliding time respectively for a 10N load reciprocating at a frequency of 1Hz and 2Hz. The error bars represent one standard deviation taken across the three test repetitions at various points, the trace line indicates the mean cumulative RMS voltage.

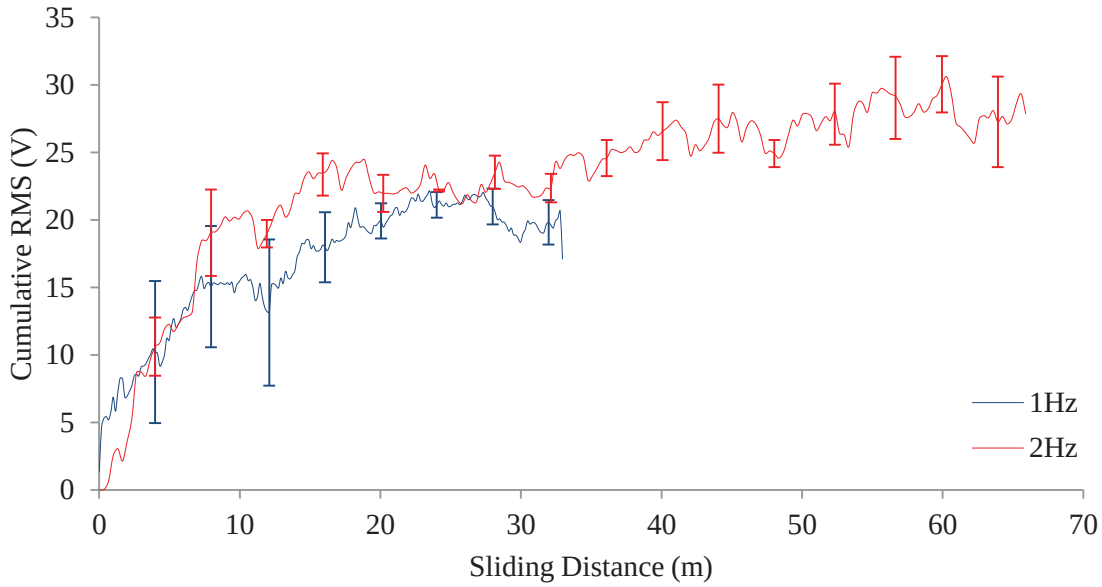

Figure 6-13: Cumulative AE RMS vs. Sliding distance for a non-conformal ball (9.2mm radius) and plane contact configuration, reciprocating at frequencies of 1Hz and 2Hz under an applied load of 10N. Error bars represent 1 standard deviation across the three replicated test. Trace line identifies the mean of the three tests.

Observed is the similarity with the coefficient of friction, where the 1Hz test registered a higher AE RMS voltage in the initial stages of sliding. However, there was no apparent steady state sliding regime attained for either sliding speeds where both tended to increase at an approximately similar rate. It can be seen that large variations exist between independent tests, highlighted by the standard deviation error bars. Moreover, there is a clear distinction between the two sliding conditions indicating a difference in the magnitude of signal captured.

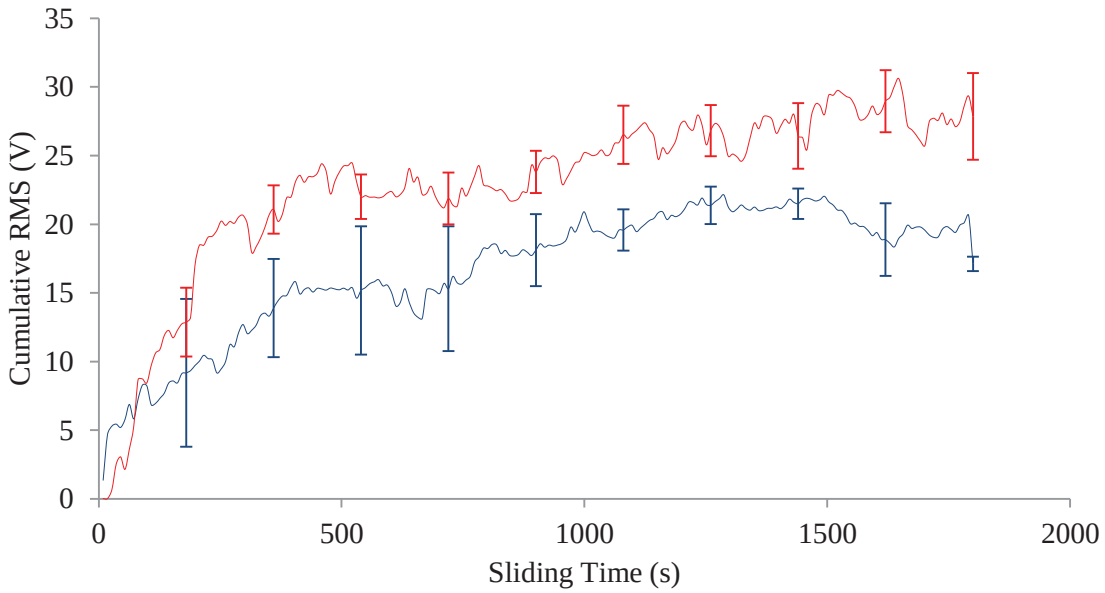

Figure 6-14: Cumulative AE RMS vs. Sliding time for a non-conformal ball (9.2mm radius) and plane contact configuration, reciprocating at frequencies of 1Hz and 2Hz under an applied load of 10N. Error bars represent 1 standard deviation across the three replicated test. Trace line identifies the mean of the three tests.

The plots presented in Figure 6-15 and Figure 6-16 show the cumulative RMS voltage as a function of sliding distance and sliding time respectively for a 30N loading. Observed is that at 1Hz sliding frequency the cumulative RMS voltage increases throughout the test. For a sliding frequency of 2Hz the acoustic emission output increased before levelling and attaining a steady state at approximately 30 meters. Similar to the 10N tests large variations in the standard deviation error bars appoint to fluctuations between the three test repetitions. Furthermore, there is a clear distinction between the cumulative RMS voltages for the tests subjected to different sliding conditions. Comparing the plots concerning the 10N and 30N AE response the cumulative AE RMS voltage increased for the higher loaded tests, indicating that the AE response is sensitive to variations in load.

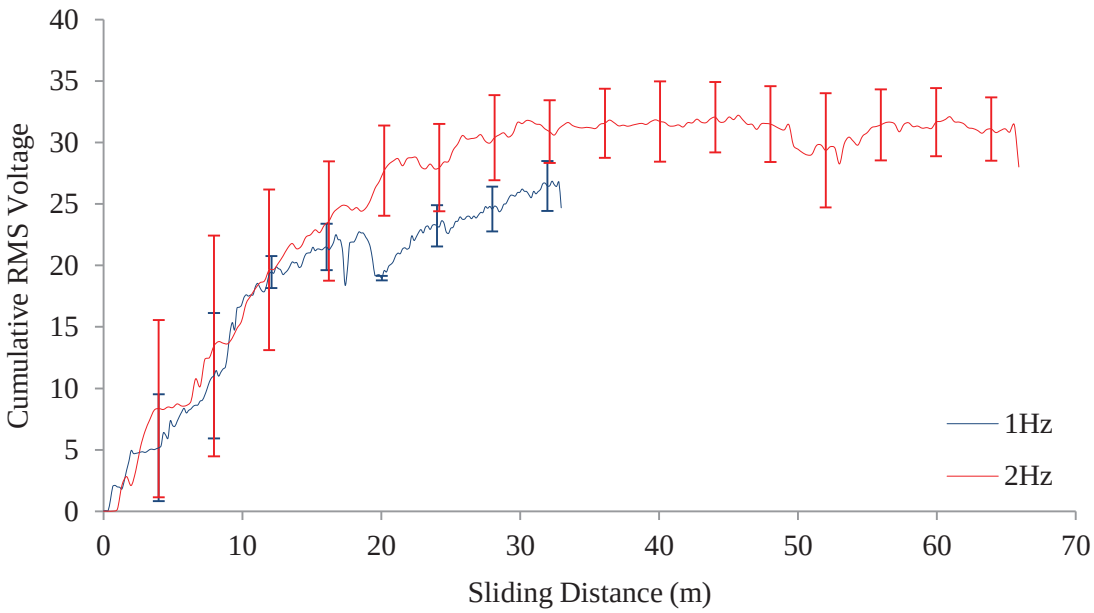

Figure 6-15: Cumulative AE RMS vs. Sliding distance for a non-conformal ball (9.2mm radius) and plane contact configuration, reciprocating at frequencies of 1Hz and 2Hz under an applied load of 30N. Error bars represent 1 standard deviation across the three replicated test. Trace line identifies the mean of the three tests.

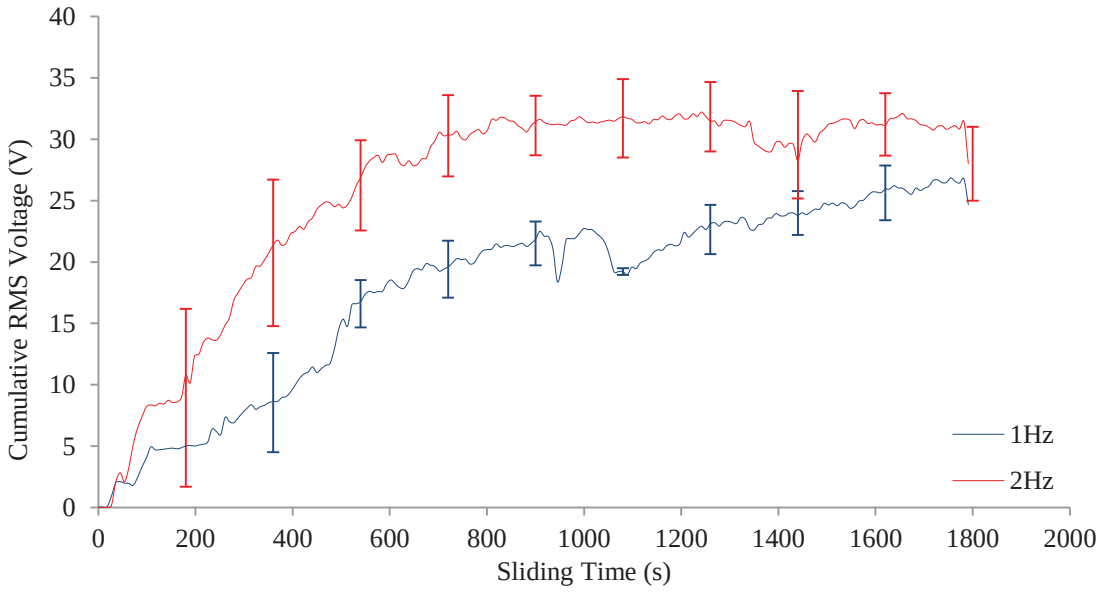

Figure 6-16: Cumulative AE RMS vs. Sliding time for a non-conformal ball (9.2mm radius) and plane contact configuration, reciprocating at frequencies of 1Hz and 2Hz under an applied load of 30N. Error bars represent 1 standard deviation across the three replicated test. Trace line identifies the mean of the three tests.

6.3.4 Comparison of Measurement Parameters

In order to quantify the acoustic emission response for the purpose of comparing to the wear scar diameter and average coefficient of friction the cumulative RMS voltage was integrated with respect to time according to;

$\int Cum.RMS\ (t)$ = Integrated RMS value

Figure 6-17 and Figure 6-18 shows the wear scar diameter as a function of the integrated cumulative RMS and average coefficient of friction respectively for each of the sliding conditions assessed.

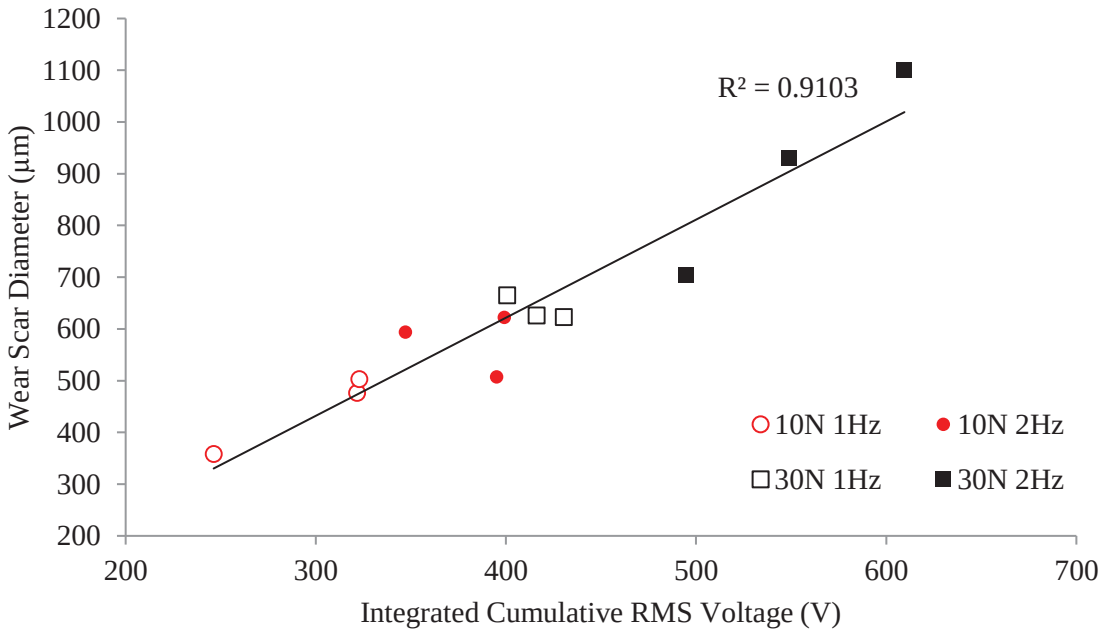

Figure 6-17: Wear Scar Diameter (WSD) vs Integrated Cumulative RMS voltage from AE signal for a ball-plane configuration subjected to a reciprocating frequency of 1Hz and 2Hz loaded at 10N and 30N under water lubrication at 25°C. Trend-line illustrates a linear correlation between WSD and Integrated RMS Voltage.

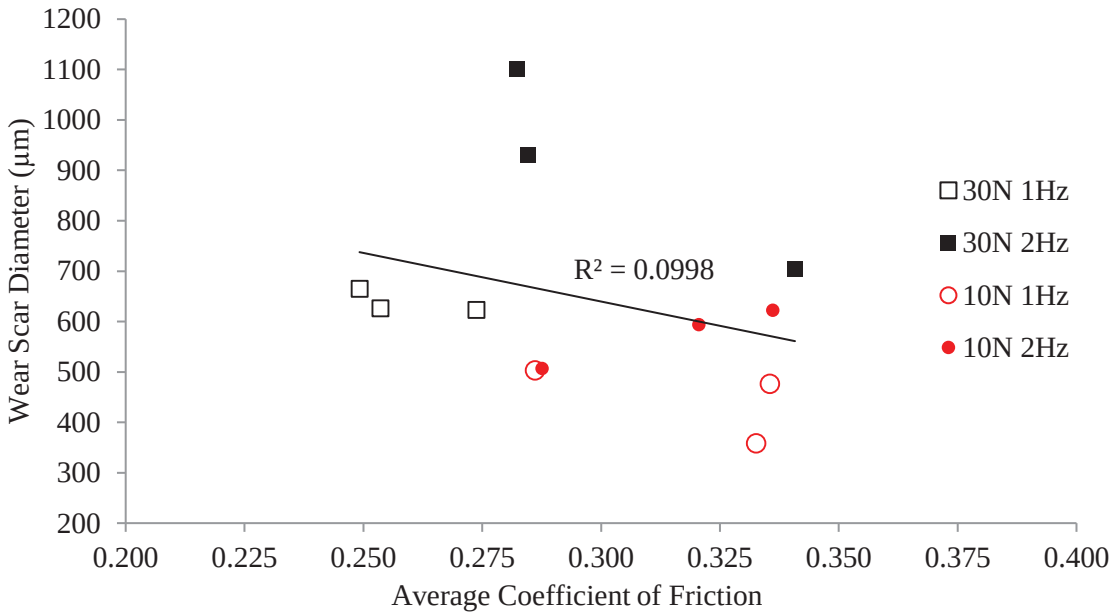

Figure 6-18: Wear Scar Diameter (WSD) vs Coefficient of Friction for a ball-plane configuration subjected to a reciprocating frequency of 1Hz and 2Hz loaded at 10N and 30N under water lubrication at 25°C. Trend-line illustrates the lack of any linear correlation between WSD and Av. COF.

The variation in wear scar diameter and integrated RMS voltage shows a linear correlation across the different sliding conditions. Furthermore, an increase in the severity of the sliding conditions corresponding to both load and sliding velocity, showing an increase in the integrated RMS voltage corresponding to increases in the wear scar diameter.

Conversely the average coefficient of friction showed a limited correlation pertaining to the wear scar diameter. This is illustrated by the trend line highlighting the disparity of the friction data. The range in which the average coefficient of friction resides for each individual test is confined between 0.25 and 0.35. With only a span 0.1 (average coefficient of friction) separating 12 data points over four different sliding conditions elucidates the difficulty in characterising tribological phenomena of polymeric surfaces based upon frictional data.

The correlation between the three parameters is shown in Table 6-1. The strength of correlation is presented by Pearson's correlation coefficient, calculated according to Equation 6-2. Where *r* is the Pearson's correlation coefficient, *n* is the sample size and *x* relate to the integrated RMS voltage and average coefficient of friction and *y* is the wear scar diameter.

$$r = \frac{n(\sum xy) - (\sum x)(\sum y)}{\sqrt{[n\sum x^2 - (\sum x)^2][n\sum y^2 - (\sum y)^2]}}$$ **Equation 6-2**

Table 6-1: Measurement parameter and correlation coefficient results

Parameter Combination	**Correlation Coefficient**
Wear Scar Diameter – Integrated RMS Voltage	0.876
Wear Scar Diameter – Average Coefficient of Friction	-0.193
Integrated RMS Voltage – Average Coefficient of Friction	-0.366

The criteria regarding the strength of fit between the data is signified by a result close to unity, where it can be seen that the wear scar diameter and integrated RMS voltage provide a high correlation value of 0.876. However, the correlation of the average coefficient of friction with respect to both the wear scar diameter and integrated cumulative RMS voltage was diminutive registering a correlation coefficient of -0.193 and -0.366 respectively.

6.4 Discussion

Recalling the source of acoustic emissions are the release of an elastic waveform emanating from a point of loading. The waveform is released due to some displacement that is attributed to the accumulation of stress until it exceeds a certain limit. Hence, the degree and the type of contact would affect the acoustic emission response. The acoustic emissions can be related to physical tribological phenomena by recalling the effect of load and speed on the frictional behaviour of polymers where at moderate loading and sliding speed conditions the force opposing friction is either due to one or a mixture of viscous and elastic behaviour. The time-dependent relationship to strain for a visco-elastic material under cyclic loading can be seen below in Figure 6-19.

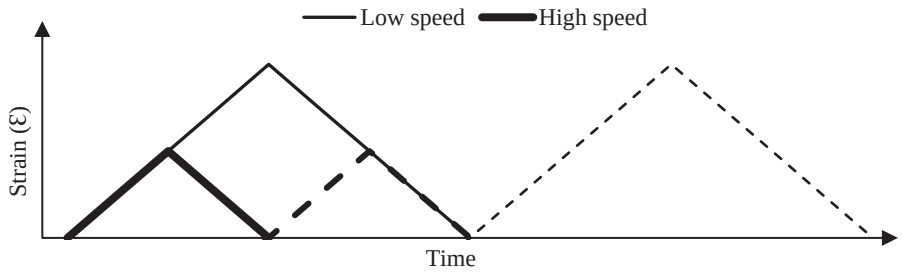

Figure 6-19: Graphical interpretation of the strain-time relationship for a visco-elastic material undergoing cyclic loading

It has been shown that the average coefficient of friction and cumulative RMS voltage are higher at the beginning of the test for studies conducted at the lower speed of 1Hz. Figure 6-19 shows that increasing the time of contact between the two surfaces increases the strain, attribute to the viscous resistance of the material. Conversely, at the higher sliding speed the time of contact reduces; due to the increase in sliding force the moving body overcomes the viscous resistance. As sliding continues the acoustic emission output for 2Hz sliding speed rises above that of 1Hz, this is attributed to the expulsion of

lubricating fluid from the contact region culminating in the rise of frictional heating. The rise in surface temperature causes an increase in the elasticity of the material. As the test continues a proliferation in the penetration depth of the upper sample ensues, increasing the viscous resistance.

A similar mechanism explains the difference when increasing the load. Augmenting the load increases the initial deflection in the direction normal to the load therefore increasing the area of contact and the volume of material resisting motion. This can be expressed by assuming Hertzian theory in the region of contact between the two opposing bodies. The displacement in the normal direction is proportional to the elastic constant$(1-2v)/G$, where two bodies of equal elastic constant the magnitude of the forces acting on either body at the contact interface is equal and opposite in direction. Therefore, the displacement replicates the shape of the opposing bodies and geometric conformity between the profiles of the contacting bodies transpires. Hence, an increase in load intensifies the stress and strain the moving body experiences, this correlates with the rise in cumulative RMS voltage between 10N and 30N.

6.5 Conclusion

The aim of the work presented was to assess the viability of employing the acoustic emission technique to monitor the tribological performance within an all polymer sliding contact.

The motives behind incorporating an additional measurement parameter was to address the diminutive effect that sliding conditions within a given load and speed has upon the resultant friction. A distinct lack of correlation between the resultant wear and the coefficient of friction was found. Furthermore, the friction coefficient showed little

variation across the sliding conditions. It has been shown that the integrated cumulative RMS voltage is proportional to the wear scar diameter and the volumetric wear, indicating that the raw acoustic emission signal can possess pertinent information regarding the level of wear and magnitude of contact between the opposing surfaces. The WSD increased when more rigorous sliding conditions were applied and a positive correlation was found between the integrated RMS voltage and the WSD.

CHAPTER 7

Evaluating the Durability of Surface Textures

7.1 Introduction

Surface textures have been shown to reduce friction through improving the wetting characteristics of a surface, facilitating a hydrodynamic effect that boosts lubrication between two surfaces. However, surface preservation is paramount to ensuring the longevity of components, particularly those incorporating textures.

In order to ascertain an understanding of how surface textures perform, in terms of their longevity, the following chapter assesses the durability of textured and un-textured surfaces when subjected to rigorous sliding conditions. For evaluating the integrity of the surfaces three forms of measurements were taken. Acoustic emissions were captured with the AE root-mean-square (RMS) of the signal acting as an in-test condition monitoring technique and the raw signal treated in post processing to assess captured signals within the time and frequency domain. Frictional data in the form of the coefficient of friction (COF) was also monitored during the test, and high-speed-data (HSD) acquisition provided friction force measurements over two individual and consecutive strokes. Evaluation of the wear was undertaken by observing the wear morphology. The data extrapolated over the three forms of measurement, for textured surfaces was then compared to that of an un-textured, control surface.

7.2 Experimental Method

Reciprocating sliding tests were undertaken on a TE-77 tribometer. Set at a stroke length of 6.5mm the upper specimen reciprocated at a frequency of 1Hz. The contact geometry was a flat-on-flat configuration with an applied load of 120N. Employing the same method as in Chapter 4 (Equation 4-1) the contact pressure was calculated to be 24.5MPa. The lubricant was Reagent grade purified water maintained at a temperature of 37°C throughout the experiments. Initial tests were conducted over a period of 1200 seconds and each test was conducted three times.

Frictional data was taken at a rate of 1/second and HSD was acquired over a 2.5 second interval at the start of each test at a data acquisition frequency of 200 kHz. Acoustic emission signals were captured using a Nano30 medium frequency miniature acoustic emission sensor from Mistras. The AE sensor was housed in a purpose made capsule and acoustically coupled to the top of the upper specimen via general purpose silicon grease. The sensor captured raw AE waveforms at a rate of 1MHz and was connected to a pre-amplifier that applied 60dB gain to the original signal. From the pre-amplifier the signal was passed to a computer where the raw signal was processed and the signal RMS was extrapolated. Waveform monitoring captured 4 seconds of raw signal data at 60second intervals. Wear assessment and surface morphology was undertaken using an Alicona Infinite focus surface measurement device.

The upper sample was produced from an extruded 8mm rod of Victrex PEEK 450G. The rod was machined to provide a contact diameter of 2.5mm and is shown in Figure 7-1. The sample was held within the specimen capsule arrangement described in Chapter 6 and secured to the specimen holder on the TE-77. The lower sample was a rectangular

section of 65x25mm, 4mm thick and was machined from a PEEK block. The surfaces were polished using Silicone Carbide (SiC) polishing paper to an average surface roughness (Ra) of 0.12µm (+/-0.02µm).

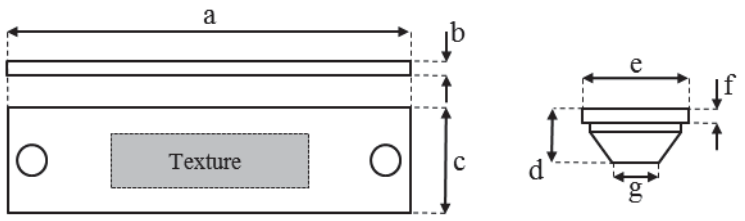

Figure 7-1: Schematic of lower specimen (flat plate, PEEK) and upper specimen (cylindrical pin, PEEK). (a) 60mm (b) 4mm (c) 25mm (d) 4mm (e) 8mm diameter (f) 1.5mm (g) 2.5mm

The textures were applied using an Yb-doped femtosecond laser. The texture parameters employed within the study were a diameter and depth of 50µm and 20µm respectively, dispersed over the surface at a density of 20%. These particular parameters were chosen in relation to the experimental findings in Chapter 3 and Chapter 4. The density of 20% was found to provide optimum frictional and wetting capabilities and was agreed upon by sourced literature and study conducted in Chapter 3. The diameter and depth parameters of 50µm diameter and 20 µm depth was found to provide enhanced friction reducing capabilities within Chapter 4, where the findings in Chapter 5 suggest the presence of hydrodynamic phenomena contribute to the reduction in friction recorded for the stipulated parameters.

7.3 Results

7.3.1 Coefficient of Friction

Figure 7-2 shows the coefficient of friction (COF) as a function of time for un-textured and textured surfaces over 1200 seconds. The error bars illustrate the highest and lowest

recorded COF trace within the three repeated tests for each surface type. The trace line represents the average COF taken across the three repeated test per surface treatment. The control (un-textured) surface shows a proliferation in friction from the start, taking approximately 240 seconds to attain a steady state. Conversely the COF for the textured surface attains a steady state considerably earlier than the control specimen. The COF at which each surface achieves a steady frictional output differs dramatically between the two surface treatments. The control surface achieves an average COF from 240 seconds to the end of the test of 0.95 with a standard deviation of +/-0.015 and the textured surface obtains an average COF from 5 seconds to the end of the test of 0.2 with a standard deviation of +/- 0.003.

It was assumed that once the COF reached 1.0 (+/-0.1) then the surface had failed. As shown in Figure 7-2 the textured surface maintains a steady COF of 0.2 until the test ends at 1200 seconds. In order to provide an indication of the longevity of the textured surface compared to the control specimen the third test, of the three test repetitions, was extended; initially for a further 1500 seconds and then another 1000 seconds. The experimental conditions remained constant throughout the extended runs and the specimens and AE sensor was not disturbed. Figure 7-3 shows the COF up to surface failure (COF = 1) for textured and un-textured surfaces plotted as a function of sliding time. The COF initially maintains a steady state output until approximately 1800 seconds where the friction steadily rises until the test was halted at 2700 seconds. On the re-initiation of the test the friction proliferates rapidly until reaching the failure criteria of a coefficient of 1 at 3100 seconds.

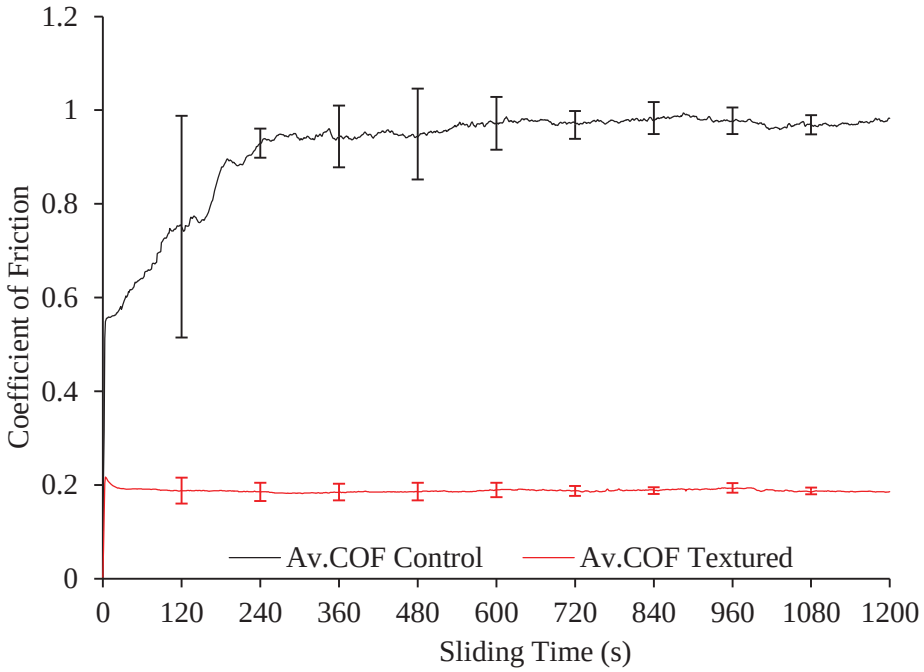

Figure 7-2: COF vs. Sliding time for water lubricated conformal contact under the following conditions; Load 120N, frequency 1Hz, stroke length 6.5mm, lubricant temperature 37°C. Tests performed with an un-textured and a textured surface of 50µm diameter and 20µm depth at a density of 20%. Error bars provide the upper and lower COF for each test at specific time intervals and the trace-line depicts the AV COF taken across the three test repetitions per surface type.

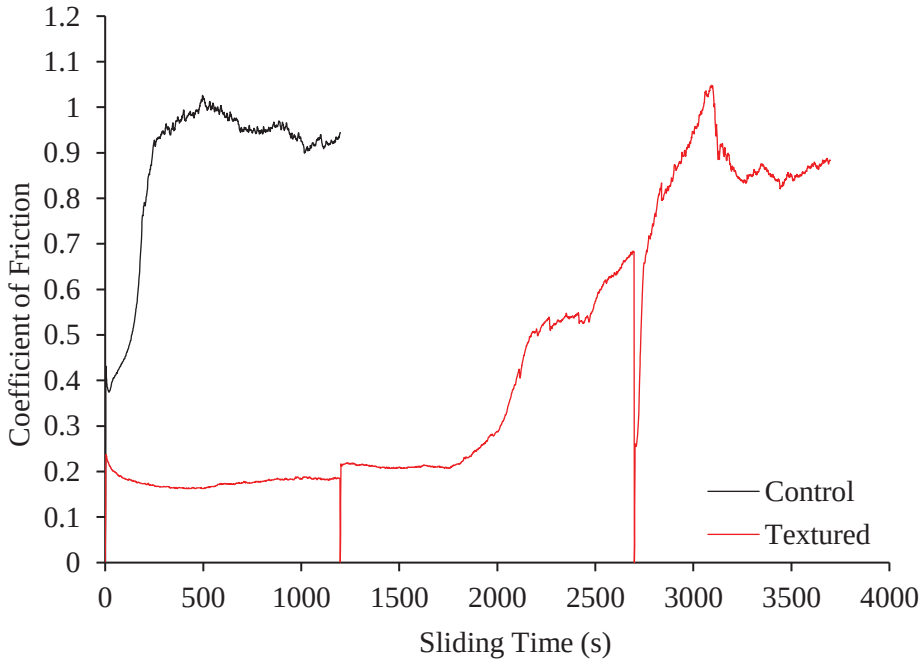

Figure 7-3: COF vs. Sliding time for water lubricated conformal contact under the following conditions; Load 120N, frequency 1Hz, stroke length 6.5mm, the lubricant temperature 37°C. Tests performed with an un-textured and a textured surface of 50µm diameter and 20µm depth at a density of 20%. Texture test was extended to failure.

7.3.2 Acoustic Emissions

It has been shown that friction reduces when textures are applied to the surface. This reduction is attributed to the presence of lubricating fluid being retained with the contact zone, reducing both the force required for sliding to initiate and during sliding. The following section compares the AE response at various intervals between the control (un-textured) and textured surfaces.

Control (un-textured) Surfaces

Figure 7-4 shows the AE signal baseline from the motor running but no load or contact between the upper and lower samples. Figure 7-5 shows the acoustic emissions captured over a 4 second period at 60 seconds into the test.

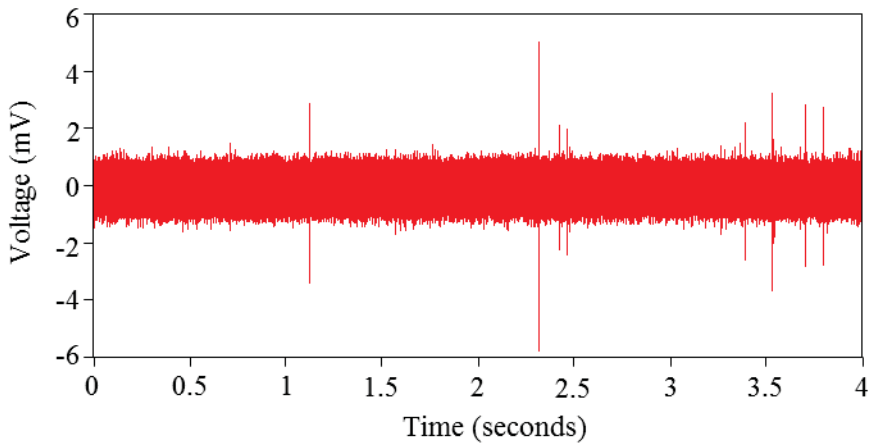

Figure 7-4: AE base-line signal

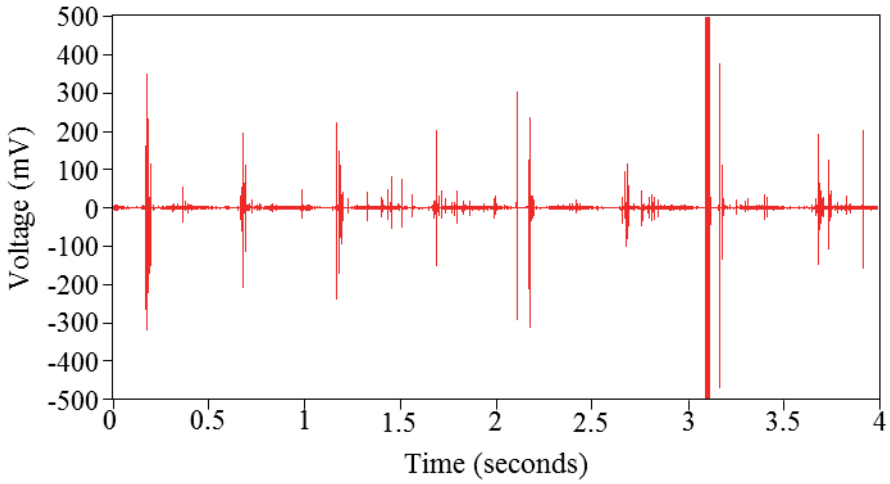

Figure 7-5: AE response of control (un-textured) surface at 60 seconds into durability test capturing a 4 second period

As can be seen in Figure 7-5 the signal displays peaks of a periodic nature. Observing the time scale in relation to the periodic peaks it can be seen that they occur relative to individual strokes. Figure 7-6 displays a 1 second window taken from between 0.65 and 1.65 seconds in Figure 7-5. The one second data encapsulates two substantial periodic peaks and contains one complete revolution of the motor, corresponding to 2 complete stroke lengths. It is assumed that the AE activity would be at a minimum at the extremities of the stroke length owing to zero velocity as the upper sample reverses direction. The end of each stroke is represented in Figure 7-6 where the sinusoidal waveform crosses zero voltage. As expressed by Myshkin *et al.* once the surfaces are brought into contact the forces of attraction act between the atoms and molecules of the opposing surfaces. Owing to Van Der Waals forces and the formation of hydrogen bonds, junctions are formed at real contact spots. The interlocking of local asperities, once velocity reaches zero, allows for an increase in the formation and growth of junctions between the opposing surfaces. The attraction forces and subsequent junction growth when motion transitions from static to kinetic on the return stroke increases friction and hence generate an increase in acoustic emission activity (Myshkin, et al., 2005). During this process

elastic energy is stored within the vicinity of the contact zone. On the application of a tangential force the velocity increases from zero, once the limiting friction force is exceeded localised interfacial shear of the surface occurs. This produces a release in elastic strain energy owing to the sudden rupture of the surface junctions exciting an AE response greater in magnitude than at any other section of the stroke length. Based on these assumptions Figure 7-6 is annotated to show the AE signal corresponding to the sinusoidal motion provided by the scotch yoke mechanism, where a yoke rotation of 180° corresponds to one stroke length. For convenience, and improved resolution, the plot is scaled to elucidate the AE activity occurring at smaller amplitudes. An identical procedure was undertaken for AE signals captured at 120, 240 and 900 seconds and are shown in Figure 7-7 to Figure 7-9.

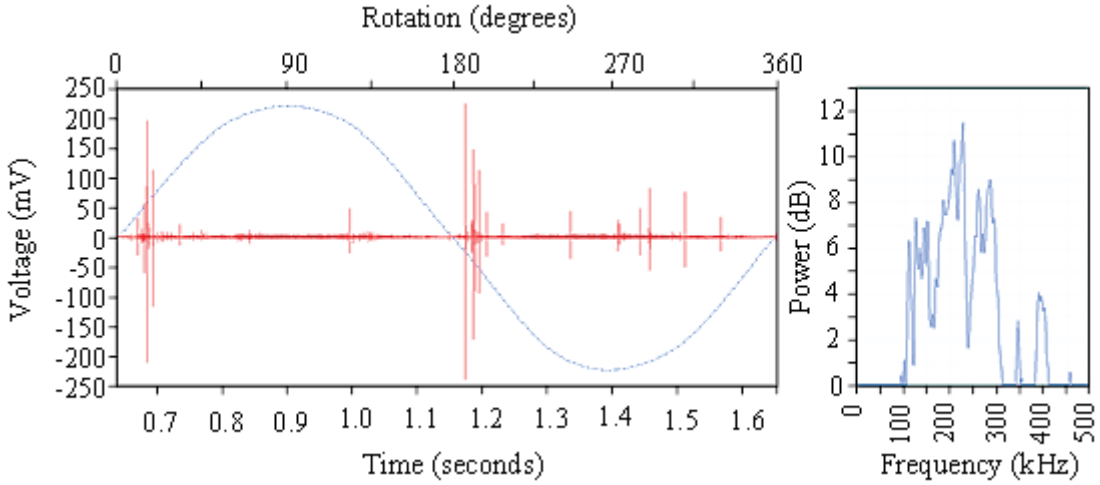

Figure 7-6: AE signal as a function of time corresponding with the angle of rotation of scotch yoke mechanism of two complete strokes (1 revolution), captured at 60 seconds into durability test. The figure emphasises the periodic nature of AE signal peaks over a 1 second interval.

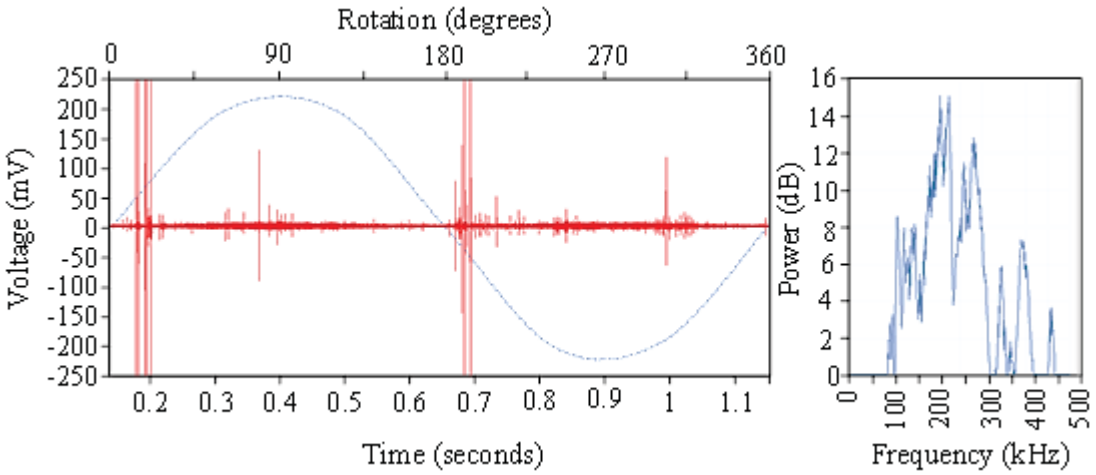

Figure 7-7: AE signal as a function of time corresponding with the angle of rotation of scotch yoke mechanism of two complete strokes (1 revolution), captured at 120 seconds into durability test. Figure Emphasises the periodic nature of AE signal peaks over a 1 second interval.

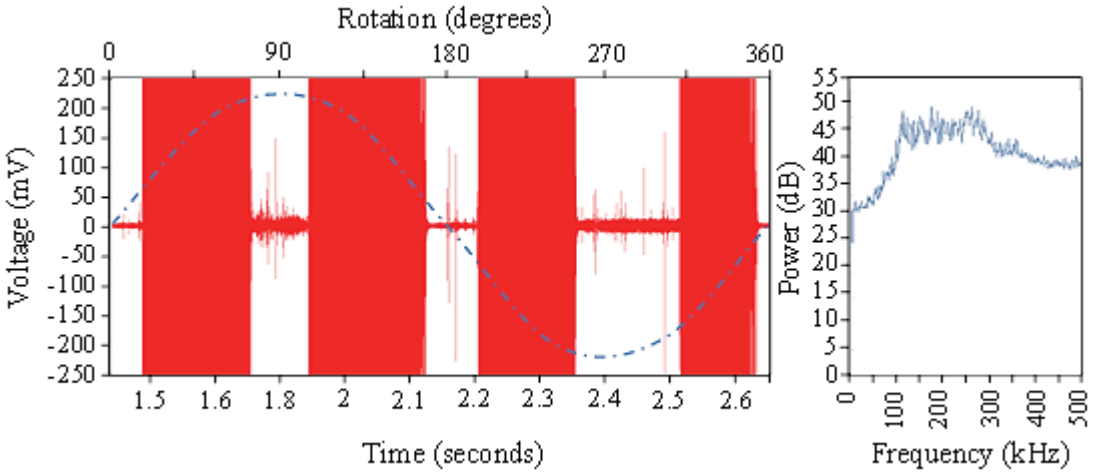

Figure 7-8: AE signal as a function of time corresponding with the angle of rotation of scotch yoke mechanism of two complete strokes (1 revolution), captured at 240 seconds into durability test. Figure Emphasises the periodic nature of AE signal peaks over a 1 second interval.

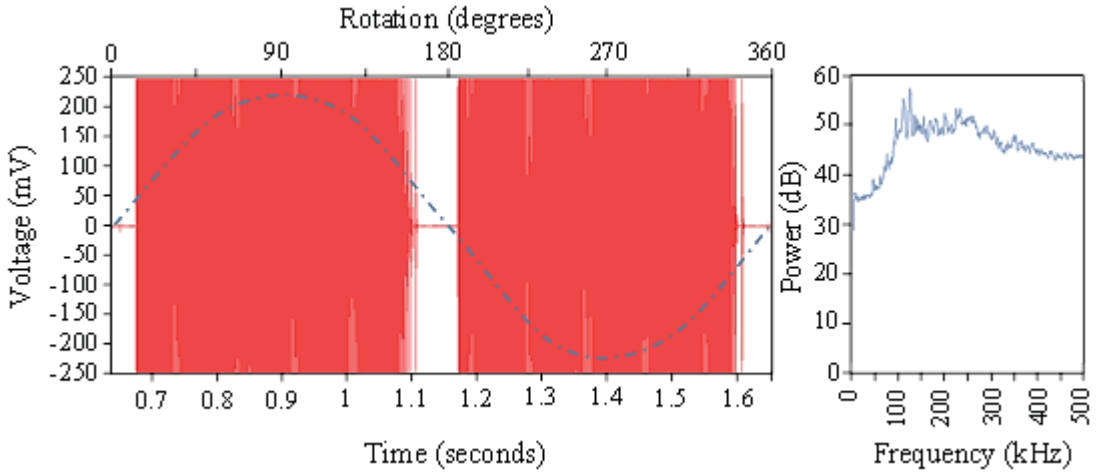

Figure 7-9: AE signal as a function of time corresponding with the angle of rotation of scotch yoke mechanism of two complete strokes (1 revolution), captured at 900 seconds into durability test. Figure Emphasises the periodic nature of AE signal peaks over a 1 second interval.

The evolution of acoustic emissions throughout the test for the control specimen shows an increase in both amplitude and frequency content, as illustrated from Figure 7-6 through to Figure 7-9.

Figure 7-6 shows how the AE response develops at 60 seconds. It can be seen that the AE signal is more substantial at the beginning of each stroke. This is attributed to the tribological mechanisms described above as motion transitions from static to kinetic, phenomena associated with the adhesive wear mechanism. The acoustic emission signal generated at 60 seconds possesses characteristic frequencies between 100Hz and 400Hz. At 120 seconds (Figure 7-7) the power increases across a similar frequency range. The increase in power across the frequency range points to a heightening of tribological activity as the sliding distance increases. It is assumed that between 60 seconds and 120

seconds the tribological processes occurring within the system are similar yet become more pronounced.

Figure 7-8 shows the AE signal and frequency content at 240 seconds taken from where the friction coefficient proliferates. Similar to the AE traces for 60 and 120 seconds the signal acquired at the onset on sliding substantial increases, moreover the frequency content increases substantially both in the power and frequency range. Furthermore, the AE signal also increases towards the end of the stroke before the velocity reaches zero and minimal AE activity is detected. The manifestation of AE content arises as the upper surface reduces velocity.

Figure 7-9 shows the AE signal acquired where the friction coefficient attains a steady state, by which point the surface had been adjudged to have failed. Comparing the power spectra between the signals captured at 240 and 900 seconds it can be seen that the frequency content increases in amplitude across the spectra.

Textured Surfaces

Figure 7-10 shows the AE content acquired at 60 seconds into the test. Comparing the AE signal and power spectra with that obtained for the control specimen at the same time interval it can be seen that the magnitude of the signal and frequency content differ. The textured AE signal displays a low voltage amplitude response; furthermore, the frequency content detected above the threshold criteria provides a low frequency response. It is envisaged that these low frequency signals are produced at the extremities of the stroke where the upper specimen ‘pulls off’ from a static position when the stroke is reversing direction. Owing to the steady frictional response throughout the initial 1200 seconds of the test Figure 7-11 to Figure 7-13 shows the AE content captured from 2400 seconds.

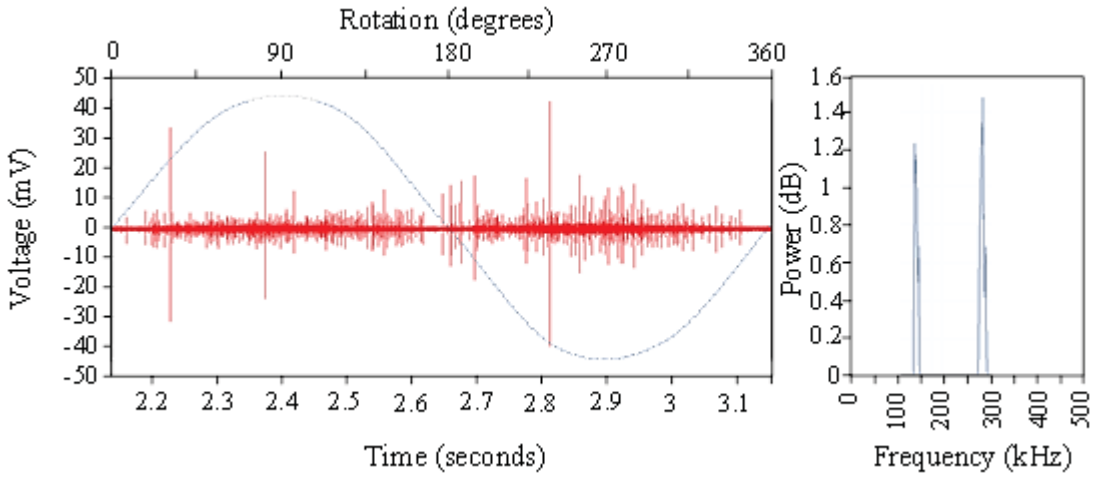

Figure 7-10: AE signal captured at 60 seconds as a function of time corresponding with the angle of rotation of scotch yoke mechanism of two complete strokes (1 revolution), captured at 60 seconds into durability test.

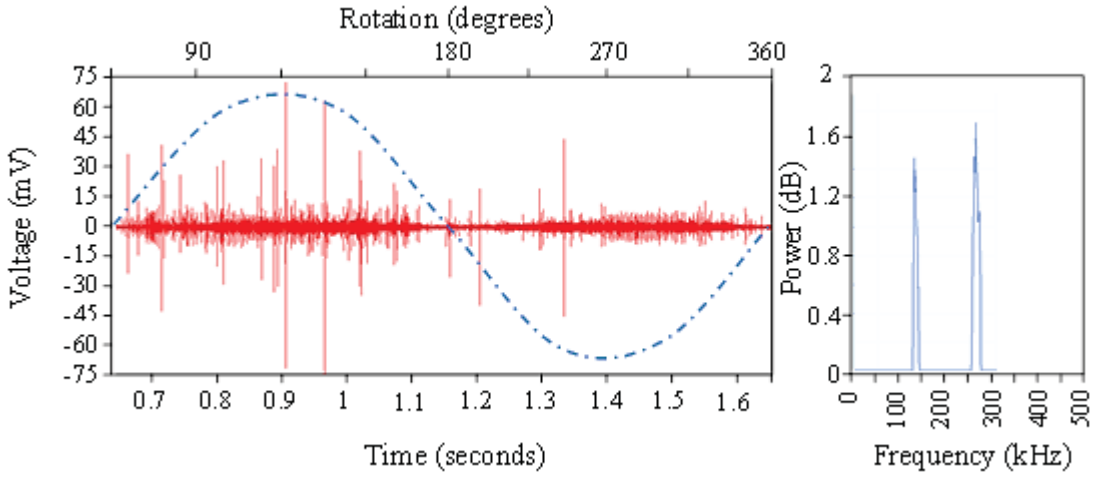

Figure 7-11: AE signal captured at 2400 seconds as a function of time corresponding with the angle of rotation of scotch yoke mechanism of two complete strokes (1 revolution), captured at 1600 seconds into durability test.

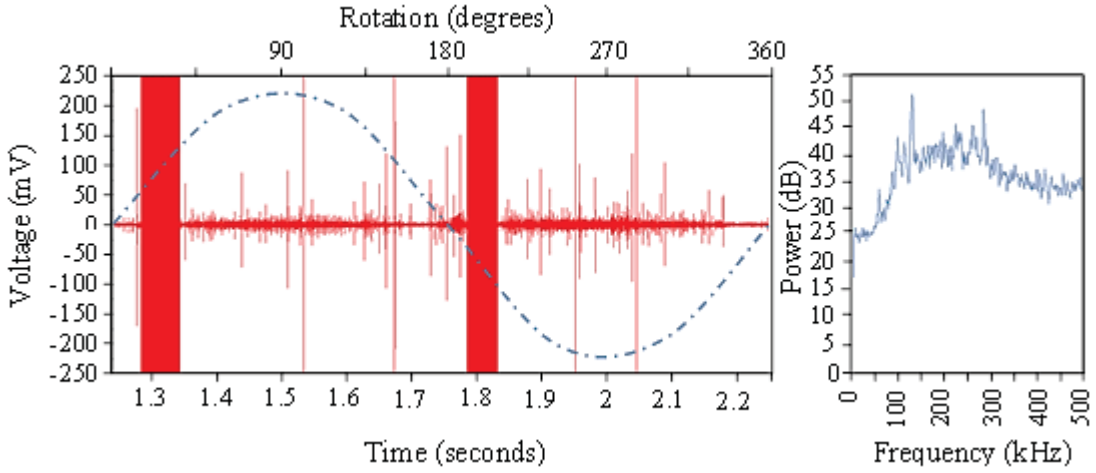

Figure 7-12: AE signal captured at 3000 seconds as a function of time corresponding with the angle of rotation of scotch yoke mechanism of two complete strokes (1 revolution), captured at 3000 seconds into durability test.

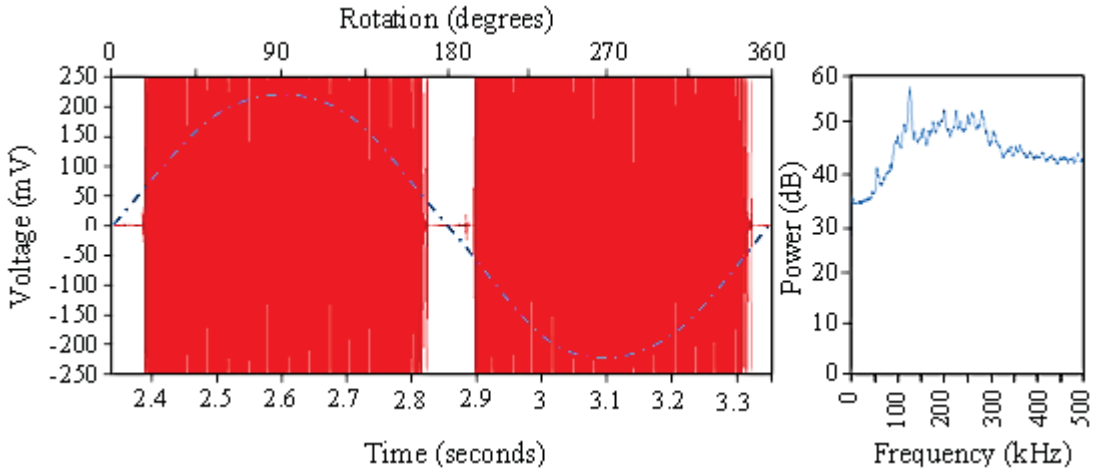

Figure 7-13: AE signal captured at 3480 seconds as a function of time corresponding with the angle of rotation of scotch yoke mechanism of two complete strokes (1 revolution), captured at 3500 seconds into durability test.

Figure 7-10 to Figure 7-11 shows that only small variations occur in the raw signal with slight increases in amplitude, however frequency slightly increases as can be seen in the power spectrum. The lack of AE activity compared to the control specimens acoustic emission response is attributed to a reduction in interfacial contact and surface wear suggesting that some form of lubrication is present partially separating the surfaces. In this sense the presence of low amplitude AE activity suggests the system is operating within the mixed lubrication regime. A notion that is also substantiated by the lower friction response of the textured surface compared to the un-textured. As the friction coefficient increases; Figure 7-12 shows the AE response at 3000 seconds. The AE signal increases in magnitude specifically at the stroke extremities as the specimen changes direction. It should be noted that for Figure 7-12 and Figure 7-13 the plots are scaled to enable a greater resolution for lower voltage responses and that the peaks attain a voltage of 500mV similar to that obtained for the control AE response. Figure 7-13 shows the AE response at 3480 seconds where the friction peaks. Similar to the AE captured for the control sample the voltage magnitude increases across the entire stroke. The frequency content for the textured surface increases across a similar range to that of the control sample. At this point both surfaces are assumed to have failed.

Quantification of AE Activity

In order to quantify the AE response relating to in-test monitoring Figure 7-14 and Figure 7-15 shows the average coefficient of friction and the average root-mean-square (RMS) of the voltage signal for the 1200 seconds test for the control and textured surfaces respectively. Both the textured and control AE RMS are averaged across a 2 second window, the error bars show the variation between the three traces to one standard deviation obtained across the three test repetitions.

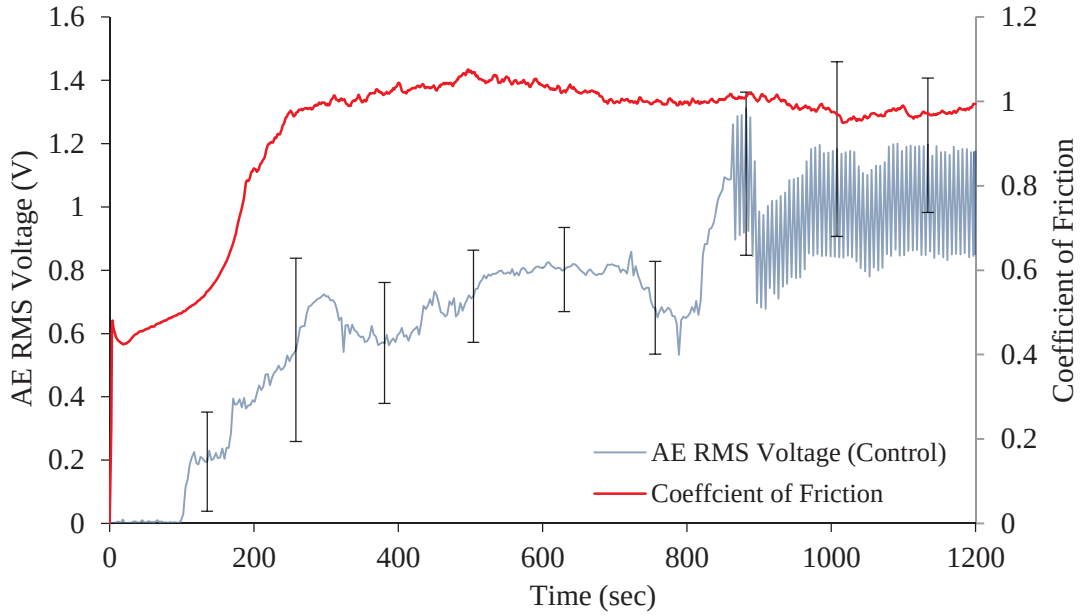

Figure 7-14: Comparison of AE RMS voltage and coefficient of friction vs time for an un-textured (control) surface. Sliding at a stroke length of 6.2mm at 1Hz under a load of 120N, lubricated with Regency grade water heated to 37°C.

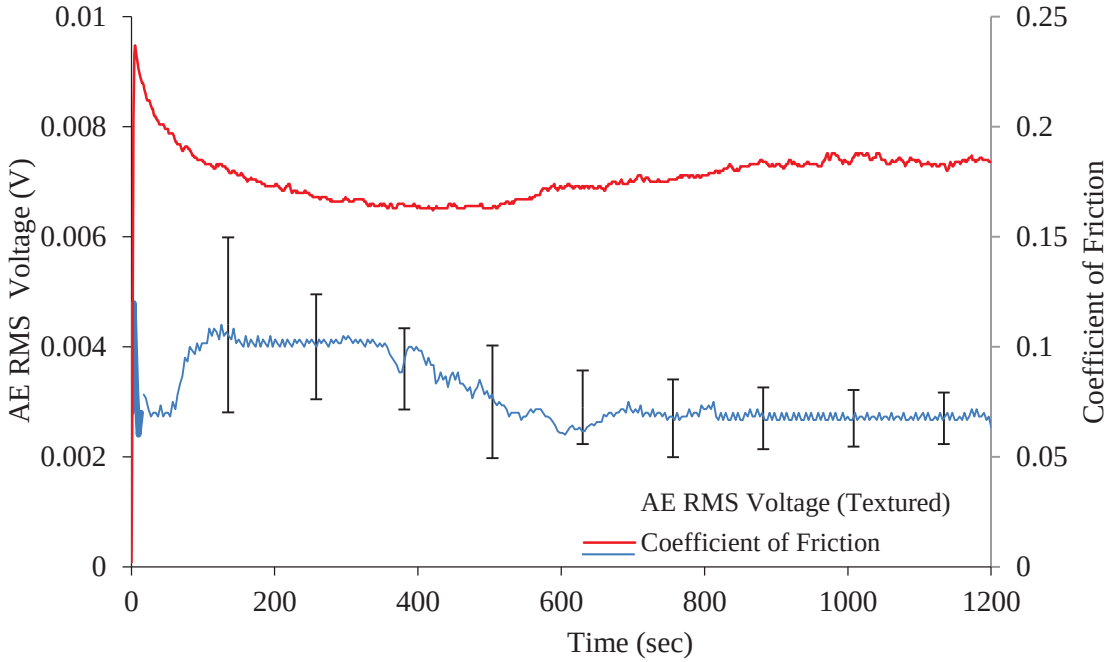

Figure 7-15: Comparison of AE RMS voltage and coefficient of friction vs time for a textured surface with diameter, depth and density parameters of 50µm, 20µm and 20% respectively. Sliding at a stroke length of 6.2mm at 1Hz under a load of 120N, lubricated with Regency grade water heated to 37°C.

The variation in the AE signal between control and textured surfaces approximately replicates that of the friction coefficient. The textured surface exhibits a low AE output with minimal fluctuation in the signal after reaching a steady state at approximately 600 seconds. The AE output for the control surface, shown in Figure 7-14, increases from when the test is initiated. After the AE RMS reduces at 720 seconds the response rises. The reduction and then increase in AE RMS is attributed to the material yielding, creating an increase in wear track depth and width. At which point large fluctuations can be observed at approximately 840 seconds as the wear particles become trapped within the wear track. Third-body abrasion followed by second-body abrasion occurs as wear particles adhere to the upper surface and continue to plough the lower surface generating further wear debris. The large fluctuations in AE RMS are attributed to this cyclic wear behaviour of third and second body abrasive wear followed by deformation before the process is repeated. It is assumed therefore that material failure is signified by a reduction then sudden increase in AE RMS. It should be noted that such large fluctuations are not observed within the friction readings that stabilise between 1.3 -1.4 coefficient of friction from approximately 250 seconds.

Figure 7-16 shows the coefficient of friction and AE RMS voltage for the final test which was extended to failure. The AE response initially increases before reaching a steady state. This is maintained until 1800 seconds where the AE response intensifies as the coefficient of friction increases. At 2200 seconds a further increase occurs until the test is halted at 2700. Once the test is re-initiated the AE RMS voltage steadily rises until 3200 seconds when the AE RMS proliferates substantially. The final 500 seconds is absent from the plot in Figure 7-16 due to the scale of the AE response peaking at 1.284 RMS voltage would render the initial 3200 unreadable.

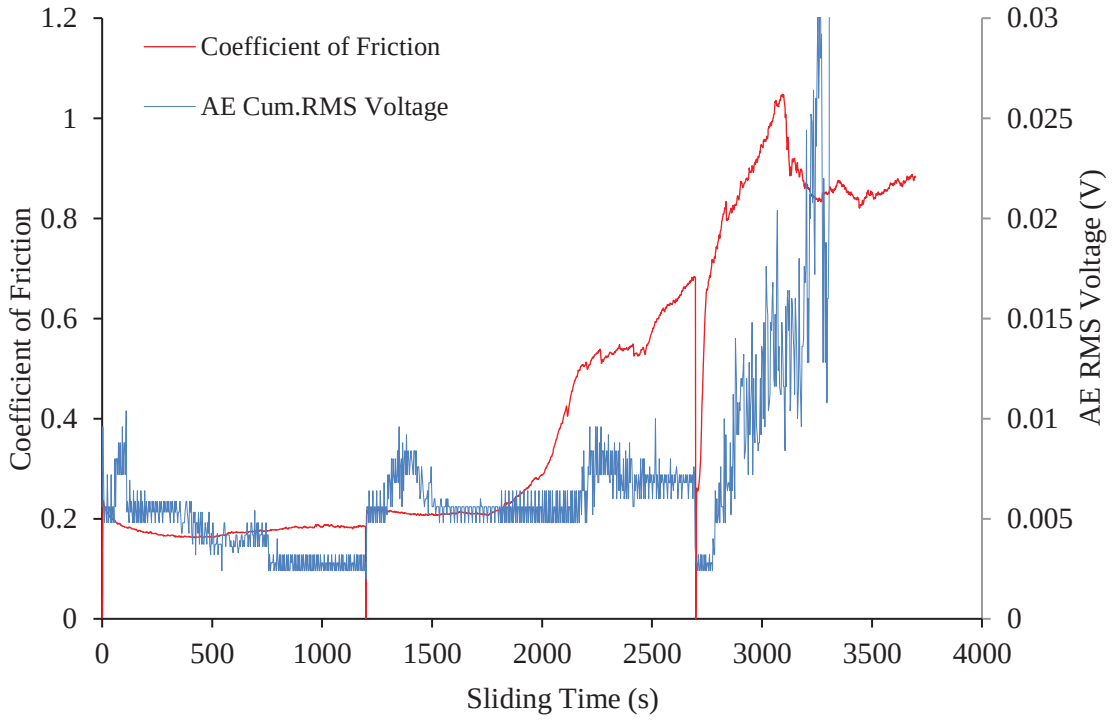

Figure 7-16: Comparison of AE RMS voltage and coefficient of friction vs time for a textured surface with diameter, depth and density parameters of 50µm, 20µm and 20% respectively when sliding time was elongated to surface failure. Sliding at a stroke length of 6.2mm at 1Hz under a load of 120N, lubricated with Regency grade water heated to 37°C.

7.4 Wear

7.4.1 Control (lower sample)

Figure 7-17a, d and c shows the wear scars from each control surface test in the form of a heat map, illustrating the depth of the scar relative to the surface. In addition, Figure 7-17d illustrates the cross sectional image of the wear track taken across the centre and along the length of the wear scar indicated by the red hashed line in Figure 7-17a, b and c. The depth for each wear track is at its deepest at the centre of the scar corresponding to the centre of the stroke. This is caused by the reciprocating motion of the upper surface subjecting the lower surface to cyclic loading. The average depth taken from the lowest point within the wear track across the three independent test runs was 73µm.

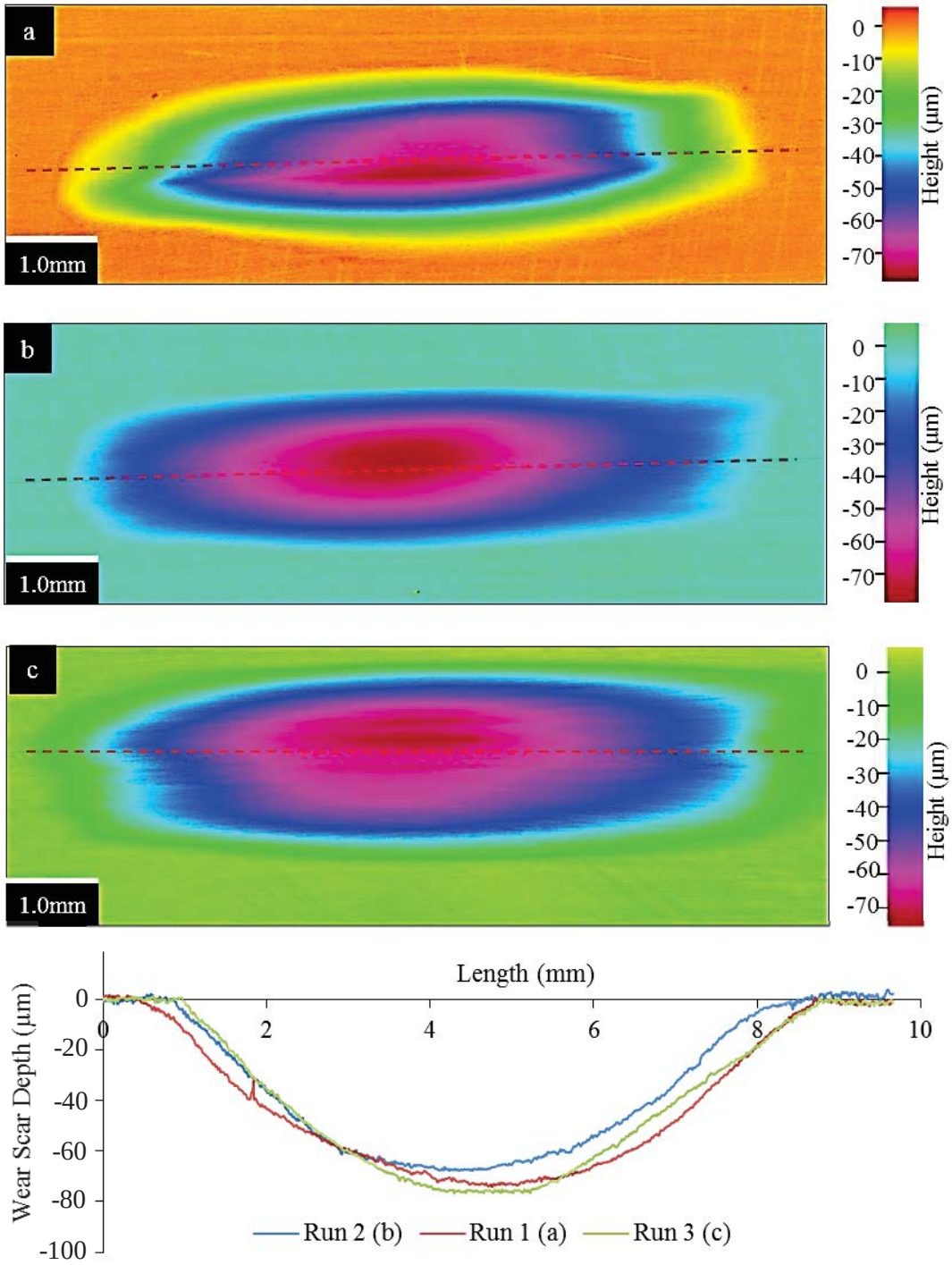

Figure 7-17: Wear scar heat map for un-textured samples after durability test. (a) Run 1, wear scar depth - 76µm. (b) Run 2, wear scar depth - 70µm. (c) Run 3, wear scar - 73µm. (d) Cross-section view of wear scars taken trough the centre of the wear scar length indicated on Figures a, b and c by the dashed red-line.

7.4.2 Textured (lower surface)

Figure 7-18 a and b shows the wear track heat map illustrating the scar depth relative to the surface from the first two tests conducted over a duration of 1200 seconds. The wear track heat map illustrates the wear trapping capabilities of the textured surface where many of the textures still remain active and yet to reached a point of saturation. The wear scar for the elongated test in Figure 7-18c shows the complete eradication of the surface textures with a substantial wear scar produced on the same scale of that seen for the control surfaces.

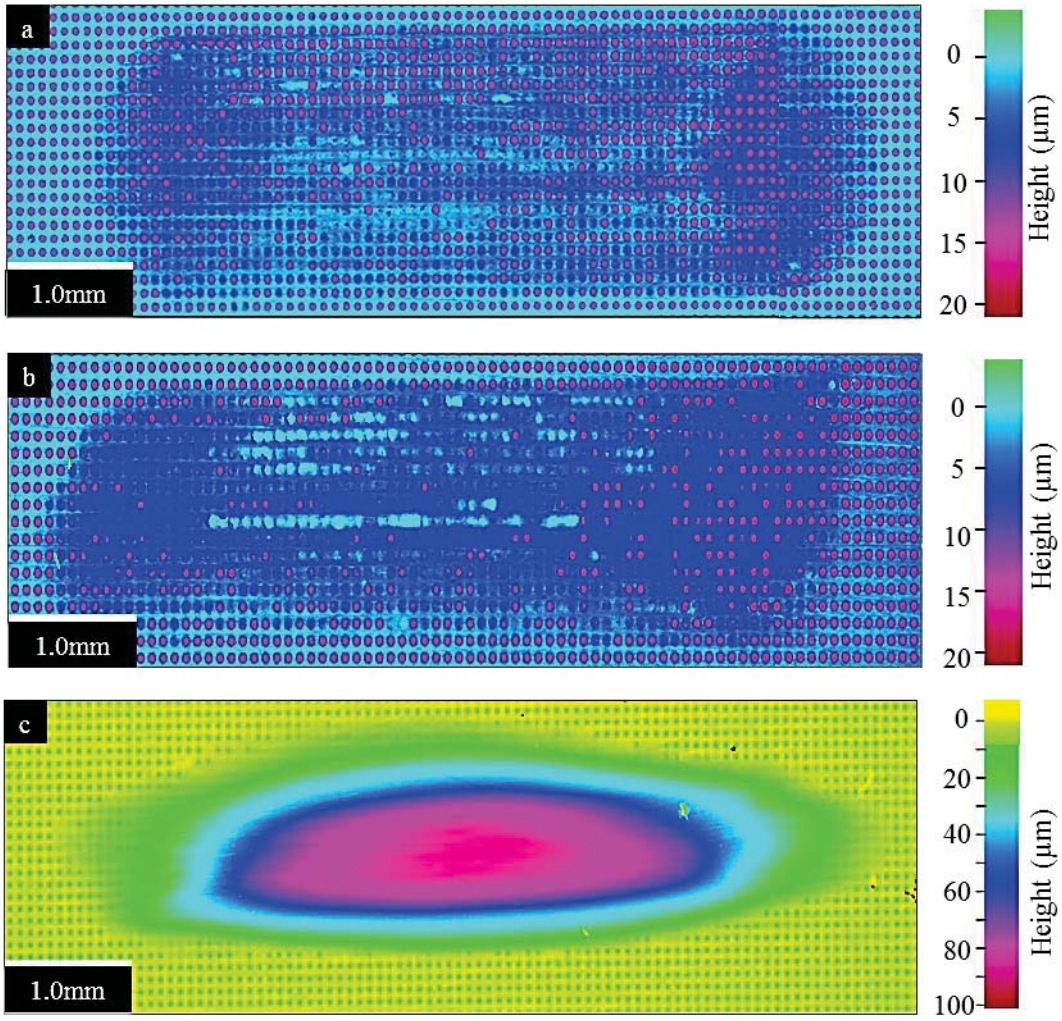

Figure 7-18: Wear scar heat map for textured samples after durability test. (a) Run 1, (b) Run 2, (c) Run 3, (extended to failure).

7.4.3 Control (upper surface)

Figure 7-19a, b and c shows the post-test surface of the upper sample. Evident is the scale of material transfer. The lack of heavy scarring on the original surface alludes to the transfer film being that of the wear debris of the lower specimen. The material transferred has an irregular form producing a non-conformal contact. Furthermore it can be observed that the material transfer is biased and more pronounced towards one side of each surface.

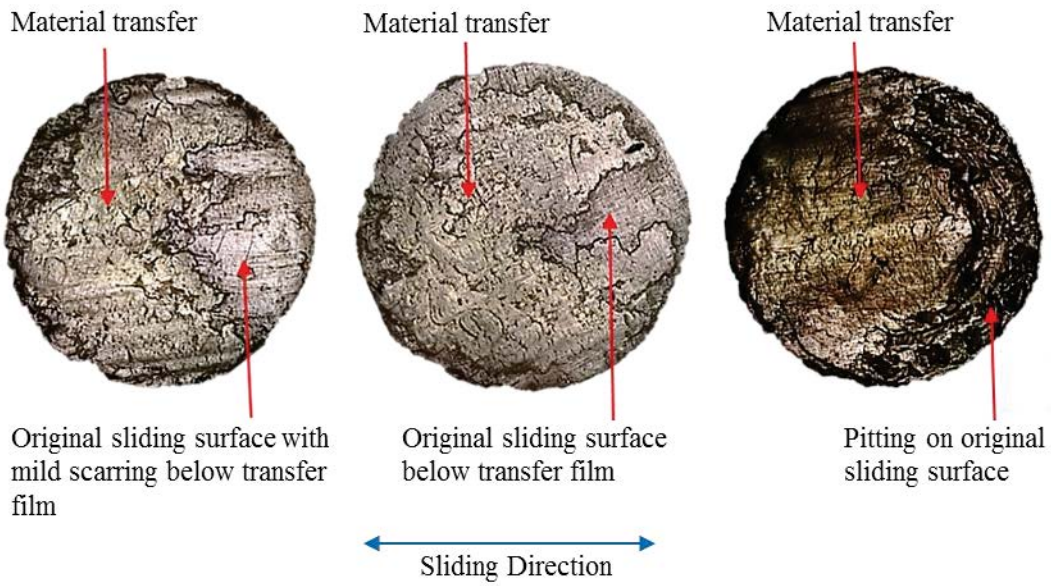

Figure 7-19: Post-test surface of upper specimens for an un-textured (control) surface. The three identical tests were conducted under the following test conditions of 1Hz reciprocating frequency subjected to a 120N load with water as the lubricating fluid at room temperature (37°C). (a) Run 1 (b) Run 2 (c) Run 3. Annotations identify features within the wear morphology.

7.4.4 Textured (upper surface)

Figure 7-20a, b and c shows the post-test surfaces of the upper samples that were sliding against a textured surface. Observed within Figure 7-20a and b is the gradual build-up of transfer film. The wear morphology shows similarities where light scratches and polishing of the surfaces can be seen by the difference in colour producing a 'shinier' complexion. The surface from the test run elongated to failure shown Figure 7-20c and is comparable to that of the surface morphology of the control test upper surfaces. Substantial material transfer is evident producing an irregular non-conformal surface. Moreover it can be seen that the surface below the transfer film shows a degree of surface scratches in the direction of sliding. Similar to that of the control test surfaces is the build-up of the transfer film being biased towards one side of the surface.

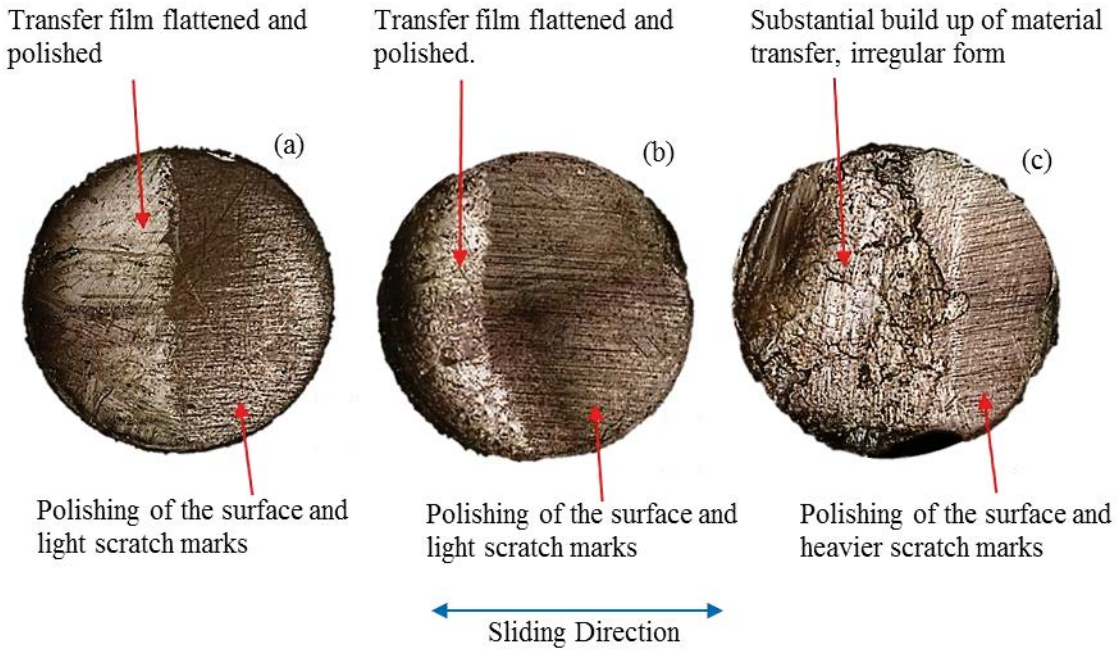

Figure 7-20: Post-test surface of upper specimens for the textured surface durability tests. The three identical tests were conducted under the following test conditions of 1Hz reciprocating frequency subjected to a 120N load with water as the lubricating fluid at room temperature (37°C). (a) Run 1 (b) Run 2 (c) Run 3. Annotations identify features within the wear morphology.

The wear morphology of both the control and textured surfaces shows a tendency for material build biased to one side. This is attributed to the difference in applied force during the ‘pull’ and ‘push’ strokes of the reciprocating motion. Figure 7-21 illustrates the force components occurring during each motion. It is important to note that this occurrence is due to the horizontal force being applied towards the top of the upper specimen which produces an additional downward force component driving the upper specimen into the lower surface during the ‘push’ stroke. Conversely, the ‘pull’ stroke has a force component in the opposite direction resulting in less force being applied to the lower surface during sliding compared to the ‘push’ stroke.

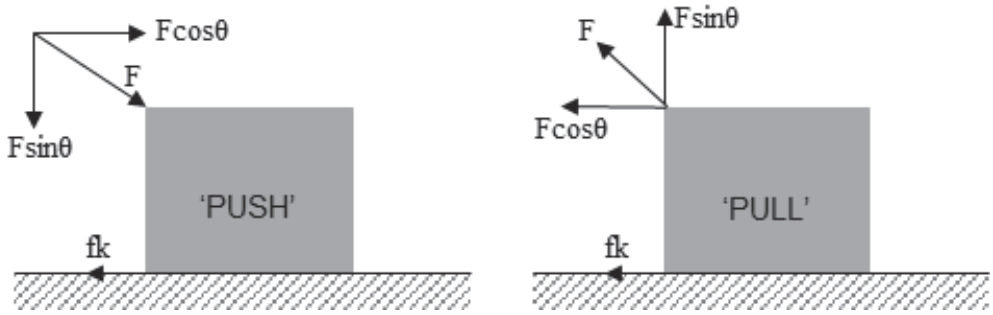

Figure 7-21: Force components of a 'push' and 'pull' stroke and the resultant force (F), fk denotes the kinetic friction force.

The result of which is that the leading edge moves material towards the extremity of the wear track during the ‘push’ stroke. This can be observed in Figure 7-18a and b where more textures are filled on the left side (extreme of the push stroke) than the right hand side (extreme of the pull stroke). Once the textures have been saturated, the wear particles reside on the surface, at which point the transfer of material occurs at the leading edge of the upper sample at the extremities of the push stroke.

7.5 Discussion

The textured surface exhibited a high degree of durability compared to the control surface. Sliding time increased substantial where the textured surface lasted approximately 3 times longer than that of the control surface before reaching the failure criteria. The longevity of the textured surface is attributed to the improved wetting capabilities and lubricant retention of the textured pores in addition to the wear trapping capabilities of the textured surface. However the poor wetting capabilities of un-textured surfaces repels the fluid, in doing so, once the upper surface slides against the lower surface the fluid is pushed and removed from the contact area. This creates a boundary lubrication regime, leading to asperity contact, higher flash temperatures and increasing both friction and wear.

The lubrication mechanism of the textured surface is assumed to be a mixture of hydro-static/hydro-dynamic. Considering two opposing surfaces separated some distance *x*, with the region between the two bodies filled by an incompressible as shown in Figure 7-22. When a substantial load (*L*) is applied the surface compresses. However, the fluid contained within the textured pore is trapped and exerts an opposing force through the static pressure generated to counter the load. Figure 7-23a shows that due to no motion at this point, the pressure generated is hydro-static which supports the load. Once a tangential force (*F*) is applied as in Figure 7-23b, relative motion commences between the two surfaces and the pressure generated shifts to the leading edge of the pore. Fluid is expelled to the surface and the pressure generated is hydro-dynamic.

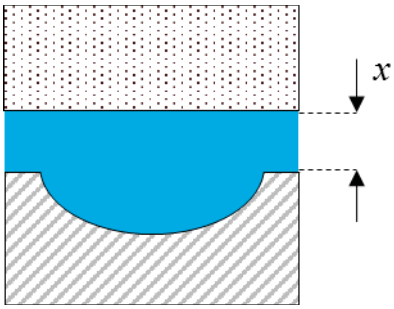

Figure 7-22: Diagram showing two surfaces, the upper plane surface and lower surface with a textured pore separated by distance x with the area between the two surfaces filled by an incompressible fluid.

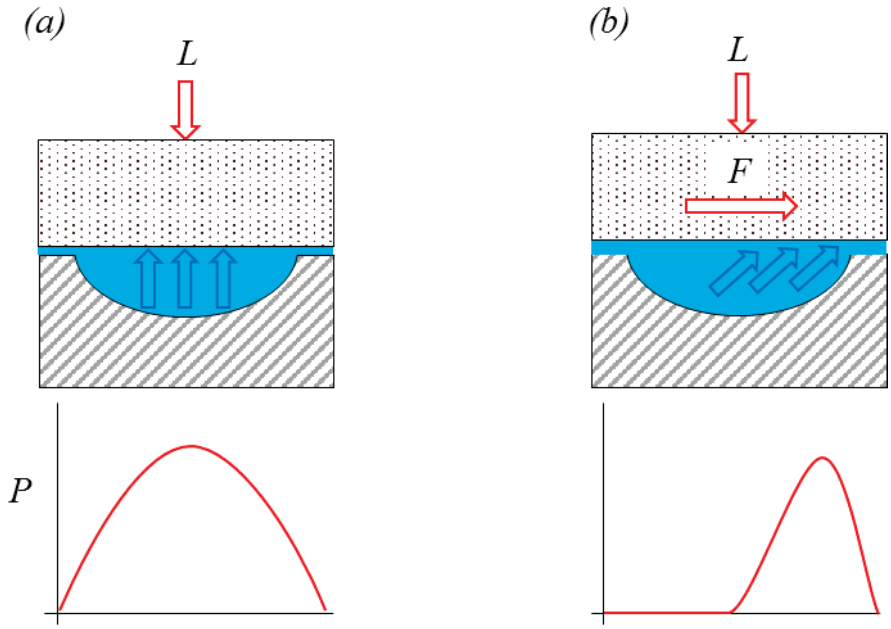

Figure 7-23: (a) shows the generation of hydro-static pressure as a load (L) is applied trapping the incompressible fluid within the textured pore increasing the fluid pressure and supporting the applied load. (b) Shows the generation of hydro-dynamic pressure as a force (F) is applied the fluid is expelled to the surface creating a shift in pressure towards the leading edge of the textured pore.

The process described reduces the COF at the extremities of the stroke length as the specimen reverses direction and the velocity increases from zero, as well as during the stroke. The effect of which is observed more pertinently in Figure 7-24 that shows the friction force over two consecutive strokes taken from one of the test repetitions for the textured and control surfaces. Observed is the reduction of friction force for the textured

surface during both the stroke and at the extremities of the stroke where the sliding direction reverses and the friction transitions from static to kinetic.

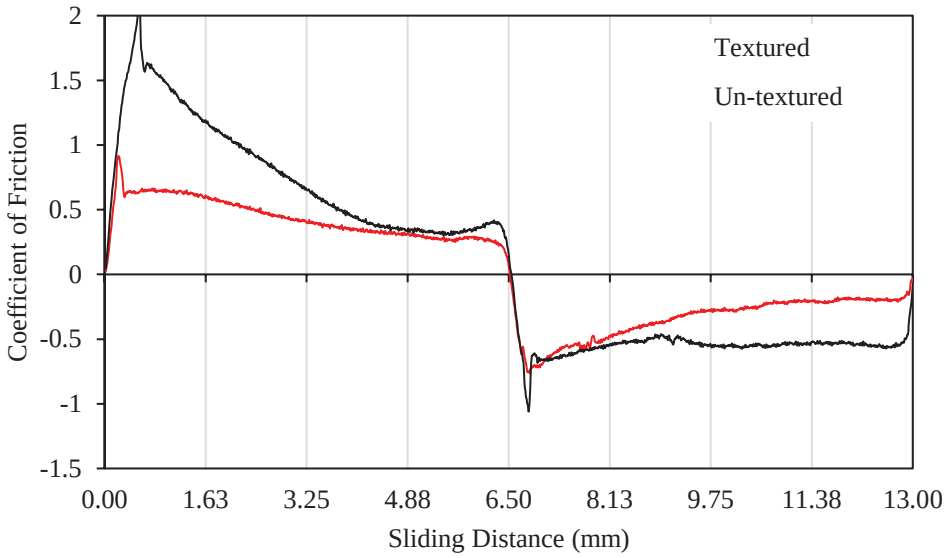

Figure 7-24: HSD friction force vs Sliding distance for an un-textured (control) and textured surface. High speed data was acquired at Hz and the plot shows 1 second of data encapsulating one complete revolution and 2 consecutive strokes.

Similar findings can be observed within the acoustic emission signals captured for both the textured and control surfaces. For convenience the signals captured at 60 seconds are presented again in Figure 7-25a and b. The AE response for the control surfaces shows evident peaks where the stroke reverses direction and friction transitions from static to kinetic. The textured surface however, shows diminutive activity at the stroke extremities compared to those captured for the control sample.

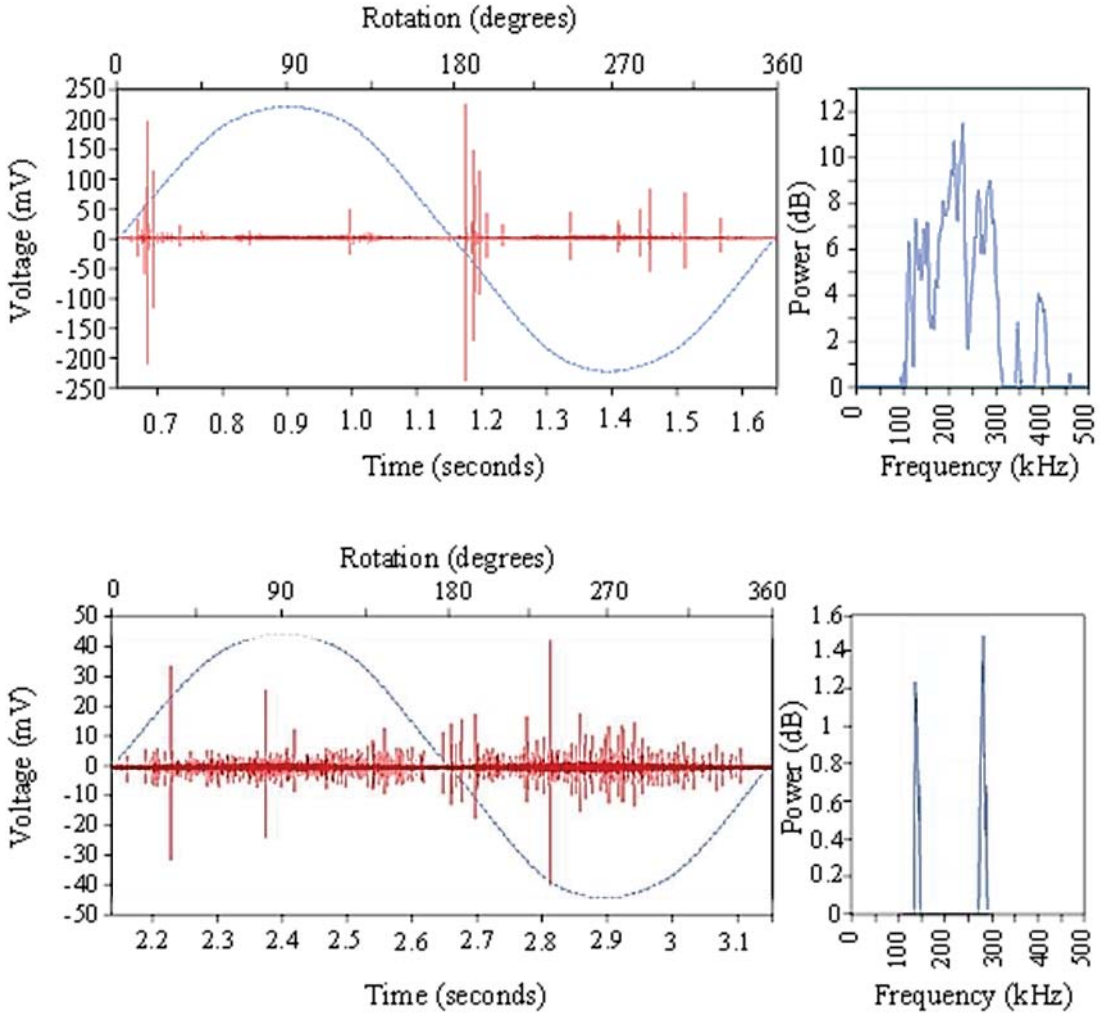

Figure 7-25: Acoustic emission signals captured at 60 seconds into durability for (a) control (un-textured) and (b) textured.

In order to investigate the variation in friction force between the control and textured surface at the beginning of each stroke, a separate experimental study was established. The aim was to develop an understanding and comparison of the frictional behaviour occurring within the transition from static to kinetic friction. The same experimental layout and conditions were employed, with the exception of the reciprocating frequency. In order to capture and ascertain a greater understanding of the transition from static to kinetic friction the reciprocating frequency was reduced to 0.05Hz and the stroke length was 5mm. High speed data was acquired at a frequency of 224Hz, capturing 6 seconds of

frictional data. The raw signal was treated with a Savitzky Golay data smoothing filter. The basis for employing the method was to preserve distribution features of the raw data but remove the noise. The Savitzky–Golay smoothing filter executes a local polynomial regression of the n^{th} degree on a series of values within a fixed width moving window of samples from the raw data. This convolution process was applied to consecutive parts until the entire data had been smoothed (Hargittai, 2006).

Figure 7-26 shows how the sliding distances within the stroke and how the friction evolves from static to kinetic friction for the control and textured specimens respectively.

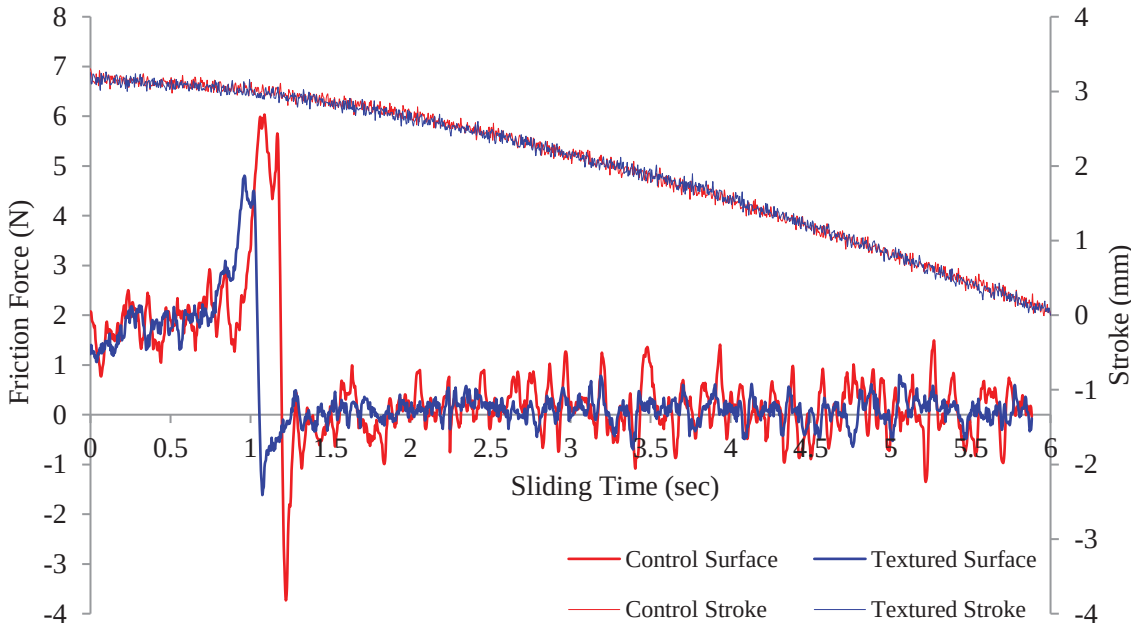

Figure 7-26: Friction force vs sliding time for a control (un-textured) and textured surface. Raw frictional data was captured at 224Hz over 1 second. Raw data was treated by a Savitzky–Golay smoothing filter to a window length of 9 data points.

Figure 7-26 illustrates the difference in friction force between textured and un-textured surfaces. The un-textured (control) case displays a higher limiting friction point when transitioning from static to kinetic friction. Moreover, the time it takes for the upper sample to overcome the static frictional force is more than that of the textured surface.

Once sliding commences the textured surface exhibits small variations in friction force providing a smoother running condition. Conversely, the control surface displays larger variations in friction force during sliding. The fluctuations in friction are attributed to stick-slip phenomena. Stick-slip motion between two opposing surfaces is a friction induced oscillation which is a result of the interaction of an elastic system (Zhang, 2006). The phenomenon occurs when the static friction exceeds that of the kinetic friction force, a description of both frictional forces is provided in Chapter 1.3.1. The condition predominantly occurs within a low speed system containing a relatively soft material for one or both of the sliding surfaces (Zhang, 2006).

In this sense the smoother sliding condition exhibited by the textured surface is attributed to the presence of a lubricating media, easing both the pull-off, from a static position and during sliding. The reduction in contact area between the upper and textured lower samples owing to the surface may play a minor role in friction reduction, however it is envisaged that solid contact under a load, W, between the upper and lower surface, as shown in Figure 7-27, would lead to the upper surface impinging on the textures. Once a tangential force is applied, $F_{T,}$ the force required to initiate sliding from a static position would increase. The impingement of the upper surface on the textures would also occur once sliding commences, increasing the kinetic friction force, F_k.

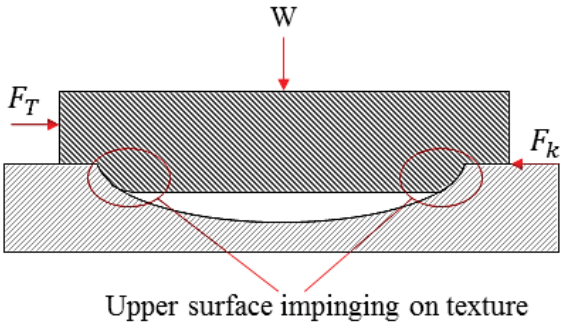

Figure 7-27: Surface of upper specimen impinging on the textures in the absence of a lubricating fluid. Once a tangential force, F_T is applied the force required to initiate sliding increases culminating in a rise of friction force F_k,

In order to ascertain a comprehensive understanding of the frictional content short time fast Fourier transform (STFFT) was performed on the friction signal to elucidate the variations in frequency in relation to time for the control and textured specimens. The friction signal was partitioned into 21 equally spaced windows of 0.281 seconds. Fast Fourier Transforms was then undertaken on each partitioned section. The frequency band analysed was between 0 and 110Hz according to Nyquist's theorem, where the maximum frequency that can be determined is given by Equation 7-1, where T_{int} is the time interval of 0.004457.

$$Frequency\ Band = \frac{1}{2 * T_{int}} \qquad \text{Equation 7-1}$$

Figure 7-28 and Figure 7-29 shows the friction signal as a function of frequency and time. Observed in both cases is the low frequency high amplitude response of both surfaces at the beginning of the test, as the friction transitions from static to kinetic, the control surface registers a higher magnitude response compared to that of the textured surface. In this instance, as the tangential load is applied potential energy is stored and increases as the force continues to rise. Once the limiting friction force is reached gross slip of the surfaces transpires and sliding commences. The point at which gross slip occurs produces

the highest peak observed in Figure 7-28 and Figure 7-29 and is comparable to the friction traces in Figure 7-26 with respect to time. It can be deduced, therefore, that the low frequency content exhibited is related to increases in static friction force, whereby the surfaces effectively stick; absorbing potential energy until the force increases to a point where slip of the surfaces ensues. Analysing the plots after gross slip has occurred it can be seen that the frequency content for the control surface remains low; eluding to the notion that stick-slip is evident during sliding. The frequency content after gross slip differs between the control and textured surfaces, where the textured surface exhibits higher frequencies once normal sliding has been initiated. The lower frequency content of the control specimen is in the same range of that observed during the initial transition from static to kinetic motion. It can be therefore deduced that the periodic fluctuations in friction force observed in Figure 7-26 are attributed to abrupt stick-slip behaviour and is symbolised by the low frequency frictional response shown in Figure 7-28. The smoother frictional output in terms of the textured sample coincides with a high frequency response one sliding occurs. This attributed to by an uncompressible fluid being trapped within the texture cavities creating a hydrostatic effect which partially supports the applied load and reduces stick-slip phenomena.

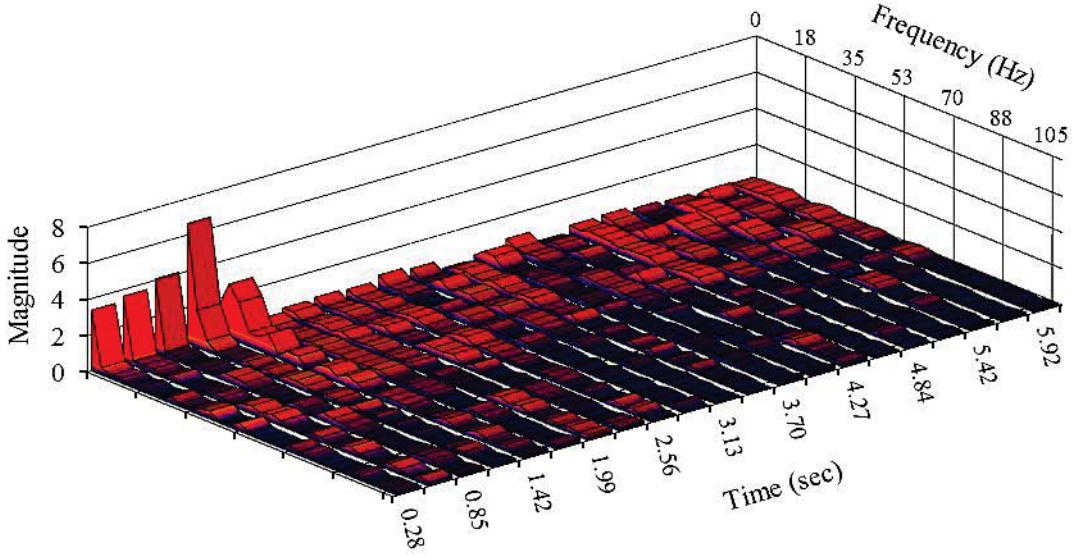

Figure 7-28: Short-time-Fourier-Transform of friction signal obtained from an all PEEK sliding couple under a load of 120N sliding at a frequency of 0.05Hz, lubricated by water at room temperature. Displaying the magnitude of friction force as a function of time and frequency for a control (un-textured) surface. The friction signal was partitioned into 21 equally portions of 0.281 seconds and the frequency band analysed was 0-110 in adhering to Nyquist's theorem.

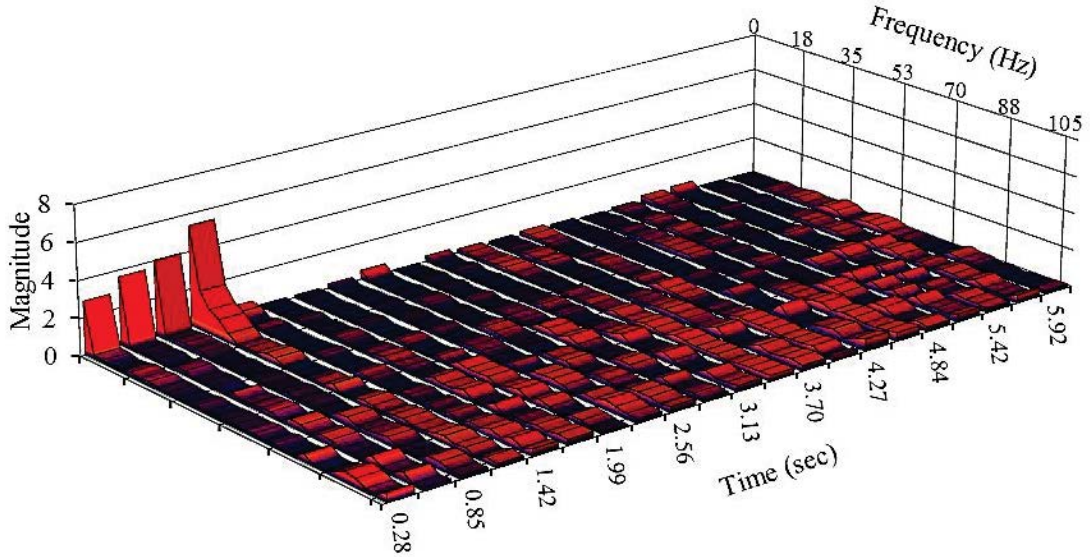

Figure 7-29: Short-time-Fourier-Transform of friction signal obtained from an all PEEK sliding couple under a load of 120N sliding at a frequency of 0.05Hz, lubricated by water at room temperature. Displaying the magnitude of friction force as a function of time and frequency for a textured surface. The friction signal was partitioned into 21 equally portions of 0.281 seconds and the frequency band analysed was 0-110 in adhering to Nyquist's theorem.

The previous section describes the friction reducing mechanisms during ‘pull off’ from a static position. Once plain sliding occurs during the primary durability tests similar hydrostatic mechanisms are believed to be active, initiated by the compression of the surface upon which reside textured cavities filled with an incompressible fluid. The presence of surface textures, however, provides additional friction reducing benefits. As explained the textures contribute to the reduced friction and wear through the secondary supply of lubrication whilst also reducing the frictional heat compared to the control sample. As the sliding time increases the friction for the control surface increases until failure, however the textured surface exhibits a lower steady state frictional output. The AE captured at 120 seconds for the control surface depicts large spikes at the extremities of the stroke. This burst type AE signal is attributed to the adhesive wear mechanism whereby the peak of the AE signal represents the sudden release of energy as gross slip commences, similar to that shown within the stick-slip experimental study. Increases in AE content at the stroke extremities is attributed to wear debris being developed and pushed to the stroke extremities.

The manifestation of AE content as the upper surface reduces in velocity is attributed to wear particles being trapped between the surfaces. It is assumed that an element of lubrication is present during the stroke and this serves to aid in the removal of wear debris as not to inflict damage to the surface. However, as the velocity reduces at the stroke extremities the surfaces come more into contact, expelling the fluid from the contact zone and hence losing the capability to effectively remove wear debris. The wear debris entrapped between the surfaces causes 3rd body abrasive wear. Owing to the lack of lubrication and increase in surface temperature wear particles adhere to the upper specimen leading to the formation of transfer film as shown by the wear morphology in

Figure 7-19a, b and c. Second body abrasion causes an increase in wear through the deformation of the surface, intensifying the AE response. As the velocity reduces to zero and reverses in direction the transfer film flattens and the system undergoes the same process until the lubricant is fully expelled from the contact zone, encouraging further damage to the surfaces. The expulsion of lubricant from the contact zone leads to an increase in frictional heat, essentially weakening the material. The transfer film then becomes the dominant surface, whereby flattening of the transferred material does not occur and becomes non-uniform is its structure. This causes mass ploughing of the weakened lower surface. The loss in the wear removal capabilities of the system encourages the formation of transfer film further increasing abrasive wear generating a proliferation in AE activity. With no friction or wear reducing mechanisms the processes described for the control surface culminates in material failure.

As described the removal of lubricant not only increases the asperity contact but also reduces the system's ability to remove wear debris and expel frictional heat. The insulating property of many polymers, including PEEK, severely hinders any heat transfer mechanisms via conduction as heat generated is contained locally to the source. The rise in surface temperature weakens the surface altering the mechanical properties of the material. Under such circumstances the centre of the wear track that undergoes cyclic loading is the area most prone to increases in frictional heat as shown in the wear morphology in Figure 7-17a, b and c for the control and Figure 7-18c for the textured surface. The excitation of the surface on a molecular level, caused by a proliferation in heat consequentially allows the upper specimen to more readily penetrate the lower surface and plough through the bulk material of the lower specimen.

The lack of AE activity for the textured surface compared to the control specimens is attributed to a reduction in abrasive wear. The lubricating fluid is assumed to be provided by a secondary source from within the texture cavities, reducing the friction coefficient whilst also acting as a means to reduce frictional heat and expel wear particles that are not captured within the textures.

The wear track heat map, shown in Figure 7-18a and b, illustrates the wear trapping capabilities of the textured surface that contributes to the low friction and wear. Shown is the build-up of wear debris upon the surface and within the textures where the cavities appear to have been filled in. Figure 7-30 and Figure 7-31 further demonstrates the wear capturing capabilities where the image is taken from the centre of the wear track. Figure 7-30 shows the textures filled with wear particles and Figure 7-31 is the heat map corresponding to Figure 7-30.

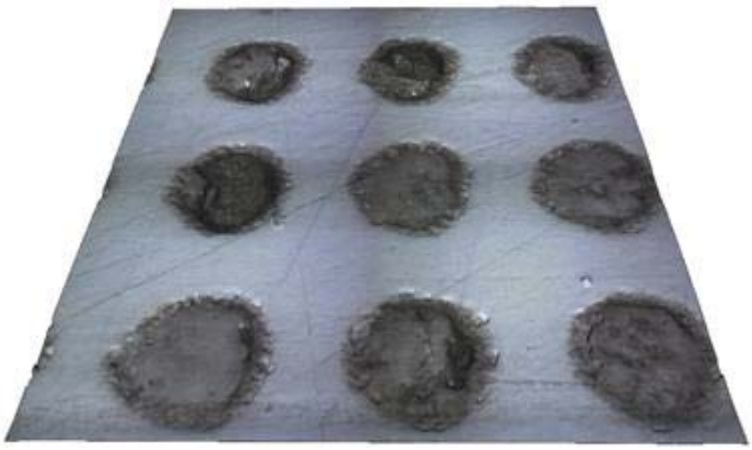

Figure 7-30: Surface textures after 1200 seconds durability test. Image shows textured cavities filled in by wear debris taken from the centre of the wear shown in Figure 7-18a.

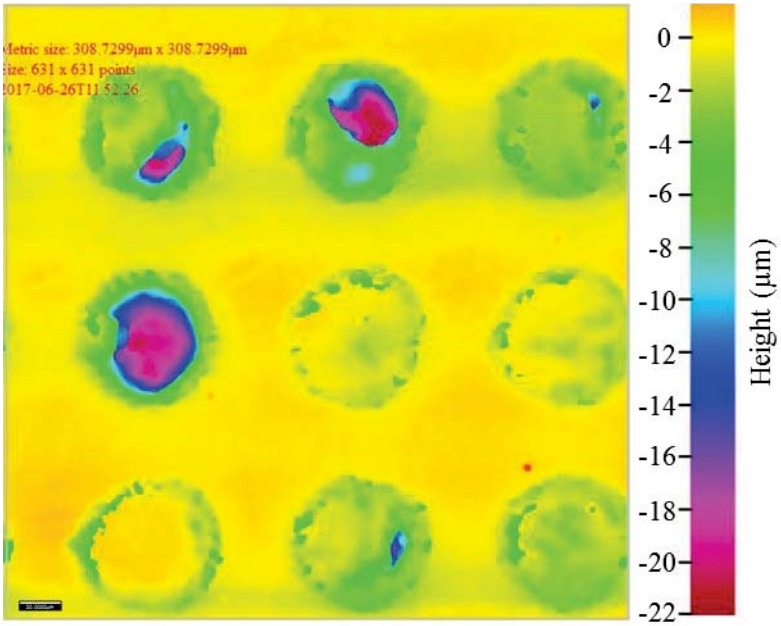

Figure 7-31: Heat map of surface textures shown in Figure 7-30 after 1200 seconds durability test. Image shows the depth of each texture relative to the surface, corresponding to the colour bar on the right hand side.

After the initial 1200 seconds of the durability test many of the textures remain active, allowing for the provision of lubricating fluid and the friction reducing mechanisms described earlier. The fluid aids in maintaining the surface temperature. The removal of wear debris between the surfaces and a reduction in frictional heat reduces the formation of transfer film. Moreover these reductions allow for the transfer film to flatten and become uniform as shown in Figure 7-20a and b compared to the upper surface of the control examination. However, the secondary supply of lubricant and the wear trapping capabilities of the textured cavities becomes counter-intuitive as the generation of wear increases. The generated wear particles fill the cavities to a point where the volume of the texture becomes saturated and no longer facilitates the capture of wear debris and nullifies the source of secondary lubrication. This phenomenon culminates in the rise in friction and acoustic emissions. Once the textured surface has reached complete saturation; with no secondary supply of lubrication, in addition to the removal of a wear capturing

mechanism, the surface undergoes a similar wear process as that described for the control surface. The increase in frictional heat and the build-up and formation of irregular and non-uniform transfer film that results in the upper surface ploughing the lower surface causing failure at a friction coefficient of 1.

7.6 Conclusions

Durability tests were undertaken in order to assess the longevity of a textured surface compared to an un-textured, control sample. Three forms of parameters were analysed; friction coefficient, acoustic emission response and wear morphology. The results across all measurements illustrated the superior performance of a textured surface where it was shown that the longevity of the textured surface exceeded that of an un-textured surface by almost three times. The mechanisms associated with the surfaces ability to increase its longevity are multi-facetted. An additional experimental investigation was initiated in order to explore friction reducing mechanisms during highly loaded contact. This was achieved by performing low speed, high load tests and employing high speed frictional data acquisition in order to analyse the response.

The retention of lubricant within the contact zone provided a secondary source of lubrication, limiting the rises in surface temperature by frictional heating. The generation of wear particles were shown to have demonstrable consequences in terms of the un-textured (control) surface. Second-body abrasion which then developed into third-body abrasive wear by the transfer of wear particles to the moving surface created an irregular non-conformal surface that ploughed through the lower surface causing excessive wear. Conversely, however, the presence of fluid within the contact zone aided in the expulsion of wear debris from the contact zone, furthermore, wear particles that were not expelled

become trapped within the texture cavities, reducing excessive wear through abrasive mechanisms. However, the mechanism of wear particle capturing was found to become counter intuitive when the test was extended to failure. The texture cavities became saturated and the surface lost the ability to provide both a secondary source of lubrication and to capture abrasive wear particles. Once saturation occurred the resultant acoustic emission and frictional response indicates that the textured surface undergoes an identical wear process to that seen for the control surface resulting in excessive ploughing of the lower surface to a point of failure.

CHAPTER 8

Conclusions

The body of work undertaken demonstrates the application of surface textures for friction and wear control for a PEEK on PEEK sliding couple. Textures in the form of dimple shaped cavities were applied to a PEEK surface via laser ablation using a femto-second laser and tribologically examined within an all polymer sliding couple. Laser ablation of the PEEK surface resulted in no bulges being present on the rim of the cavity post texturing and required no additional machining.

The surface wettability was found to have a profound impact upon the friction and wear performance of PEEK. Compared to an un-textured surface the friction and wear reduced as hydrophilicity increased. Increasing the hydrophilicity of the surface enabled the lubricant fluid to be retained within the contact zone and act as a secondary supply of lubrication encouraging further friction and wear reducing mechanisms. However, as the texture density increased the friction reducing effect diminishes and the friction increases.

Reciprocating sliding tests revealed that reductions in friction were prominent across all textures when compared to an un-textured plane surface. Optimization of texture parameters showed that cavities of a diameter of 50μm and depth of 20μm, dispersed over the surface at 20% density produced the lowest coefficient of friction.

A novel approach was employed during durability testing in the form of acoustic emission monitoring in order to capture tribological phenomena occurring between the two PEEK surfaces. AE was able to capture phenomena relating to individual strokes and show the

manifestation of acoustic emission magnitude and frequency content corresponding to surface condition throughout the test.

Improved wear performance of textured surfaces was shown within durability tests, with a textured surface lasting approximately three times longer than that of an un-textured plane surfaces. Tribological phenomena captured using the acoustic emission technique showed prominent spikes at the start of each stroke for the un-textured surface. The spikes in AE activity initially occurred at the beginning and end of each stroke as the upper specimen reversed in direction. The spikes were attributed to body to body contact encouraging the adhesive wear mechanism. The adhesive wear mechanism was responsible for the transfer of material to the counter-face and the presence of wear particles within the contact zone. The presence of wear debris, along with transfer film adhering to the counter-face, resulted in the ploughing of the lower sample, expedited by the removal of lubricant from the contact region and an increase in surface temperature through frictional heating.

In the case of the textured sample, limited AE content was detected in the first portion of durability testing. Major AE spikes were less obvious during these early stages and was attributed to a hydrostatic/hydrodynamic mechanism that lubricated the surface. Minor wear occurred within the early stages of testing with wear particles being trapped within the texture cavities. As the test time increased however, the debris capturing capabilities became detrimental to the friction and wear behaviour of the tribological system. The fluid that was previously expelled to the surface from the textured cavities under a hydrostatic/hydrodynamic mechanism was no longer present owing to the pores becoming saturated with wear debris. With the system unable to self-lubricate, the surfaces underwent the same wear modes as that described for the un-textured surface.

Provided below are the key findings from the research presented within this thesis.

1) Friction and wear reduced for all surface textures examined throughout the research conducted.
2) Improving the hydrophilicity of the surface enables fluid retention within the contact zone acting as a secondary source of lubrication as well as encouraging further lubrication mechanisms.
3) The hydrophobic nature of un-textured PEEK served to expel fluid from the contact zone accelerating adhesive and abrasive wear mechanisms.
4) Friction reduces along with wetting contact angle as texture density increases until a limit is reached and friction, wear and wetting contact angle increases.
5) The PEEK surface deforms under an applied load which enables a boost in lubrication by the entrapment of an incompressible fluid that generates a hydrostatic and hydrodynamic lubrication effect.
6) The wear trapping capabilities of the surface textures reduces abrasive wear and transfer film generation on the counter face.
7) The longevity of a textured surface is three times that of an un-textured surface owing to the above stated tribological enhancing mechanisms.
8) The operational of a PEEK surface, textured and un-textured, was captured by acoustic emission monitoring showing adhesive wear mechanism occurring at the stroke extremities signified by burst type signals. As the surface deteriorates the abrasive wear mechanism was dominant and was shown to produce a high frequency and amplitude signal throughout the stroke length.

9) Once textures become saturated by being filled with wear debris the textured surface undergoes similar wear modes to that of an un-textured surface, thus showing that there is an operational life span of surface textures applied to a PEEK surface before being worn away.

8.1 Contributions to Knowledge

The primary aim of this thesis was to explore the functionalisation of a Poly-ether-ether-ketone surface via the application of surface textures for friction and wear control within an all PEEK tribological system.

The following summary of contributions to knowledge have been made through the work presented within this thesis:

1. Arrays of dimple shaped textures were applied to the surface of PEEK through laser ablation. Textured pores with diameters ranging from 50μm to 200μm at depths of between 50μm and 20μm were dispersed over the surface at densities of between 5% and 30%. The laser ablation resulted in no ‘bulges’ evident around the rim of the diameter contrary to metallic materials that require additional material removal processes to remove bulges.
2. Friction within a PEEK-PEEK sliding couple can be reduced with the application of surface textures owing to improved lubrication from the texture cavities.
3. Fluid retention within the textures resulted in a hydrostatic/dynamic mechanism that served to support the load under static loading. Once relative motion commenced the mechanism converted to a hydrodynamic mode to support the applied load.

4. Friction and wear reduced within an all PEEK sliding couple resulting in improved durability. A textured surface was able to function for 3 times longer than an un-textured PEEK surface with texture parameters of 50μm diameter, and 20μm depth with a density of 20%.
5. The wear trapping capabilities of a PEEK textured surface resulted in a reduction in transfer film and abrasive wear. Once cavities became saturated the textured surface underwent a similar wear process to that of an un-textured surface.
6. The acoustic emission technique was employed as a means of monitoring tribological phenomena within an all PEEK sliding contact. It was shown that despite the insulation properties of PEEK an acoustic emission signal was transmitted through the material and was proportional to the extent of visual damage and measured wear of the surfaces post-test.
7. Clear correlation has been presented between the reciprocating stroke and AE signal generated. Early wear within the system was characterised by high amplitude spikes occurring at either end of the reciprocating stroke and was attributed to the adhesive wear mechanism. As the surface condition of PEEK deteriorated the AE signal increased in amplitude. Increases in frequency and magnitude also occur within the frequency domain and have been attributed to abrasive wear and surface deformation.

8.2 Critical Assessment and Further Work

The application of surface textures via femto-second laser ablation vaporises the material surface under substantial heat. Under such circumstance the effects of the machining process from a metallurgical stand point should be investigated. Focussing on the

morphology and transformations in crystalline and amorphous structure which could have an effect on the mechanical and thermal properties of the PEEK surface.

The methodology for deriving friction can be expanded to incorporate the density parameter. Although this would have increased the number of test runs, experimental methodologies can be employed to limit test and texture production. Adopting a partial factorial experimental design and regression modelling the friction results would enable the assessment of empirical results over a wider range that would be too costly and time consuming to undertake. The concept of friction mapping through regression modelling could also be adopted to introduce wear mapping of textured surfaces with varying parameter combinations.

Future analytical modelling of hydrodynamic behaviour within polymeric contacts should investigate the effect of surface compression where higher loads could change the depth profile of the textures. The cavitation regions within textures needs more understanding in order to create more robust and accurate models. Experimental investigations could involve using a high speed microscope camera to evaluate the cavitation region at the inlet of the texture pore.

The application of acoustic emissions within frictional contacts represents an opportunity to accumulate real-time data relating to tribological activity. The measurement of lubricant film could be a realistic possibility, a notion of which would benefit polymeric contacts. Using AE wave velocity and magnitude the system can be configured to detect the level of contact and hence monitor film thickness in real-time.

CHAPTER 9

WORKS CITED

Ahmed, M. H. & Bryne, J. A., 2012. Effect of surface structure and wettability of DLC and N-DLC thin films on adsorption of glycine. *Applied Surface Science*, 258(12), pp. 5166-5174.

Anderson, P. et al., 2007. Microlubrication effect by laser-textured steel surfaces. *Wear*, 262(3-4), pp. 369-379.

ASTM F732-00, 2011. Standard Test Method for Wear Testing of Polymeric Materials Used in Total Joint Prostheses. *ASTM International, West Conshohocken, PA, 2011, www.astm.org, DOI: 10.1520/F0732-00R11.*

Berkovits, A. & Fang, D., 1995. Study of fatigue crack characteristics by acoustic emission. *Engineering Fracture Mechanics*, 51(3), p. 401–409.

Bhushan, B., 2002. *Introduction to Tribology.* New York: John Wiley & Sons.

Bogdan , A., 2012. The effect of laser surface texturing on frictional performance of a sliding pair. *Scientic Journals*, 103(31), pp. 14 - 18.

Boness, R. J., McBride, S. L. & Sobczyk, M., 1990. Wear studies using acoustic emission techniques. *Tribology International*, 23(5), pp. 291-295.

Borghi, A. et al., 2008. Tribological effects of surface texturing on nitriding steel for high-performance engine applications. *Wear*, 265(7-8), pp. 1046-1051.

Bovington, C. H., 2010. Friction,Wear and the Role of Additives in Controlling Them. In: R. M. Mortier, M. F. Fox & S. T. Orszulik, eds. *Chemistry and Technology of Lubricants.* 3rd ed. London: Springer, pp. 77-105.

Bowden, F. P. & Tabor, D., 1966. Friction, lubrication and wear: a survey of work during the last decade. *British Journal of Applied Physics,* Volume 17, pp. 1521-1544.

Brizmer, V., Kligerman, Y. & Etsion, I., 2003. A laser surface textured parallel thrust bearing. *Tribology Transactions,* 46(3), pp. 397-403.

Brown, S. A., 2006. Sythetic Biomaterials for Spinal Applications. In: S. M. Kurtz & A. A. Edidin, eds. *Spine Technology Handbook.* London: Elsevier, pp. 11-33.

Castrol, 2014. *Castrol Product Data Sheet.* [Online] Available at: https://msdspds.castrol.com/bpglis/FusionPDS.nsf/Files/4C6EC640BA38BC3E80257DB00016D29B/$File/BPXE-9SSM3N.pdf

Catlin, J. B., 1983. *The use of ultrasonic diagnostic technique to detect rolling element bearing defects.* Houston, TX, Vibration Institute, pp. 123-130.

Charnley, J. W., 1960. The lubrication of animal joints in relation to surgical reconstruction by arthroplasty. *Annals of the Rheumatic Diseases,* 19(1), pp. 10-19.

Chen , P. et al., 2016. Effect of triangular texture on the tribological performance of die steel with TiN coatings under lubricated sliding condition. *Applied Surface Science,* Volume 389, pp. 361-368.

Cho, M. & Choi, H. J., 2014. Optimization of surface texturing for contact between steel and ultrahigh high molecular weight polyethylene under boundary lubrication. *Tribology Letters,* 56(3), pp. 409-422.

De Aza, A. H. et al., 2002. Crack growth resistance of alumina, zirconia and zirconia toughened alumina ceramics for joint prostheses. *Biomaterials,* 23(3), pp. 937-945.

Dowson, D., 1966. Modes of lubrication in human joints: Lubrication and wear in living and artificial human joints. *Proceedings of the Institution of Mechanical Engineers,* 181(10), pp. 45-54.

Dowson, D. & Higginson, G. R., 1977. *Elasto-Hydrodynamic Lubrication.* Oxford: Pergamon Press Ltd.

Dumitru, G. et al., 2000. Laser microstructuring of steel surfaces for tribological applications. *Applied Physics,* 70(4), pp. 485-487.

Dwyer-Joyce, R. S., Reddyhoff, T. & Zhu, J., 2011. Ultrasonic Mesurement for Film Thickness and Solid Contact in Elastohydrodynamic Lubrication. *Journal of Tribology,* 133(3), pp. 1-11.

East, R. H., Briscoe, A. & Unsworth, A., 2015. Wear of PEEK-OPTIMA® and PEEK-OPTIMA®-wear performance articulating against highly cross-linked polyethylene. *Journal of Engineering in Medicine,* 229(3), pp. 187-193.

Ebner, M. et al., 2018. On the effect of starved lubrication on elastohydrodynamic (EHL) line contacts. *Tribology International,* Volume 118, pp. 515-523.

Eckold, D. G., Dearn, K. D. & Shepherd, D. E. T., 2015. The evolution of polymer wear debris from total disc arthroplasty. *Biotribology,* Volume 1-2, pp. 42-50.

Etsion, I., 2004. Improving tribological performance of mechanical components by laser surface texturing. *Tribology Letters,* 17(4), pp. 733-737.

Etsion, I., 2005. State of the art in laser surface texturing. *Journal of Tribology,* 127(1), pp. 248-253.

Etsion, I., 2013. Modeling of surface texturing in hydrodynamic lubrication. *Friction,* 1(3), pp. 195-209.

Etsion, I. & Burstein, L., 1996. A model for mechanical seals with regular microsurface structure. *Tribology Transactions,* 39(3), pp. 677-683.

Etsion, I. & Halperin, G., 2002. A surface textured hydrostatic mechanical seal. *Tribology Transactions,* 45(3), pp. 430-434.

Gao, L. M. et al., 2010. The effect of aspherical geometry and surface texturing on the elastohydrodynamic lubrication of metal-on-metal hip prostheses under physiological loading and motions. *Journal of Mechanical Engineering Science,* 224(12), pp. 2627-2636.

Grischke, M., Hieke, A., Morgenweck, F. & Dimigen, H., 1998. Variation of the wettability of DLC-Coatings by network modifications using silicon and oxygen. *Diamond and Related Materials,* 7(2-5), pp. 454-458.

Grosse, C. U. a. M. O., 2008. *Acoustic emission testing.* Berlin: Springer Science & Business Media.

Hammouti, S. et al., 2015. Elaboration of submicron structures on PEEK polymer by femtosecond laser. *Applied Surface Science,* Volume 327, pp. 277-287.

Haque, T. et al., 2009. Effect of oil additives on the durability of hydrogenated DLC coating under boundary conditions. *Wear,* 266(1-2), pp. 147-157.

Hargittai, S., 2006. *Savitzky-Golay Least-Squares Polynomial Filters in ECG Signal Processing.* Lyon, IEEE.

Hase , A., Mishina, H. & Wada, M., 2012. Correlation between features of acoustic emission signals and mechanical wear. *Wear,* Volume 292-293, pp. 144-150.

Hase, A., 2015. *Acoustic Emissions during Tribological Processes.* Tokyo, Japanese Society of Tribologists.

Hase, A., Mishina, H. & Wada, M., 2016. Fundamental study on early detection of seizure in journal bearings using acoustic emission technique. *Wear,* Volume 346-347, pp. 132-139.

Hisakado, T. & Warashina, T., 1998. Relationship between friction and wear properties and acoustic emission characteristics: iron pin on hardened bearing steel disk. *Wear,* 216(1), p. 1–7.

Hori, Y., 2006. *Hydrodynamic Lubrication.* Tokyo: Springer-Verlag.

Hsu, S. M., Jing, Y., Hua, D. & Zhang, H., 2014. Friction reduction using discrete surface textures: principle and design. *Journal of Physics D: Applied Physics,* 47(33).

Huang, W., Jiang, L., Zhou, C. & Wang, X., 2012. The lubricant retaining effect of micro-dimples on the sliding surface of PDMS. *Tribology International,* Volume 52, pp. 87-93.

Hutchings, I. M., 2016. Leonardo da Vinci′s studies of friction. *Wear,* Volume 360-361, pp. 51-66.

Hu, T. & Hu, L., 2012. The study of tribological properties of laser-textured surface of 2024 aluminium alloy under boundary lubrication. *Lubrication Science,* 24(2), pp. 84-93.

Ingham, E. & Fisher, J., 2005. The role of macrophages in osteolysis of total joint replacement. *Biomaterials,* 26(11), pp. 1271-1286.

Ito, H. et al., 2000. Reduction of polyethylene wear by concave dimples on the frictional surface in artificial hip joints. *The Journal of Arthroplasty*, 15(3), pp. 332-338.

Jiaa, C. L. & Dornfeld, D. A., 1990. Experimental studies of sliding friction and wear via acoustic emission signal analysis. *Wear,* 139(2), pp. 403-424.

Kalin, M. & Polajnar, M., 2014. The wetting of steel, DLC coatings, ceramics and polymers with oils and water: The importance and correlations of surface energy, surface tension, contact angle and spreading. *Applied Surface Science,* Volume 293, pp. 97-108.

Khonsari, M. M. & Booser, E. R., 2017. *Applied Tribology: Bearing Design and Lubrication.* 3RD ed. Chichester: Wiley.

Kovalchenko, A. et al., 2005. The effect of laser surface texturing on transitions in lubrication regimes during unidirectional sliding contact. *Tribology International*, 38(3), pp. 219-225.

Kurtz, S. M. et al., 2007. Polyethylene wear and rim fracture in total disc arthroplasty. *The Spine Journal,* 7(1), pp. 12-21.

Kustandi, T. S., Choo, J. H., Low , H. Y. & Sinha, S. K., 2009. Texturing of UHMWPE surface via NIL for low friction and wear properties. *Journal of Applied Physics D: Applied Physics,* 43(1).

Lingard, S., Yu, C. W. & Yau, C. F., 1993. Sliding wear studies using acoustic emission. *Wear,* Volume 162, p. 597–604.

Liu, Y. & Li, G., 2012. A new method for producing "Lotus Effect" on a biomimetic shark skin. *Journal of Colloid and Interface Science,* Volume 388, pp. 235-242.

Ljubas, D., Krpan, H. & Matanovic, I., 2010. Influence of engine oils dilution by fuels on their viscosity, flash point and fire point. *Nafta,* 61(2), pp. 73 - 79.

MacConaill, M. A., 1932. The function of intra-articular fibrocartilages, with special reference to the knee and inferior radio-ulnar joints. *Journal of Anatomy,* Volume 66, pp. 210-227.

Mba, D., 2003. Acoustic emissions and monitoring bearing health. *Tribology Transactions,* 46(3), pp. 447-451.

Mba, D. & Rao, R. B., 2006. Development of acoustic emission technology for condition monitoring and diagnosis of rotating machines; bearings, pumps, gearboxes, engines and rotating structures. *The Shock and Vibration Digest,* 38(1), pp. 3-16.

McCutchen, C. W., 1959. Mechanism of animal joints: Sponge-hydrostatic and weeping bearings. *Nature,* Volume 184, pp. 1284-1285.

Myshkin, N. K., Protrokovets, M. I. & Kovalev, A. V., 2005. Tribology of polymers: Adhesion, friction, wear, and mass-transfer. *Tribology International,* 38(11-12), pp. 910-921.

Pettersson, U. & Jacobson, S., 2003. Influence of surface texture on boundary lubricated contacts. *Tribology International,* 36(11), pp. 857-864.

Pollock, A. A., 1973. Acoustic emission - 2: Acoustic emission amplitudes. *Non-Destructive Testing,* 6(5), pp. 264-269.

Qin, L. et al., 2013. Influence of surface wettability on the tribological properties of laser textured Co–Cr–Mo alloy in aqueous bovine serum albumin solution. *Applied Surface Science,* Volume 268, pp. 79-86.

Rahmani, R., Shirvani, A. & Shirvani, H., 2007. Optimization of Partially Textured Parallel Thrust Bearings with Square-Shaped Micro-Dimples. *Tribology Transactions,* 50(3), pp. 401-406.

Reynolds , O., 1886. On the theory of lubrication and its application to Mr Beauchamp Tower's experiments. *Philosophical Transactions of the Royal Society of London,* Volume 177, pp. 157-234.

Roberts, T. M. & Talebzadeh, M., 2003. Acoustic emission monitoring of fatigue crack propagation. *Journal of Constructional Steel Research,* 59(6), p. 695–712.

Ronen, A., Etsion, I. & Kligerman, Y., 2001. Friction-reducing surface-texturing in reciprocating automotive components. *Tribology Transactions,* 44(3), pp. 359-366.

Ryk, G., Kligerman, Y. & Etsion, I., 2002. Experimental investigation of laser surface texturing for reciprocating automotive components. *Tribology Transactions,* 45(4), pp. 444-449.

Sabri, L. & El Mansori, M., 2009. Process variability in honing of cylinder liner with vitrified bonded diamond tools. *Surface Coating and Technology,* 204(6-7), pp. 1046-1050.

Sagbas, B. & Durakbasa, M. N., 2013. Effect of surface patterning on frictional heating of vitamin E blended UHMWPE. *Wear,* 303(1-2), pp. 313-320.

Schmid, S. R., Hamrock, B. J. & Jacobson, B. O., 2014. *Fundamentals of Machine Elements.* 3rd ed. Boca Ratin: CRC Press.

Scholes, S. C. & Unsworth, A., 2009. Wear studies on the likely performance of CFR-PEEK/CoCrMo for use as artificial joint bearing materials. *Journal of Materials Science: Materials in Medicine,* 20(1), pp. 163-170.

Singh, A. & Kahp-Yang Suh, 2013. Biomimetic patterned surfaces for controllable friction in micro-and nanoscale devices. *Micro and Nano Systems Letters,* 1(6).

Speich, G. R. & Schwoeble, A. J., 1975. Acoustic emission during phase transformation in steel. *Monitoring Structural Integrity by Acoustic Emission,* pp. 40-58.

Stachowiak, G. & Batchelor, A. W., 1993. *Engineering Tribology.* 1 ed. Oxford: Butterworth-Heinemann.

Sun, J. et al., 2005. Wear monitoring of bearing steel using electrostatic and acoustic emission techniques. *Wear,* 259(7-12), p. 1482–1489.

Swindlehurst, W., 1973. Acoustic emission - 1 Introduction. *Non-Destructive Testing,* 6(3), p. 152–158.

Tang, W., Zhou, Y., Zhu, H. & Yang, H., 2013. The effect of surface texturing on reducing the friction and wear of steel under lubricated sliding contact. *Applied Surface Science,* Volume 273, pp. 199-204.

Tanner, R. I., 1966. An alternative mechanism for the lubrication of synovial joints. *Physics in Medicine & Biology,* 11(1), pp. 119-127.

Tomanik, E., 2013. Modelling the hydrodynamic support of cylinder bore and piston rings with laser textured surfaces. *Tribology International,* Volume 59, pp. 90-96.

Venables, W. N. & Ripley, B. D., 1999. *Modern Applied Statistics with S-PLUS.* 3 ed. New York: Springer Science & Business Media .

Victrex, 2014. *Victrex PEEK 450G Data Sheet.* [Online] Available at: https://www.victrex.com/~/media/datasheets/victrex_tds_450g.pdf [Accessed 06 09 2015].

Wang, W. et al., 2013. The Effect of Triangle-Shaped Surface Textures on the Performance of the Lubricated Point-Contacts. *Journal of Tribology,* 135(2).

Wonham, J., 1967. Effect of pressure on the viscosity of water. *Nature,* Volume 215, pp. 1053-1054.

Xin, H., Shepherd, D. T. & Dearn, K. D., 2013. A tribological assessment of a PEEK based self-mating total cervical disc replacement. *Wear,* 303(1-2), pp. 473-479.

Yan, D., Qu, N., Li, H. & Wang, X., 2010. Significance of dimple parameters on the friction of sliding surfaces investigated by orthogonal experiments. *Tribology Interactions,* 53(5), pp. 703-712.

Yuan, S., Huang, W. & Wang, X., 2011. Orientation effects of micro-groves on sliding surfaces. *Tribology International,* 44(9), pp. 1047-1054.

Yu, H., Wang, X. & Zhou, F., 2010. Geometric Shape Effects of Surface Texture on the Generation of Hydrodynamic Pressure Between Conformal Contacting Surfaces. *Tribology Letters,* 37(2), pp. 123-130.

Zeh, A. et al., 2007. Release of cobalt and chromium ions into the serum following implantation of the metal-on-metal maverick-type artificial lumbar disc (Medtronic Sofamor Danek). *Spine,* 32(3), pp. 348-352.

Zhang, B., Huang, W., Wang, J. & Wang, X., 2013. Comparison of the effects of surface texture on the surfaces of steel and UHMWPE. *Tribology International,* Volume 65, pp. 138-145.

Zhang, B., Huang, W., Wang, J. & Wang, X., 2013. Comparison of the effects of surface texture on the surfaces of steel and UHMWPE. *Tribology International,* Volume 65, pp. 138-145.

Zhang, B., Huang, W. & Wang, X., 2012. Biomimetic surface design fot ultra high molecular weight polyethylene to improve the tribological properties. *Proceedings of the Institute of Mechanical Engineers, Part J: Journal of Engineering Tribology,* 226(8), pp. 705-713.

Zhang, S. L., 2006. Chapter 3 - Friction, Damage and Stick-Slip in the Scratching of Polymers. *Tribology and Interface Engineering Series*, Volume 51, pp. 56-84.